

Cross sections data adjustment for KRITZ-2:13

Abdulaziz Ahmed^{*,1,2}, H. Boukhal¹, E. Chakir³, S. EL Ouahdani⁴.

¹*Radiations and Nuclear Systems Laboratory, University Abdelmalek Essaadi
Faculty of Sciences of Tetuan, Morocco*

²*Dept. of Physics, University of Abyan, Faculty of Lawder, YEMEN*

³*SIMO-LAB, Faculty of Sciences, Ibn Tofail University, Kenitra, Morocco*

⁴*Dept. of Physics ,Laboratory, , Sultan Moulay Slimane University, Beni Mellal, Morocco*

**Corresponding author: azezs84@hotmail.com*

Abstract

Over the past years, the cross-sections reaction data has been re-evaluated several times, in order to approximate the nuclear model measurements with the predictions with great reliability. In our work, uncertainty analysis caused by the data on the neutron factor (K_{eff}) and the reactivity temperature coefficient (RTC), in addition to nuclear data adjustment related to the nuclear reactor physics have been done for KRITZ-2:13 reactor, with ENDF/B - VII.1, ENDF/B - VIII.0 and JENDL - 4.0 evaluations by the nuclear code MCNP6.1. Our analysis detects that the greatest uncertainty on K_{eff} and RTC in the studied libraries comes from the capture and fission reaction contributions respectively, for U-238 and U-235. The previous reactions and their covariances were adjusted using the generalized least squares method (GLLSM), in order to contribute to improve the data needed for neutron simulation of experiments and to ensure the installations safety, where K_{eff} and RTC represent neutron parameters reflecting the modification effects in the data.

Keywords: Covariance matrix; KRITZ; nuclear uncertainty; sensitivity; temperature coefficient.

1. Introduction

Practical necessity is the main motivation for research in the field of nuclear uncertainty and its re-evaluation. These uncertainties can propagate through nuclear system simulations into safety and operation related parameters. Inaccurate treatment of uncertainty in nuclear reactor operating and design can affect the economic efficiency and thus the sustainability of nuclear power. It is therefore important in the study and design of nuclear reactors to carry out an accurate re-evaluation of the cross section uncertainties on the critical neutron coefficients as K_{eff} and RTC.

Cross-section data helps reveal the reaction phenomenon's mechanisms within the process of a nuclear reaction (Hasan Özdoğan *et al.*, 2021). This data depended on nuclear experiments, is the fundamental component of Monte Carlo and deterministic methods that are constantly being improved to reduce the uncertainties related to this data. Nuclear uncertainty can be improved by a variety of statistical techniques (C. de Saint-Jean *et al.*, 2010) such as Lagrange multipliers, Monte Carlo total, etc. But the generalized least squares

technique stays the most suitable. This current work is dedicated to the study and re-evaluation of data uncertainty regarding nuclear reactor physics for the important isotopes in a structure of 15-group energy. The capture cross-section of U-238 and fission of U-235 have significant uncertainty values on both K_{eff} and RTC coefficients in all the libraries studied ENDF/B - VII.1 (Chadwick *et al.*, 2011), ENDF/B - VIII.0 (D. A. Brown *et al.*, 2018) and JENDL - 4.0 (K. SHIBATA *et al.*, 2011) (that will be mentioned later as the two ENDF/Bs and JENDL libraries). These reactions are the main cause of deviations between the calculated and benchmark values of the two coefficients. It is recommended to modify these cross-sections as well as their covariance matrices in all libraries. Adjustment of these reactions data will contribute to reducing the uncertainty values on K_{eff} and RTC and thus correcting the calculated values of these neutron coefficients.

KRITZ benchmarks performed in Sweden, during the 70s and included three experiments that will be critical at cold temperatures (KRITZ-2:1C, KRITZ-2:13C and KRITZ-2:19C) and at hot temperatures (H configurations), the first two are with uranium rods, and the last one with fuel of mixed-oxide. The rods are on a square pitch, surrounded by a light water reflector. KRITZ-2:13 core (the study axis) was square and consisted of a regular lattice of UO₂ fuel rods on a 1.635 cm pitch. Its C configuration was at 22.1C and the H configuration at 243.0 C. Additional details on KRITZ benchmarks are in Refs. (L. SNOJ *et al.*, 2009; I. REMEC *et al.*, 2002; International Handbook of Evaluated Reactor Physics Benchmark Experiments, 2011; Benchmark on the KRITZ-2 LEU and MOX Critical Experiments, 2006).

Experimental uncertainties of the benchmark values of K_{eff} were 210 and 200 pcm, respectively, for C and H configurations of KRITZ-2:13, where the modeling uncertainties were 8 pcm for both configurations. The small value of the statistical uncertainty was obtained from the following data: 40,000 neutrons per cycle for 1600 effective cycles from total number of 1750.

The old versions (4B and 4C) of the code MCNP with old versions of some libraries: (3.2 and 3.3) of JENDL, (90.2 and 2002) of IRDF and (V and VI) of ENDF/B have been used in one of the studies of the KRITZ reactor (Benchmark on the KRITZ-2 LEU and MOX Critical Experiments, 2006), which is concerned with the analysis of sensitivity and nuclear uncertainty about the K_{eff} . This study showed that the greatest participation in sensitivity and nuclear uncertainty for KRITZ-2:13 comes from the capture reaction of U-238. Sensitivities were nearly identical for all libraries, while uncertainty varied from one library to another.

2. Methodology

By using the card KSEN from the code MCNP6.1 (Denise *et al.*, 2014) we have generated the sensitivity coefficients of isotope reactions at 22.1C and 243C, respectively, for KRITZ-2:13C and KRITZ-2:13H in an energy range partitioned into 15 groups (table 1) for the neutron coefficients K_{eff} and RTC. These sensitivities have been calculated based on the adjoint-weighting technique that does not take into account disturbances that may appear from fission spectra or scattering laws (Romojaro *et al.*, 2017), which may lead to spurious and false results in the measurements (Denise *et al.*, 2014). NJOY system (Macfarlane *et al.*, 2017) has been used to convert the ENDF6 data of the libraries into ACE format necessary for

MCNP code, as well as to generate the covariances, by means of ERRORJ module. Sensitivities G and covariances M will be combined according to the first equation in order to calculate the nuclear uncertainty on K_{eff} :

$$\frac{\Delta k_{eff}}{k_{eff}} = G^+ M G, \quad G^+ \text{ is a transpose of } G \quad (1)$$

Table 1. Energy groups (A. Ahmed *et al.*, 2019)

Numbers	Energy groups (ev)
1	1.00E-5 - 0.110
2	0.110 – 0.540
3	0.540- 4.00
4	4.00 - 22.6
5	22.6 - 454
6	454 - 2030
7	2030 - 9120
8	9120 - 24800
9	24800 - 67400
10	67400 - 1.83E+5
11	1.83E+5 - 4.98E+5
12	4.98E+5 - 1.35E+6
13	1.35E+6 - 2.23E+6
14	2.23E+6 - 6.07E+6
15	6.07E+6 - 1.96E+07

For a temperature range $[T_1, T_2]$, with neutron factors $[K_{eff1}, K_{eff2}]$, the RTC could be obtained by the following formula (El Ouahdani *et al.*, 2015):

$$\alpha = \frac{1}{\Delta T} \frac{K_{eff2} - K_{eff1}}{K_{eff1} K_{eff2}} \quad (2)$$

Considering the quantity $\Delta T = T_2 - T_1$ is constant, we can find:

$$\Delta \alpha = \left[\frac{\Delta K_{eff2}}{(K_{eff2})^2} - \frac{\Delta K_{eff1}}{(K_{eff1})^2} \right] \frac{1}{\Delta T}$$

So, the nuclear uncertainty on the RTC can be expressed as:

$$\frac{\Delta \alpha}{\alpha} = \left[\frac{K_{eff1} \frac{\Delta K_{eff2}}{K_{eff2}} - K_{eff2} \frac{\Delta K_{eff1}}{K_{eff1}}}{K_{eff2} - K_{eff1}} \right] \quad (3)$$

K_{eff1} : Is the neutron multiplication factor at T_1

$\frac{\Delta K_{eff1}}{K_{eff1}}$: Is the relative uncertainty on K_{eff1} due to nuclear data at T_1

K_{eff2} : Is the neutron multiplication factor at T_2

$\frac{\Delta K_{eff2}}{K_{eff2}}$: Is the relative uncertainty on K_{eff2} due to nuclear data at T_2

Statements requiring adjustments in nuclear data (reactions that are important in the sensitivity analysis with uncertainty larger than 100 pcm (C. de Saint-Jean *et al.*, 2010)) that would produce the best agreement between the measured and calculated values of integral experiments - as GLLSM supposes-, have been carefully selected. Depending on GLLSM, this reactions data can be adjusted according to these equations (C. de Saint-Jean *et al.*, 2010 ; H. Kuroi & H. Mitani, 1975; V. Sobes *et al.*, 2016; Makhloul *et al.*, 2018):

$$T^{Adj} = T_0 + MG^t [GMG^t + V_e + V_m]^{-1} [R_e - R_c(T_0)] \quad (4)$$

$$M^{Adj} = M - MG^t [GMG^t + V_e + V_m]^{-1} GM \quad (5)$$

Where

T_0 and T^{Adj} are the cross sections before and after adjustment

M and M^{Adj} are the covariances before and after adjustment

R_e and R_c are measured and analytical values of integral experiments

V_e and V_m are experimental and modeling errors of integral experiments

3. Results

3.1./Critical Calculations

One of the advantages of the Monte Carlo method is to focus on the nuclear uncertainties by reducing the errors related to modeling and design. The critical coefficients (K_{eff} and RTC) for KRITZ-2:13 were calculated by the card KCODE from the code MCNP6.1, which offers complex geometry modeling capabilities with high accuracy 3-D calculations of the physical system (Zuhair *et al.*, 2021).

The calculated values of K_{eff} for the two configurations of KRITZ-2:13 with the three evaluations, the benchmark values, the experimental uncertainties and the relative differences are listed on table 2.

Table 2. Benchmark (Ivan Kodeli & Luka Snoj, 2012) And Calculated Values Of K_{eff}

KRITZ- Experiment		Benchmark		JENDL - 4.0		ENDF/B - VII.1		ENDF/B - VIII.0	
		K_{eff}	S.d pcm	K_{eff}	C/E-1 (%)	K_{eff}	C/E-1 (%)	K_{eff}	C/E-1 (%)
2:13	C	1.0013	210	0.99887	0.24	0.99892	0.23	0.99896	0.23
	H	1.0019	200	0.99800	0.38	0.99797	0.39	0.99835	0.35

For our two configurations of KRITZ-2:13 in the two ENDF/Bs and JENDL libraries, the simulated values of K_{eff} were underestimated from benchmark values. This underestimation will be explained by the uncertainty analysis. Due to the temperature effect, the underestimation in H configuration is less than of the C. There was a noticeable agreement between these calculated values for the three investigated libraries, with large deviations between them and the benchmark values. For all the studied configurations and libraries, the relative deviations are greater than the analytical and modeling errors, this calls for an uncertainty analysis of the nuclear data.

The library that gives calculated values for the K_{eff} closer to the benchmarks - Least deviations according to Figure 1 - in the two configurations, is the new library ENDF/B-VIII.0, ENDF-6 formats for some components and sections of fissile isotopes have been improved for this library.

Simulated values of the RTC for KRITZ-2:13 in the two ENDF/Bs and JENDL libraries are listed on table 3.

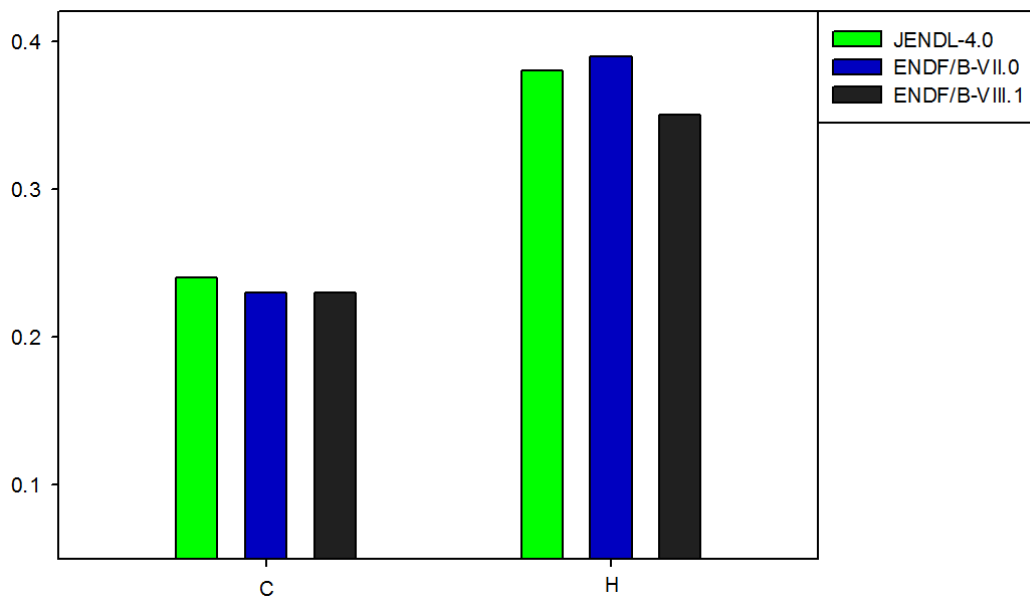


Fig. 1. Deviations Between Benchmark And Simulated Values Of K_{eff} For C and H Configurations Of KRITZ-2:13.

Table 3. Calculated Values Of RTC

α in pcm/°C			
Benchmark*	JENDL-4.0	ENDF/B-VII.1	ENDF/B-VIII.0
-0.03	-0.39	-0.43	-0.27

*/ According to the benchmark values of K_{eff} .

All the simulated values of RTC were systematically negative, as for safety standards, it is required that the RTC be negative (Kaddour *et al.*, 2013). The results showed a very good agreement between the considered libraries in the two configurations of KRITZ-2:13, with big deviations between them and the benchmark values. The absolute values of the RTC obtained

in our study for both evaluations JENDL-4.0 and ENDF/B-VII.1 are lower than of other study (El Ouahdani *et al.*, 2015) whose results were (-1.49 and -0.88) pcm/°C respectively for JENDL-4.0 and ENDF/B-VII.1. In that study the data was treated using the assistant code Makxsf (interpolation between two temperatures) along with the NJOY code. While in our study, we treated the data only with NJOY code for each temperature without the need for an assistant code.

3.2./ K_{eff} Sensitivity

Figures 2 and 3 show the integrated sensitivities over the 15 energies for C and H configurations of KRITZ-2:13. The reactions sensitivity to the K_{eff} is almost identical in the two ENDF/Bs and JENDL evaluations. The KRITZ-2:13 reactor with its critical configurations was very sensitive to the fission reaction of U-235 and the capture of U-238. The negative sensitivity of the latter reaction means that the large uncertainty value of this reaction will cause a decrease in the calculated values of K_{eff} in the three libraries. The reactions of capture for U-235 and the elasticity for H-1 also have important sensitivities in the investigated libraries.

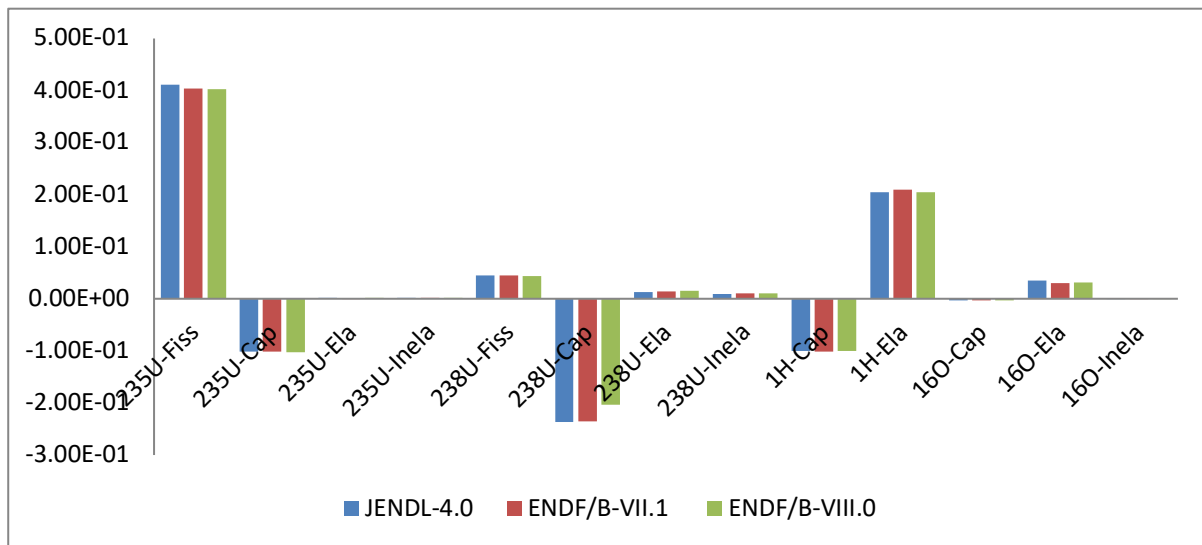


Fig. 2. Integrated sensitivities of K_{eff} for KRITZ-2:13C

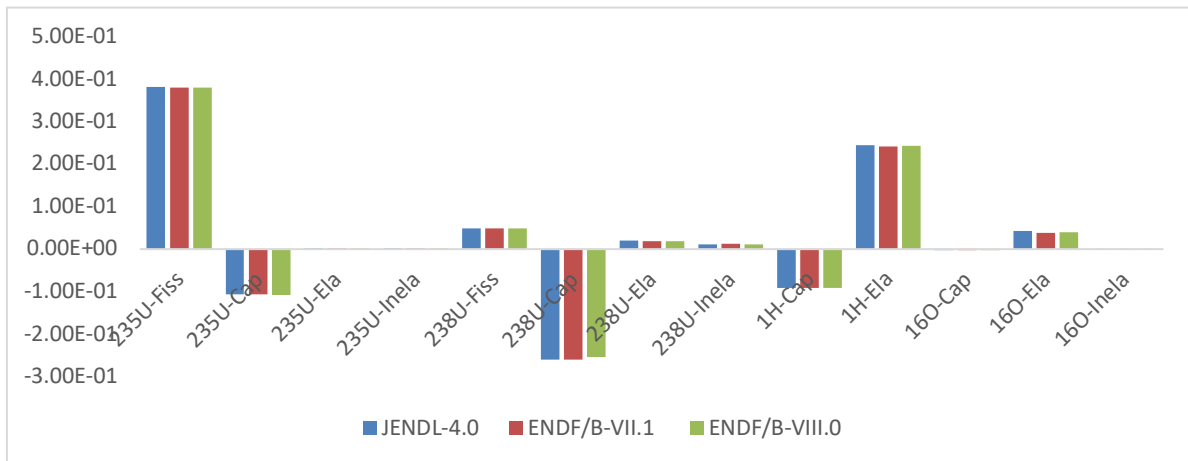


Fig. 3. Integrated sensitivities of K_{eff} for KRITZ-2:13H

3.3./RTC Sensitivity

According to equation 3, the uncertainty value of the reactivity coefficient depends to a large degree on the uncertainty values of the K_{eff} and, accordingly, on the values of its sensitivity coefficients. In other words, the values of the RTC uncertainty are not dependent on its own sensitivity values. However, we did analyze the RTC sensitivity to the reaction cross sections of the two ENDF/Bs and JENDL evaluations for KRITZ-2:13 experiment. The purpose of this analysis is to identify reactions for which the sensitivity to the cross-sections is large, whereas those reactions themselves have a significant contribution to the uncertainty on RTC. These will be the reactions that really need to be adjusted.

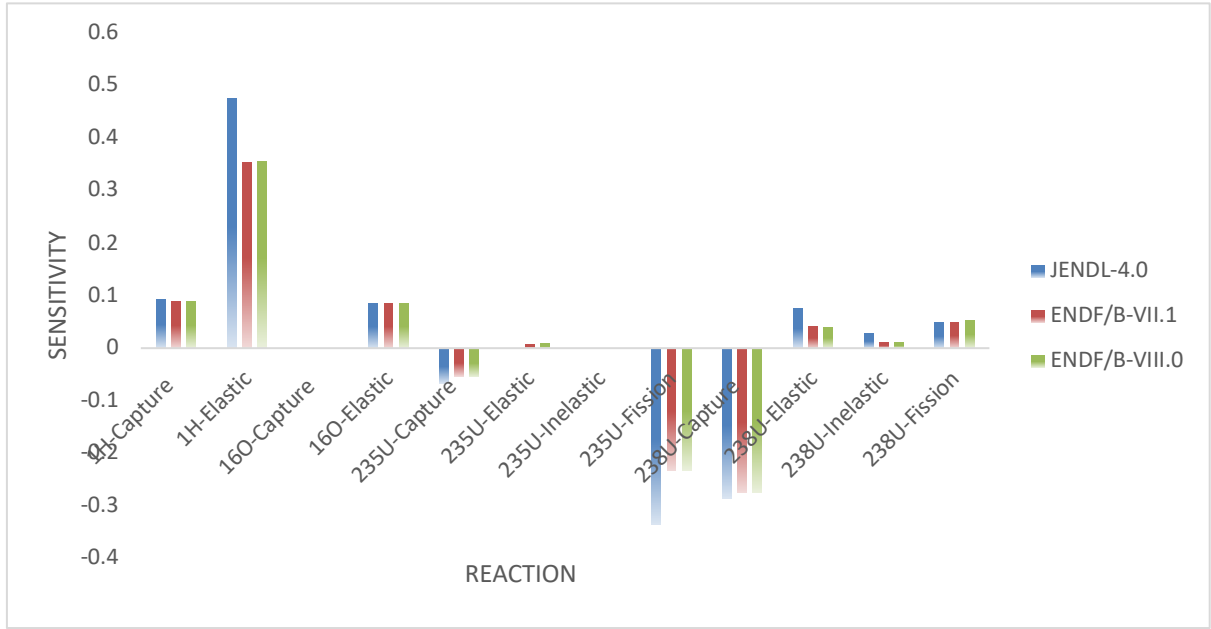


Fig. 4. Sensitivities of RTC for KRITZ-2:13

As shown on the previous figure, sensitivity analysis results showed a good consistency between the three different libraries reactions. The RTC in KRITZ-2:13 was large sensitive to fission and capture reactions, respectively of U- 235 and U-238 that are the most sensitive reactions in the three evaluations. Elastic cross section of H-1 is a considered reaction in the sensitivity analysis of RTC in all libraries, but its contribution to uncertainty is small as we will see in the uncertainty analysis.

3.4./Nuclear uncertainty

Data uncertainties on the K_{eff} , due to reactions of the four isotopes: H-1, O-16, U-235 and U-238 are shown on tables 4 and 5, respectively, for C and H configurations of KRITZ-2:13 with the two ENDF/Bs and JENDL evaluations. The reaction that contributes the most to the uncertainty on the K_{eff} and that which gives the greatest contribution to the total uncertainty for this coefficient is the capture reaction of U-238. The underestimation found in the calculated values of K_{eff} is mainly due to the great uncertainty of this reaction, as well as its large negative sensitivity in the three evaluated libraries for the two configurations of KRITZ-2:13. Fission reaction of U-235 in the three libraries, capture of the same isotope in ENDF/B-VII.1 and JENDL-4.0, and elastic of H-1 only in ENDF/B-VII.1 are also important in this

analysis for both configurations of KRITZ-2:13. In order to reduce the data uncertainties on the K_{eff} , all cross-sections of the previous reactions must be adjusted as well as their covariance matrices according to their mentioned libraries.

As we can see from figure 5, the greatest nuclear uncertainty on the RTC for KRITZ-2:13 is due to the capture reaction of U-238 in the three libraries. The fission reaction of U-235 also has a significant contribution to uncertainty on the RTC in all libraries, but by a smaller range from the capture of U-238.

Table 4. Uncertainties (in pcm) due to cross-sections for the configuration KRITZ-2:13C

cross-sections		JENDL-4.0	ENDF/B-VII.1	ENDF/B-VIII.0
		Uncertainty (pcm)	Uncertainty (pcm)	Uncertainty (pcm)
1H	(n, γ)	50.05	230.01	87.2
	(n,n)	51.95	118.52	95.0
16O	(n, γ)	61.50	132.35	16.03
	(n,n)	47.16	72.488	68.5
235U	(n, γ)	157.2	144.1	41.32
	(n,n)	1.043	0.555	0.269
	(n,n')	1.579	1.323	0.370
	(n,f)	172.8	138.1	165.3
238U	(n, γ)	322.3	356.76	202.3
	(n,n)	30.73	22.349	30.73
	(n,n')	59.32	174.15	30.86
	(n,f)	26.38	23.104	53.95
Total		418	536	310

Table 5. Uncertainties (in pcm) due to cross-sections for the configuration KRITZ-2:13H

cross-sections		JENDL-4.0	ENDF/B-VII.1	ENDF/B-VIII.0
		Uncertainty (pcm)	Uncertainty (pcm)	Uncertainty (pcm)
1H	(n, γ)	49.12	234.8	85.12
	(n,n)	53.51	123.9	90.70
16O	(n, γ)	65.50	130.23	18.65
	(n,n)	55.16	74.16	64.3
235U	(n, γ)	160.73	148.1	44.32
	(n,n)	1.103	1.444	0.634
	(n,n')	1.621	0.755	0.828
	(n,f)	164.82	129.5	157.8
238U	(n, γ)	342.7	395.7	224.23
	(n,n)	32.36	30.03	32.36
	(n,n')	63.16	189.9	29.84
	(n,f)	29.43	25.56	58.63
Total		434	570	320

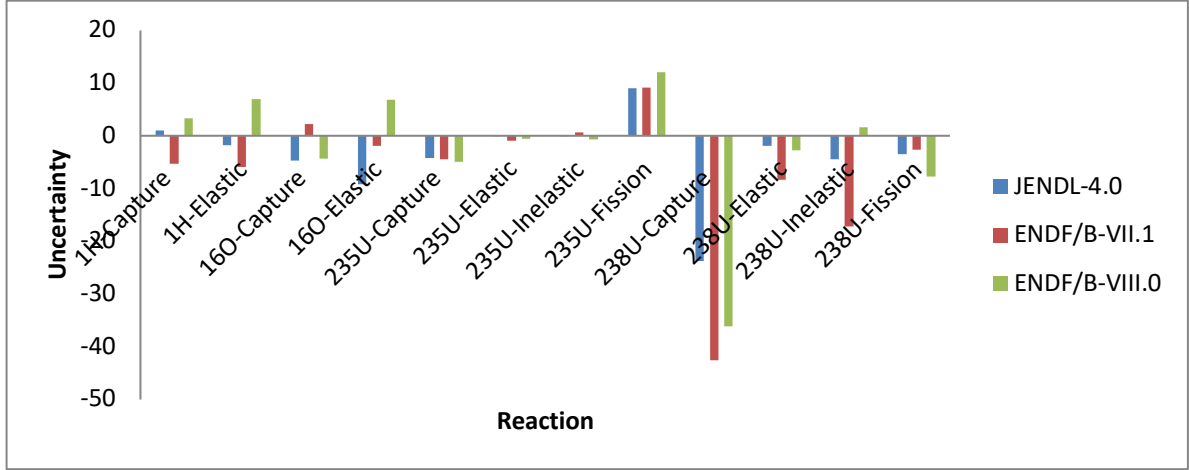


Fig. 5. Cross section uncertainties (in %) on RTC for KRITZ-2:13

4. Nuclear data adjustment

Ad-hoc adjustment were performed in this work on KRITZ:2-13 experiment in the three investigated nuclear data evaluations: the two ENDF/Bs and JENDL. The improvement of the multigroup cross sections for U-235, U-238, and H-1, and of the corresponding covariance matrices are executed using the generalized linear-least-squares methodology (GLLSM). Previous isotopes reactions that required modifications in the nuclear data for the K_{eff} and RTC coefficients were carefully selected. The results obtained for our benchmark will be given in term of adjusted covariance matrices, reduced uncertainty for K_{eff} and corrected values of RTC for the library ENDF/B-VII.1 that has the greatest uncertainty values, corrections for other libraries are not very different from this library.

Figures 6 to 9 illustrate the correlation matrices before and after adjustment for the cross sections of the U-235, U-238 and H-1. In each figure, we had to put the two matrices before and after adjustment in different colors. Drawing the two matrices with the same color - in principle - will give two completely identical shapes, because the differences between prior and posterior matrix are so small. The differences between the two matrices can be discerned by looking at the boundaries of them.

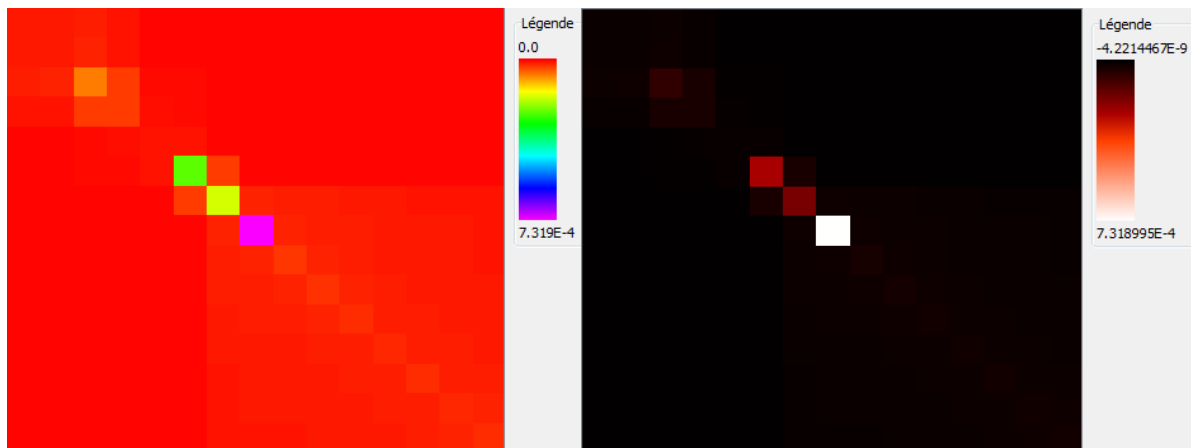


Fig. 6. Prior and posterior correlation matrices of the ^{235}U -fission cross section, respectively

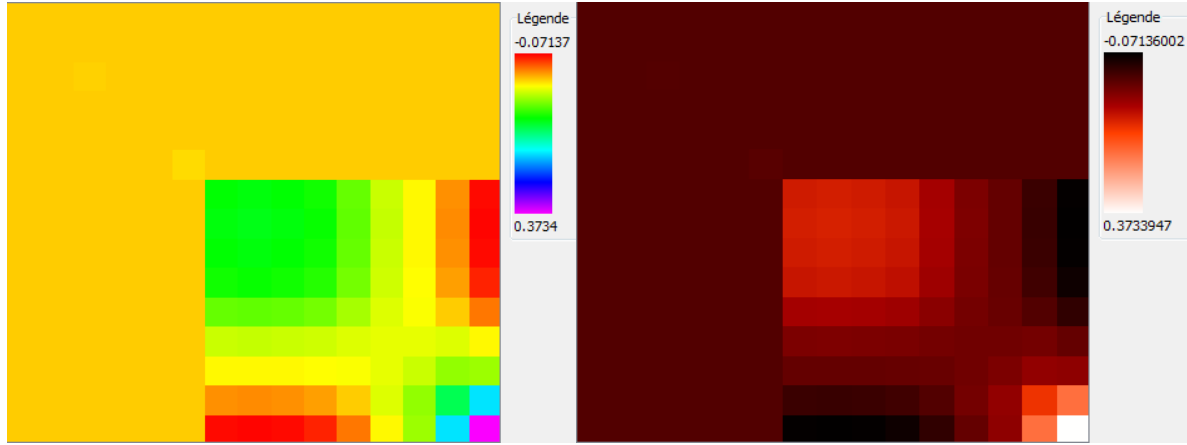


Fig. 7. Prior and posterior correlation matrices of the ^{235}U -capture cross section, respectively

From the latter figures, we notice that the correlations between the multigroup fission and capture cross sections of U-235 are decreased after adjustment, they changed from the range $(0 : 7.319\text{E-}04)$ to $(-4.22\text{E-}09 : 7.318\text{E-}04)$ for fission reaction, and from the range $(-0.07137 : 0.3734)$ to $(-0.07136 : 0.3733)$ for the capture. A reduction in nuclear uncertainty is expected as a result of adjusting the covariance matrices for these reactions.

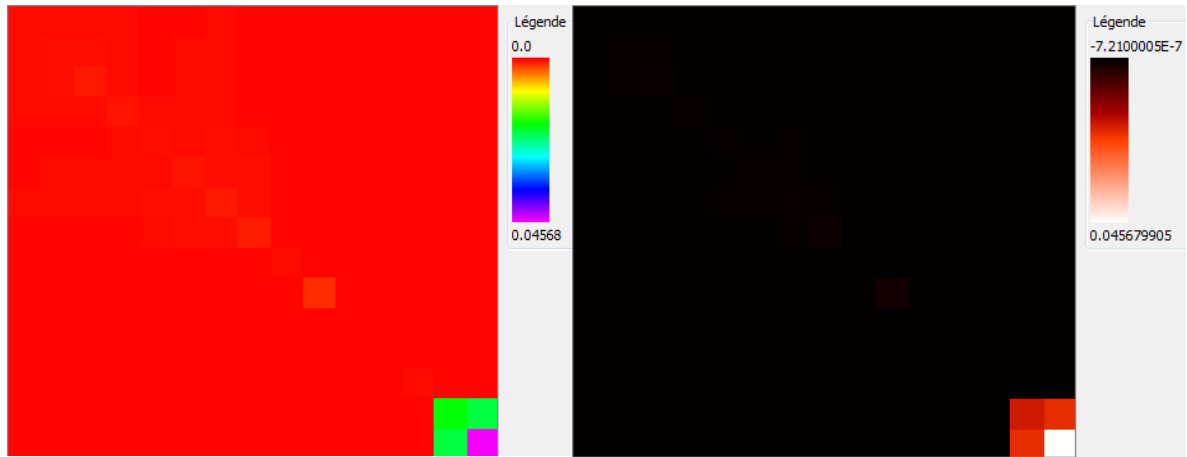


Fig. 8. Prior and posterior correlation matrices of the ^{238}U -capture cross section, respectively

It can be seen from figure 8 that some correlation coefficients are indeed reduced after adjustment and even negative correlations for some energy groups have appeared, where these negative correlation coefficients indicate anti-correlations. Consequently, the nuclear data uncertainties on K_{eff} due to the uncertainties of the capture cross section of U-238 will be reduced after adjustment. Even though some deviations from zero appear in this figure, those remain tiny, since the absolute values of these negative numbers are very small.

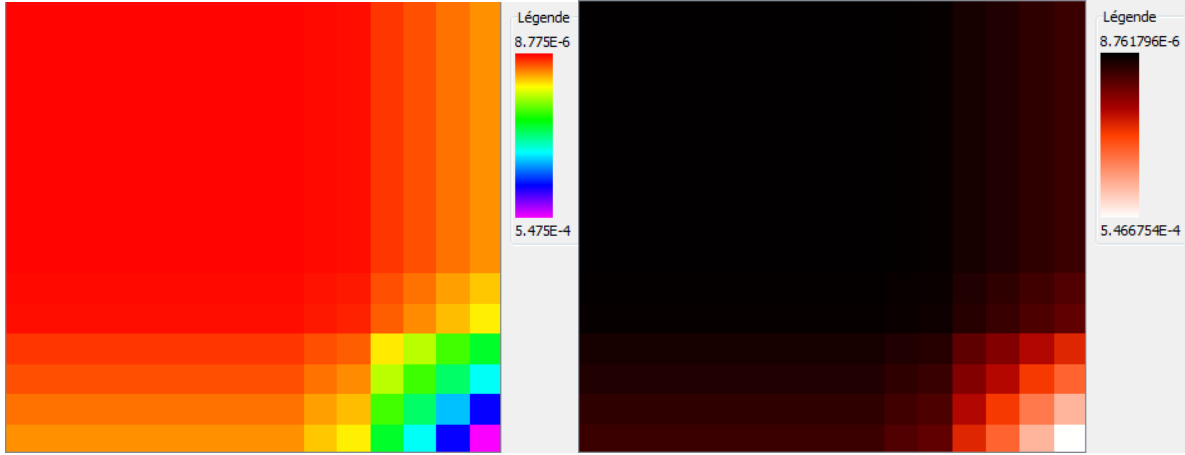


Fig. 9. Prior and posterior correlation matrices of the 1H-elastic cross section, respectively

From the figure 9, we can see that the correlation coefficients of the elastic cross section of H-1 are already reduced after adjustment, they changed from the range (8.77E-06 : 5.47E-04) to (8.76E-06 : 5.46E-04). The K_{eff} uncertainties due to this cross section will be reduced after adjustment, because of the attenuation in correlations.

Figure 10 represents a comparison of the uncertainty values on the K_{eff} for KRITZ-2:13C before and after adjustment.

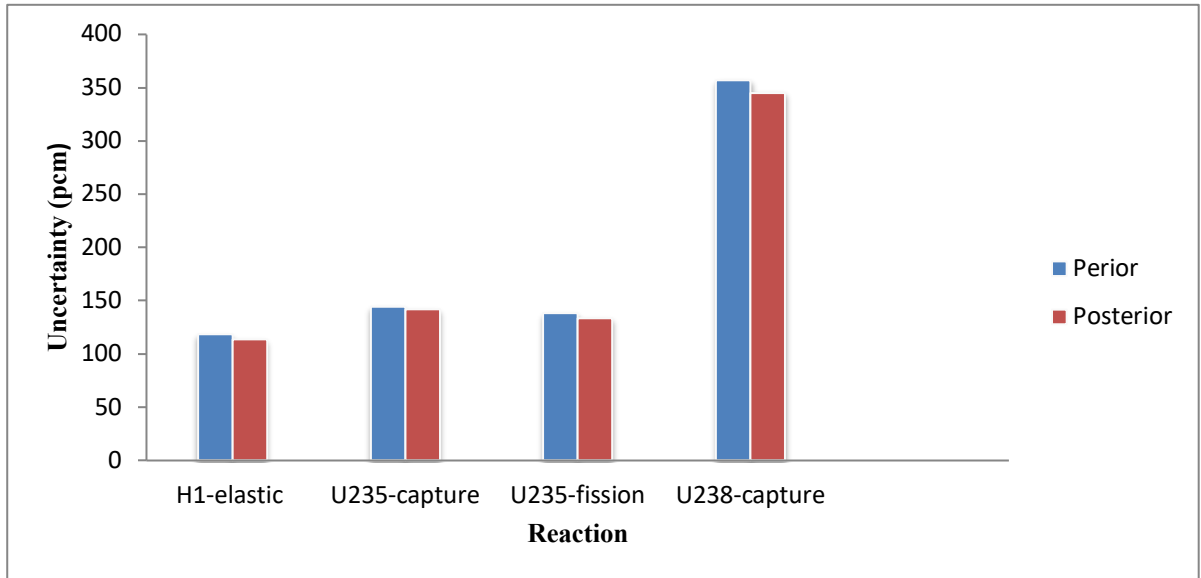


Fig. 10. Prior and posterior K_{eff} uncertainties

Carefully identified cross sections needing adjustments would make significant improvements in the C / E ratios of the benchmark used. Indeed, the use of the adjusted covariance data in the estimation of the posterior nuclear uncertainties has generated - according to figure 10 - noticeable reductions of these uncertainties. The greatest decrease in the uncertainty of the adjusted cross-sections was for the capture reaction of U-238, which we confirmed as the most important cross-section that needs to be modified in this study.

The corrected values of the reactivity temperature coefficient (Absolut values) caused by the improvement of the cross sections are shown on Figure 11.

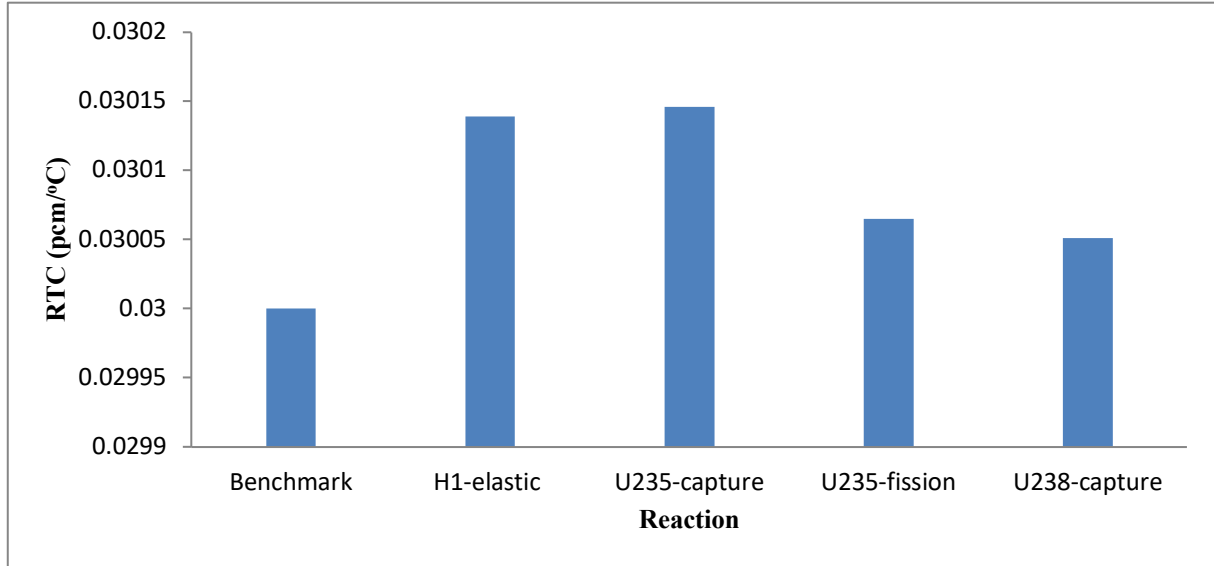


Fig. 11. Corrected value of RTC

In the framework of our study, we did not take into account the phenomenon of correlation between reactions, we are only interested in the contribution of the individual uncertainty of each cross-section as well as the amount of correction that this cross section will have. According to the previous figure, we note that the improvement performed on the nuclear data individually, made noticeable corrections for the calculated value of RTC, the absolute values of this coefficient were close to the benchmark values, where the calculated values before adjustment reached 0.76 pcm/°C. The largest correction for the RTC was, respectively, for the capture reaction of U-238 and fission of U-235, that have a significant uncertainty on this coefficient as well as on K_{eff} .

Capture reaction of U-235 and elastic of H-1 do not have a significant effect on the uncertainty of the RTC, yet their correction corrected the calculated value of this parameter. Cross-sections adjustment of these reactions contributed to decreasing the uncertainty value on the K_{eff} , and since the nuclear uncertainty of the RTC depends on the K_{eff} uncertainty, accordingly the RTC uncertainty will be reduced and the calculated value of this coefficient will be corrected.

5. Conclusion

K_{eff} and RTC nuclear uncertainty dependent on the sensitivity of nuclear data of the three libraries was calculated in this work for KRITZ-2:13 reactor at 22.1°C and 243°C using MCNP6.1 code (calculation of sensitivities) and the NJOY system (prepare data in ACE format and calculate covariance matrices).

Capture and fission, respectively, for U-238 and U-235 are the most important reactions in sensitivity as well as uncertainty analysis for both coefficients K_{eff} and RTC in the three libraries. In addition to capture and elastic reactions of U-235 and H-1 respectively, that are important just for the K_{eff} . Previous cross section reactions have been improved depending on GLLSM in an ad-hoc adjustment for KRITZ-2:13.

The results of this improvement, according to our presented study, contributed to decreasing the values of the reactions correlations, thus reducing the data uncertainty on the K_{eff} and correcting the calculated values of the RTC.

Reactions data adjustment for KRITZ-2:13 in parallel with many benchmarks such as those include in the ICSBEP Handbook will be the focus of our future work in order to increase the prediction accuracy of the calculations.

References

Ahmed, H. Boukhal, T. El Bardouni, M. Makhoul, E. Chakir & S. EL Ouahdani., (2019). Sensitivity and uncertainty analysis on keff due to nuclear data in the KRITZ-2:19 – Comparison between JENDL-4.0 and ENDF/B-VII.1. *Annals of Nuclear Energy*, vol. 129, p. 308–315.

“Benchmark on the KRITZ-2 LEU and MOX Critical Experiments,” NEA/NSC/DOC (2005) 24, Nuclear Energy Agency (2006). https://www.oecd-nea.org/jcms/pl_18320/benchmark-on-the-kritz-2-leu-and-mox-critical-experiments-final-report?details=true

C. de Saint-Jean *et al.*, (2010). Assessment of Existing Nuclear Data Adjustment Methodologies. Report NEA/NSC/WPEC/DOC-429.

Chadwick, M. B., Herman, M., Obložinský, P., Dunn, M. E., Danon, Y., Kahler, A. C., White, M. C., (2011). ENDF/B-VII.1 nuclear data for science and technology: Cross sections, covariances, fission product yields and decay data. *Nuclear Data Sheets*, 112(12), 2887-2996. DOI: 10.1016/j.nds.2011.11.002.

D. A. Brown *et al.*, (2018). ENDF/B-VIII.0: The 8th Major Release of the Nuclear Reaction Data Library with CIELO-project Cross Sections, New Standards and Thermal Scattering Data, *Nucl. Data Sheets*, 148.

Denise B. Pelowitz, Andrew J. Fallgren, and Garrett E. McMath., (2014). MCNP6 User's Manual: Code Version 6.1.1 beta, Los Alamos National Laboratory manual LA-CP-00745, Rev. 0.

El Ouahdani S., H. Boukhal, L. Erradi, E. Chakir, T El Bardouni, O. Hajjaji, Y. Boulaich, K. Benaalilou & M. Kaddour (2015). Monte Carlo analysis of KRITZ-2 critical benchmarks on the reactivity temperature coefficient using ENDF/B-VII.1 and JENDL-4.0 nuclear data libraries. *Ann. Nucl. Energy*, vol. 1, p. 107–118.

H. Kuroi & H. Mitani. (1975). Adjustment to cross section data to fit integral experiments by least squares method. *J. Nucl. Sci. Technol*, vol. 12, no 11, p. 663–680.

Hasan Özdoğan, Mert Şekerci, et Abdullah Kaplan, (2021). Production cross-section and reaction yield calculations for 123-126I isotopes on 123Sb(α ,xn) reactions. *Kuwait Journal of Scienc.* Vol. 48 No. 2, DOI: <https://doi.org/10.48129/kjs.v48i2.9310>.

“International Handbook of Evaluated Reactor Physics Benchmark Experiments,” NEA/NSC/DOC(2006)1, Nuclear Energy Agency (Mar. 2011).
https://inis.iaea.org/search/search.aspx?orig_q=RN:40064937

I. Remec *et al.*, (2002). OECD/NEA KRITZ-2 UO₂ and MOX Benchmarks. Proc. Int. Conf. New Frontiers of Nuclear Technology: Reactor Physics, Safety and High-Performance Computing, Seoul, Korea, October 7–10, 2002, American Nuclear Society.

Ivan Kodeli & Luka Snoj., (2012). Evaluation and Uncertainty Analysis of the KRITZ-2 Critical Benchmark Experiments. Nuclear Science and Engineering, vol. 171:3, p. 231-238, DOI: 10.13182/NSE11-62.

K. Shibata *et al.*, (2011). JENDL-4.0: A New Library for Nuclear Science and Engineering. J. Nucl. Sci. Technol, 48, 1, 1.

Kaddour *et al.*, (2013). Sensitivity and uncertainty analysis of the Keff due to ENDF/B-VII.0 cross sections uncertainties of the major isotopes in nuclear reactors. Advances in Energy and Power, vol. 1(1), p. 30-43.

L. SNOJ *et al.*, (2009). KRITZ-2:19 Experiment on Regular H₂O/ Fuel Pin Lattices with Mixed Oxide Fuel at Temperatures 21.18C and 235.98C, in “International Handbook of Evaluated Reactor Physics Benchmark Experiments,” NEA/NSC/DOC(2006)1, Nuclear Energy Agency.

Macfarlane. R, Muir D.W, Boicourt. R.M, Kahler A.C and Conlin, J.L, (2017). The NJOY Nuclear Data Processing System, Version 2016. Los Alamos National Laboratory (LANL).

Makhloul, M., Boukhal, H., El Bardouni, T., Kaddour, M., Chakir, E., & El Ouahdani, S. (2018). 235U elastic crosssection adjustment in criticality benchmarks – Comparison between JENDL-4.0 and ENDF/-VII.1. Ann. Journal of Nuclear Energy, vol. 114, p. 541–550.

P. Romojaro, F. Álvarez-Velarde, I. Kodeli, A. Stankovskiy, C.J. Díez, O. Cabellos, N. García-Herranz, J. Heyse, P. Schillebeeckx, G. Van den Eynde, G. Žerovnik f, (2017). Nuclear data sensitivity and uncertainty analysis of effective neutron multiplication factor in various MYRRHA core configurations. Annals of Nuclear Energy, vol. 101, p. 330–338.

V. Sobes, L. Leal, G. Arbanas & B. Forget, (2016). Resonance Parameter Adjustment Based on Integral Experiments. Nucl. Sci. Eng, vol. 183, no 3, p. 347-355, doi: 10.13182/NSE15-50.

Zuhair, R. Andika Putra Dwijayanto, Suwoto, et Topan Setiadipura, (2021). The implication of Thorium fraction on neutronic parameters of pebble bed reactor. Kuwait Journal of Scienc, Vol. 48 No. 3, p. 1-16, DOI: <https://doi.org/10.48129/kjs.v48i3.9984>.

Submitted: 27/08/2021

Revised: 10/10/2021

Accepted: 07/11/2021

DOI : 10.48129/kjs.15919

Enhancement of optical chaos generator using double delayed feedback

Raghad I. Ibrahim

*Dept. of Physics, College of Education, Mustansiriyah University,
Baghdad-Iraq.*

**Corresponding author: raghedismail@yahoo.com*

Abstract

Chaotic lasers are widely used in secure communication, optical detection and other applications due to their noise-like randomness, excellent anti-jamming and other advantages. This research looks into the chaotic laser's performance at a low cost. The performance related to a semiconductor laser with double delayed feedback is observed and its characteristics are determined in experimental research utilizing OptiSystem simulator. The chaotic laser output is fed back to the Mach-Zehnder modulator (MZM) to make the original system. The gain coefficient changes dynamically, and a second time delay is introduced into the system. The feedback time and feedback strength of the improved chaotic system are studied under varying input bias current, frequency and modulation peak current. Bifurcation diagram results show that the chaotic laser output by the optoelectronic oscillator (OEO) is more complex and has lower delay characteristics. This method does not increase too much. Under the premise of system cost, more complex chaotic signals can be generated, and the signal delay characteristics can be reduced, which is conducive to improving the security of the communication system.

Keywords: Chaos generation; double delayed; Mach-Zehnder modulator (MZM); optisystem simulator; optoelectronic feedback.

1. Introduction

Lasers are sources of light with very special properties, for that reason, there is a great variety of laser applications (Kokaj *et al.*, 2018; Noroozi *et al.*, 2017). Many studies have been conducted to improve laser work and benefit from it in applications (Cheng *et al.*, 2018). Chaotic laser secure communication has received widespread attention because of its high speed, hardware encryption, and compatibility with existing optical fiber communication systems. (Ekhande & Deshmukh, 2014; Oppenheim & Cuomo, 1999; Alvarez & Li, 2006). With possible applications in signal processing and communications, chaotic systems offer a significant approach for signal design and generation. Because of its sensitivity to the initial conditions, chaotic signals are often noise-like, broadband, and complicated to predict. The two states, which are initially extremely similar, become radically distinct following a given amount of time has passed. This makes it impossible to predict the system's form with great precision at random. (Pecora & Carroll, 1990).

The generation of laser chaos mainly includes light injection, optical feedback, optoelectronic feedback and non-linear device-based optoelectronic delay feedback (Chembo, *et al.*,2019).. Among them, the optoelectronic delay feedback method based on non-linear devices has a higher spectral bandwidth and a more flexible adjustment method. (Kovanis *et al.*,1995; Suárez-Vargas *et al.*,2012; Guangjian *et al.* ,2017).

An optoelectronic oscillator (OEO) based on a Mach-Zehnder modulator (MZM) is a common way to generate chaotic lasers (Al Khafaji & Al Naimee, 2017). This kind of OEO has the advantages of simple structure, flat frequency spectrum and wide bandwidth, so there are many related researches. Callan *et al.*,2010 pointed out that the broadband chaotic signal generated by OEO can be used in distributed sensor networks and chaos-based ranging equipment (Callan *et al.*,2010). With the continuous deepening of related research and the rapid development of computer technology, the complexity of this basic chaotic laser based on OEO is no longer sufficient to counter certain cracking methods for the system. For example, an eavesdropper can extract the chaotic time-delay characteristics through time series analysis, reconstruct the OEO system (Udaltsov *et al.*,2003; Udaltsov *et al.*,2005), So threaten the security of chaotic laser secure communication. Therefore, for the basic OEO chaotic generation system, many improvements have been proposed to increase the complexity of chaotic lasers, thereby improving the security of chaotic laser secure communication. For example, if two OEOs are cascaded together, the chaotic laser generated by the first-level OEO is injected into the MZM of the second-level OEO instead of the original constant-power laser, so that the chaotic laser parameters generated by the second-level OEO will dynamically change(Zhiliang & Lingfeng, 2013). Many works are based on performance analysis and security implementation of optical communication system based on advance modulation formats (Qamar *et al.*,2017).

This work deals with the chaos generation through semiconductor lasers with double delay feedback by using Optisystem software (Optisystem16 ,2019). The erbium-doped fiber amplifier (EDFA) is utilized for reinjecting the output laser into the MZM to generate a chaotic laser signal with dynamically changing parameters. The dynamic change of the OEO parameters is realized without adding too many devices, and an additional time delay is introduced. The system can achieve higher chaotic complexity, which conceals the time delay characteristics of chaotic signals to a certain extent and improves the practicability of the system. Different parameters are considered and simulated to see the impact of chaotic behavior produced through semiconductor lasers.

2. Theoretical Model

The chaotic system with double feedback scheme is shown in Figure 1. In figure1: LD is continuous light Laser; PD is a photodetector with a certain amplification effect; Frequency (RF) driver is used to drive the MZM modulator; OC1 and OC2 are couplers, the output of MZM is divided into two by OC2 Light, all the way through the PD and RF driver to the MZM optoelectronic reflection Feedback. All the way through the EDFA to the MZM optical feedback, so that MZM produces chaotic laser output, and the output power is P_{out} .

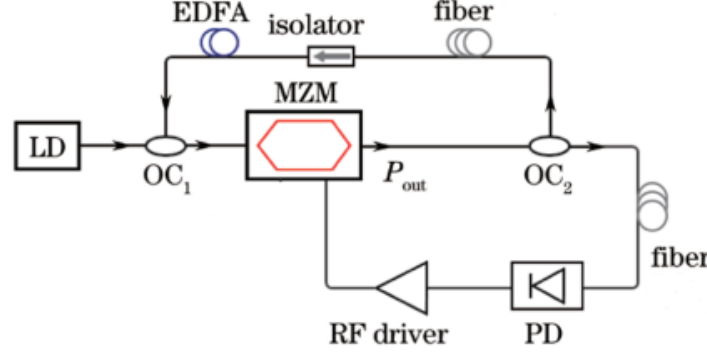


Fig. 1. Schematic diagram of the OEO chaotic system with double delay feedback

The output characteristic of the non-linear device MZM of the OEO chaotic system with double delay feedback is represented in equation (1):

$$P_{out} = P_{in} \cos^2 \left[\frac{\pi V(t)}{2V_{\pi RF}} + \frac{\pi V_B}{2V_{\pi DC}} \right], \quad (1)$$

Where: P_{in} represents the input optical power; $V(t)$ represents the load on MZM Modulation voltage; V_B is the bias voltage; $V_{\pi RF}$ represents the RF half-wave voltage; $V_{\pi DC}$ represents the bias half-wave voltage.

The original OEO system equation is:

$$\left(1 + \frac{f_L}{f_H}\right) V(t) + \frac{1}{2\pi f_H} \frac{d}{dt} V(t) + 2\pi f_L \int_{t_0}^t V(t) dt = P g G A \frac{\pi}{2V_{\pi RF}} \cos^2 \left[\frac{\pi V(t-T_1)}{2V_{\pi RF}} + \frac{\pi V_B}{2V_{\pi DC}} \right], \quad (2)$$

The formula: T_1 is the optoelectronic feedback delay time of the system itself; f_H and f_L are the high and low cut off frequencies of the band pass filter; A is the light of the entire system; g is the gain of the photodetector; G is the gain of the RF driver; P is the static power of the continuous light laser.

The chaotic time series output by OEO is $x(t) = \frac{\pi V(t)}{2V_{\pi RF}}$, Cut-off time $t_H = \frac{1}{2\pi f_H}$, When low pass is off time $t_L = \frac{1}{2\pi f_L}$, MZM phase $\phi = \frac{\pi V_B}{2V_{\pi DC}}$, Enter 2 Line normalization and ignoring the smaller terms, we can get the Ikeda equation (Kouomou,2005):

$$x(t) + t_H \frac{d}{dt} x(t) + \frac{1}{t_L} \int_{t_0}^t x(t) dt = \beta_1 \cos^2[x(t - T_1) + \phi] \quad (3)$$

Where the strength of the optoelectronic feedback gain $\beta_1 = PgGA \frac{\pi}{2V_{\pi RF}}$. Because of the delay time, The chaotic behavior generated by the system based on this equation has extremely high Attractor dimension, whose Lyapunov dimension can be reached under certain conditions 1,000 or more (Nguimdo, 2011). From equation (3), we can see that the chaotic output of OEO is

$$C_1(t) = P \cos^2[x(t) + \phi]$$

The chaotic light output at the output of the original optoelectronic oscillator is 3dB. The coupler is equally divided into two beams of light, one of which is amplified by EDFA. Then, it is coupled with the static fixed power laser emitted by the continuous laser, and then Enter the MZM for a second time to perform non-linear modulation and generate chaotic lasers. The delay time of the light path feedback is T_2 , and the EDFA magnification is A_1 . The improved system equation is

$$\begin{aligned} \left(1 + \frac{f_L}{f_H}\right) V(t) + \frac{1}{2\pi f_H} \frac{d}{dt} V(t) + 2\pi f_L \int_{t_0}^t V(t) dt = \\ [P + A_1 C_1(t - T_2)] gGA \frac{\pi}{2V_{\pi RF}} \times \\ \cos^2 \left[\frac{\pi V(t - T_1)}{2V_{\pi RF}} + \frac{\pi V_B}{2V_{\pi DC}} \right] \end{aligned} \quad (5)$$

From (4) and (5), we can get

$$\begin{aligned} \left(1 + \frac{f_L}{f_H}\right) V(t) + \frac{1}{2\pi f_H} \frac{d}{dt} V(t) + 2\pi f_L \int_{t_0}^t V(t) dt = \\ PgGA \frac{\pi}{2V_{\pi RF}} \cos^2 \left[\frac{\pi V(t - T_1)}{2V_{\pi RF}} + \frac{\pi V_B}{2V_{\pi DC}} \right] + \\ PgGA \frac{\pi}{2V_{\pi RF}} \cos^2 \left[\frac{\pi V(t - T_2)}{2V_{\pi RF}} + \frac{\pi V_B}{2V_{\pi DC}} \right] \times \\ gGAA_1 \frac{\pi}{2V_{\pi RF}} \cos^2 \left[\frac{\pi V(t - T_1)}{2V_{\pi RF}} + \frac{\pi V_B}{2V_{\pi DC}} \right] \circ \end{aligned} \quad (6)$$

$\beta_2 = gGAA_1 \frac{\pi}{2V_{\pi RF}}$ is the gain intensity of the optical path feedback. The hysteresis differential equation of the double-delay system is Derived (Juan *et al.*, 2016):

$$\begin{aligned} x(t) + t_H \frac{d}{dt} x(t) + \frac{1}{t_L} \int_{t_0}^t x(t) dt = \\ \beta_1 \cos^2[x(t - T_1) + \phi] \times \\ \{1 + \beta_2 \cos^2[x(t - T_2) + \phi]\}_0 \end{aligned} \quad (7)$$

To facilitate numerical simulation, let $y(t) = \int x(s)ds$. The output OEO characteristic is Improved by differential equation (8):

$$\begin{cases} \frac{dx(t)}{dt} = -\frac{1}{t_H} \left\{ x(t) + \frac{1}{t_L} y(t) - \beta_1 \cos^2[x(t - T_1) + \phi] \{ 1 + \beta_2 \cos^2[x(t - T_2) + \phi] \} \right\} \\ \frac{dy(t)}{dt} = x(t) \end{cases} \quad (8)$$

This equation discuss the chaotic behavior caused by the two delay times and gain coefficients in the system. The influence of signal dynamics for communication systems, unpredictable, therefore, it is necessary to enhance the chaotic carrier signal.

3. Experimental Model

OptiSystem 16 software is used for developing and simulating an optical chaos generating circuit with double delay feedback. In addition, OptiSystem can be defined as a software package for optical communication devices that allows users to create, test, and simulate optical links in advanced optical networks' transmission layer. The suggested approach's simulated circuit design, where built-in components have been utilized with suitable specifications, is shown in Figure 2. It is made up of an SL, MZM, amplifier and photo-detector (PD). The MZM can be defined as a device which is utilized for the determination of the relative phase shifting between two collimated beams from coherent source of the light either through changing the length of one of the arms or through placing a sample in one of beams' paths. MZM includes two input and two output ports. A fundamental MZM is constructed with the use of two couplers, one of them at input, which plays the role of a splitter and the other one is at output, acting like combiner.

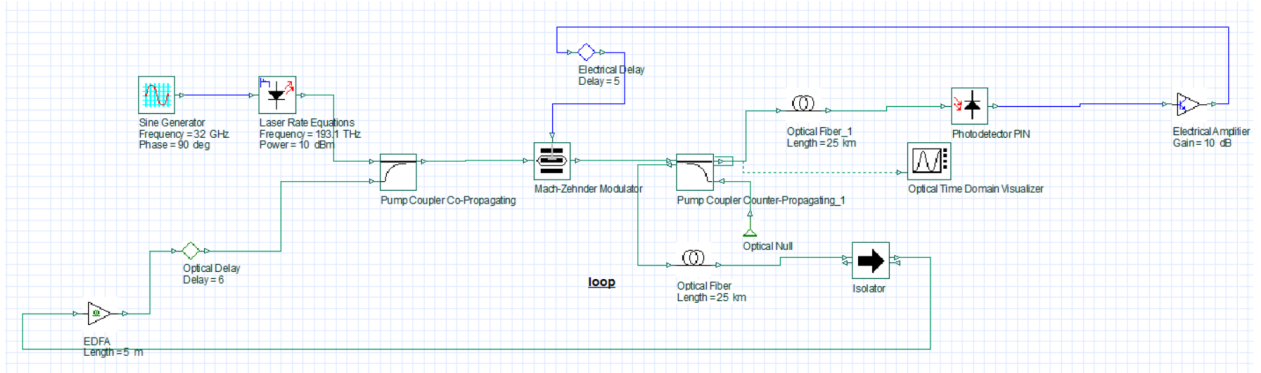


Fig. 2. Block diagram of the OEO chaotic system with double feedback by using OptiSystem.

In Figure 2, Light is split in two interferometer arms by input coupler and re-combined at output-by-output coupler. The coupler is equally divided into two beams of light, one of which is amplified by EDFA. Then, it is coupled with the static fixed power laser emitted by the continuous laser, and then Enter the MZM for a second time to perform non-linear modulation and generate chaotic lasers. The other one is from MZM then into the PD for the purpose of converting optical signal into electrical signal, the photodetector is coupled to the amplifier then

to the feedback arm (MZM). The length of the optical path of two arms is not equal, which makes phase shift that corresponds to the delay be a wave-length function of input signal. OEFB's chaotic behavior has been researched under impacts of MZM bias voltage.

The output of the optoelectronic oscillator is feedback to the MZM through a delayed optical path, So that the gain coefficient of the original OEO is dynamically changed, and an additional time delay is introduced to the system to make the system output a more complex chaotic laser signal. The above characteristics are conducive to building a chaotic secure communication system with higher security.

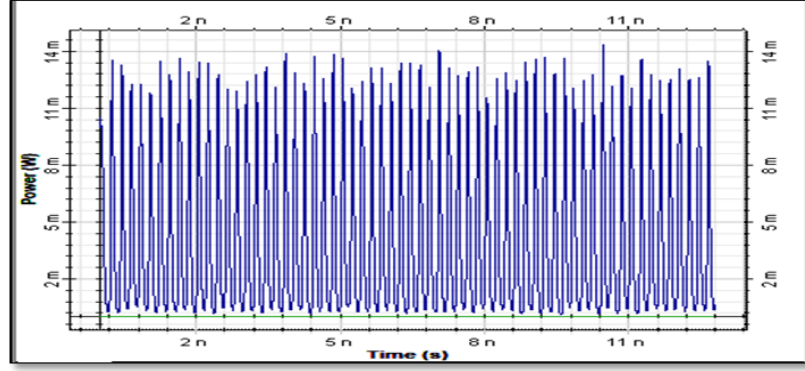
Different parameters are considered to see the impact of chaotic behavior produced through semiconductor lasers. Chaotic laser has been controlled under varying input bias current, frequency and modulation peak current as follow.

3.1 Changing Bias Current (Route of Quasi-Periodic & Chaos)

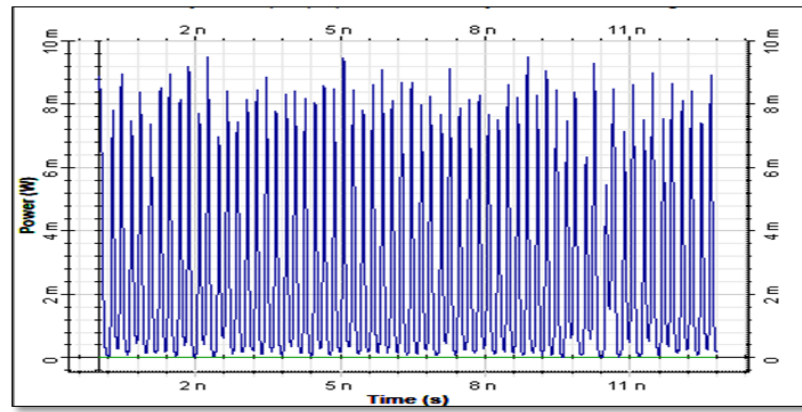
Parameters of semiconductor lasers to generate chaos are given in Table 1. Quasi periodic behavior of chaotic pulses can be observed when the Modulation peak current is fixed at 40 mA. Bias current is varied from 70 mA to 36 mA, route from quasi-periodic to chaos can be observed in Figure. 3(a,b,c). The span of each bunch is approximately equal to 1 ns. After 1 ns, new bunch of chaotic pulses starts. With the rise in bias current, the frequency of Bunches increase, which overlapped with each other giving rise to chaotic route.

Table 1. Semiconductor Laser Parameters (with different bias current)

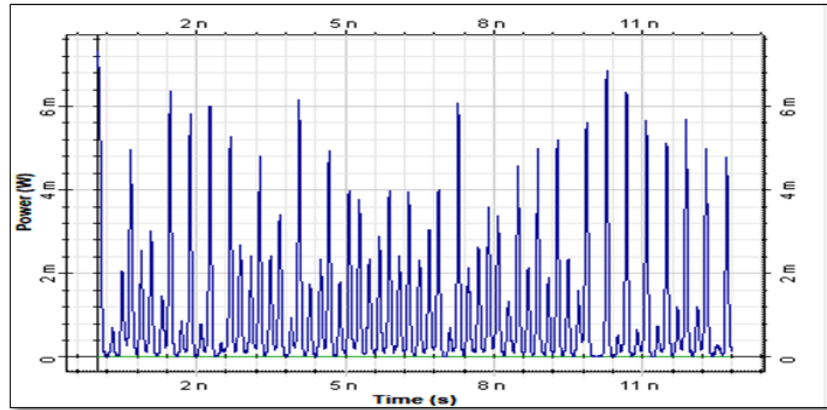
Parameter Name	Value	Parameter Name Value Unit
Wavelength	1550	nm
Power	10	dBm
Bias current	36-70	mA
Threshold power	0.0154	mW
Power (at bias current)	0	dBm
Modulation peak current	40	mA
Threshold current	33.46	mA



(a)



(b)



(c)

Fig. 3. Semiconductor laser output at bias current (a)- 60 mA, (b)-50 mA, (c)- 40mA.

With the decrease in value of bias current, clear variation in amplitude of pulses can be observed in Figure. 3(a,b,c) in which many low amplitude pulses are followed by high amplitude pulses. that is mean, chaotic behavior increased.

The bifurcation diagram, shown in Figure 4, summarizes the scenario that leads to chaotic behavior. The bifurcation diagram shows the intensity related to laser output (peak-to-peak) with the modification of control parameter (bias current of laser source). Within the steady increase (2mA) in the control parameter (bias current), the bifurcation diagram is established.

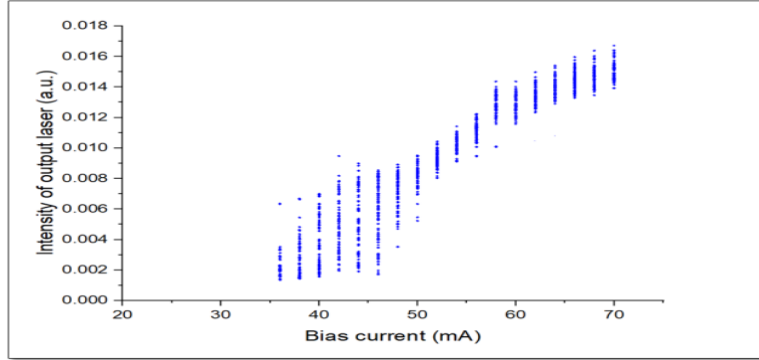


Fig. 4. Bifurcation diagram for the variation of bias current.

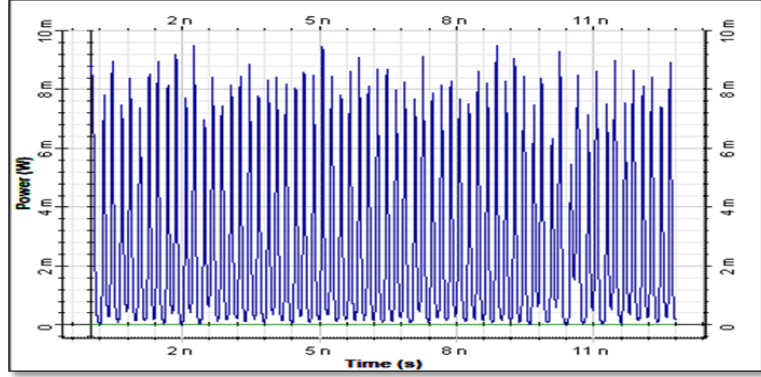
The bifurcation diagram is explained the region from (35-70) mA, as follows: At the beginning, the first region from (35-50) mA, will demonstrates the chaotic oscillation. Gradually increasing the bias current, the quasi- periodic behavior begins to appear. there is the presence of some points in the diagram which indicated to a stable equilibrium, therefore the dynamics of SL is in the form of quasi- periodic motion at (52-70) mA. This mean that, the variation in the bias current led the system to change from chaos at (35-50) mA to quasi periodic at (52-70) mA.

3.2 Changing Modulation Peak Current (High Amplitude Pulses)

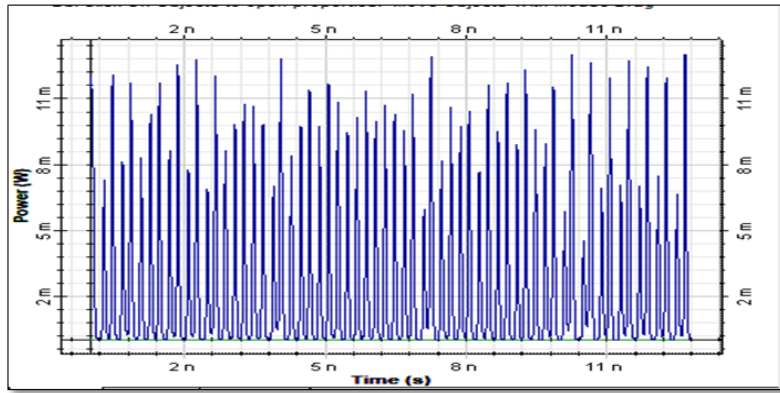
Table 2 shows the parameters to generate chaotic behavior through semiconductor lasers with variations in Modulation peak current. Keeping the bias current 50mA, Modulation peak current is changed from 30 mA to 105 mA. At low Modulation peak current, amplitude of generated pulses is extremely low which not only deviate these pulses from chaotic behavior but also of no use for any suitable fiber length. With the increase in value of Modulation peak current, clear variation in amplitude of pulses can be observed in Figure.5(a,b,c) in which many low amplitude pulses are followed by high amplitude pulses.

Table 2. Semiconductor Laser Parameters (with different modulation peak current)

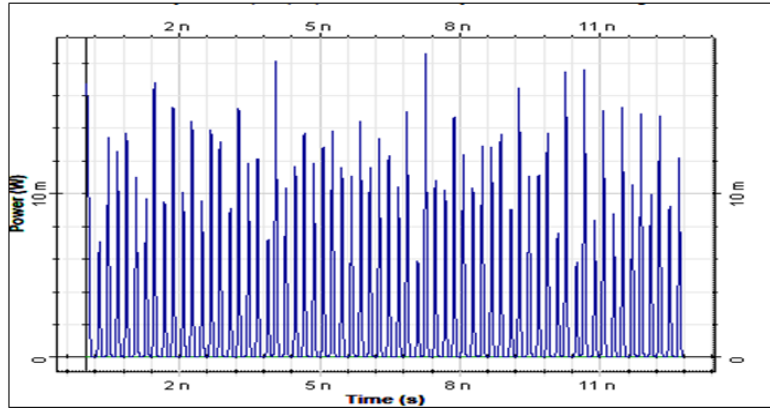
Parameter Name	Value	Parameter Name Value Unit
Wavelength	1550	nm
Power	10	dBm
Bias current	50	mA
Threshold power	0.123	mW
Power (at bias current)	0	dBm
Modulation peak current	30-105	mA
Threshold current	33.46	mA



(a)



(b)



(c)

Fig. 5. Semiconductor laser output at modulation peak current (a) 40 mA,(b) 70 mA,(c) 80 mA.

With the increase in value of modulation peak current, clear variation in amplitude of pulses can be observed in Figure. 5(a,b,c) in which many low amplitude pulses are followed by high amplitude pulses, that is mean, chaotic behavior increased.

The ideal amount of increment and frequency of amplitude are connected to the regularity of a non-linear dynamic system, the shift from a quasi-periodic to a chaotic state is depicted. In addition, the bifurcation diagram is used for checking the chaotic routes as well as evolutions of output in non-linear systems as a function of control parameter variations. The bifurcation diagram, Another important characteristic of chaos is the transition among different dynamical states (steady state, periodic, and chaotic sequences), referred to as "bifurcation". A definition of bifurcation mathematically is the qualitative change in a phase portrait under the variation of parameters. A chaos idea and how it occurs in a system can be imagined by the diagram of bifurcation. Figure 6 shows a bifurcation diagram for various modulation peak currents.

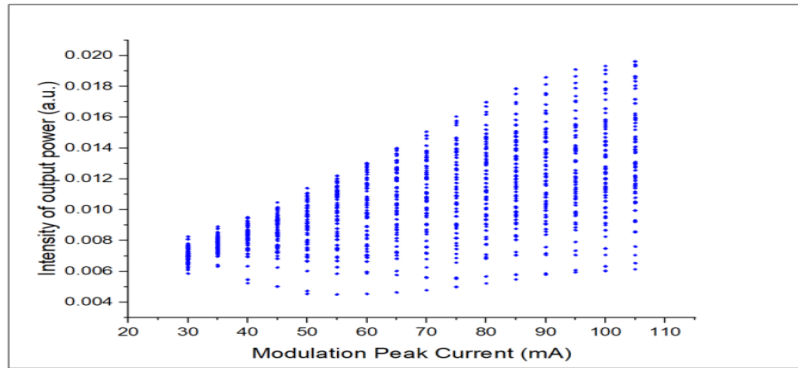


Fig. 6. Bifurcation diagram with various modulation peak current.

This figure shows these values of modulation peak current led the system to change from Quasi-Periodic at (30-64) mA and to chaos at (65-105) mA. The results show that the modulation peak current might be considered a parameter at an ideal frequency (5 GHz) that controls the system's collective dynamics, and that the varied amplitudes were used to regulate the chaotic system from quasi periodic to chaos, and after that to periodic. bifurcation diagram

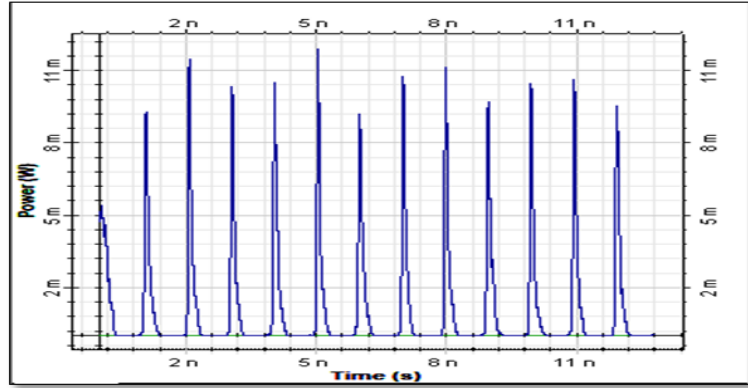
3. 3 Changing Frequency of Current Source (Random Amplitude Pulses)

Suitable pumping power or current is required to achieve the chaotic nature of pulses. At low frequency of current source when the strength of electric field is not very high, pulses of same amplitude are observed. Increasing the frequency results in the variation of amplitude of pulses due to increase in field strength. The modulation peak current and bias current have been fixed at 28mA and 38mA sequentially. Table 3 shows the parameters of current source applied for external modulation by setting the frequencies from 0.75 to 8 GHz.

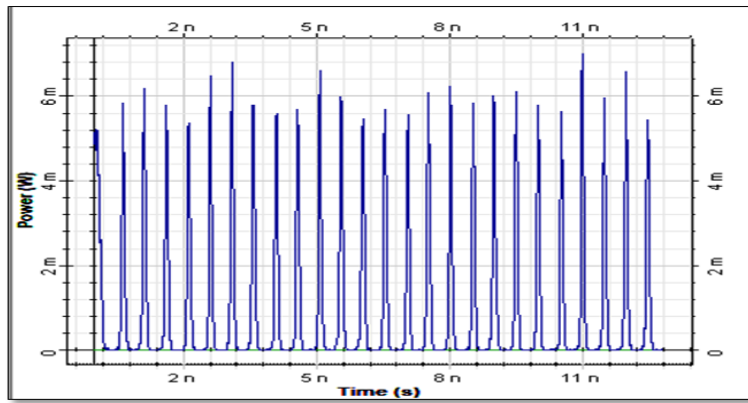
Table 3. Current Source Parameters (with different frequencies)

Parameter	Name Value	Unit
Frequency	0.75-8	GHz
Amplitude	1	a.u.
Phase	90	Deg
Bias	0	a.u.

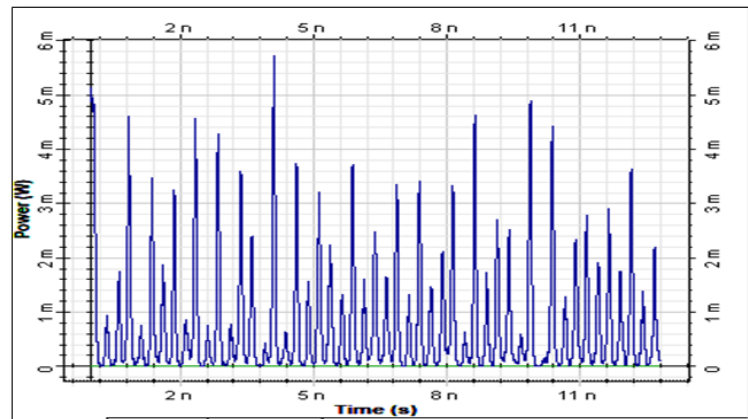
Figure.7(a,b,c) are the outputs of semiconductor lasers in response to change the frequency of the current source. These values of frequencies led the system to change from Quasi-Periodic to chaos.



(a)



(b)



(c)

Fig. 7. Semiconductor laser output at frequency of current source (a) 2 GHz,(b) 3GHz,(c) 4 GHz.

In the Figure .7(c), ‘Gain Quenching’ which is one of the properties of chaotic pulses can be observed in which few pulses of high amplitude are immediately followed by pulses of very low amplitude. The pulses produced in this way are Gaussian in nature and can be checked by applying Gaussian Fit. External frequency modulation is an important method to control chaos. The bifurcation is shown in Figure 8, summarizes the frequency modulation utilized to the source through a function generator.

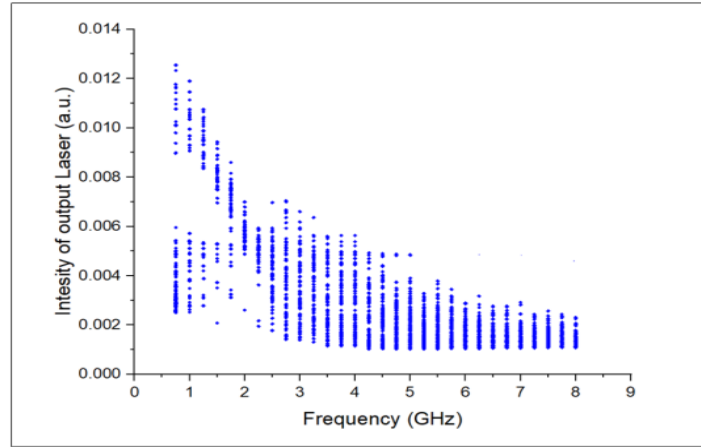


Fig. 8. Bifurcation diagram with different frequency modulation.

The findings suggest that frequency modulation can be used as a control parameter for the system's collective dynamics. The chaotic system has been controlled at several frequencies, ranging from quasi periodic at (0.5-2.5) GHz to chaos at (2.75-4.75) GHz, and ultimately periodic at (5-8) GHz. As a result, highly intriguing outcomes were found when frequency is added to chaotic systems.

4. Conclusion

In this work, the chaotic behavior produced through semiconductor laser by using double delay feedback is studied. The output of the OEO is feedback to the MZM through a delayed optical path, so that the gain coefficient of the original OEO is dynamically changed, and an additional time delay is introduced to the system to make the system output a more complex chaotic laser signal. The above characteristics are conducive to building a chaotic secure communication system with higher security. Moreover, by adding a light path feedback delay, the parameter interval that could not produce chaos also enters chaos, the path into chaos increases, and the practicability of the system is improved. The results show that semiconductor laser and their effect on chaos are observed and controlled by varying different parameters such as bias current, modulation beak current and frequency. These parameters are adjusted and optimized to produce useful chaos to be utilized as carrier to hide high data rate message for long distance communication. However, this method additionally introduces another set of oscillator structure, which is complex and has many restrictions and is difficult to popularize and apply.

ACKNOWLEDGMENTS

The author would like to thank Mustansiriyah University(www.uomustansiriyah.edu.iq) Baghdad-Iraq for its support in the present work.

References

- Al Khafaji, R.K. and Al Naimee, K.A. (2017).** Chaos Modulation by Mach-Zehnder Interferometer, *International Journal of Engineering Research & Science (IJOER)*,3(1), 15-23.
- Alvarez, G. and Li, S. (2006).** Some basic cryptographic requirements for chaos-based cryptosystems. *International journal of bifurcation and chaos*, 16(08), 2129-2151.
- Callan, K.E., Illing, L., Gao, Z., Gauthier, D.J. and Schöll, E. (2010).** Broadband chaos generated by an optoelectronic oscillator. *Physical review letters*, 104(11), 113901.
- Chembo, Y. K., Brunner, D., Jacquot, M., & Larger, L. (2019).** Optoelectronic oscillators with time-delayed feedback. *Reviews of Modern Physics*, 91(3), 035006.
- Cheng, X., Xu, F., Shang, J. and Li, C.(2018).** A study on the amplification of active-mirror Yb: YAG lasers. *Kuwait Journal of Science*, 45(4).
- Ekhande, R. and Deshmukh, S. (2014).** Chaotic signal for signal masking in digital communications. *International organization of Scientific Research Journal of Engineering*, 4(2), 29-33.
- Guangjian, Z., Baofu,Z., Chengxin,L. & Yichao,T. (2017) .**Chaotic photonic compressed sampling based on optoelectronic oscillator , *Chinese Journal of Lasers* , 44(11):1106002.
- Juan, Y., Wei, P., Nian-Qiang, L., Li-Yue, Z. and Qing-Xi, L. (2016).** Two broadband chaotic signals generated simultaneously by semiconductor ring laser with parallel chaotic injection. *ACTA PHYSICA SINICA*, 65(20).
- Kokaj, J., Shuaib, A., Makdisi, Y., Nair, R. and Mathew, J. (2018).** Femtosecond laser based deposition of nanoparticles on a thin film and its characterization. *Kuwait Journal of Science*, 45(4).
- Kouomou, Y.C., Colet, P., Larger, L. and Gastaud, N. (2005).** Chaotic breathers in delayed electro-optical systems. *Physical review letters*, 95(20), 203903.
- Kovanis, V., Gavrielides, A., Simpson, T.B. and Liu, J.M. (1995).** Instabilities and chaos in optically injected semiconductor lasers. *Applied physics letters*, 67(19), 2780-2782.
- Ngumdo, R.M. (2011).** Chaos and synchronization in opto-electronic devices with delayed feedback.
- Noroozi, M.J., Saedodin, S. and Ganji, D.D.,(2017).** A new approximate-analytical method to solve non-Fourier heat conduction problems. *Kuwait Journal of Science*, 44(2).

Oppenheim, A.V. and Cuomo, K.M. (1999). "Chaotic Signals and Signal Processing" Digital Signal Processing Handbook Ed. Vijay K. Madisetti and Douglas B. Williams Boca Raton: CRC Press LLC.

Optisystem 16 [Computer software]. (2019). Retrieved from www.optiwave.com.

Pecora, L. M., & Carroll, T. L. (1990). Synchronization in chaotic systems. Physical review letters, 64(8), 821.

Qamar, F., Islam, M. K., Shah, S. Z. A., Farhan, R., & Ali, M. (2017). Secure duobinary signal transmission in optical communication networks for high performance & reliability. IEEE Access, 5, 17795-17802.

Suárez-Vargas, J.J., Márquez, B.A. and González, J.A. (2012). Highly complex optical signal generation using electro-optical systems with non-linear, non-invertible transmission functions. Applied Physics Letters, 101(7), 071115.

Udaltsov, V.S., Goedgebuer, J.P., Larger, L., Cuenot, J.B., Levy, P. and Rhodes, W.T. (2003). Cracking chaos-based encryption systems ruled by nonlinear time delay differential equations. Physics Letters A, 308(1), 54-60.

Udaltsov, V.S., Larger, L., Goedgebuer, J.P., Locquet, A. and Citrin, D.S. (2005). Time delay identification in chaotic cryptosystems ruled by delay-differential equations. Journal of optical technology, 72(5), 373-377.

Zhiliang, H.H.S.W.Y. and Lingfeng, L. (2013). Chaos Generation of Variable Parameters and Secure Communication Based on Optoelectronic Feedback Oscillation [J]. Acta Optica Sinica, 5.

Submitted: 14/11/2021

Revised: 04/01/2022

Accepted: 05/01/2022

DOI: 10.48129/kjs.17025

Modeling of field emission from laser etched porous silicon

H. R. Dehghanpour *

Dept. of Physics, Tafresh University, Tafresh, Iran

** Corresponding author: hamid.r.dehghanpour@gmail.com*

Abstract

In many modern sciences, electron transfer is required, such as electron microscopes, microwaves, and screens. There have been numerous reports of the formation of microstructures on silicon surfaces using lasers in halogen-containing media and their optical, electrical and other physical properties. A silicon microstructured field emitter is modeled with Fowler-Nordium field diffusion theory, and the breakdown currents are consistent. Breakdown voltage, field gain coefficient, current and current density, and emitter region (in case of breakdown) are considered in the simulation. Comparison between simulation and experimental results shows that the microstructure has field emitter properties and can be used as a new field emitter.

Keywords: Field emission; fowler-nordheim relation; laser; microstructure; porous silicon.

1. Introduction

The special importance of semiconductors in science and engineering is obvious. There are many scientific reports on this subject by Yang *et al.*, (2010) and Kadim *et al.*, (2022). Today, silicon and silicon-containing materials have found increasing applications in research and technology see Dubey *et al.*, (2022), Dehghanpour *et al.*, (2010) and Takai *et al.*, (1995a). Electron microscopy, X-ray tube and cathode ray tube are examples of field diffusion applications that have been repeatedly investigated in various ways. In addition, the applications of field diffusion matrices for flat plates, electron multipliers and microelectronics were extensively studied by Zhirnof *et al.*, (1995) and Hawley & Zaky, 1967. Local increase of the electric field at the cathode surface leads to diffusion in the microprojects of that surface. Under critical voltage for a group of cathodes, the pre-failure currents depend on the electric field as long as the electric field remains constant. At critical voltage (breakdown voltage), a constant current is converted into a spark. Then, the impedance of the circuit, see Dubey *et al.*, (2022), limits the spark current. An encouraging form of electron source is the cathode field-emitting array (FEA) due to its unique working mechanism and the properties of its cathodic materials. However, there are some significant limitations of small manufacturing FEAs in their performance and accuracy, according Busta *et al.*, (1994). The mentioned disability can be solved in two next ways: development of production techniques and selection of other suitable diffuser materials. Researchers have proposed various types of materials such as carbon nanotubes, Gohier *et al.*, (2007), Rakhi *et al.*, (2008) and Liao *et al.*, (2007), diamond films Lu *et al.*, (2007), Joseph *et al.*, (2008) and Orlanducci *et al.*, (2008), zinc oxide nanowires Yeong & Thong, 2008, Xiao *et al.*, (2008) and Zhang *et al.*, (2006). For the above applications, the optimal conditions are high current density at low extraction voltage and stable performance for cathodes. Due to economic considerations, the use of silicon structures as emitters is particularly attractive. After irradiating hundreds of laser pulses on the silicon surface with

halogen-containing ambient gases, the fabrication of regular self-organizing microstructures (conical microstructures) was reported by Her *et al.*, (1998) and Her *et al.*, (2000). Without any processing operations, the regular conical microstructure showed high and stable field diffusion. Light emission from porous silicon has been extensively investigated. However, its electron field propagation has also been studied by Boswell *et al.*, (1995) and Boswell *et al.*, (1996) as well as according Biaggi-Labiosa *et al.*, (2008). In addition, changes in greenhouse gas emissions due to different porous silicon morphologies have been investigated by Wilshaw & Boswell, 1994. The maximum diffusion current and uniformity of diffusion between different cones can be increased by creating a brittle layer on the silicon wafer using a femtosecond laser as a silicon cone emitter, see Carey *et al.*, (2001). This work provides a model for diffusion of conical microstructure on silicon and experimental results reported by Carey *et al.*, (2001) are used to evaluate the results of the developed model.

2. Theory

Metal surfaces emit electrons at high temperatures T_s or strong electric fields E_s . There are generally three regimes for this phenomenon: (1) the emission of a field where the temperature is low and the electric field is strong, (2) the thermion emission which occurs at high temperatures and weak electric fields, and (3) Heat field (TF) emission, which occurs at high temperatures and strong electric fields. Field diffusion from silicon microstructures (just like metals) is explained in terms of the Fowler-Nordheim relationship, according Reich *et al.*, (2009):

$$j = A \frac{1}{\phi} E^2 \exp\left(-\frac{B\phi^{3/2}}{E}\right) \quad (1)$$

Here, A and B (properties of the cathode material) are constants that are independent of both the external field (E) and the working function ϕ . The answer to the problem of quantum mechanics for an electron in an electric field at a good potential is the Fowler-Nordheim equation. The exponential coefficient in Equation (1) determines the transparency of the barrier tunnel D (E), so that $j \sim D(E)$. The height of the barrier is defined by the work function ϕ , that is, the work that must be done to dissipate electrons from the cathode, and the width of the barrier by the strength of the external field. The work function can be obtained from the experimental relation j (E). The performance of any material (e.g. silicon) can be inferred from non-diffusion phenomena, for example, from optical effect measurements by Groning *et al* (1997). In this case, if current I is uniformly propagated in region A, the density of current j is related to the applied electric field E by the expression of Williams & Williams, 1974:

$$j = \frac{1.54 \times 10^{-6} \beta^2 E^2}{\phi t^2(y)} \exp\left(-\frac{6.83 \times 10^7 \phi^{3/2} v(y)}{\beta E}\right) \quad (2)$$

Where β and ϕ represent the working function of the cathode material and the field magnification coefficient (for microprojects on the cathode surface), respectively, and v (y) and t (y) are functions of the variable, see Williams & Williams, 1974:

$$y = \frac{3.79 \times 10^{-4} (\beta E)^{3/2}}{\varphi} \quad (3)$$

whose values have been tabulated by Good & Muller, 1956. Equation (2) can be rearranged as, see Williams & Williams, 1974:

$$\frac{I}{E^2} = \frac{1.54 \times 10^{-6} \beta^2 A}{\varphi t^2(y)} \exp \left(-\frac{6.83 \times 10^7 \varphi^{3/2} v(y)}{\beta E} \right) \quad (4)$$

Thus, a straight line of m gradient is obtained in the semi-logarithmic diagram $\ln (1/E^2)$ against $1/E$, where, see Williams & Williams, 1974:

$$m = -\frac{6.83 \times 10^7 \varphi^{3/2} s(y)}{\beta} \quad (5)$$

$s(y)$ is another function of the variable y .

Assuming that the work function remains constant, see Williams & Williams, 1974, β is determined from the gradient, and hence the magnitude of the increased breakdown field in the breakdown, $F_s (= \beta E_s)$, may be calculated. Since I_s , the current at which breakdown begins, is determined from measurements, then from Equations (2) and (3), j_s and A_s , the current density and radiative region at failure are calculated, respectively. Thus, the fracture parameters β , F_s , I_s , j_s and A_s are calculated for each E-I characteristic, and therefore their change is determined by the number of breakdowns for a given set of electrodes.

3. Experiments

On a $3 \times 3 \text{ mm}^2$ area on an n-type silicon wafer (800-1200 $\Omega \cdot \text{cm}$), a regular self-organizing conical microstructure using 100 femtosecond laser pulses and a raster scan with a flux of 10.9 kJ / m^2 at 100 mm/s was formed. The height of the tiny cones is 10 to 14 μm and they are separated from the tip to the tip of 6 to 10 μm . The voltage applied between the cathode to the anode was in the range of 300 to 1150 volts and measurements were made for the gaps separating the anode from the cathode 20 μm , 40 μm and 60 μm . V-I characteristics were obtained for each separation gap.

4. Simulation

The main purpose of the simulation is to investigate the correlation between the experimental results and the classical field diffusion formula for conical silicon microstructure. An n-type silicon with a $3 \times 3 \text{ mm}^2$ microstructure with regular periodic cone arrays (height of cones $\sim 10\text{-}14 \mu\text{m}$, spacing of cones $\sim 6\text{-}10 \mu\text{m}$, tip curvature radius $\sim 0.25 \mu\text{m}$, tip angles less than 20°) Intended for simulation. The cathode-anode separation gap was considered to be 20, 40 and 60 μm separately. The applied voltage across the cathode anode is in the range of 300-1100 volts. When using a conical cathode, the equation of the known electric field $E = V/d$ must be modified as, see Gomer (1961):

$$E = \beta V \quad (6)$$

where β is the field magnification factor and is obtained by Gomer (1961):

$$\beta = \frac{1}{kr} \quad (7)$$

where r is radius of the tip curvature and k is given by Gomer (1961):

$$k = 0.59 \epsilon^{\frac{1}{3}} \left(\frac{x}{r}\right)^{0.13} \quad (8)$$

where ϵ is cone's tip angle and x is the cathode-anode separation gap.

An approximation of $v(y)$ in Eq.2 is given as below:

$$v(y) = 1 - n + \frac{1}{6}n \ln(n) \quad (9)$$

Where n is obtained by:

$$n = 1.43556 \left(\frac{E}{\phi^2}\right) \quad (10)$$

Where E is the electric field and ϕ is the work function (for silicon ~ 4.5 eV).

The approximate form of $t(y)$ is as below:

$$t(y) = v(y) - \left(\frac{2y}{3}\right) \left(\frac{dv(y)}{dy}\right) \quad (11)$$

After some algebra operations:

$$t(y) = v(y) - \left(\frac{2n}{18}\right) (\ln(n) - 5) \quad (12)$$

5.Results and discussion

Figure 1 shows the voltage-current diagrams for the experimental and simulation results related to the 20 μm cathode-anode separation gap. As we can see, there is a good agreement between the experimental and simulation results at voltages below 1000 volts. Over 1000 V there is a maximum error of $\sim 0.5\%$ between the simulation and the experimental results. The threshold voltage for both simulation and experimental results is ~ 600 volts.

The voltage-current diagrams for the simulation and experiments for the 40 μm gap are shown in Figure 2. Again, the experimental results confirm the simulation results with satisfactory accuracy. The maximum error is close to 5%. The field propagation starts with an applied voltage of about 700 volts, which is a logical result due to the expansion of the separation gap. In both figures, there is a nonlinear increase in current against voltage rise, which is consistent with the classical theory of field emitters. This indicates that microstructured silicon behaves like conventional field emitters. This feature and characteristics of silicon semiconductors introduce microstructured silicon as an interesting field emitter.

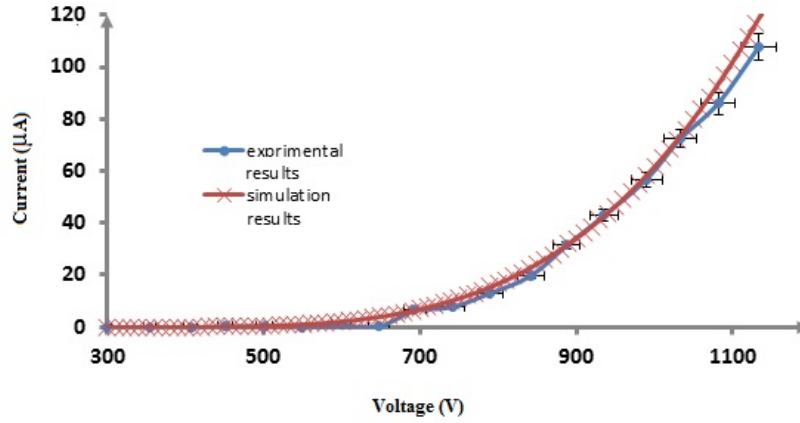


Fig. 1. Voltage-Current diagram with 20 μm cathode-anode separation gap

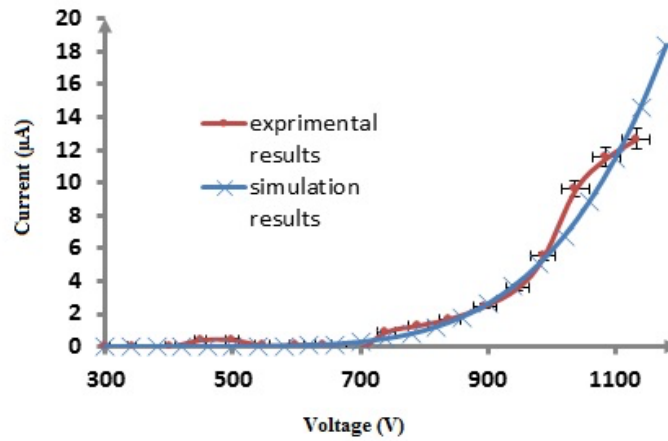


Fig. 2. Voltage-Current diagram with 40 μm cathode-anode separation gap

Figure 3 shows the V-I curves for experimental and simulation results for a 60 μm separation gap between the cathode and anode. The deviation of the experimental results according to the simulation results is greater than this deviation for Figures 1 and 2. The maximum error in the figure 3 is $\sim 8\%$. The threshold voltage is about 800 V. The main reason for this deviation is the significant separation gap for experiment.

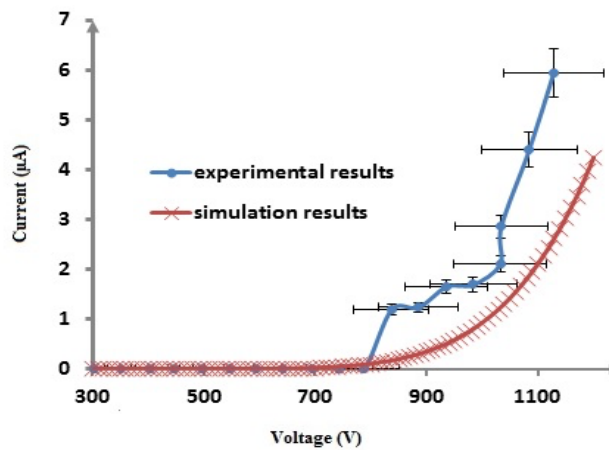


Fig. 3. Voltage-Current diagram with 60 μm cathode-anode separation

The logarithmic form of Equation 4 shows that $\ln(I/v^2)$ versus v^{-1} is theoretically linear. Then, reviewing the experimental results and simulation with linear forms is an essential task to show the field emitting competence. For this reason, the $\ln(I/v^2)$ versus v^{-1} diagrams for the 20, 40, and 60 μm separation gaps are summarized in Figures 4-6, respectively. Figure 4 shows the logarithmic form of Equation 4 (Fowler-Nordheim equation) for a gap of 20 μm . Obviously, the experimental results are in good agreement with the linear simulation results in the voltage range of 700 to 1250 volts, but there are significant deviations at voltages below 700 volts. According to Figure 1, the voltage is close to the field emitter threshold voltage and is a logical deviation.

Figure 5 shows the F-N logarithmic equation for the cathode-anode separation gap of 40 μm . The applied voltage range is 600 to 1100 volts. There is a good correlation between the simulation and experimental results, and both results are correlated on a straight line (as predicted by the logarithmic equation F-N). The F-N equation is logarithmically shown in Figure 6 for the 60 μm separation gap. Simulation curves and experimental results have significant deviations. In addition, experimental curves in the form is significantly nonlinear. As before, it is due to the large separation gap (reduction of the electric field strength between the cathode and the anode). There is a maximum deviation of $\sim 7\%$ for the experimental results with respect to the simulation curves.

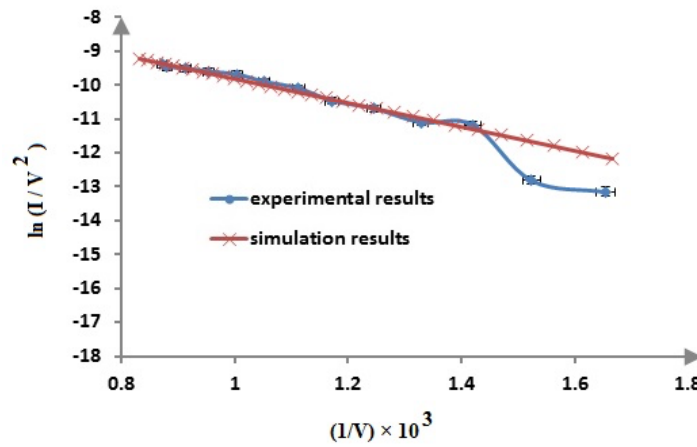


Fig. 4. The logarithmic F-N equation for the cathode- anode separation gap equal to 20 μm

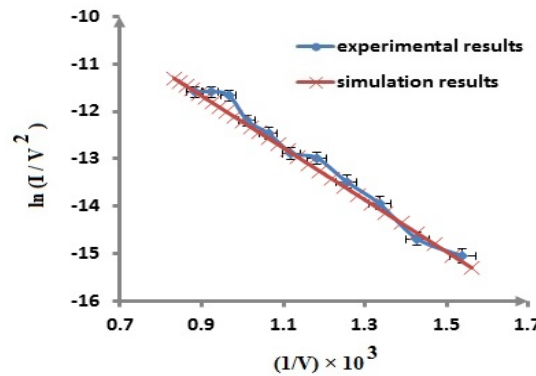


Fig. 5. The logarithmic F-N equation for the cathode- anode separation gap equal to 40 μm

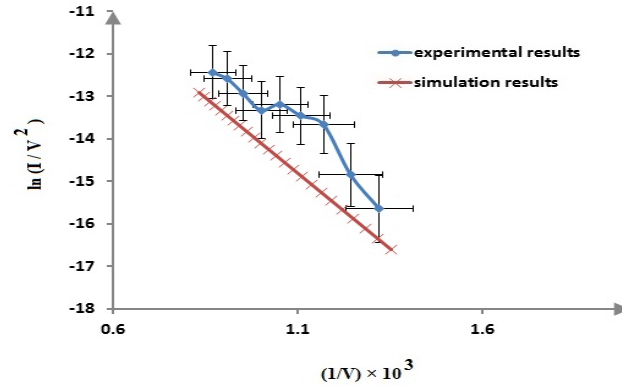


Fig. 6. The logarithmic F-N equation for the cathode- anode separation gap equal to 60 μm

Finally, in order to be more confident in the simulation results, a qualitative comparison with the experimental results of field emission with silicon micro-cones in the last three decades by Evsikov *et al.*, (2012), Prommesberger *et al.*, (2017), Serbun *et al.*, (2013), Ding *et al.*, (2002), Shang *et al.*, (2002), Rangelowa *et al.*, (2001), Colgan & Brett, 2001, Jessing *et al.*, (1998), Rakhshandehroo *et al.*, (1997), Mehr *et al.*, (1996) and Takai *et al.*, (1995 *b*) is collected in Table 1. Because none of the micro-cones tested in these reports were based on the interaction of the laser with the silicon surface and in sulfur hexafluoride atmosphere, a direct comparison with the simulation results was not possible. Therefore, only a qualitative comparison with the trend of the output curves of these works has been considered. However, there is a very good qualitative agreement between the results of the existing experimental work and the simulation results in this work. This shows that the simulation is very reliable.

Table 1. Qualitative comparison of experimental results with emitters including silicon tips with simulation results of the present work

Authors	Field emitter	V-I results	F-N Results	Agreement with the present work
Ilya D. Evsikov <i>et al</i> 2021 [30]	Silicon pyramidal microstructures	Nonlinear	Linear	Good
C. Prommesberger <i>et al</i> 2017 [31]	p-type Si tip arrays	Nonlinear	Nonlinear	Fair
P. Serbun <i>et al</i> 2013 [32]	p-type silicon tip arrays	Nonlinear	Nonlinear	Fair
M. Ding <i>et al</i> 2002 [33]	Silicon tips	Nonlinear	Linear	Reasonable
N. Shang <i>et al</i> 2002 [34]	High density silicon cone arrays	Nonlinear	Linear	Good
I.W. Rangelow & St. Biehl 2001 [35]	Silicon tips	Nonlinear	Nonlinear	Reasonable
M.J. Colgan & M.J. Brett 2001 [36]	Silicon tips	Nonlinear	-----	Good
J. R. Jessing <i>et al</i> 1998 [37]	Porous silicon	Nonlinear	Linear	Good
M. R. Rakhshandehroo & S. W. Pang 1997 [38]	Si emitter tips	Nonlinear	-----	Good
W. Mehr <i>et al</i> 1996 [39]	Single crystal silicon field emission tip arrays	Nonlinear	Linear	Good
M. Takai <i>et al</i> 1995 <i>b</i> [40]	n-type porous Si	Nonlinear	Linear	Good

6. Conclusion

The self-organizing regular microstructure on silicon had previously been proposed as a field emitter. In this paper, with a known formulation for field emission, a model for silicon microstructure is introduced and the simulation results are compared with the experimental results. The agreement between the model and the experiment in the small separation gap (40 and 60 μm) between the cathode and the anode is satisfactory. Increasing the separation gap (60 μm) leads to a deviation between the model and the experiment. These results indicate that the microstructure on silicon can be used as a field emitter in the cathode-anode separation gap below 50 μm .

References

- Biaggi-Labiosa, A. Solá, F. Resto, O. Fonseca, L. González-Berríos, A. De Jesus, J. Morell, G. (2008).** Porous silicon field emitter for display applications. *Phys. Status Solidi C* **5** (11), 3479
- Boswell, E. C. Huang, M. Smith, G. D. W. Wilshaw, P. R. (1996).** Characterization of porous silicon field emitter properties. *J. Vac. Technol. B* **14**, 1895
- Boswell, E. Seong, T. Y. Wilshaw, P. R. (1995).** Studies of porous silicon field emitters. *J. Vac. Technol. B* **13**, 437
- Busta, H. H. Pogemiller, J. E. Zimmerman, B. J. (1994).** Scaling of emission currents and of current fluctuations of gated silicon emitter ensembles. *J. Vac. Sci. Technol. B* **12**, 689
- Carey, J. E. Zhao, L. Crouch, C. Wu, C. Mazur, E. (2001).** Field Emission from Silicon Microstructures Formed by Femtosecond Laser Assisted Etching. *Proc. CLEO Baltimore, MD*, 555-557
- Colgan, M.J. Brett, M.J. (2001).** Field emission from carbon and silicon films with pillar microstructure. *Thin Solid Films* **389**, 1
- Dehghanpour H. R. Parvin, P. (2010).** Fluorine penetration into amorphous SiO_2 glass at SF_6 atmosphere using Q-switched Nd: YAG and excimer laser irradiations, *Jpn. J. Appl. Phys.* **49** (7R): 07580.
- Ding, M. Sha, G. Akinwande, A. I. (2002).** Silicon Field Emission Arrays With Atomically Sharp Tips: Turn-On Voltage and the Effect of Tip Radius Distribution. *IEEE Trans. Elec. Devices* **49**(12), 2333
- Dubey, R.S., Venkatesh, Y. (2022).** Engineering of Ultra-Violet Reflectors by varying Alternate Layers of Titania/Silica for Harmful UV-Protection, *Kuwait J. Sci. KJS - Online-First Articles*, DOI: 10.48129/kjs.16633

Evsikov, I. D. , Demin, G. D. Gryazneva, T. A. Makhaboroda, M. A. Djuzhev N. A. Pankratov, O. V. Popov E.O. Filippov, S.V. . Kolosko A. G. Chumak, M. A. (2021). Experimental study of the multi-tip field emitter based on the array of silicon pyramidal microstructures. 34th International Vacuum Nanoelectronics Conference (IVNC).

Gohier A, Djouadi M A, Dubosc M, Granier A, Minea T M, Sirghi L, Rossi F, Paredez P and Alvarez F. (2007). Single- and Few-Walled Carbon Nanotubes Grown at Temperatures as Low as 450 °C: Electrical and Field Emission Characterization. *J. Nanosci. Nanotechnol.* **7**(9), 3350

Gomer, R. (1961) Field emission and field ionization. Harvard Monographs In Applied Science No 9. **Cambridge**, Massachusetts.

Good, R.H., Muller, E.W. (1956). Handbook of Physics. Springer-Verlag, **Berlin**
Groning, O. Kuttel, O. Groning, M. Groning, P. Schlappbach, L. (1997). Field emitted electron energy distribution from nitrogen-containing diamondlike carbon. *Appl. Phys. Lett.* **71**, 2253

Hawley, R. Zaky, A. A. (1967). Progress in Dielectrics. Vol. 7. pp. 115-215. Heywood, London

Her, T. H. Finlay, R.J. Wu, C. Mazur, E. (2000). Femtosecond laser-induced formation of spikes on silicon. *Appl. Phys. A* **70**, 383

Her, T.H. Finlay, R.J. Wu, C. Deliwala, S. Mazur, E. (1998). Microstructuring of silicon with femtosecond laser pulses. *Appl. Phys. Lett.* **73**, 1673

Jessing, J. R. Kim, H. R. Parker, D. L. Weichold M. H. (1998). Fabrication and characterization of gated porous silicon cathode field emission arrays. *J. Vac. Sci. Technol. B* **16** (2), 777

Joseph, P. T. Tai, N. H. Lee, C. Y. Niu, H. Pong, W. F. Lin, I. N. (2008). Field emission enhancement in nitrogen-ion-implanted ultrananocrystalline diamond films. *J. Appl. Phys.* **103**, 043720

Kadim A. (2022). Fabrication of Nano Battery from CdS Quantum Dots and Organic Polymer, *Kuwait J. Sci.* **49** (1): 1-9.

Liao, L. Lie, J. C. Liu, C. Xu, Z. Wang, W. L. Liu, S. Bai, X. D. Wang, E. G. (2007). Field Emission of GaN-Filled Carbon Nanotubes: High and Stable Emission Current. *J. Nanosci. Nanotechnol.* **2** (11), 2875

- Lu, X. Yang, Q. Xiao, C. Hirose, A. (2007).** Effects of hydrogen flow rate on the growth and field electron emission characteristics of diamond thin films synthesized through graphite etching. *Diam. Relat. Mater.* **16** (8), 1623
- Mehr, W. Wolff, A. Frankenfeld, H. Skaloud, T. Hoppner, W. Bugiel, E. Lgrz, J. Hunger, B. (1996).** Ultra sharp crystalline silicon array used as field emitter. *Microelec. Engin.* **30**, 395
- Orlanducci, S. Fiori, A. Sessa, V. Tamburri, E. Toschi, F. Terranova, M. L. (2008).** Nanocrystalline Diamond Films Grown in Nitrogen Rich Atmosphere: Structural and Field Emission Properties. *J. Nanosci. Nanotechnol.* **8**(6), 3228
- Prommesberger, C. Langer, C. Lawrowski, R. Schreiner, R. (2017).** Investigations on the long-term performance of gated p-type silicon tip arrays with reproducible and stable field emission behavior. *J. Vac. Sci. Technol. B* **35**(1), 012201-1
- Rakhi, R. B. Sethupathi, K. Ramaprabhu, S. (2008).** Field emission from carbon nanotubes on a graphitized carbon fabric. *Carbon*. <https://doi.org/10.1016/j.carbon.2008.07.024>.
- Rakhshandehroo, M. R. Pang, S. W. (1997).** Field emission from gated Si emitter tips with precise gate–tip spacing, gate diameter, tip sharpness, and tip protrusion. *J. Vac. Sci. Technol. B* **15**(6), 2777
- Rangelowa, I.W. Biehlb, St. (2001).** High aspect ratio silicon tips field emitter array. *Microelec. Engin.* **57–58**, 613
- Reich, K. V. Eidelman, E. D. (2009).** Effect of electron-phonon interaction on field emission from carbon nanostructures. *Euro. Phys. Lett.* **85**(4), 47007
- Serbun, P. Bornmann, B. Navitski, A. Muller G. (2013).** Stable field emission of single B-doped Si tips and linear current scaling of uniform tip arrays for integrated vacuum microelectronic devices. *J. Vac. Sci. Technol. B* **31**(2), 02B101-1
- Shang, N. G. Meng, F. Y. Au, F. C. K. Li, Q. Lee, C. S. Bello, I. Lee, S. T. (2002).** Fabrication and field emission of high density silicon cone arrays. *Adv. Mater.* **14**(18), 1308
- Takai, M. Yamashita, M. Wille, H. (1995a).** Enhancement in emission current from dry-processed n-type Si field emitter arrays after tip anodization. *J. Vac. Sci. Technol. B* **13** (2), 441
- Takai, M. Yamashita, M. Wille, H. Yura, S. Horibata, S. Ototake, M., (1995b).** Enhanced electron emission from n-type porous Si field emitter arrays *Appl. Phys. Lett.* **66**, 422
- Williams, D. W. Williams, W. T. (1974).** Pre-breakdown and breakdown characteristics of stainless steel electrodes in vacuum. *J. Phys. D: Appl. Phys.* **7**(8), 1173

Wilshaw, P. R. Boswell, E. (1994). Field emission from pyramidal cathodes covered in porous silicon. *J. Vac. Sci. Technol. B* **12**, 662

Xiao, J. Zhang, G. M. Bai, X. Yu, L. G. Zhao, X. Y. Guo, D. Z. (2008). Field emission from zinc oxide nanostructures and its degradation. *Vacuum*. **83**(2), 265

Yang, Y., McDowell, M., Jackson, A., Cha, J., Hong, S., and Cui, Y., (2010). New nanostructured Li₂S/silicon rechargeable battery with high specific energy. *Nano Lett.*, **10**: 1486–1491

Yeong, K. S. Thong, J. T. L. (2008). Field emission properties of individual zinc oxide nanowire field emitter. *J. Vac. Sci. Technol. B* **26**, 983

Zhang, Y. S., Yu, K. Ouyang, S. X. Zhu, Z. Q. (2006). Selective-area growth and field emission properties of Zinc oxide nanowire micropattern arrays. *Phys. B* **382**(1-2), 76

Zhirnof, V. V. Givargizov, E.I. Plekhanov, P.S. (1995). Field emission from silicon spikes with diamond coatings. *J. Vac. Sci. Technol.* **13**, 418

Submitted: 06/11/2021

Revised: 15/02/2022

Accepted: 20/02/2022

DOI: 10.48129/kjs.17069

Diffusion coefficient calculation of iron in liquid lead using molecular dynamics method with new mixing rule for Lennard-Jones potential parameters

Artoto Arkundato^{1,*}, Fiber Monado², Iwan Sugihartono³, Abu Khalid Rivai⁴, Zaki Su'ud⁵

¹ Dept. of Physics, Faculty of Mathematics and Natural Sciences,
Universitas Jember, Jember, Indonesia

² Dept. of Physics, Faculty of Mathematics and Natural Sciences,
Universitas Sriwijaya, Palembang, Indonesia

³ Dept. of Physics, Faculty of Mathematics and Natural Sciences,
Universitas Negeri Jakarta, Jakarta, Indonesia

³ Dept. of Physics, Faculty of Mathematics and Natural Sciences, ITB, Bandung, Indonesia

⁴ Research Center For Radiation Detection and Nuclear Analysis, Research Organization For
Nuclear Energy, National Research and Innovation Agency BRIN,
Puspiptek Kawasan Sains dan Teknologi KST B.J. Habibie Tangerang Selatan Indonesia

* Corresponding author: a.arkundato@unej.ac.id

Abstract

The diffusion coefficient data of materials are crucial for several applications, and can be calculated theoretically up to considerable accuracies. Using molecular dynamics simulation it is possible to compute this property for several conditions as temperature and pressure. The corrosion phenomena of steel types in the fast nuclear reactor can be correlated and studied based on the the diffusion process of iron atoms that dissolve into a liquid lead coolant via molecular dynamics methods using certain potential energy. A widely type of the interatomic interaction potential of materials is the Lennard-Jones potential. Regarding this potential, for a pair of different elements A and B, we can determine the potential parameter ($\sigma_{AB}, \epsilon_{AB}$) using a formula. However for a metal system as the liquid metal corrosion, the Lennard-Jones potential could be inefficiently accurate. In this study we propose a novel mixing rule to determine ($\sigma_{AB}, \epsilon_{AB}$) for better property calculation results, similar to iron diffusion coefficient. We propose a novel formula for the metal system. Using this novel formula, the molecular dynamics simulation exhibits relatively accurate results. The iron diffusion coefficient can be estimated as $D_{Fe \rightarrow Pb}(T) = 1.98847 \times 10^{-7} \exp(-37064.47/RT)$ [m²/s], with an error of apporoximately < 7.2% and > 10% for < 1073 K and $T > 1073$ K, respectively. The best calculation for $D_{Fe \rightarrow Pb}(T)$ has an error of approximately 1.55% for temperature 923 K.

Keywords: Diffusion; lennard-jones potential; liquid metals corrosion; mixing rules; molecular dynamics.

1. Introduction

Liquid lead and/or lead alloys are already known to have high potential application as coolant materials in liquid metal cooled reactors. Liquid lead has several physical and chemical advantage properties: high boiling temperature (approximately 1740 °C), low melting temperature (approximately 327 °C), and also high thermal conductivity (more than water), such that those making the liquid lead have potential applications for fast nuclear reactor designs (Zhang & Li, 2008). However, it is also well known for a long time that the structural materials (steels) used in the liquid lead cooled reactor exhibit very high corrosion when they interact with this coolant. The steel components (iron, nickel, chromium, etc) experience high dissolution within liquid lead (Kashezhev *et al.*, 2010; Zelenskii *et al.*, 2006; Zelenskii *et al.*, 2007; Zhang & Li, 2008; Zhang *et al.* 2010). Hence, with a comprehensive appropriate method of corrosion inhibition and/or finding a novel high temperature resistant material are major goals in liquid metal cooled reactor designs.

Several studies have been conducted for the aforementioned purposes by an experimental or theory/computational method. From this perspective, computational methods are very powerful and efficient approaches. In particular, the molecular dynamics (MD) method is a very good tool for studying the corrosion based on the diffusion concept. Maulana *et al.* (2008) applied the MD method to study the penetration depth of liquid lead atoms entering FeNiCr steel. In our previous studies (Arkundato *et al.*, 2010; Arkundato *et al.*, 2012; Arkundato *et al.*, 2013a; Arkundato *et al.*, 2013b; Arkundato *et al.*, 2013c; Arkundato *et al.*, 2015; Arkundato *et al.*, 2017; Arkundato *et al.*, 2019) we have used the Lennard-Jones potential to observe the corrosion of iron in lead and lead-bismuth coolant based on Lorentz-Bertholet mixing formula and obtained important results. In these studies we could present the range of oxygen concentration for the best corrosion inhibition. Sa'adah *et al.*, (2020a) adopted the Lennard-Jones potential with the Lorentz-Bertholet mixing formula to demonstrate the corrosion of iron in Pb-Mg liquid. We also applied this type of potential to investigate the corrosion of ceramics in liquid metal. Triwardani *et al.*, (2020b) also adopted the same potential and mixing rule, but by suggesting more accurate potential parameters.

In facts we actually simplified the atomic interaction of material using the Lennard-Jones potential following the Lorentz-Bertholet mixing formula for the pair interaction of two different elements. Several researchers have mentioned that the Lennard-Jones potential is not sufficient accurate in representing metals. Other potential types should be adopted to support the interaction among metallic atoms as EAM potential or others. Belashchenko (2009) adopted the EAM potential for liquid sodium. Mendelev *et al.*, (2008), as well as other researchers, employed the EAM potential for liquid Al dan Cu.

However, the Lennard-Jones potential is a simple and easy method for computing the physical properties via molecular dynamics simulation. It can be adopted as first prediction to arrive at a more general conclusion before involving more accurate investigations. In general the Lennard-Jones potential is useful in describing liquid or gaseous systems (Brodholt & Wood, 1993). Evidently, the liquid metal corrosion and its inhibition adopts the injection of oxygen gas, following diffusion process, and it is a system of solid metal-liquid-gas mixture. Hence it can

describe the corrosion of iron in liquid lead also adopting the Lennard-Jones potential with a few improvements.

At this stage, there are several mixing formulas in the scheme of the Lennard-Jones potential that have been proposed by many researchers for a number of objectives that will be discussed later. We can use these formulas in our corrosion research. However, *how accurate are these physical property calculations as diffusion coefficient?* Then this is the focus and objective of current work. We want to study the effectiveness of several available mixing rules to describe the liquid lead corrosion phenomena. First, we want to compare several available mixing rules (Lorentz-Bertholet, Halgren HHG, Waldman Hagler, etc) for the use of diffusion coefficient calculation of liquid metal system, and then attempt to develop a novel formula for mixing rule better. We compare all formulas with experimental data and determine that it is most accurate to represent the interaction of metal atoms. We expect that this novel mixing formula will be a better mixing formula to represent the interaction among atoms of metals (especially for hot corrosion in liquid molten metals) in the scheme of the Lennard-Jones potential. In this study we use the open-source Moldy molecular dynamics program for simulations (Refson, 2000), and we believed that this program can produce significant results and may be used for the general purpose of calculations. This code may be download freely from two website addresses:

(1) <http://ccl.net/cca/software/SOURCES/C/moldy/>

(2) <https://data.mendeley.com/datasets/rgnh52j3st/1>

2. Molecular dynamics method and mixing rules

The molecular dynamics simulation method is an effective method for simulating interactions among atoms/molecules of materials (solids, liquids or gases) and calculating physical properties. The simulation will be run under a certain ensemble (NPT/NVT/NVE, etc.). In fact, in the MD simulation, atoms move following the Newton's 2nd law of motion:

$$m_i \{d^2 r_i / dt^2\} = F_i \quad (1)$$

$$F_i = -\nabla \sum u_{ij}(r_{ij}) \quad (2)$$

where \mathbf{r} is the position of atom, \mathbf{F} is the total force experienced by an atom, $u(r)$ is the potential energy related to the force, and index i represents an atom label while index j labels other atoms, such that $i \neq j$. For the material system in MD method we usually solve the Newton equation numerically. Using the Moldy program, the Equation (1) can be solved using certain algorithm as the modified Beeman algorithm, under specific potential function of interacting atoms (Refson, 2000). One of the popular potential function $u(r)$ for representing the interaction between pair of two atoms is 12-6 form of the Lennard-Jones potential (Zhen & Davies, 1983):

$$u(r) = 4\epsilon \left[\left(\frac{\sigma}{r} \right)^{12} - \left(\frac{\sigma}{r} \right)^6 \right] \quad (3)$$

Figure 1 describes the LJ potential and the physical meaning of its parameters σ and ϵ .

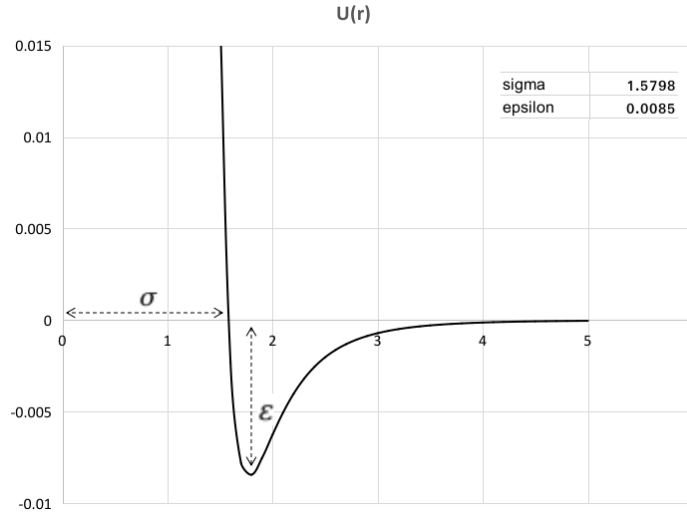


Fig. 1. Lennard-Jones potential form

This 12-6 LJ potential has two parameters, “the size parameter ” σ , and “the strength or depth parameter ” ϵ . In the MD simulation force and energy are usually evaluated only within a certain cut-off distance $r_{\text{cut-off}}$ to solve the equation of motion, for $r_{\text{cut-off}} = 2.5\sigma$.

Meanwhile, Equation (3) will be applied for the same type of atoms generally. For a pair of different types of atoms (for example iron and lead), usually we need to define specific potential parameter. Simply, we need to determine a suitable mixing rule to mix two parameters σ and ϵ that belong to each interacting elements. In this study we check several available mixing rules and use them to calculate the diffusion coefficient of iron in liquid molten lead, compare with experimental data, and then try to develop a novel mixing rule for the best calculation.

2.1 The Mixing formula/rules

2.1.1 Lorentz-Bertholet mixing formula

The cross interactions among different elements of material system could follow the very popular Lorentz-Berthelot mixing rule (Brodholt & Wood, 1993; Al-Matar & Rockstraw, 2004; Maulana, 2008). This form uses arithmetic average for defining “collision diameter” σ_{AB} and geometric average for defining “the well depth” ϵ_{AB} :

$$\sigma_{AB} = 0.5 \times (\sigma_{AA} + \sigma_{BB}) \quad (4a)$$

$$\epsilon_{AB} = (\epsilon_{AA} \times \epsilon_{BB})^{0.5} \quad (4b)$$

2.1.2 Fender-Halsey mixing formula

Another mixing formula is Fender-Halsey (FH) (Fender & Halsey, 1962). The formula is likely:

$$\sigma_{AB} = 0.5 \times (\sigma_{AA} + \sigma_{BB}) \quad (5a)$$

$$\varepsilon_{AB} = 2 (\varepsilon_{AA} \times \varepsilon_{BB}) / (\varepsilon_{AA} + \varepsilon_{BB}) \quad (5b)$$

2.1.3 Madar-Rockstraw mixing formula

Matar and Rockstraw (2006) suggested the mixing formula as (Al-Matar & Rockstraw, 2006)

$$\sigma_{AB} = \left(\frac{0.5640\sigma_{AA}^6 + 0.9464\sigma_{AA}^3\sigma_{BB}^3 + 0.4896\sigma_{BB}^6}{2} \right)^{1/6} \quad (6a)$$

$$\varepsilon_{AB} = \left(\frac{0.0799\varepsilon_{AA} + 1.912939769(\varepsilon_{AA} \times \varepsilon_{BB})^{1/2} + 0.0071\varepsilon_{BB}}{2} \right) \left(\frac{\sigma_{AA}^3 \times \sigma_{BB}^3}{\sigma_{AB}} \right) \quad (6b)$$

2.1.4 Lee-Sandler mixing formula

Later, Lee and Sandler (Kontogeorgis & Folas, 2010) suggested the mixing formula of two different atoms as:

$$\sigma_{AB} = 0.5 \times (\sigma_{AA} + \sigma_{BB}) \quad (7a)$$

$$\varepsilon_{AB} = \left(\frac{\varepsilon_{AA}^{2/3} + \varepsilon_{BB}^{2/3}}{2} \right)^{3/2} \quad (7b)$$

2.1.5 Halgren-HHG mixing formula

The Halgren HHG mixing rule implemented a weighted average of the arithmetic-mean rule for a collision diameter as (Al-Matar & Rockstraw, 2004):

$$\sigma_{AB} = (\sigma_{AA}^3 + \sigma_{BB}^3) / (\sigma_{AA}^2 + \sigma_{BB}^2) \quad (8a)$$

$$\varepsilon_{AB} = 4(\varepsilon_{AA} \times \varepsilon_{BB}) / (\varepsilon_{AA}^{1/2} + \varepsilon_{BB}^{1/2})^2 \quad (8b)$$

2.1.6 Smith-Kong mixing formula

Smith developed a combine rule by considering the repulsive interaction of simple molecules. His mixing rule includes the atomic distortion theory for repulsion interaction. Kong then used Smith's approach and a geometric mean relationship for the attractive interactions and applied it to the LJ mixing formula as (Schnabel *et al.*, 2009)

$$\sigma_{AB}^{SK} = \left\{ \frac{[(\epsilon_{AA} \times \sigma_{AA}^{12})^{1/13} + (\epsilon_{BB} \times \sigma_{BB}^{12})^{1/13}]^{13}}{2^{13} \sqrt{(\epsilon_{AA} \times \sigma_{AA}^6) \times (\epsilon_{BB} \times \sigma_{BB}^6)}} \right\}^{1/6} \quad (9a)$$

$$\epsilon_{AB}^{SK} = \left\{ \frac{2^{13} \times (\epsilon_{AA} \times \sigma_{AA}^6) \times (\epsilon_{BB} \times \sigma_{BB}^6)}{[(\epsilon_{AA} \times \sigma_{AA}^{12})^{1/13} + (\epsilon_{BB} \times \sigma_{BB}^{12})^{1/13}]^{13}} \right\}^{1/6} \quad (9b)$$

2.1.7 Waldman-Hagler mixing formula

Waldman and Hagler also formulated the cross interaction term for rare gas van der waals parameters as presented below (Waldman and Hagler, 1993)

$$\sigma_{AB} = \left\{ \frac{\sigma_{AA}^6 + \sigma_{BB}^6}{2} \right\}^{1/6} \quad (10a)$$

$$\epsilon_{AB} = \{\epsilon_{AA} \times \epsilon_{BB}\}^{1/2} \left\{ \frac{\sigma_{AA}^3 \times \sigma_{BB}^3}{\sigma_{AB}^6} \right\} \quad (10b)$$

2.1.8 New mixing formula

In this work, we develop a novel mixing formula or rule by modifying the collision diameter σ_{AB} and the well depth ϵ_{AB} as:

$$\sigma_{AB} = \{\sigma_{AA}^2 + \sigma_{BB}^2\}^{1/6} \quad (11a)$$

$$\epsilon_{AB} = \{\epsilon_{AA}^2 + \epsilon_{BB}^2\}^{1/2} \quad (11b)$$

3. Diffusion coefficient calculation

The liquid lead corrosion may be observed as an effect of high dissolution of steel components into liquid lead. In particular, for the hot corrosion as in the liquid lead corrosion, we can consider the corrosion as a diffusion process where no transfer of electrons (Manly, 1959). Subsequently, we can run MD simulation as a classical MD simulation. The most prevalent component of steel material is iron, and the steel corrosion in liquid lead may be modelled mostly as the iron corrosion in liquid lead. The diffusion coefficient that describes the diffusion of iron may be calculated by following these equations below (Kupryazhkin *et al.*, 2008):

$$\text{MSD} = \left\langle |\vec{R}(t) - \vec{R}(0)|^2 \right\rangle \quad (\text{mean square displacement}) \quad (12)$$

$$D = \text{MSD}/6t \quad (\text{diffusion coefficient}) \quad (13)$$

where t is time and $R(t)$ is related to atomic trajectory. The temperature dependence of the diffusion coefficient can be predicted by following the Arrhenius formula,

$$D(T) = D_0 \exp(-A/RT) \quad (14)$$

where T represents temperature, A is an activation energy for diffusion to be happen, and R is a universal gaseous constant. This Arrhenius form of temperature dependent diffusion coefficient is prevalent in several application fields (Abidli *et al.*, 2021).

4. Simulation procedure and calculation

The objective of this study is to find the best mixing formula that produces the diffusion coefficient of iron within liquid lead that agree with experimental data. We calculate the iron diffusion coefficient $D_{Fe \rightarrow Pb}$ for different types of mixing formulas (Equation (4 – 11)) and then compare them with available experimental data. There were two experimental results for the comparison, develop by Robertson: (1) single value of iron diffusion at temperature 750 °C and (2) temperature dependent of iron diffusion (Zhang & Li, 2008). Robertson reported that the single value of iron diffusion coefficient measurement was $D_{Fe \rightarrow Pb} = 2.80 \times 10^{-9} \text{ m}^2/\text{s}$ at 750 °C, and developing the formula of the temperature dependent diffusion coefficient of iron as:

$$D_{Fe \rightarrow Pb}(T) = 4.9 \times 10^{-7} \cdot \exp(-44100/RT) \quad [\text{m}^2/\text{s}] \quad (15)$$

Based on the Equation (15), $D_{Fe \rightarrow Pb} = 2.74 \times 10^{-9} \text{ m}^2/\text{s}$ at 750 °C. Comparing several mixing formulas, the best formula is one that produces the smallest discrepancy compared with the value, $D_{Fe \rightarrow Pb} = 2.73 \times 10^{-9} \text{ m}^2/\text{s}$.

After the simulation, the diffusion coefficient D can be easily determined and calculated from MSD file of Moldy MD simulation output, following Equation (12 – 14). The procedure of (corrosion) simulation follows these below steps:

- (I) Prepare the values of potential parameter ($\sigma_{AB}, \epsilon_{AB}$), for the mixing formula calculated by Equation (4 – 11).
- (II) Prepare inputs of the Moldy simulation in two files: specification and control files.
 - 1). Specification file comprises the potential parameter (σ, ϵ), number of atoms, type of atoms, coordinates of atoms in material, etc. In this simulation, the material system under study (FePb) was designed with 22815 Fe atoms in the form of bcc solid crystals and 11189 Pb atoms in the form of liquid state. We place the iron bcc crystal at the center of the liquid lead material.

Potential parameters for interaction among atoms following the Lennard-Jones potential (Equation (3)) is given by Table 1, including for different types of the mixing formula (Equation (4 - 11)). In Table 1., we adopt data of potential parameters from Zhen & Davies (1983) for the interaction of same type of atoms Fe-Fe and Pb-Pb. The potential parameter of Fe-Fe is $\sigma_{AA} = 2.3193 \text{ \AA}$ and $\epsilon_{AA} = 0.4007 \text{ eV}$, and for Pb-Pb is $\sigma_{AA} = 3.1888 \text{ \AA}$ and $\epsilon_{AA} = 0.191 \text{ eV}$.

Table 1. List of Fe-Pb potential parameters for different mixing formulas

Potential parameters	Lorentz-Bertholet	Fender Halsey	Madar-Rockstraw	Lee-Sandler	Halgren-HHG	Smith-Kong	Waldman-Hagler	New formula
Equation	(4)	(5)	(6)	(7)	(8)	(9)	(10)	(11)
$\sigma_{AB} (\text{\AA}) \square$	2.7541	2.7541	2.8104	2.7541	2.8880	1.1289	2.9070	1.5798
$\epsilon_{AB} (\text{eV}) \square$	0.3503	0.3248	0.2928	0.3687	0.3371	0.3207	0.2348	0.5705

2) The control file demonstrates how the simulation will be run. This includes temperature T (1023K), pressure P (0 Mpa), integration step $nsteps$ (100000), timestep (0.0001 ps), ensemble NPT (Andersen constant pressure, Nose Hoover Thermostat), equilibration condition *begin-average* (at step 50000), $r_{\text{cut-off}} = 8.125 \text{ \AA}$.

(III) Running simulation

To run the simulation using the command line as: `$moldy control_name output_name`

There are two kind of simulations here,

- (1) The first simulation is to compute the diffusion coefficient calculation (D) for all of the mixing formulas at temperature 1023 K or 750 °C,
- (2) The second simulation will be run at temperatures 623 K, 723 K, 823 K, 923 K, 1023 K, 1123 K, 1223 K, 1323 K. This step will be run after the best mixing formula can be found after comparison of the mixing formulas. This step determines the temperature dependent diffusion coefficient $D(T)$ based on the Arrhenius formula.

(IV) Calculation of diffusion coefficient D , Equation (13). The diffusion coefficient of Fe into Pb can be computed by extracting the output of simulation using Moldy's utility command line (as in manual):

`$msd -r save_file -d dump_file -t x-xx -m x-xx -o output_name`

(V) Comparison of the obtained diffusion coefficients with available experimental data using the data as reported by Zhang & Li (2008) which was explained before. The choice of simulating the phenomena at a temperature of 750 °C because of following the temperature of experimental data.

5. Results and discussions

5.1 Diffusion coefficient of iron in liquid lead

The iron diffusion coefficients calculation for different mixing formulas can be summarized as presented in Table 2. The corrosion of iron was regarded as diffusion of iron atoms flowing into the liquid lead coolant. The higher the diffusion coefficient of iron ($D_{Fe \rightarrow Pb}$), more corrosion of iron in liquid lead. The corrosion was evaluated at temperature 1023 K (or 750 °C). The diffusion coefficient was measured in m^2/s . To justify which mixing rule is better than others, we compared the diffusion coefficient from simulation results with $D_{Fe \rightarrow Pb} = 2.73 \times 10^{-9} [m^2/s]$ of available experimental data (Zhang & Li, 2008). From our calculation, the diffusion coefficient of iron in liquid lead can be presented as in Table 2.

Table 2. Comparison D of different mixing formulas and experiment $D_{Fe \rightarrow Pb} = 2.73 \times 10^{-9} [m^2/s]$.

No.	Mixing rule/formula	$D_{Fe \rightarrow Pb} [m^2/s]$ (simulation)	% discrepancy (simulation and experiment)
1	Lorentz-Bertholet (LB)	1.295×10^{-9}	52.56%
2	Fender-Halsey (FH)	1.306×10^{-9}	52.16%
3	Madar-Rockstraw (MR)	1.308×10^{-9}	52.09%
4	Lee-Sandler (LS)	1.311×10^{-9}	51.98%
5	Halgren-HHG (HHG)	1.312×10^{-9}	51.94%
6	Smith-Kong (SK)	1.313×10^{-9}	51.90%
7	Waldman-Hagler (WH)	1.289×10^{-9}	52.78%
8	New formula (NF)	2.719×10^{-9}	0.40%

W.M. Robertson stated that this formula will be valid for calculation of diffusion coefficient of iron in liquid lead for the temperature 500 °C to 750 °C (Zhang & Li, 2008). From Table 2, it can be observed that all mixing formulas No.1 to No.7 have the discrepancy of approximately 52%. However, using the new mixing formula (NF), the discrepancy between simulation and experiment is only about 0.40%. Hence, our mixing formula has shown better result for treating the different type of atom Fe and Pb, especially for studying corrosions of this metal systems that is iron in liquid lead.

The diffusion process should be a temperature dependent process. We need to know how the new formula above can also consistently be used to calculate the diffusion coefficient of iron at various temperatures. From single temperature we got very good result, the error is only approximately 0.40%.

5.2 Temperature dependent diffusion coefficient of iron in liquid lead

Is there any certain temperature area that shows a mismatch between the simulation results and the experimental results? Now we discuss about the temperature dependent diffusion coefficient $D(T)$ or rather is $D_{Fe \rightarrow Pb}(T)$ for iron in liquid lead. To determine this physical variable, we will use the Arrhenius equation model to determine the relationship between D diffusion coefficient and T temperature as Equation (14), or rather is

$$D_{Fe \rightarrow Pb}(T) = D_0 \exp(-A/RT) \quad (16)$$

To determine the parameter D_0 and A (an activation energy such that the diffusion process can occur), we need to obtain a linear graph between $\ln D$ and $1/T$:

$$\ln D_{Fe \rightarrow Pb}(T) = (-A/R)(1/T) + \ln D_0 \quad (17)$$

The data of this graph were collected from simulations for eight temperatures to produce the diffusion coefficients of iron in liquid lead as in Table 3. All of the simulations using our new formula of potential parameter as in equation (11).

Table 3. The plot graph between $\ln D_{Fe \rightarrow Pb}(T)$ and $1/T$ for iron diffusion coefficient

No.	T [K]	$D_{Fe \rightarrow Pb}$ [m ² /s]	$1/T$	$\ln D_{Fe \rightarrow Pb}(T)$
1	623	$2.3456795783 \times 10^{-10}$	0.001605	-22.17328
2	723	$3.9752703205 \times 10^{-10}$	0.001383	-21.64576
3	823	$8.4197082436 \times 10^{-10}$	0.001215	-20.89528
4	923	$4.9522904843 \times 10^{-10}$	0.001083	-21.42600
5	1023	$2.78602483974 \times 10^{-9}$	0.000978	-19.69865
6	1123	$4.47737065256 \times 10^{-9}$	0.000890	-19.22423
7	1223	$6.68402505385 \times 10^{-9}$	0.000818	-18.82355
8	1323	$8.89067945514 \times 10^{-9}$	0.000756	-18.53826

The plot of $\ln D_{Fe \rightarrow Pb}(T)$ and $1/T$ for iron diffusion coefficient based on the above Table 3 can be observed as following Figure 2.

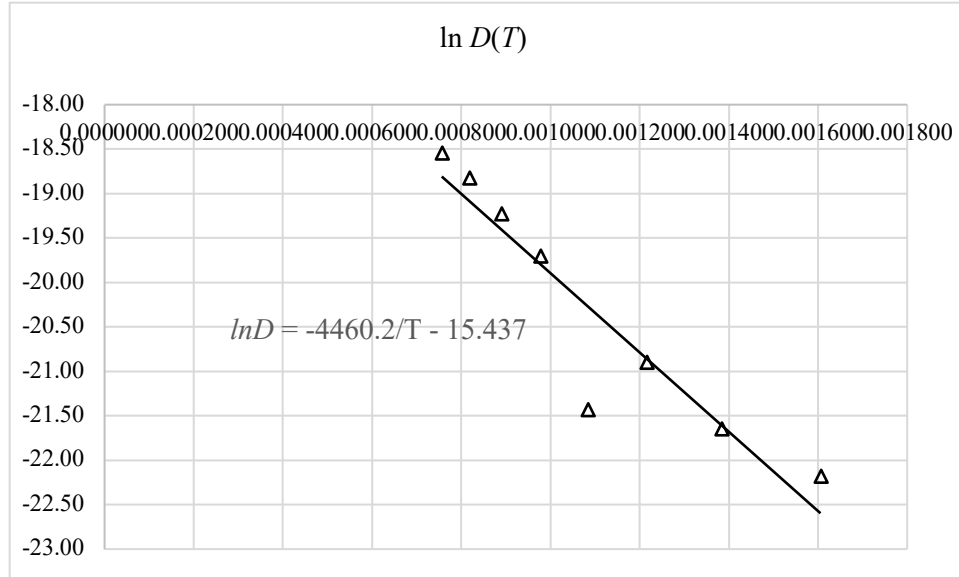


Fig. 2. Plot of $\ln D_{Fe \rightarrow Pb}(T)$ and $1/T$ for iron diffusion coefficient

From Figure 2 we can determine that $D_0 = 1.98847 \times 10^{-7} \text{ m}^2/\text{s}$ and also activation energy $A = 37064.47279 \text{ kJ/mol}$. Based on these values, the temperature dependent diffusion coefficient of iron in liquid lead can be written as

$$D_{Fe \rightarrow Pb}(T) = 1.98847 \times 10^{-7} \exp(-37064.47/RT) \quad [\text{m}^2/\text{s}] \quad (18)$$

This result, Equation (18), can be compared with Robertson experimental result (equation (15)) as in Figure 3 below.

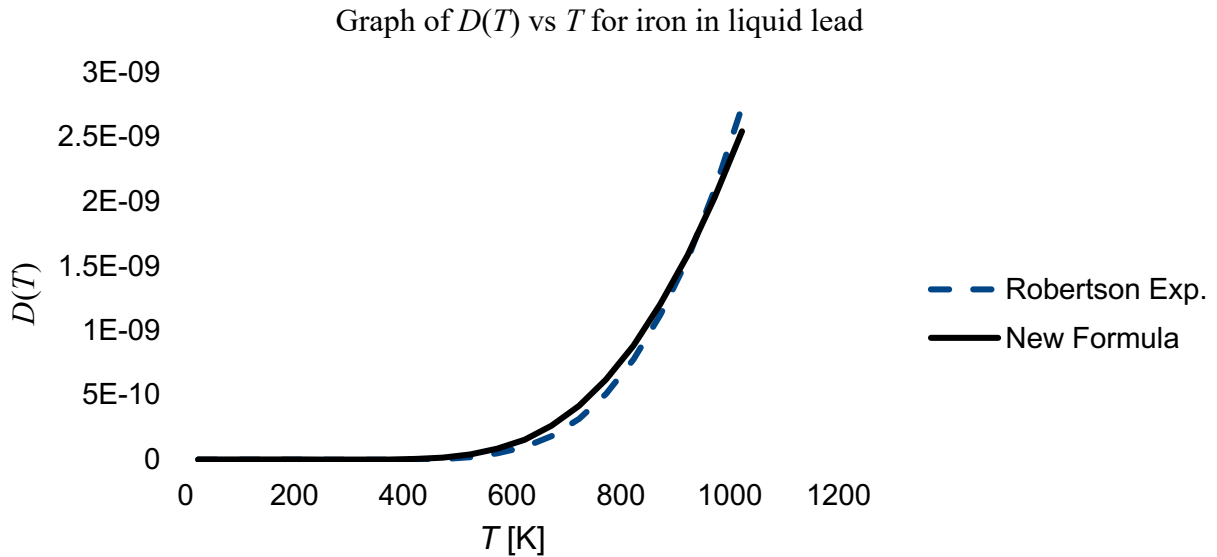


Fig. 3. Plot of equation (15) and (18)

Now we can discuss more details about the simulation result. Lets us to compare for some points at higher temperatures (873 K to 1423 K). Table 4 shows the comparison between Robertson curve (Equation (15)) and our calculation using new formula (equation (18)).

Table 4. Comparison between experiment and simulation results of $D(T)$

T [K]	Robertson Curve	New Formula	% discrepancy
873	1.12247×10^{-9}	1.20137×10^{-9}	7.03%
923	1.56022×10^{-9}	1.58443×10^{-9}	1.55%
973	2.09653×10^{-9}	2.03103×10^{-9}	3.12%
1023	2.73699×10^{-9}	2.54108×10^{-9}	7.16%
1073	3.48543×10^{-9}	3.11353×10^{-9}	10.67%
1123	4.3440×10^{-9}	3.74654×10^{-9}	13.75%
1173	5.31338×10^{-9}	4.43767×10^{-9}	16.48%
1223	6.39292×10^{-9}	5.18403×10^{-9}	18.91%
1273	7.58084×10^{-9}	5.98242×10^{-9}	21.08%

From Table 4, we can obtain important points: that is the New Formula will relatively match with experimental result for temperature interval of 873 K to 1023 K, with discrepancy not more than 7.2% and has a very good agreement at a temperature of approximately 923 K with discrepancy is about only 1.55%. At a temperature more than 1023 K, the discrepancy will increase to value about 21% at temperature 1273 K. Based on this simulation results it seems that we can state that the New Formula can be used to describe, explain and predict the properties and phenomena of liquid lead (and alloy) metal, for example for studying the liquid lead corrosion. The novel formula may applied accurately at temperature not more then 1023 K if we limit our calculation error not more then 7.2%, compared to experimental result. At least, the important thing is the Lennard-Jones potential remains a good approximation to study a metal system, especially for preliminary prediction, with a modified potential parameters, as we suggested in our current work.

6. Conclusions

Based on the molecular dynamics simulation using the Lennard-Jones potential with the novel mixing formula to compute the cross-term of potential parameters, the diffusion coefficient calculation of iron in liquid lead has shown a significant improvement of accuracy in comparison with the experimental value. In this study, for liquid metal system as in the corrosion liquid metal phenomena, using the novel mixing rule for calculating the cross-term of Lennard-Jones potential parameter ($\sigma_{AB}, \epsilon_{AB}$), we have the following accurate results:

1. novel mixing rules:

$$\text{sigma parameter } \sigma_{AB} = \{\sigma_{AA}^2 + \sigma_{BB}^2\}^{1/6} [\text{\AA}]$$

$$\text{epsilon parameter } \epsilon_{AB} = \{\epsilon_{AA}^2 + \epsilon_{BB}^2\}^{1/2} [\text{eV}],$$

2. diffusion coefficient:

$$D_{Fe \rightarrow Pb}(T) = 1.98847 \times 10^{-7} \exp(-37064.47/RT) \quad [\text{m}^2/\text{s}],$$

3. calculation error of $D_{Fe \rightarrow Pb}(T)$:

< 7.2% and > 10% for $T < 1073 \text{ K}$ and $T > 1073 \text{ K}$, respectively, with the best prediction of $D_{Fe \rightarrow Pb}(T)$ for the error of approximately 1.55% at the temperature 923 K.

In this study, we have applied our novel mixing formula just for liquid metal system including only two types of atom (Fe and Pb). We haven't implemented to other materials, yet. It is important to verify this new formula for other materials and phenomena for the next study. However, at least, for liquid lead corrosion, as our simulation results we believe this novel formula can be adopted to study the corrosion phenomena in liquid metals better.

References

Abidli, I. Souissi, N., Novoa, X.R., (2021) Corrosion inhibition of iron in chloride media by the aqueous extract of Curcuma longa rhizome powder, Kuwait Journal of Science, Vol. 48 No. 2 (2021) DOI: <https://doi.org/10.48129/kjs.v48i2.8855>

Al-Matar, A.K., & Rockstraw, D.A. (2004) A Generating Equation for mixing rules and two new rules for interatomic potential energy parameters, J Comput Chem 25: 660-668.

Al-Matar, A.K., & Rockstraw, D.A. (2006) Assessment of the Effect of Mixing Rules on Predicting the Second Virial Coefficient and a Further Evidence of the Inadequacy of the Lorentz-Berthelot Rules, Dirasat, Engineering Sciences, Volume 33, No. 1

Arkundato, A., Su'ud, Z. & Mikrajuddin, A. (2010) Corrosion study of Fe in a stagnant liquid Pb by molecular dynamics methods, *AIP Conf. Proc.* 1244 136-144.

Arkundato, A., Su'ud, Z., Mikrajuddin, A., Widayani, S. & Massimo, C. (2012), Numerical study: iron corrosion-resistance in lead-bismuth eutectic coolant by molecular dynamics method, *AIP Conf. Proc.* 1454, 65.

Arkundato, A., Su'ud, Z., Mikrajuddin, A. & Widayani, S. (2013a) Study of liquid lead corrosion of fast nuclear reactor and its mitigation by using molecular dynamics method, *International Journal of Applied Physics and Mathematics*, Vol. 3, No. 1, January 2013, , Singapore.

Arkundato, A., Su'ud, Z., Mikrajuddin, A. & Widayani, S. (2013b) Molecular dynamic simulation on iron corrosion-reduction in high temperature molten lead-bismuth eutectic, *Turkish Journal of Physics*, DOI: 10.3906/fiz-1112-12

Arkundato, A., Su'ud, Z., Mikrajuddin, A. & Widayani, S. (2013c) Inhibition of iron corrosion in high temperature stagnant liquid lead: A molecular dynamics study, Vol 62, Pages 298–306, *Annals of Nuclear Energy*, Elsevier.

Arkundato, A., Su'ud, Z., Sudarko, Hasan, M. & Celino, M. (2015) Molecular dynamics simulation of corrosion mitigation of iron in lead-bismuth eutectic using nitrogen as corrosion inhibitor, *Journal of Physics: Conference Series*, Vol. 622 (2015) 012009, IOP Publishing.

Arkundato A., Monado F., & Su'ud Z. (2017) Effect of temperature on the corrosion inhibition of iron in liquid lead using oxygen inhibitor: studied by MD simulation, *IOP Conf. Series: Journal of Physics: Conf. Series* 012046 doi :10.1088/1742-6596/853/1/012046.

Arkundato, A., Monado, F., Supeno, Misto & Su'ud, Z. (2019) Performance of the Fe-Ni-Cr steel alloy in high temperature molten liquid lead, *IOP Conf. Series: Journal of Physics: Conf. Series* 1170, 012010, IOP Publishing, doi:10.1088/1742-6596/1170/1/012010.

Belashchenko, D.K. (2009) Application of the embedded atom model to liquid metals: Liquid sodium, *High Temperature* 47(4):494-507. DOI: 10.1134/S0018151X09040063.

Brodholt, J. & Wood, B. (1993) Molecular dynamics simulations of the properties of CO₂-H₂O mixtures at high pressures and temperatures, *American Mineralogist*, 78, 558.

Fender, B.E.F. & Halsey, G.D. (1962) Second Virial Coefficient of Argon, Krypton and Argon-Krypton Mixtures at Low Temperature, *The Journal of Chemical Physics*, 36, 1881-1888.

Kashezhev, A. Z, Ponegev, M. Kh, Sozaev, V. A., Khasanov, A. I., & Mozgovo, A. G., (2010) An experimental investigation of the wetting of reactor steels with molten lead and bismuth, *High Temp.*48(5), 756.

Kontogeorgis, G.M. & Folas, G.K. (2010) Thermodynamical Models for Industrial Application: From Classical and Advanced Mixing rules to Association Theorie, John Wiley and Sons, Ltd.

Kupryazhkin, A.Y., Zhiganov, A. N., Risovany, D. V., Nekrassov, K. A. & Golovanov, V. N., (2008) Simulation of diffusion of oxygen and uranium in uranium dioxide nanocrystals, *J. Nucl. Mater.*372.

Waldman, M. & Hagler, A.T. (1993) "New combining rules for rare gas van der waals parameters", *Journal of Computational Chemistry*, 14 (9): 1077-1084.

Maulana, A., Su'ud, Z. and Hermawan, K. D. & Khairurrijal (2008) Simulation study of steels corrosion phenomenon in liquid lead-bismuth cooled reactors using molecular dynamics methods, *Prog. Nucl. Energy*, 50, 616-620.

Mendelev, M.I. , Kramer , M.J. , Becker, C.A. & Asta , M. (2008) Analysis of semi-empirical interatomic potentials appropriate for simulation of crystalline and liquid Al and Cu, *Philosophical Magazine* , Volume 88, 2008 - Issue 12.

Refson, K. (2000) Moldy: A Portable molecular dynamics simulation program for successive and parallel computers, *Comp. Phys. Commun.* 126(3) 309-328.
<http://ccl.net/cca/software/SOURCES/C/moldy/>
<https://data.mendeley.com/datasets/rgnh52j3st/1>

Sa'adah, U., Arkundato, A. & Hasan, M. (2020a) Simulation of iron corrosion in lead magnesium eutectic using oxygen inhibitor, *Jurnal Sains Materi Indonesia* 21 (3), 129-134.

Schnabel, H., Vrabec, J. & Hasse, H. (2009) “Unlike Lennard-Jones Parameters for Vapor-Liquid Equilibria, *arXiv.0904.4436v1[physics. chem-ph]* 28 Apr 2009.

Triwardani, A., Arkundato, A., Sutisna, Maulina, W. & Purwandari, E. (2020b), Investigation of iron in high temperature molten liquid lead using the Lennard-Jones potential, *AIP Conference Proceedings* 2278 (1), 020041.

Zelenskii, G.K., Ivanov, Y.A, Ioltukhovskii, A.G., Naumenko, I.A. & Shkabura, I.A (2006) Possible ways for protecting fuel claddings from corrosion on the side of the heat-transfer lead sublayer, *Metal Sci. Heat Treat.*, 48, 412.

Zelenskii, G.K., Ioltukhovskii, A.G., Leont’eva-Smirnova, M.V., Naumenko, I.A. & Tolkachenko, S.A. (2007) Corrosion resistance of fuel element steel cladding in a lead coolant, *Metal Sci. Heat Treat.*, 49, Nos.11-12, 533 - 538.

Zhang, J. & Li, N. (2008) Review of the studies on fundamental issues in LBE, *J. Nucl.Mater.* 373 351-377.

Zhang, V., Hosemann, P. & Maloy, S. (2010) Models of liquid metal corrosion, *J. Nucl.Mater.*404, 82.

Zhen, S. & Davies, G.J. (1983) L-J n-m potential energy parameters: calculation of the LJ n-m pot energy parameters for metals, *Phys.Stat.Sol.(a)*,78, 595.

Submitted: 13/11/2021

Revised: 11/02/2022

Accepted: 26/02/2022

DOI: 10.48129/kjs.17205

Scattering of gamma radiation by air in the ambient environment using gamma ray spectrometry

Anita Mishra*, Raju Khanal

*Central Dept. of Physics, Tribhuvan University, Kirtipur,
Kathmandu 44613, Nepal*

**Corresponding author: anita.745711@cdp.tu.edu.np*

Abstract

The intensity of gamma radiation reduces as it traverses through matter. The gamma radiation from Earth's surface is attenuated by non-radioactive burden between the ground and the detector. The relative intensity of unscattered to scattered gamma radiation by air in ambient atmosphere is measured using in-situ gamma spectrometric method. The air thickness up to 300 cm is used for studying attenuation of terrestrial gamma radiation. No significant attenuation is measured up to 100 cm thickness of air between the detector and the ground. The attenuation by air is found to increase with increasing thickness of air. Also, the attenuation of terrestrial gamma radionuclides (^{40}K) is found higher than ^{238}U and ^{232}Th as ^{40}K has lower energy compared to them.

Keywords: Attenuation; gamma radiation; gamma spectrometry; intensity; terrestrial radionuclides.

1. Introduction

The intensity of gamma radiation reduces as it traverses matter. This is known as attenuation of gamma radiation. The attenuation is caused by scattering and absorption of gamma ray by the matter. The attenuation of gamma ray passing through a material depends upon the thickness and the type of material. Terrestrial radiation is attenuated by a material between the detector and the source. The peak of the spectra reduces with increase in attenuation. Thus, the measured spectra can be different depending on its height from the ground and on the thickness of the non-radioactive material between the ground and the detector (IAEA, 2003).

Measured radiation will be affected by about 7% by 10 meters of air. The radiation from the Earth's surface is reduced remarkably by non-radioactive material between the Earth's surface and the detector. Dense vegetation can reduce 35% of the radiation. Snow covers also attenuate radiation in significant amount from the ground. The attenuation coefficient of snow for gamma rays is around 100 times larger than due to ambient air. In ambient air, the attenuation coefficient depends on the energy of gamma rays and has almost linear dependency with density of the air. This implies that the temperature and pressure also affect the attenuation. Moisture content in the soil is another important factor to attenuate the gamma radiation. The increase in

soil moisture of 10% will decrease the fluence rate measured by same amount. However, uranium ground concentrations are increased by rain (Charbonneau & Darnley, 1970). The anomalous surface activity decays away only after about three hours. The variable attenuation of gamma rays is resulted by seasonal and daily precipitation due to snow cover and soil moisture (Rubin *et al.*, 1980).

The relative intensity of the gamma radiation (unscattered) to that scattered increases with materials between the detector and the source as it depends on the material density. Linear attenuation coefficient increases with density and thus mean free path decreases, which reduces the fluence rate at the detector (Allyson, 1994). The attenuation of gamma ray is mainly due to interactions with atomic electrons and depends upon atomic number of the materials (shielding) and energy of gamma ray. The attenuation coefficient (μ) measures the quantity of attenuated radiation by an absorbing material thickness.

$$\mu = -\frac{\Delta I}{I\Delta x} \quad (1)$$

Integrating equation (1), we get

$$I = I_0 e^{-\mu x} \quad (2)$$

Attenuation of gamma rays by any media takes place by one or more of the following interaction: photoelectric absorption, Compton scattering and pair production. The photoelectric interaction occurs when the energy of incident photon is nearly equal to the binding energy of that electron. The photoelectric interaction decreases with increase in photon energy. A Compton scattering occurs when the incident photon collides with free electrons and is deflected in new direction with reduced energy. The Compton scattering decreases for higher energy photon. Pair production occurs when high energy photon (> 1.02 MeV) interact with atomic nucleus. Therefore, Compton interaction is dominating in terrestrial radiation range.

The total linear attenuation coefficient is given by equation (3),

$$\mu_{total} = \mu_{P.E.} + \mu_{C.S.} + \mu_{P.P.} \quad (3)$$

Many studies have been done on non-radioactive burden. Grasty had developed the direct determination method for estimating amount of attenuation material through suitable calibration. A snow-water equivalent thickness was estimated for airborne gamma ray spectrometry. In this method, the change in gamma spectrum shape due to gamma ray attenuation in snow mass and low energy photons built up by Compton scattering was measured (Grasty, 1982). The original photons energies are reduced in the detector, in the source and the matter between them by Compton scattering. Thus, the relative contribution of unscattered and scattered photons to the fluence rate depends on the amount of material between the detector and the source. The spectral count for NORM by removing Compton continuum counts is studied for better photo peak visibility in cases where radioisotopes is weakly present (Demir *et al.*, 2018). Martin & Gomes found daily fluctuation in the intensity of environmental gamma radiation with some increase during the rainfall (Martin & Gomes, 2021). The intensity variation is also studied theoretically (simulation) for shielding properties (Ismail *et al.*, 2021). Since, low energy photons are attenuated more easily than high energy photons, source thickness effect is more significant at

lower energies. The measured gamma radiation is affected by the attenuating material's amount between the detector and the source. The aim of the study is to study the relative intensity of terrestrial gamma radiation (unscattered) to that scattered for different thickness of air by increasing the height of detector from the ground.

2. Methods

The process is carried in-situ using gamma ray spectrometer, PGIS2. The detector is equipped with 0.347 liters of NaI(Tl) crystals and is coupled with multi-channel analyzer having 512 channels. It is automated calibrated with natural radionuclides peaks ^{40}K , ^{232}Th or ^{238}U and can operate between -20°C to 50°C temperature. The energy range of detector is within 20 keV to 3 MeV. The start-up stabilization time of the instrument is less than 60 seconds and it can measure spectra per second. The data is recorded in data logger unit (android device) which has wireless communication with the detector. It is based on advanced microprocessor and mobile technologies and gives real-time navigation guidance.

The measurements are carried out for six different thickness of air in ambient environment by raising the height of detector to 50 cm, 100 cm, 150 cm, 200 cm, 250 cm and 300 cm from the ground in open field. The measurements for each thickness were taken for at least two minutes and our instrument records spectra every second. So, at least 120 measurements were taken for each thickness. The spatial variability and the land have impact on environment (Amiri & Mesgari, 2018; Al-Jiboori *et al.*, 2020). For the measurements to be comparable, the conditions on the ground and in the air for all measurements were ensured to be the same. For this, the measurements were carried at the same place within half an hour. The measurement is done using gamma ray spectrometric method. The ^{40}K is directly measured from its emission line at 1.461 MeV while the Uranium and Thorium decay series is measured from the gamma emission of ^{214}Bi at 1.764 MeV and ^{208}Tl at 2.614 MeV respectively. The example of accumulated spectra during analysis is shown in Figure 1.

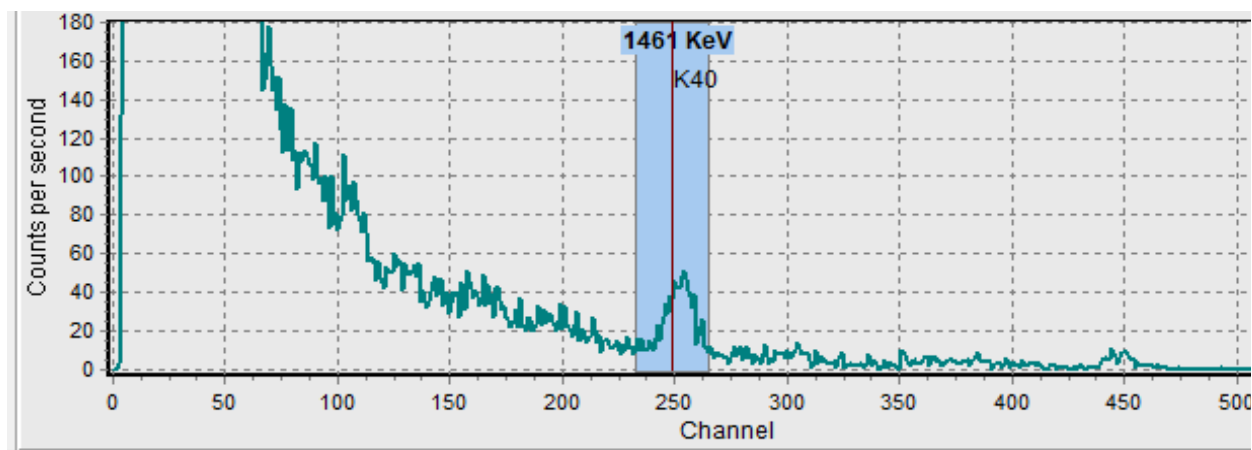


Fig. 1. Gamma ray spectra of ^{40}K

The mass attenuation coefficient of air; considering mixture of 78.08 % N₂, 20.95 % O₂, 9.34×10^{-3} % Ar and 3.45×10^{-4} % CO₂ (Allen & Cox, 2000); for 1.41 MeV (⁴⁰K), 1.76 MeV (²³⁸U) and 2.61 MeV (²³²Th) gamma rays were calculated using the NIST XCOM online calculator (<https://physics.nist.gov/PhysRefData/Xcom/html/xcom1.html>). The corresponding linear attenuation coefficients, and hence the attenuation lengths in air were calculated from linear attenuation coefficient.

3. Results and Discussion

The variation of the intensity of the environmental gamma radiation can be studied by measuring count rates (Katase *et al.*, 1982). The intensity of gamma radiation is found decreasing with the thickness of air as total count is decreasing with the height of the detector (Table 1). The decrease in total count is considerable with the change of 100 cm thickness of air as the attenuation coefficient is very low for air. The change in intensities of gamma rays from terrestrial radionuclides (⁴⁰K, ²³⁸U and ²³²Th) is listed in Table 2. The bar plot of total count rate is shown in Figure 2. The total count rate from ⁴⁰K is found higher than ²³⁸U and ²³²Th (Figure 3). The count rates from ²³⁸U are found slightly greater than ²³²Th.

Table 1. Intensity of terrestrial gamma radiation with height of detector

Thickness of air (cm)	Total count rate (cps)		
	Range	Mean	S.E.
50	91 to 130	107.0	0.1
100	86 to 130	107.7	0.1
150	82 to 127	105.6	0.1
200	71 to 126	98.1	0.1
250	71 to 115	98.2	0.1
300	65 to 109	88.9	0.1

Table 2. Intensity of particular terrestrial gamma radiation with height of detector

Thickness of air (cm)	Mean Total count (cps)		
	⁴⁰ K	²³⁸ U	²³² Th
50	9.9±0.4	2.3±0.3	1.9±0.2
100	9.8±0.4	2.0±0.3	1.9±0.2
150	10.2±0.4	2.2±0.4	1.9±0.2
200	8.5±0.5	2.2±0.3	1.7±0.2
250	8.8±0.3	2.0±0.3	1.8±0.2
300	8.7±0.4	1.8±0.3	1.7±0.2

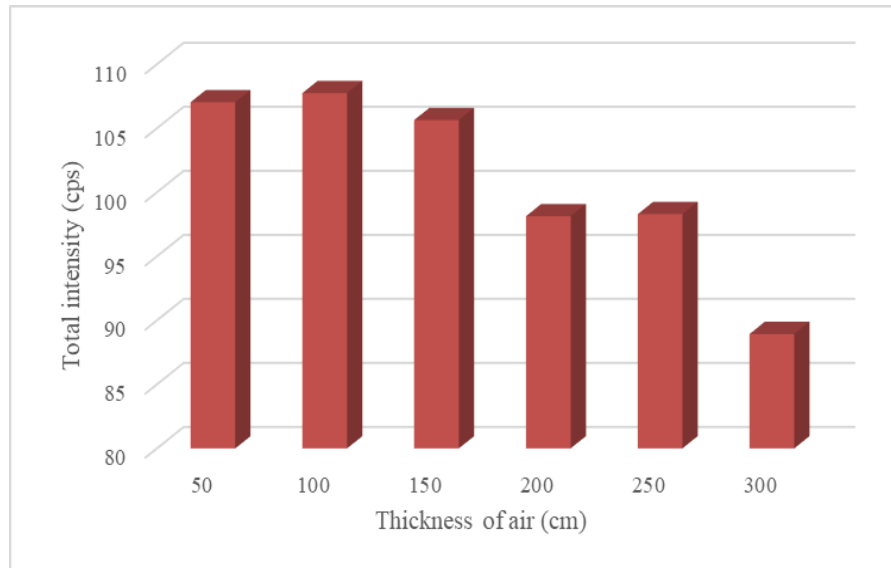


Fig. 2. Intensity of gamma ray with increasing thickness of air

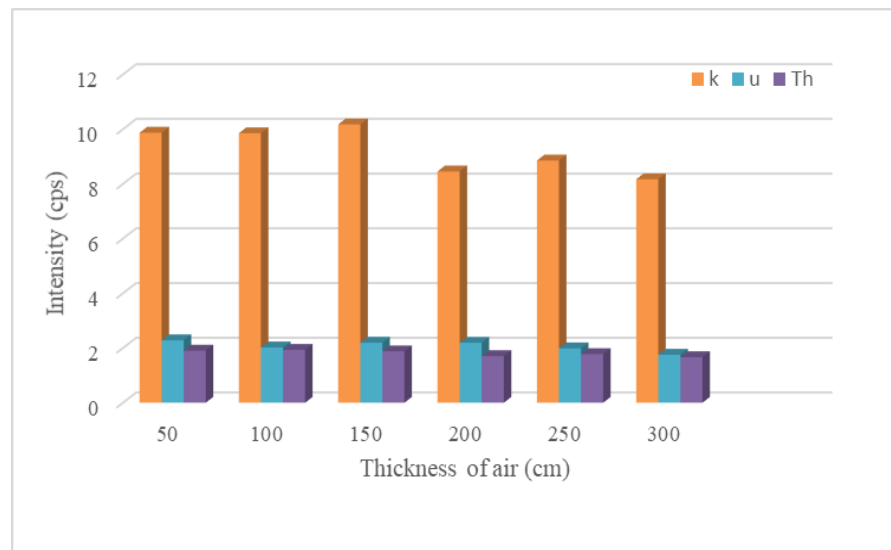


Fig. 3. Intensity of gamma ray from particular terrestrial radionuclides with increasing thickness of air

The nature of attenuation of terrestrial gamma radiations in air in ambient atmosphere is shown in Figure 4. As the detector sensitivity to primary and scatter photons are different, the detector response can affect attenuation curve in broad-beam geometries. The nature is found similar for high energy (Badawy & El-latif, 2017; Vargas *et al.*, 2002). As the energy of terrestrial gamma radionuclides is high, we can say that the results are comparable.

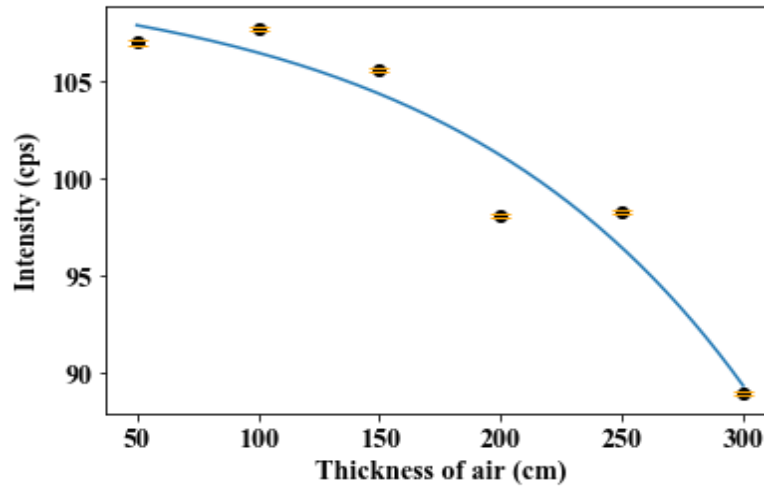


Fig. 4. Attenuation of gamma ray with increasing thickness of air

The intensity of gamma rays decreases with thickness and energy which can be seen from Figure 5. The attenuation is found higher for ^{40}K compared to ^{238}U and ^{232}Th as ^{40}K has lower energy. Also, it can be seen that attenuation is increasing exponentially with the increase in thickness of air. Since, no significant attenuation was found up to 100 cm height of detector from ground, the height of the detector from ground is always maintained below 1 m during in-situ survey. The total mass attenuation coefficient of air for 1.41 MeV (^{40}K), 1.76 MeV (^{238}U) and 2.61 MeV (^{232}Th) gamma rays were calculated $5.342 \times 10^{-3} \text{ cm}^2/\text{g}$, $4.762 \times 10^{-3} \text{ cm}^2/\text{g}$ and $3.854 \times 10^{-3} \text{ cm}^2/\text{g}$ respectively. The attenuation of gamma ray in air is mainly due to scattering as absorption is very less compared to scattering. Also, coherent scattering is not considerable for high energy. The attenuation length in air for 1.41 MeV (^{40}K), 1.76 MeV (^{238}U) and 2.61 MeV (^{232}Th) gamma rays were calculated to be 10775.9 cm, 12087.9 cm and 14934.6 cm respectively. This justifies that no significant attenuation was measured up to 300 cm in air for these energy range.

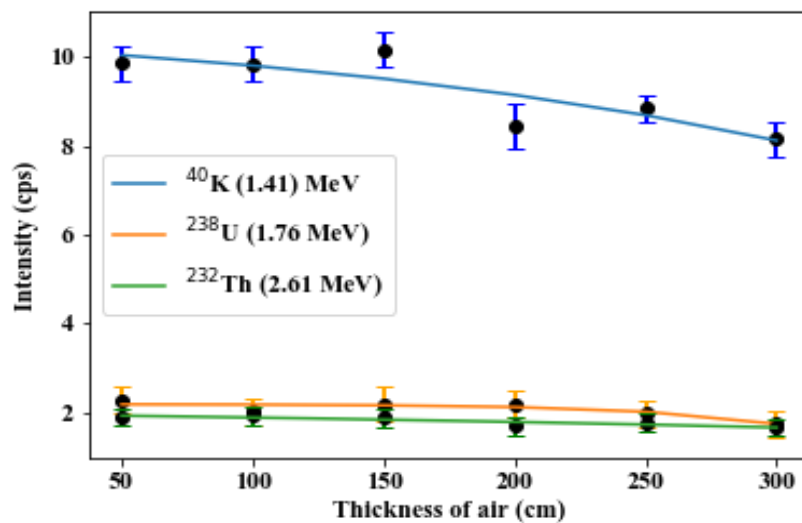


Fig. 5. Attenuation of gamma ray energy with increasing thickness of air

4. Conclusion

The relative intensity of unscattered to scattered gamma radiation by air is studied in ambient atmosphere using gamma ray spectrometric method. No considerable attenuation was found up to 100 cm thickness of air between the detector and ground. The intensity of terrestrial gamma radiation was found decreasing with thickness of air between the ground and the detector. Also, the attenuation of low gamma ray energy (^{40}K) was found higher compared to high gamma ray energy (^{238}U , ^{232}Th). The attenuation of gamma rays was considerable with 100 cm change in thickness of air as it has low attenuation coefficient. The scattering of gamma ray in air for high energy is not so significant due to their high attenuation lengths.

ACKNOWLEDGEMENTS

We would like to acknowledge the support from International Atomic Energy Agency (IAEA) through TC project NEP0002 (2014-2017), Ministry of Education, Science and Technology, Government of Nepal for coordination with IAEA, and University Grants Commission, Nepal for PhD fellowship to Anita Mishra (award number PhD- 74/75-S&T-15).

References

- Al-Jiboori, H. M., Abu-Alshaeer, M., J. & Ahemd, M. .M. (2020)** Impact of Land Surface Changes on Air Temperatures in Baghdad City. *Kuwait Journal of Science*, **47**(4): 118-126.
- Allen, C. W., & Cox, A. N. (2000)** *Allen's astrophysical quantities*. Springer Science & Business Media, New York.
- Allyson, J. D. (1994)** Environmental γ -ray spectrometry: simulation of absolute calibration of in-situ and airborne spectrometers for natural and anthropogenic sources. Ph.D. thesis, The University of Glasgow, Glasgow, Scotland.
- Amiri, M. A., & Mesgari, M. S. (2018)** Analyzing the spatial variability of precipitation extremes along longitude and latitude, northwest Iran. *Kuwait Journal of Science*, **45**(1): 121-127.
- Badawy, S. M., & Abd El-latif, A. A. (2017)** Synthesis and characterizations of magnetite nanocomposite films for radiation shielding. *Polymer Composites*, **38**(5): 974-980.
- Charbonneau, B.W., & Darnley, A.G. (1970)** Radioactive precipitation and its significance to high sensitivity gamma ray spectrometer surveys. *Geological Survey of Canada, Paper* **70**(1): 32-36.
- Demir, N. S., Nageswaran, T., & Alrefae, T. (2018)** Anti-Compton system for environmental radioactivity studies at Kuwait University. *Kuwait Journal of Science*, **45**(3): 46-52.
- Grasty, R.L. (1982)** Direct snow-water equivalent measurement by airborne gamma ray spectrometry. *Journal of Hydrology*, **55**(1-4): 213-235.

International Atomic Energy Agency (2003) Guidelines for radioelement mapping using gamma ray spectrometry data, IAEA-TECDOC-1363, Vienna, Austria.

Ismail, A. I., Samir, A., Ahmad, F., Soliman, L. I., & Abdelghany, A. (2021) The effect of radiation on the structure and ligand field of borate glasses containing Cr ions. *Optical and Quantum Electronics*, **53**(4): 1-15.

Katase, A., Narahara, Y., Ishihara, Y., Tanaka, K., & Matsuyama, H. (1982) Variation of intensity of environmental gamma-rays measured with Ge (Li) spectrometer. *Journal of Nuclear Science and Technology*, **19**(11): 918-927.

Martin, I. M., & Gomes, M. P. (2021) Intensity variation of gamma radiation on ground level interface in São Jose Dos Campos, SP, Brazil. *Latin American Journal of Development*, **3**(2): 853-858.

Rubin, R.M., Legget, D. & Wells, M.B. (1980) Effects of Overburden, Biomass and Atmospheric Inversions on Energy and Angular Distribution of Gamma Rays from U, K, Th and Airborne Radon Sources. US Department of Energy.

Vargas, M. J., Timón, A. F., Díaz, N. C., & Sánchez, D. P. (2002) Monte Carlo simulation of the self-absorption corrections for natural samples in gamma-ray spectrometry. *Applied Radiation and Isotopes*, **57**(6): 893-898.

Submitted : 16/11/2021

Revised : 14/02/2022

Accepted : 26/02/2022

DOI : 10.48129/kjs.17253

Investigation of V_2O_5 - $ZnAl_2O_4$ composite nanoparticles for C-band microstrip patch antenna applications

Srilali Siragam¹, R.S. Dubey^{2,3,*}, Lakshman Pappula⁴

¹*Dept. of ECE, Swarnandhra College of Engineering & Technology, Narsapur-534 280, West Godavari (AP), India*

²*University Institute of Engineering & Technology, Guru Nanak University, Ibrahimpatnam, R. R. District, Hyderabad-501 506 (T.S.), India*

³*Dept. of Electronics & Communication Engineering, Guru Nanak Institutions Technical Campus, Ibrahimpatnam, R. R. District, Hyderabad, (T.S.), India*

⁴*Dept. of ECE, Koneru Lakshmaiah Education Foundation, Greenfields, Vaddeswaram, Guntur, Andhra Pradesh, India*

**Corresponding author: rag_pcw@yahoo.co.in*

Abstract

This paper reports the prototype fabrication and characterization of microstrip patch antenna using the sol-gel derived composite nanoparticles of vanadium pentoxide oxide (V_2O_5) and zinc aluminate ($ZnAl_2O_4$). The prepared composite nanoparticles were characterized using X-ray diffraction (XRD), which exhibited the dominant peaks of $ZnAl_2O_4$ and V_2O_5 . The crystallite size of the nanoparticles was estimated to be 16 nm. The sample was also studied using the Fourier transform infrared spectroscopy (FTIR), field-emission scanning electron microscopy (FESEM), and energy dispersive spectroscopy (EDS) to examine the functional groups morphology and elemental composition present in the composite nanoparticles. Further, these nanoparticles were employed in fabricating the prototype microstrip patch antenna to evaluate its characteristics. The fabricated antenna showed its return loss of -17.13 dB at a resonant frequency of 4.64 GHz.

Keywords: Bandwidth ; return loss; sol-gel synthesis; vanadium oxide, zinc aluminate.

1. Introduction

Dielectric microstrip antennas have received much interest in recent microwave communications because of their small size, better radiation efficiency, and ease of excitation. A microstrip antenna material should have the following properties: i) a high Q-factor to achieve better radiation efficiency (ii) reasonably a large dielectric constant as it facilitates in a small dimension of the antenna and (iii) zero temperature coefficient of resonant frequency (Li *et al.*, 2018; Jimago *et al.*, 2020; Tachafine *et al.*, 2021). Wireless communication has become a need in occurs day to day life. This communication method is comparable to wired communication networks in terms of data rate and service quality. As technology advances, wireless communication systems must incorporate new functionalities and more components.

Zinc aluminate (ZnAl₂O₄) is a spinel group material that has been investigated and attracted the interest of researchers. This is due to their distinct features, which allow them to be widely used as catalyst support, ceramic material, electrical and optical materials (Kolthoum *et al.*, 2019; Khasan *et al.*, 2017; Chaudhary *et al.*, 2018; Mane *et al.*, 2020; Sommer *et al.*, 2020). Aluminum spinel has good thermal stability, a high mechanical resistance, and minimal surface acidity (Kim *et al.*, 2019). This material can be employed as a catalyst and a carrier for active metals (Younis *et al.*, 2021). The cubic cell of ZnAl₂O₄ comprises 32 tightly packed oxygen atoms with cations in tetrahedral and octahedral interstices. Divalent cations occupy tetrahedral positions in typical spinel structures (Santos *et al.*, 2017; Wu *et al.*, 2011). ZnAl₂O₄ material is commonly utilized as microwave dielectric ceramics, where it has the potential for the future study focused on microwave applications (Akkika *et al.*, 2020). Further, the properties of ZnAl₂O₄ can be manipulated by doping or adding desired elements for specific applications. The combination of ZnAl₂O₄ and V₂O₅ can facilitate the alteration of various properties. The combination of Vanadium oxide is a phase transition material with many valences. Its oxide has valence states of 2+, 3+, 4+, 5+, etc., as well as various intermediate oxide states. The phase transition temperature of each variation differs. Despite various synthesis methods such as solid-state and co-precipitate, the sol-gel method is well established to synthesize doped or composite nanoparticles (Mishra *et al.*, 2018; Dwiwedi *et al.*, 2017; Priya *et al.*, 2020; Tangchareon *et al.*, 2019). At a low-temperature process, one can produce fine, and impurity-free particles (Rahman *et al.*, 2015). Wang *et al.* (2009) employed the (1-x)(0.79ZnAl₂O₄-0.21Mg₂TiO₄)-xSrTiO₃ composite material in fabricating the microstrip patch antenna. The fabricated patch antenna showed its resonant frequency of 1.575 GHz with VSWR less than 2. Naidu *et al.* (2012) used the magnesium ferrite doped with double Samarium (Sm) and Dysprosium (Dy) for fabricating the microstrip patch antenna. The efficiency of the patch antenna was noticed to be 69.82 at frequency 14.9 GHz, which its gain of about 5.73 dB. Rahman *et al.* (2015) studied the patch antenna prepared using the ZnAl₂O₄ nanoparticles prepared by the sol-gel technique. They studied the antenna's performance and claimed its return loss of -25.4 dB at the resonant frequency of 12.78 GHz, having a bandwidth of 760 MHz. Further, they explored the application of the prepared antenna in X-band communication. Wu *et al.* (2011) prepared the dielectric ceramics of ZnAl₂O₄, TiO₂, and MgTiO₃ using gel casting. They prepared nanoparticles that exhibited their dielectric permittivity in the range from 11.75-12.25 and employed them to fabricate the GPS patch antenna, demonstrating its resonant frequency at 1.75 GHz. Wee *et al.* (2012) reported the fabrication of 2, 4, 6-element arrays of the barium strontium titanate (BST) based microstrip patch antennas. They reported the 6-element BST array antenna's enhanced gain compared to the 4-element BST antenna and suggested their applications in Wi-MAX and WLAN communications.

This work reports the synthesis of composite nanoparticles of 0.1V₂O₅-0.9ZnAl₂O₄ using the sol-gel process. The prepared nanoparticles were employed to fabricate the microstrip patch antenna, and performance was evaluated. Section 2 presents the materials and methods of the synthesis process, and the characterized results are discussed in Section 3. At last, Section 4 concludes the work.

2. Materials and Methods

Vanadium pentoxide (V_2O_5) (LR grade), Zinc acetate $(CH_3COO)_2Zn \cdot 2H_2O$ (AR) (Lobychem), aluminum nitrate nonahydrate $Al_2(NO_3)_3 \cdot 9H_2O$, (Sigma Aldrich), ethanol (C_2H_5OH , Sigma Aldrich), ethylene glycol (EG, AR grade) and nitric acid (HNO_3) (AR) were used with any further purification.

For preparing the composite nanoparticles of $xV_2O_5(1-x)ZnAl_2O_4$, the molar concentration $x=0.1$ was chosen. Initially, 37.5 gm $Al_2(NO_3)_3 \cdot 9H_2O$ was dissolved in 100 ml ethanol under constant stirring. After this, 1 ml of ethanediol was added to the above solution and stirred for 5 minutes. Subsequently, 1 gm and 16.53 gm of V_2O_5 powder and $(CH_3COO)_2Zn \cdot 2H_2O$ were added to the above solution. The stirring was maintained at a temperature of $75^\circ C$ for 60 min. Later, 0.6 ml HNO_3 was added to get the homogeneous solution. After obtaining the transparent solution of $0.1V_2O_5-0.9ZnAl_2O_4$, it was kept for drying to get powder. Finally, the prepared powder was calcined at a temperature of $800^\circ C$ for 1 hr and ground to obtain a fine powder.

3. Results and Discussion

Figure 1 depicts the XRD pattern of prepared $0.1V_2O_5-0.9ZnAl_2O_4$ composite nanoparticles calcinated at $800^\circ C$ for 1 hr, showing the polycrystalline phase. The peaks regarded the $ZnAl_2O_4$ crystal structure, which indicated the typical face-centered cubic shape and was found inconsistent with the reported work (Ding *et al.*, 2017; Dubey *et al.*, 2020; Siragam *et al.*, 2020). The XRD pattern shows the dominant peaks of $ZnAl_2O_4$ at $2\theta = 31.26^\circ, 35.02^\circ, 37.09^\circ, 44.98^\circ, 49.29^\circ, 55.93^\circ, 59.57^\circ, 65.38^\circ, 74.30^\circ$ and 77.57° corresponding to the planes (220), (101), (311), (400), (311), (422), (511), (440), (620) and (533) which shows matching with the JCPDS card No. 00-005-0669.

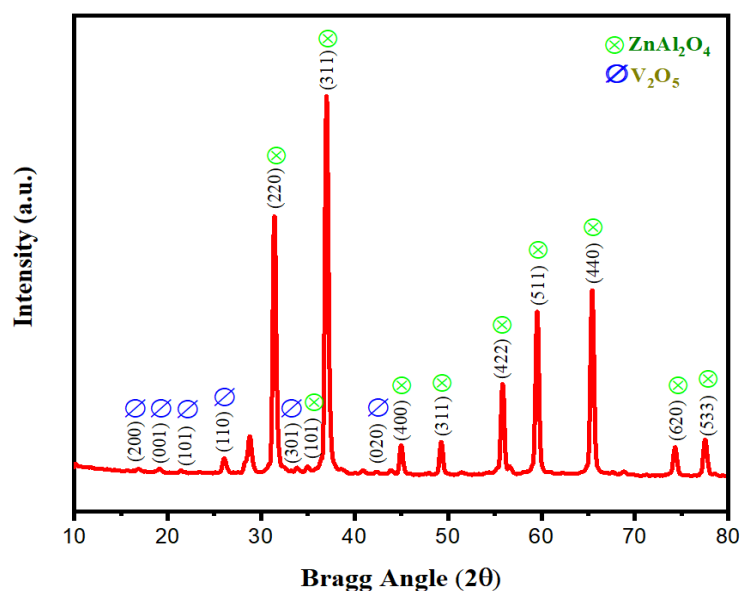


Fig. 1. XRD pattern of $0.1V_2O_5-0.9ZnAl_2O_4$ composite nanoparticles.

Furthermore, V₂O₅ peaks were noticed at $2\theta=16.86^\circ$, 19.06° , 21.55° , 26.11° , and 33.78° corresponding to the planes (200), (001), (101), (110) and (301), respectively. These diffraction peaks were found in good matching with the ICDD file 98-000-6037 and well-matched with the previous works (Chan *et al.*, 2014)[23]. The crystallite size of the 0.1V₂O₅-0.9ZnAl₂O₄ sample was estimated to be 16 nm as calculated by using Scherrer's equation.

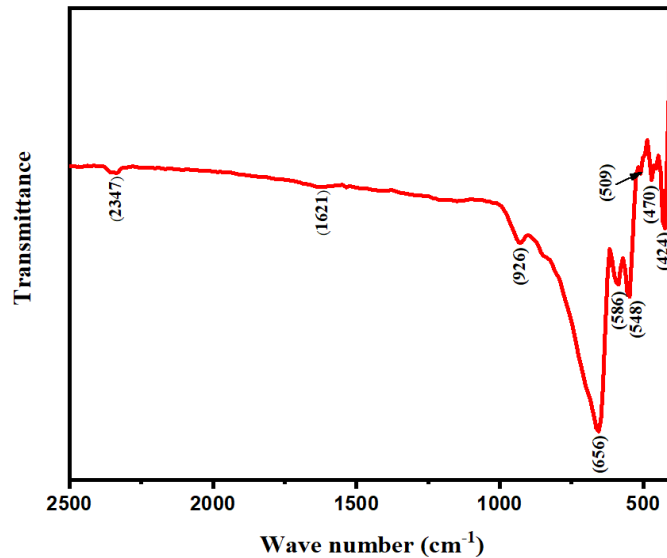


Fig. 2. FTIR spectra of 0.9ZnAl₂O₄0.1V₂O₅ composite nanoparticles.

FTIR investigation was done to know the functional groups in the prepared nanoparticles. Figure 2 depicts the FTIR spectrum of the composite nanoparticles plotted in the range 2500-400 cm⁻¹. The FTIR transmittance peak associated at wavenumbers 470, 586 cm⁻¹ are ascribed to the V₂O₅, V₂O₃ bands (Fatmeh *et al.*, 2011;). A peak observed at 509 cm⁻¹ corresponds to the stretching vibration of ZnAl₂O₄. Further, the peaks aligned at 548 and 656 cm⁻¹ are regarded as ZnO's stretching vibrations and AlO (Muhmmad *et al.*, 2011). Another peak originated at 1621 cm⁻¹ is associated with the stretching vibrations of O-H, i.e., related to H₂O molecules. We can also notice the O-O band vibration peak at 2348 cm⁻¹ related to the FCC crystal lattice of O₂ atoms (Henam *et al.*, 2021).

Figure 3 (a) depicts the SEM morphology of the 0.1V₂O₅-0.9ZnAl₂O₄ particles, which shows the formation of agglomerated spherical composite nanoparticles. The mean diameter of nanoparticles was observed to be 21 nm. EDS spectroscopy was carried out to know the presence of constituting elements present in the prepared sample. Figure 3(b) chooses the spectrum, which reveals the elemental compositions of Zn, Al, O, and V at 1.5, 1, 0.5, and 5 KeV, respectively.

We have fabricated the prototype of a microstrip patch antenna using the prepared composite nanoparticles, which were cast on the FTO substrate. Later, the silver coating was done on both sides of the FTO for the contacts. The co-axial SMA connector was connected to complete the fabrication of the microstrip patch antenna.

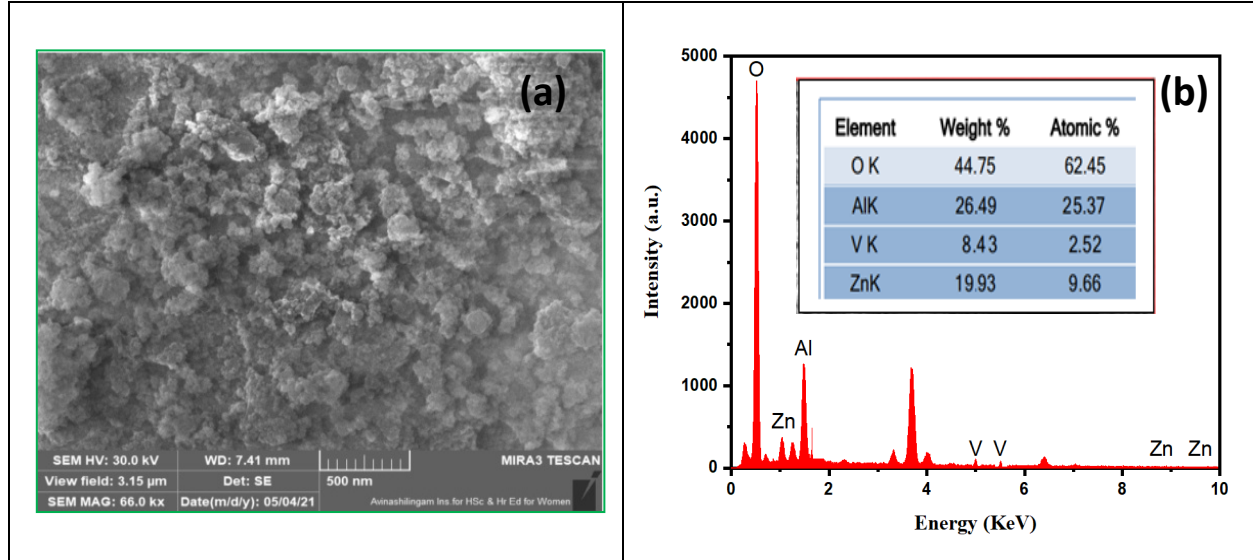


Fig. 3. (a) SEM morphology of $0.1\text{V}_2\text{O}_5\text{-}0.9\text{ZnAl}_2\text{O}_4$ (b) EDS spectrum.

Figure 4 depicts the return loss (RL) from 3-6 GHz of the fabricated antennas with respect to the operating frequency. We can notice the return loss of -17.13 dB at the resonant frequency of 4.64 GHz. In a similar work, Thirumanathan *et al.* (2016) reported the performance of a patch antenna made up of $\text{Bi}_4\text{Ti}_3\text{O}_{12}$ composite metal and claimed its return loss of -4.95 dB at resonant frequency 2.45 GHz for wireless communication applications. Our microstrip patch antenna based on $0.1\text{V}_2\text{O}_5\text{-}0.9\text{ZnAl}_2\text{O}_4$ composite nanoparticles evidenced the better return loss. Therefore, it was found suitable in C-band communication. To the best of our knowledge, no such work of microstrip patch antenna based on $\text{V}_2\text{O}_5\text{-ZnAl}_2\text{O}_4$ has been reported. The inset of figure 4 shows the digital picture of the microstrip patch antenna with its dimension $2.5 \times 1.5 \text{ cm}^2$.

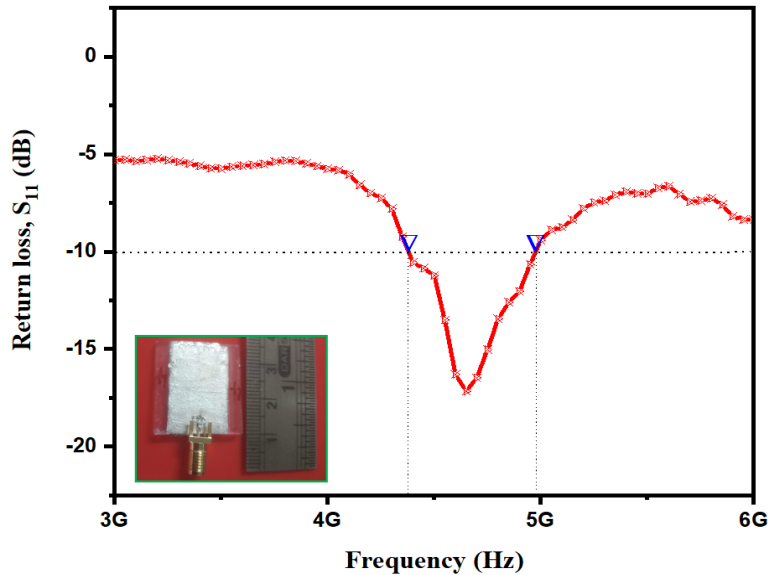


Fig. 4. Return loss of $0.1\text{V}_2\text{O}_5\text{-}0.9\text{ZnAl}_2\text{O}_4$ microstrip patch antenna.

The voltage standing wave ratio (VSWR) value is directly connected to the maximum power transmitted from the transmitter to receiving antenna in an ideal condition. This occurs only when the input impedance is matched to the transmitting antenna impedance. We can calculate the VSWR value using the expression $VSWR = V_{max}/V_{min} = (1 + |\rho|)/(1 - |\rho|) = (1 + S_{11})/(1 - S_{11})$. Accordingly, we have plotted the obtained VSWR values and reflection coefficient as shown in figure 5 as the reflected and forwarded powers of microstrip patch antenna were 1.92% and 98.07%, respectively.

At the resonant frequency of 4.64 GHz, the VSWR value of the microstrip patch antenna was found to be 1.32. In general, VSWR affects the reflection coefficient of the antenna under the test, and a larger ratio (V_{max}/V_{min}) implies a severe mismatch rather than a perfect matching (i.e., 1:1 ratio). The maximum and minimum amplitudes of the standing wave cause this match/mismatch. The obtained VSWR value is less than 2, favorable to a better return loss, as depicted in figure 5 (left axis). The microstrip patch antenna's reflection coefficient was 0.13, as shown in figure 5 (right axis). Finally, the estimated antenna's mismatch loss was 0.083 dB, whereas the reflected and forwarded powers of the microstrip patch antenna were 1.92% and 98.07%, respectively.

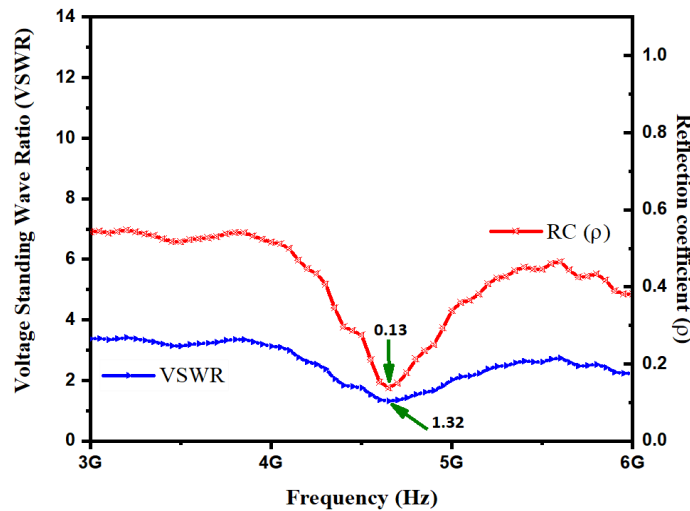


Fig. 5. VSWR & Reflection coefficient of 0.1V₂O₅-0.9ZnAl₂O₄ microstrip patch antenna.

4. Conclusions

Synthesis of 0.1V₂O₅-0.9ZnAl₂O₄ composite nanoparticles prepared by the sol-gel method is presented and analyzed. XRD pattern revealed the preparation of crystalline nanoparticles with their crystallite size of 16 nm. The presence of diffraction peaks of V₂O₅ and the dominant peak of ZnAl₂O₄ confirmed the synthesis of composite nanoparticles. The FTIR investigation evidenced various vibration peaks related to the functional groups. The FESEM micrograph confirmed the growth of the agglomerated spherical nanoparticles having their mean diameter of 21 nm. The EDX spectroscopy also affirmed the presence of Al, Zn, O, and V at 1.5, 1, 0.5, and 5 KeV, respectively. Further, we have fabricated the microstrip patch antenna, which demonstrated the

return loss of -17.13 dB at the resonant frequency 4.64 GHz, while the VSWR value was observed to be less than 2. The performance of the microstrip patch antenna based on $0.1\text{V}_2\text{O}_5$ - $0.9\text{ZnAl}_2\text{O}_4$ composite nanoparticles signify the applications in C-band communication.

References

- A, Tachafine., D, Fasquelle., R, Desfeux., A, Ferri., A, Da Costa., J.-C, Carru., & A, Outzourhit. (2021)** Doping effect on nanoscopic and macroscopic electrical properties of Barium Zirconate Titanate thin films. *Spectroscopy Letters*, 54(7): 507–519.
- Akika, F.Z., Benamira, M, Lahmar H., Trari, M., Avramova, I., Suzer, Ş. (2020)** Structural and optical properties of Cu-doped ZnAl_2O_4 and its application as photocatalyst for Cr (VI) reduction under sunlight. *Surfaces and Interfaces*, 18, 100406–100440.
- Chan, Yim-Leng., Pung, Swee-Yong., Sreekantan, Srimala. (2014).** Synthesis of V_2O_5 Nanoflakes on PET Fiber as Visible-Light-Driven Photocatalysts for Degradation of RhB Dye. *Journal of Catalysts*, 1–7.
- Chaudhary, Archana., Mohammad, Akbar., Mobin, Shaikh, M. (2018)** Facile synthesis of phase pure ZnAl_2O_4 nanoparticles for effective photocatalytic degradation of organic dyes. *Materials Science and Engineering: B*, 227: 136–144.
- Ding, Jijun., Chen, Haixia., Fu, Haiwei. (2017)** Enhanced blue emission of ZnO films deposited on AlN substrates. *Physica E: Low-dimensional Systems and Nanostructures*, 90: 61–66.
- Dubey, R.S. (2018)** Temperature-dependent phase transformation of TiO_2 nanoparticles synthesized by sol-gel method. *Materials Letters*, 215: 312–317.
- Dwibedi, Debasmita., Murugesan, Chinnasamy., Leskes, Michal., Barpanda, Prabeer. (2017)** Role of Annealing Temperature on Cation Ordering in Hydrothermally Prepared Zinc Aluminate (ZnAl_2O_4) Spinel. *Materials Research Bulletin*, 98: 219–224.
- E, Muhammad Abdul Jamal., D, Sakthi kumar., and M, R, Anantharaman. (2011)** On structural, optical and dielectric properties of zinc aluminate nanoparticles. *Bull. Mater. Sci.*, 34 (2): 251–259.
- Fatemeh, Davar., Masoud, Salavati-Niasari. (2011)** Synthesis and characterization of spinel-type zinc aluminate nanoparticles by a modified sol-gel method using new precursor. *Journal of Alloys and Compounds*, 509: 2487–2492.
- Henam, Sylvia Devi., Akshita, Mishra., Md, Samim Reza., Parvez, Akhtar., Henam, Premananda Singh., Thiyam, David Singh., Madhusudan, Singh. (2021)** Controlled phase synthesis of V_mO_n in differing oxidation states using a simplified formic acid process, quantified with a new generalized index designed for use with public domain material process information. *Green Chem.*, 23: 8200–8211.

Jiamao, Li., Zhang, Chuimin., Li, Lin., Fan Chuangang. (2020) Synthesis of NdAlO₃ with good microwave dielectric properties by stearic acid method. *Ceramics International*, 46 (11): 18940–18947.

Khasan, S. Karimov., Muhammad, Saleem, Khakim., M. Akhmedov., Taimoor, Ali. Muhammad M. (2017) BashirPhoto-thermo electric effect in Zn/orange dye aqueous solution/carbon cell. *Kuwait J. Sci.*, 44 (1): 86-90.

Kim, Hyo-Young., Shin, Jeeyoung., Jang, Il-Chan., Ju, Young-Wan. (2019) Hydrothermal Synthesis of Three-Dimensional Perovskite NiMnO₃ Oxide and Application in Supercapacitor Electrode. *Energies*, 13(1): 36–47.

Kolthoum, I Othman., M, EI Sayed Ali., and S.EI Hout. (2019) Dielectric properties of sintered BaTiO₃ prepared from barium acetate and titanium dioxide. *Kuwait J. Sci.*, 46(3): 53-59.

Li, Wei., Qu, Jing-Jing., Wei, Xing., Liu, Fei., Yuan, Chang-Lai., Chen, Guo-Hua. (2018) Structural characteristics and microwave dielectric properties of a new Sm₂O₃- Nd₂O₃-MgO-CeO₂ ceramic system. *Materials Chemistry and Physics*, 207: 44–49.

Mane, Chandrakant B., Pawar, Ramkrushna P., Patil, Rajendra P., Patil, Sarjerao B. (2020) Photocatalytic Environmental Remediation of Cassiteriteâ–Titania Nanocomposite. *Macromolecular Symposia*, 393(1): 2000176.

Mishra, Geetanjali., Dash, Barsha., Pandey, Sony. (2018) Layered double hydroxides: A brief review from fundamentals to application as evolving biomaterials. *Applied Clay Science*, 153: 172–186.

Naidu, V., Ahamed, Kandu Sahib S. K. A., Sivabharathy, M., Legadevi R, Senthil Kumar A., Prakash C., & Pandian, S. (2012) Synthesis and Characterization of Novel Nanoceramic Magnesium Ferrite Material Doped with Samarium and Dysprosium for Designing – Microstrip Patch Antenna. *Defect and Diffusion Forum*, 332: 35–50.

Priya, Ruby., Negi, Astha., Singla, Shivani., Pandey, O.P. (2020) Luminescent studies of Eu doped ZnAl₂O₄ spinels synthesized by low-temperature combustion route. *Optik*, 204:164173–164184.

Rahman, A., Islam, M. T., Zulfakar, M. S., & Abdullah, H. (2015) Synthesis and characterization of gahnite-based microwave dielectric ceramics (MDC) for microstrip antennas prepared by a sol–gel method. *Journal of Sol-Gel Science and Technology*, 74(2): 557–565.

Santos, J.L., Reina, T.R., Ivanova, S., Centeno, M.A., Odriozola, J.A. (2017) Gold promoted Cu/ZnO/Al₂O₃ catalysts prepared from hydrotalcite precursors: Advanced materials for the WGS reaction. *Applied Catalysis B: Environmental*, 201: 310–317.

Siragam, S., Dubey, R. S., & Pappula, L. (2020) Synthesis and investigation of dielectric properties of nanoceramic composite material for microwave applications. *Micro & Nanoletters*, 15 (15): 1156 –1161.

Sommer, S., Bøjesen, E. D., Reardon, H., & Iversen, B. B. (2020) Atomic scale design of spinel ZnAl_2O_4 nanocrystal synthesis. *Crystal Growth & Design*, 1789-1799.

Tangcharoen, T., T-Thienprasert., J & Kongmark, C. (2019) Effect of calcination temperature on structural and optical properties of MAl_2O_4 (M = Ni, Cu, Zn) aluminate spinel nanoparticles. *J Adv Ceram*, 8: 352–366.

Thiruramanathan., Sanjeev, K. Sharma., S, Sankar., R. Sankar. Ganesh., A. Marikani., Deuk, Young, Kim. (2016) Synthesis of bismuth titanate (BTO) nanopowder and fabrication of microstrip rectangular patch antenna. *Appl. Phys. A*, 122:1006.

Wang, X., Lei, W., & Lu, W. (2009) Novel ZnAl_2O_4 -Based Microwave Dielectric Ceramics with Machinable Property and its Application for GPS Antenna. *Ferroelectrics*, 388(1): 80–87.

Wee, F.H., Malek F., Ghani, F., Sreekantan, S., Al-Amani, A.U. (2012) High gain and high directive of antenna arrays utilizing dielectric layer on bismuth titanate ceramics. *Int. J. Antennas Propag*, 1–8.

Wu, J-M., Lu, W-Z., Lei, W., Wang, X-C. (2011) Preparation of ZnAl_2O_4 -based microwave dielectric ceramics and GPS antenna by aqueous gelcasting. *Mater Res Bull*, 46(9):1485–1489.

Younis, N., Abd-Elrahman, M. I., Afify, N., Abu El-Fadl, A., & Abu-Sehly, A. A. (2021) Structural, optical and magnetic characterizations of nanoparticles spinel $\text{Zn}_{(1-x)}\text{M}_x\text{Al}_2\text{O}_4$ (M=Co and Ni) synthesized by microwave combustion method. *Materials Science and Engineering: B*, 271: 115316.

Submitted: 18/12/2021

Revised: 26/02/2022

Accepted: 26/02/2022

DOI : 10.48129/kjs.17783

Transparent dielectric TiO₂/SiO₂ coatings for thermal shielding and self-cleaning applications

Venkatesh Yepuri¹, R.S. Dubey^{2,3,*}

¹*Dept. of Electrical and Electronics Engineering,
Swarnandhra College of Engineering and Technology,
Seetharampuram, Narsapur (A.P.), India*

²*University Institute of Engineering & Technology, Guru Nanak University,
Ibrahimpattam, R. R. District, Hyderabad-501 506 (T.S.), India*

³*Dept. of Electronics & Communication Engineering, Guru Nanak Institutions Technical
Campus, Ibrahimpattam, R. R. District, Hyderabad, (T.S.), India*

**Corresponding author: rag_pcw@yahoo.co.in*

Abstract

The economical fabrication of one-dimensional dielectric reflectors using the hybrid sol-gel spin coating process is significant compared to sophisticated chemical and physical vapor deposition techniques. In this work, we opted for alternate layers of TiO₂ and SiO₂ films to fabricate near-infrared dielectric reflectors owing to their high refractive index contrast and easy tunability of the reflection window in the desired spectral range. X-ray diffraction (XRD) studies of the monolayer TiO₂ and SiO₂ confirmed the existence of anatase-TiO₂ and amorphous-SiO₂ phases, respectively. Spectroscopic ellipsometry investigation of TiO₂ and SiO₂ films revealed the refractive indices of 2.6 and 1.5, respectively. The field-emission scanning electron microscopy (FESEM) analyses evidenced the fabrication of 2.5 stacks/bilayers of TiO₂/SiO₂ (TiO₂/SiO₂)_{2.5s}. The reflectance measurement demonstrated 100% reflection in the near-infrared region with its center wavelength of 833 nm. In addition, we have examined the water contact angle of various samples using the sessile drop technique, and 2.5 stacks-based reflector showed its lowest contact angle of 29.3°, which suggests its anti-fogging and self-cleaning applications.

Keywords: Contact angle measurement; hydrophilic coating; near-infrared reflector; sol-gel spin coating; titania.

1. Introduction

Presently, nanoscale technology is growing swiftly with its novel applications in the science and technology sectors. Nanotechnology is nothing but inspiration from nature. For example, the lotus-leaf effect and butterfly wings are a few of them, which helped researchers to develop hydrophobic coatings and transparent dielectric reflectors. Inspired by lotus leaves' characteristics, Yang *et al.*, (2015) demonstrated the superhydrophobic coating by using the strawberry-like Janus particles. The water contact angle of the coating investigation revealed its contact angle of 140°, indicating the flushing off the water quickly from the surfaces. The potential applications of TiO₂ and SiO₂ based dielectric reflectors brought these materials demanding owing to their high refractive index contrast and hydrophilic nature. This aids researchers in developing an optical component that can

be used for several purposes. In the automotive industry, alternating interfaces can be installed as a reflector for the required wavelength spectrum and as the self-cleaning and anti-fogging coatings.

Huang *et al.*, (2017) used the atomic layer deposition (ALD) technique to deposit TiO₂ thin film on a Co-Cr substrate and studied its wetting behaviour under the exposure of ultraviolet (UV) light. The static contact angle analysis of the TiO₂ films showed the contact angle of 37.3° and suggested for its use as an antifungal coating to treat denture stomatitis. Akbar & Ameneh, 2012 employed the dip-coating method for various kind of coatings (TiO₂, TiO₂-SiO₂ and TiO₂-SiO₂-In₂O₃) on the glass substrates and examined their hydrophilic nature. The coatings of TiO₂, TiO₂-SiO₂, TiO₂-SiO₂-In₂O₃ showed their contact angle of 10.3°, 4.3° and 1.1°, respectively. Further, after storing the coated samples in the dark environment for 24 hours, they noticed an increased value of contact angles of about 17.1° for TiO₂, 6.7° for TiO₂-SiO₂, and 2.9° corresponding to the samples TiO₂, TiO₂-SiO₂ and TiO₂-SiO₂-In₂O₃. This increased hydrophilicity was attributed to the acidic surface, which caused the dissociative water adsorption by adsorbing the hydroxyl groups and H₃O⁺ ions on the surface. Shokuhfar *et al.*, (2012) investigated the effect of sintering temperatures on the wetting behaviour of composite SiO₂-TiO₂ coatings on glass substrates. The variation of sintering temperature from 500°C to 700°C evidenced the increased hydrophilic nature. Further, they proposed its application in automobile windshielding for dispersing water across the surface and remove the dust particles from it. Damchan *et al.* (2008) spin-coated the composite TiO₂-SiO₂ layer while altering the precursor's molar concentrations and evaluated their wetting behaviour. Their findings showed improved hydrophilic characteristics with the increased molar concentration of SiO₂, which caused more hydroxyl groups.

A dielectric reflector is a multilayer structure of thin films with high- and low-refractive-index materials. The alternate high and low refractive index films felicitate constructive interference at the interfaces, which yields enhanced reflection from the coated surface. Dubey & Ganesan, 2017 reported the fabrication of a multilayer structure on the glass substrates using the sol-gel spin coating process and presented its optical properties. The cross-section FESEM study of the multilayer structure evidenced the periodic arrangement of bright and dark layers indicating the formation of TiO₂ and SiO₂, respectively. Similarly, UV-Vis spectroscopy analysis demonstrated a maximum 90% reflectance at the center wavelength of 617 nm i.e., in the visible spectrum. Further, they suggested the application of a fabricated reflector for light trapping in the thin-film solar cell. Lin *et al.*, (2015) analyzed the reflector made-up of thin films of TiO₂/SiO₂ prepared by the e-beam evaporation approach. The reflectance analysis using UV-Vis spectroscopy endorsed a maximum of 100% reflectance in the wavelength region between 390 and 650 nm [12]. The reflector was integrated with the LED, and they observed enhanced brightness compared to the ordinary LED. Anaya *et al.*, (2016) investigated a dielectric reflector with porous and dense films of TiO₂ and SiO₂ using the spin coating technique. The appearance of the periodic bright and dark bands in the cross-section FESEM examination confirmed the fabrication of TiO₂ and SiO₂ layers, respectively. The optical study demonstrated a 90% reflectance in the 300-500 nm spectral range. Feng *et al.*, (2013) reported the fabrication of multilayer reflector of TiO₂/SiO₂ by e-beam evaporation process. The reflectance analysis revealed about 95 % reflectance in the

wavelength from 1.1 to 1.6 μm , indicating that it can be used in various applications, such as optical amplifiers and infrared emitters. Nagayoshi & Murooka, 2015 investigated a dielectric reflector of composite TiO_2 and SiO_2 nanoparticles using the sol-gel spin coating technique. The morphological study using FESEM evidenced the alternate fabrication of $\text{TiO}_2/\text{SiO}_2$ films. Further, UV-Vis spectroscopy's reflectance analysis endorsed about 90% reflectance in the near-infrared region. The practical lifetime of the produced optical component was investigated and compared to that of TiO_2 nanoparticles coated with aluminum, evidenced a longer lifetime when combined with a thin SiO_2 passivation layer.

The above findings reported in the literature involved the high-cost fabrication using advanced equipment. Hence, to decrease the fabrication cost and increase the durability of the coating, we put forward the development of a straightforward methodology to fabricate such dielectric reflectors for their various applications. Section 2 explores the materials and methods involved in the proposed work, while Section 3 discusses the obtained results. Finally, the research work is concluded in Section IV.

2. Experimental

We have produced the coatings of titania (TiO_2) and silica (SiO_2) films on the glass substrates by the spin coating technique. The respective gels of TiO_2 and SiO_2 were synthesized by the sol-gel process, as shown in figure 1(a)-(c). For the synthesis of TiO_2 and SiO_2 gels, the solvent ethanol, chelating agents nitric acid (HNO_3 , Sdfine), and acetic acid (AcAc, Sisco Research Laboratories) were taken along with the precursors i.e., titanium isopropoxide (TTIP, Sigma-Aldrich) and tetraethyl orthosilicate (TEOS, Sigma-Aldrich), in the following molar ratios ethanol: HNO_3 :AcAc:TTIP: 1.2:0.05:0.3:0.3 and ethanol: HNO_3 :AcAc: TEOS was 1.2:0.05:0.3:0.3 respectively.

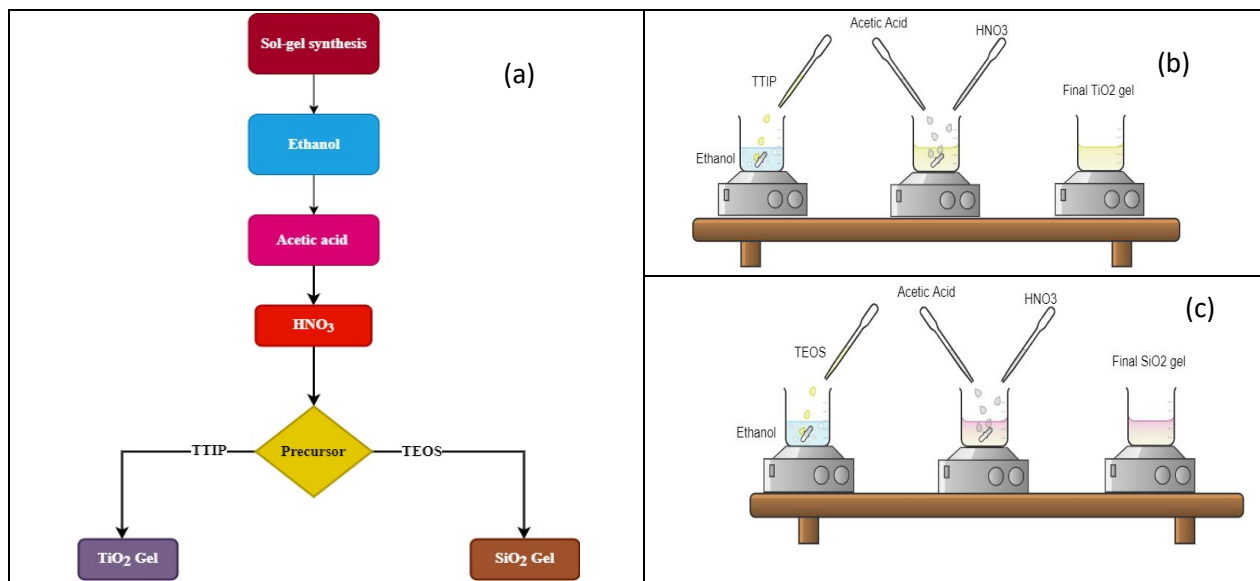


Fig. 1. Flow chart of the sol-gel process (a), sol-gel synthesis of TiO_2 (b), and SiO_2 gels (c).

Figures 1(a) and 1(b) represent the sol-gel process's flow chart and schematic. The glass substrates were thoroughly washed with the soap solution and ultrasonicated in ethanol for 30 minutes before being used. Finally, the substrates were washed with deionized water to remove any solvent residues from the surface. To fabricate the multilayer structures, titania (TiO₂) and silica (SiO₂) gels were layer by layer spin-coated on the cleaned glass substrates at a spin rate of 3000 RPM for 30 seconds. Then each layer was annealed for one hour at temperature 500 °C in a muffle furnace as shown in figure 2. The multilayer structures were fabricated following the above procedure on the glass substrates and named as (TiO₂/SiO₂)_{1.5s} and (TiO₂/SiO₂)_{2.5s}, where “s” indicates the number of stacks or bilayers on the glass substrates.

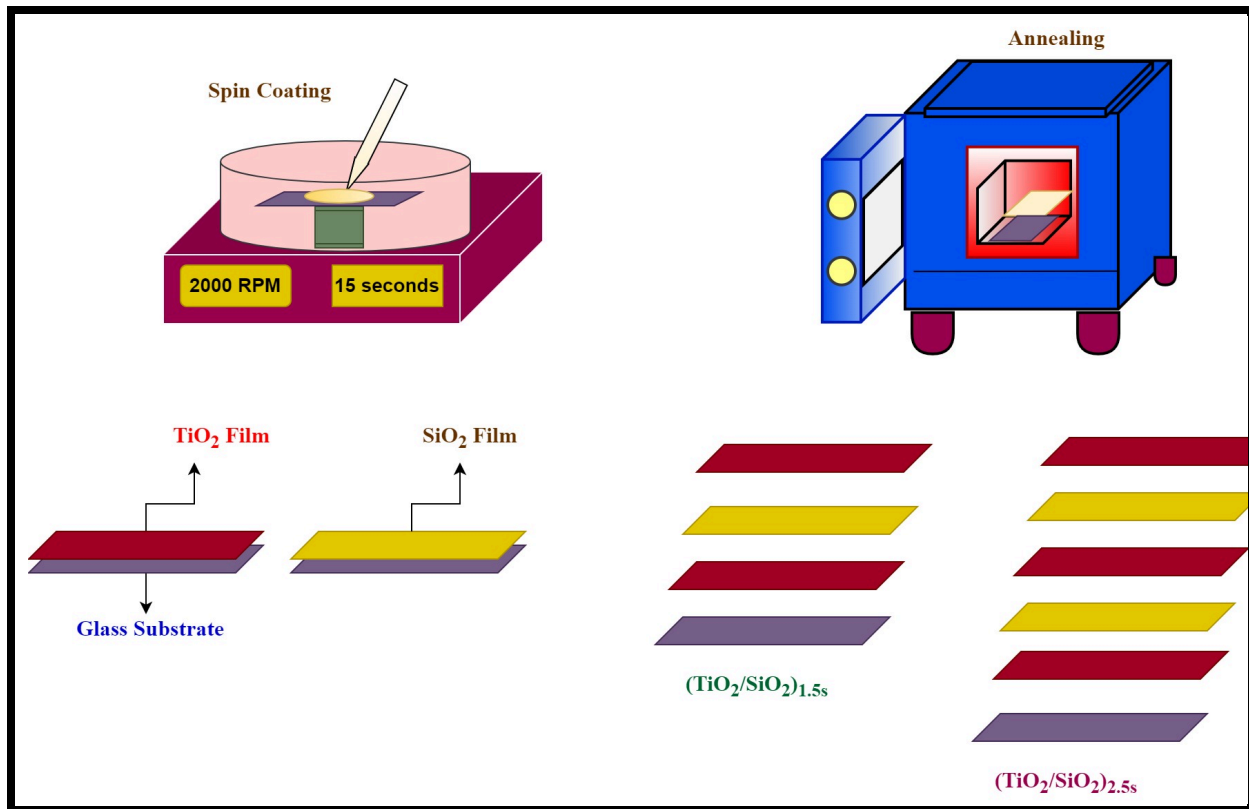


Fig. 2. Schematic illustration of the fabrication of multilayer structure.

The fabricated samples of monolayer and multilayer were characterized by using X-Ray diffractogram (Rigaku, smart lab, Japan) to know the crystallinity, ellipsometer (M-2000, J.A. Woollam Co., Inc.) to determine their optical constants, field-emission scanning electron microscopy (FESEM, MIRA3 TESCAN) to know the film thickness, ultraviolet-visible (UV-Vis, UV1800 Shimadzu, Japan) spectrophotometer having a specular reflectance attachment for reflectance analysis and contact angle meter (KYOWA DM501, Japan) to analyze the wetting behavior.

3. Results and Discussion

Figure 3 depicts X-ray diffraction (XRD) patterns of the individual of monolayer TiO_2 and SiO_2 . The XRD pattern was recorded in the Bragg angle range from 10° - 80° . Figure 3 (a) showed the anatase phase of TiO_2 coating, which is in good agreement with the JCPDS#21-1272. Furthermore, the diffraction peaks indexed at Bragg angles $2\theta=25^\circ$, 38° , 48° , 55° , 62° , and 75° , were attributed to the crystal planes of (101), (004), (200), (211), (204), and (215), respectively and well-matched with the published literature by Permana *et al.*, (2017) and Khajeh *et al.*, (2021). The XRD pattern shown in figure 3(b) represents the characteristic peak of SiO_2 at Bragg angle $2\theta=22^\circ$, which evidenced the amorphous nature of SiO_2 . This result is found well-matched with the JCPDS#29-0085 and the reported work by Deshmukh *et al.*, (2011).

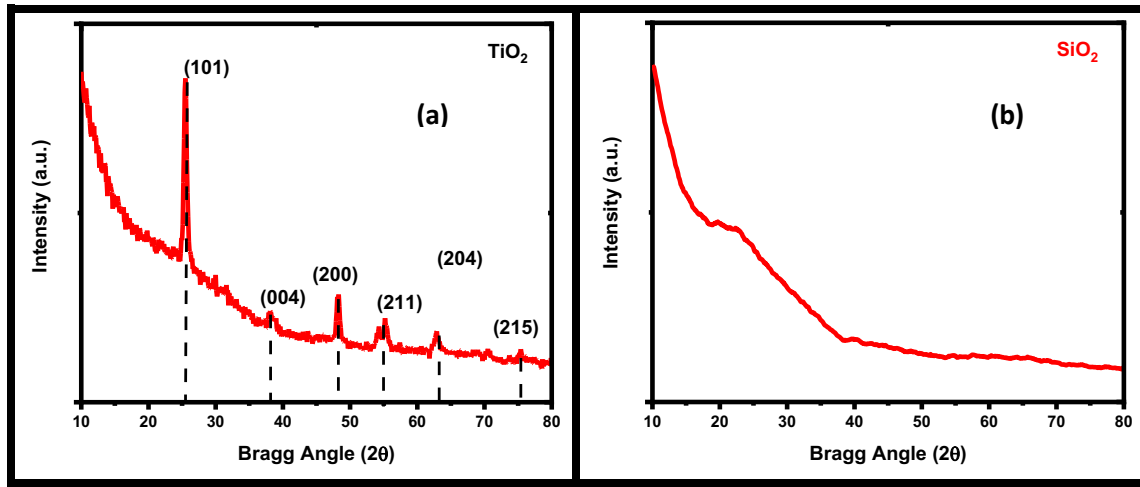


Fig. 3. XRD patterns of TiO_2 film (a) and SiO_2 film (b).

Figure 4 depicts the refractive index (a) and extinction coefficient (b) of the titania and silica films characterized by the spectroscopic ellipsometer.

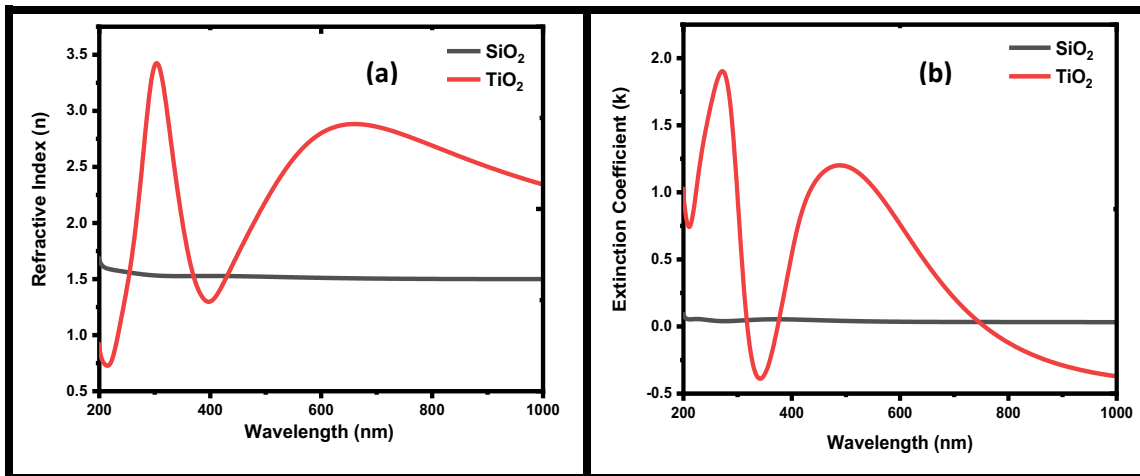


Fig. 4. Refractive index (a) and (b) extinction coefficient of TiO_2 and SiO_2 films.

The refractive index values of the titania film (red curve) are substantially higher (3.6) in the ultraviolet wavelength region and 2.6 in the near-infrared region compared to 2.2 in the visible range, as shown in figure 4(a). A similar trend can be observed for the case of extinction coefficient (red curve), as shown in figure 4(b). Furthermore, the silica film demonstrates a similar variation in the refractive index (black curve) and extinction coefficient (black curve) with respect to increased wavelength depicted in figure 4(a) and 4(b), respectively. The obtained refractive was found in good agreement with the reported work by Julia *et al.*, (2020). With the study of the refractive index and the extinction coefficient, we notice the refractive index contrast (refractive index of TiO₂/refractive index of SiO₂) with the redshift, which is desirable to achieve the reflection band in near-infrared reflector

The spin-coated monolayers of TiO₂ and SiO₂, and multilayers of TiO₂/SiO₂ composed of 1.5 stacks/bilayers (TiO₂/SiO₂)_{1.5S}, and 2.5 stacks/bilayers (TiO₂/SiO₂)_{2.5S} were investigated using the field-emission scanning electron microscopy to know their thicknesses and visualize. Figure 5 demonstrates the cross-section view of various prepared samples.

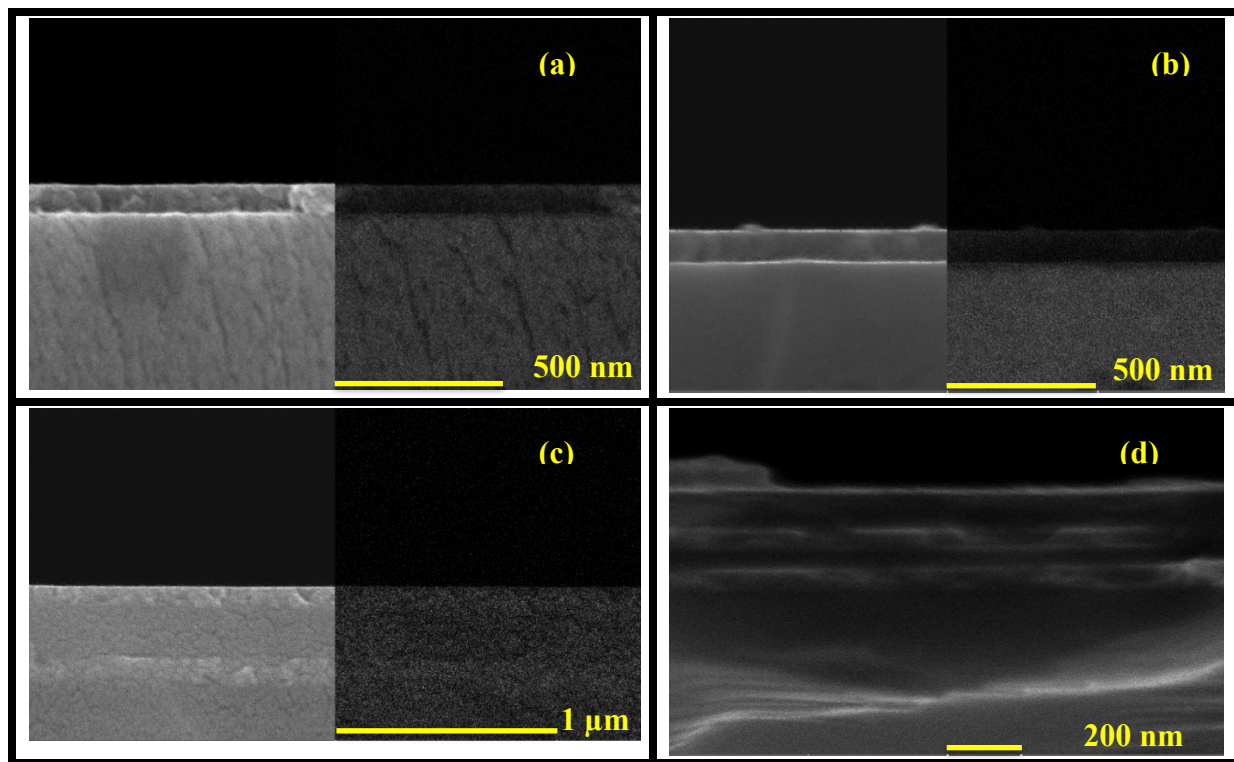


Fig. 5. FESEM cross-section images of TiO₂ (a), SiO₂ (b) and multilayer (TiO₂/SiO₂)_{1.5} (c) and (TiO₂/SiO₂)_{2.5} (d).

The bright and dark layers shown in figure 5 corresponds to the formation of TiO₂ and SiO₂ thin films. The thicknesses of the monolayers of TiO₂ and SiO₂ films were estimated to be 62.5 nm and 78.4 nm as shown in figure 5 (a) and (b), respectively. Similarly, as depicted in figures 5(c) and

5(d), the multilayer structures of 1.5 stacks $(\text{TiO}_2/\text{SiO}_2)_{1.5}$ and 2.5 stacks $(\text{TiO}_2/\text{SiO}_2)_{2.5}$ demonstrates their thicknesses of 86.3, 229.7, 78.39 and 92.06, 86.50, 75.69, 11.53, and 64.8 nm corresponding to the TiO_2 and SiO_2 layers. This arrangement of alternate layers of TiO_2 and SiO_2 is promising for the occurrence of constructive interference to produce high reflection in the specified spectral region, Dubey & Venkatesh, 2021.

The reflection of the individual TiO_2 , SiO_2 , and $(\text{TiO}_2/\text{SiO}_2)_{1.5}$ and $(\text{TiO}_2/\text{SiO}_2)_{2.5}$ were examined using UV-Visible spectroscopy, and the obtained results are shown in figure 6. The alternate arrangement of the multilayer structure endorsed a reflection window in the near-infrared region. According to reflectance studies, the monolayer of TiO_2 itself shows the opening of the reflection window in the near-infrared region, and further increases reflection with the increased number of stacks i.e. $(\text{TiO}_2/\text{SiO}_2)_{1.5}$ and $(\text{TiO}_2/\text{SiO}_2)_{2.5}$. The stacks of 1.5 and 2.5 demonstrated about 65 % and 100 % reflection in the near-infrared (NIR) spectrum with their centre wavelengths of 865 and 833 nm respectively. These kinds of coatings are useful for windows in the houses/offices and windshields in automotives as the thermal shields.

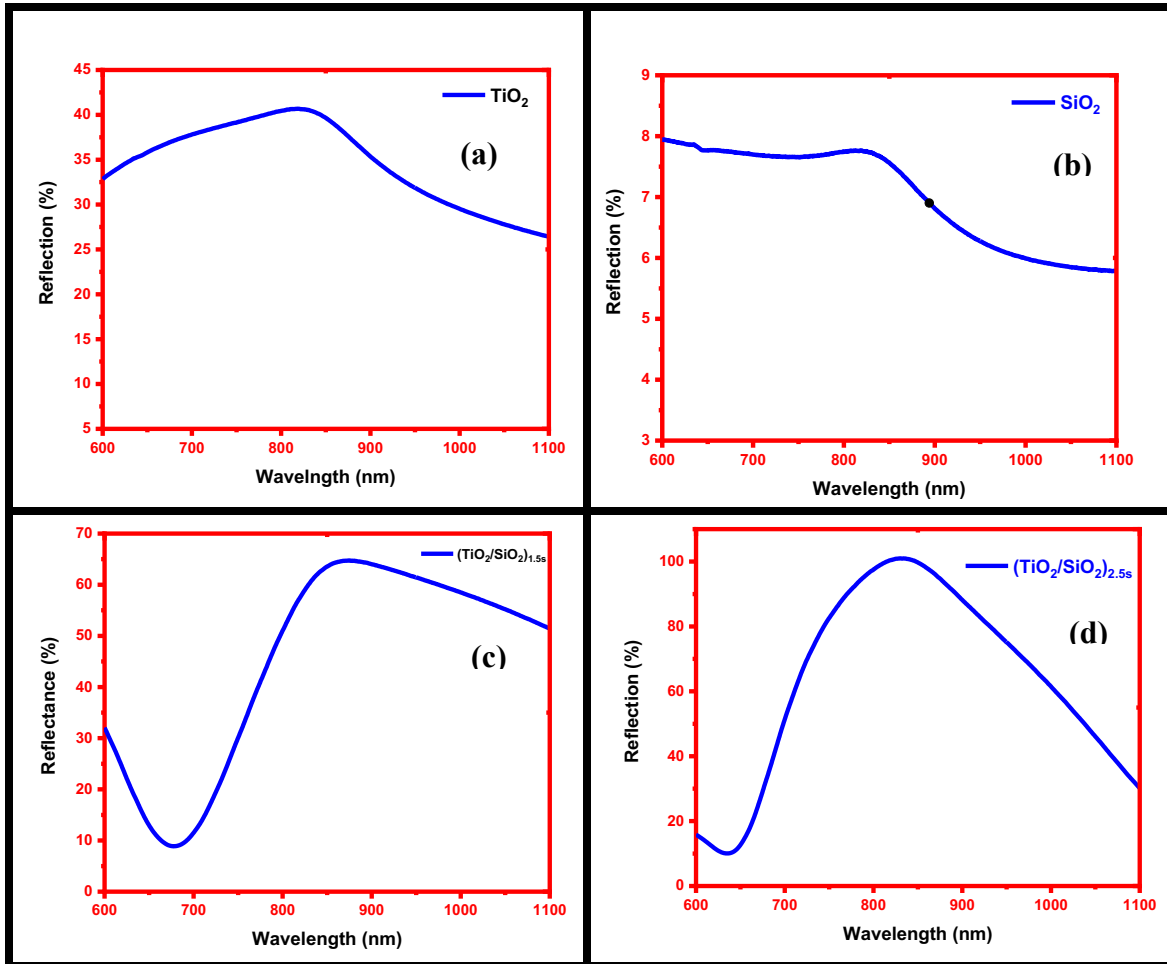


Fig. 6. Reflectance Spectra of TiO_2 (a), SiO_2 (b), multilayer $(\text{TiO}_2/\text{SiO}_2)_{1.5}$ (c) and $(\text{TiO}_2/\text{SiO}_2)_{2.5}$ (d).

Monolayers of TiO₂, SiO₂, and their multilayer structures based on 1.5 and 2.5 stacks of TiO₂/SiO₂ were examined for the contact angle to analyze the wetting behavior and presented in figure 7. Figure 7(a) of thin-film TiO₂ demonstrates the water contact angle of 16.6° and found in good agreement with the work reported by Golobostanfard *et al.*, (2013). Similarly, the contact angle of single-layer SiO₂ and multilayers (TiO₂/SiO₂)_{1.5s} and (TiO₂/SiO₂)_{2.5s} were found to be 30.9°, 23.4°, and 29.3° and shown in figure 7 (b), (c), and (d) respectively. The bar diagram shown in figure 8 represents the variation of contact angle with respect to various prepared samples. All these samples endorsed hydrophilic behavior and coincides with the reported works of Lee *et al.*, (2000) and Marcin *et al.*, (2006).

The multilayer structure (TiO₂/SiO₂)_{1.5} has a top layer thickness of about 78.9 nm which resulted in the contact angle of 23.4°, whereas the multilayer structure (TiO₂/SiO₂)_{2.5} having the top layer thickness of about 64.8 nm endorsed the contact angle of 29.3°, this conveys that the thicker TiO₂ films have a lower water contact angle and this result was found in good matching with the reported work of Zhang *et al.*, (2006). The increase in the contact angle value of the multilayer structure (TiO₂/SiO₂)_{2.5} can also be noticed and can be attributed to the cracks on the TiO₂ surface as reported by Han *et al.*, (2012).

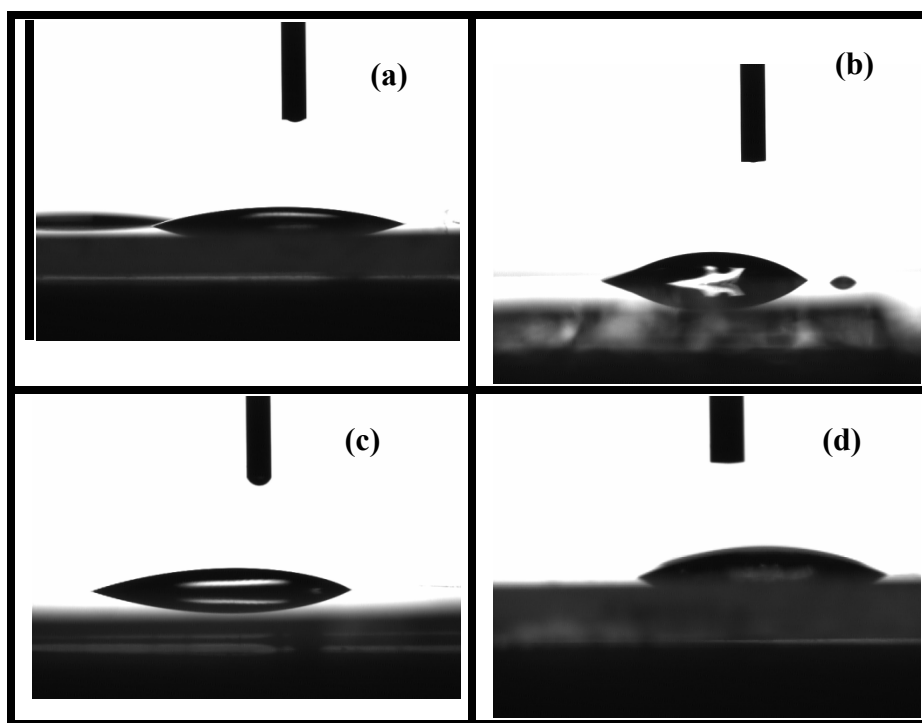


Fig. 7. Contact angle analysis of the monolayers of TiO₂ (a), SiO₂ (b), multilayer structures (TiO₂/SiO₂)_{1.5} (c) and (TiO₂/SiO₂)_{2.5} (d).

Further, the amorphous nature of the SiO₂ also induces more nucleation sites on the strongest anatase peak of TiO₂, for which the crystallite size tends to decrease and forth more, resulting in the effective change in contact angle. Thus, the hydrophilic nature obtained for these films suggest their application in windshields for their self-cleaning and anti-fogging ability. Due to the low

contact angle, the water droplets tend to spread quickly on the surface, making the surface anti-fogging and self-cleaning.

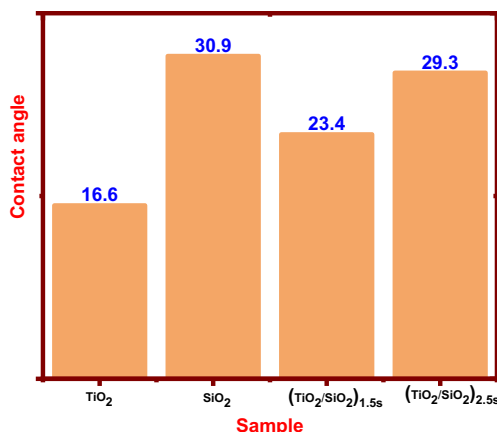


Fig. 8. Bar diagram of contact angle variation of monolayers of TiO₂, (a), SiO₂ (b), multilayer structures (TiO₂/SiO₂)_{1.5s} (c) and (TiO₂/SiO₂)_{2.5s} (d).

4. Conclusions

Monolayer and multilayer structures of TiO₂ and SiO₂ were spin-coated with their respective sol-gel synthesized solutions on the plain glass substrates. XRD investigations endorsed the anatase and amorphous phases of titania and silica films, respectively. The refractive index values were 2.66 and 1.5, corresponding to the of titania and silica films, as confirmed by the ellipsometry measurement. The FESEM investigations endorsed the formation of a multilayer structure consisting of bright and dark bands corresponding to the TiO₂ and SiO₂ films. The near-infrared reflectance of the multilayer structure was observed at its center wavelength of 833 nm. The prepared mono and multilayer structures of TiO₂ and SiO₂ were tested for the wetting behavior, which evidenced their hydrophilic activity. Finally, these reflectors exhibited the reflectance window in the near-infrared region, suggesting potential applications in houses/offices/hospitals and wind shielding in automotive for self-cleaning.

References

- Akbar, E., & Ameneh, E. (2012)** Investigation of super hydrophilic mechanism of titania nano layer thin film-Silica and indium oxide dopant effect. *Bulletin of Material Science* 35(2): 137-142.
- Anaya, M., Rubino, A., Calvo, M. E., & Míguez, H. (2016)** Solution processed high refractive index contrast distributed Bragg reflectors. *Journal of Material Chemistry C*, 4(20): 4532-4537.
- Damchan, J., Sikong, L., Kooptarnond, K., & Niyomwas, S. (2008)** Contact Angle of Glass Substrate Coated with TiO₂/SiO₂ Thin Film, *Journal of Natural Sciences*, 7(1): 19-23.

Deshmukh, P., Bhatt, J., Peshwe, D., & Pathak, S. (2011) Determination of Silica Activity Index and XRD, SEM and EDS Studies of Amorphous SiO₂ Extracted from Rice Husk Ash. Transactions of the Indian Institute of Metals, 65(1): 63–70

Dubey, R.S., & Ganesan, V. (2017). Fabrication and characterization of TiO₂/SiO₂ based Bragg reflectors for light trapping applications. Results in Physics, 7: 2271-2276.

Dubey, R.S., & Venkatesh, Y. (2021) Engineering of Ultra-Violet Reflectors by varying Alternate Layers of Titania/Silica for Harmful UV-Protection. Kuwait journal of Science, 1-7: <http://doi.org/10.48129/kjs.16633>.

Feng, I.W., Jin, S., Li, J., Lin, J., & Jiang, H. (2013) SiO₂/TiO₂ distributed Bragg reflector near 1.5 μm fabricated by e-beam evaporation. Journal of Vacuum Science Technology A, 31(6): 061514 1-4.

Golobostanfard, Mohammad Reza., & Abdizadeh, Hossein. (2013) Effects of acid catalyst type on structural, morphological, and optoelectrical properties of spin-coated TiO₂ thin film. Physica B: Condensed Matter, 413, 40–46.

Han, K., & Kim, J. H. (2012) Fabrication of TiO₂/SiO₂ multilayer film structure by the sol–gel process with efficient thermal treatment methods. Applied Surface Science, 263: 69-72.

Huang, L., Jing, S., Zhuo, O., Meng, X., & Wang, X. (2017) Surface Hydrophilicity and Antifungal Properties of TiO₂ Films Coated on a Co-Cr Substrate. BioMed Research International, 2017: 1-7.

Julia, R., Mghendi, M., Njoroge, Walter., Christopher, M., Onesmus, M., & Sylvester, H. (2020) Optical characterization of photocatalytic copper doped thin films of anodized titanium. Materials Research Express, 7(2): 025505.

Khajeh Aminian, M., Sajadi, F., Mohammadizadeh, M. R., & Fatah, S. (2021) Hydrophilic and Photocatalytic Properties of TiO₂/SiO₂ Nano-layers in Dry Weather. Progress in Color Colorants and Coatings, 14(3): 221-232.

Lee, H. Y., Park, Y. H., & Ko, K. H. (2000) Correlation between Surface Morphology and Hydrophilic/Hydrophobic Conversion of MOCVD–TiO₂ Films. Langmuir, 16(18): 7289-7293.

Lin, N.M., Shei, S.C., & Chang, S.J. (2015) Design and Fabrication of a TiO₂/SiO₂ Dielectric Broadband and Wide-Angle Reflector and Its Application to GaN-Based Blue LEDs. *IEEE Journal of Quantum Electronics*, 51(7): 1-5.

Marcin, J., Hupka, & J., Kisch, H. (2006) Hydrophilicity of TiO₂ Exposed to uv and vis radiation. *Physicochemical Problems of Mineral Processing*, 40: 287-292.

Nagayoshi, H., & Murooka, T. (2015) TiO₂ Nanoparticle/SiO₂ Composite Back Reflector for Solar Cells. *Energy Procedia*, 77: 242-247.

Permana, D.M., Navigant, A.R., Lestari, R.P., Kumada, N., Eddy, R.D., & Rahayu, I. (2021) Synthesis and Photocatalytic Activity of TiO₂ on Phenol Degradation. *Kuwait Journal of Science*, 1-9: <http://doi.org/10.48129/kjs.13509>.

Shokuhfar, A., Alzamani, M., Eghdam, E., Karimi, M., & Mastali, S. (2012) SiO₂-TiO₂ Nanostructure Films on Windshields Prepared by Sol-Gel Dip-Coating Technique for Self-Cleaning and Photocatalytic Applications, *Nanoscience and Nanotechnology*, 2(1): 16-21.

Yang, H., Liang, F., Chen, Y., Wang, Q., Qu, X., & Yang, Z. (2015) Lotus leaf inspired robust superhydrophobic coating from strawberry-like Janus particles. *NPG Asia Materials*, 7(4): 1–6.

Zhang, X., Fujishima, A., Jin, M., Emeline, A. V., & Murakami, T. (2006) Double-Layered TiO₂-SiO₂, Nanostructured Films with Self-Cleaning and Antireflective Properties. *Journal of Physical Chemistry B*, 110(50): 25142-25148.

Submitted: 18/12/2021

Revised: 09/03/2022

Accepted: 12/03/2022

DOI : 10.48129/kjs.17787

Sol-gel synthesis of $\text{CaZnAl}_2\text{O}_4$ ceramic nanoparticles and investigation of their properties

Sekhar Didde^{1,3}, R. S. Dubey^{2,3,*}, Sampad Kumar Panda⁴

¹*Dept. of ECE, Swarnandhra College of Engineering and Technology, Narsapur,
Andhra Pradesh-534275, India*

² *University Institute of Engineering & Technology, Guru Nanak University,
Ibrahimpattam, R. R. District, Hyderabad-501 506 (T.S.), India*

³*Dept. of Electronics & Communication Engineering, Guru Nanak Institutions Technical
Campus, Ibrahimpattam, R. R. District, Hyderabad, (T.S.), India*

⁴*Dept. of ECE, Koneru Lakshmaiah Education Foundation, Greenfields,
Vaddeswaram, Guntur, Andhra Pradesh, India*

**Corresponding Author: rag_pcw@yahoo.co.in*

Abstract

Dielectric ceramic materials are well-recognized in the semiconductor industry because of their exceptional thermal stability, chemical resistance, and crystallinity. Despite their potential applications, these are also demanded in wireless communication. This paper reports the structural, morphological, and dielectric properties of sol-gel-derived $\text{CaZnAl}_2\text{O}_4$ ceramic nanoparticles. X-ray diffraction (XRD) analysis exhibited the polycrystalline characteristic of the $\text{CaZnAl}_2\text{O}_4$ nanoparticles with their crystallite size of 13 nm. Fourier-Transform infrared spectroscopy (FTIR) analysis confirmed the relevant vibration peaks of various functional groups present in the ceramic nanoparticles. Surface morphology study demonstrated the preparation of spherical grains with their mean diameter of 16 nm. The concentric rings also confirm the crystallinity of the nanoparticles as appeared in the selected-area diffraction pattern. Furthermore, dielectric properties investigation showed the variation of dielectric permittivity from 23.76 to 21.67 as a function of increased frequency. Similarly, the dielectric loss is found to decrease from 0.047 to 0.039. As a result, the conductivity increased from 1.324 $\mu\text{S/m}$ to 3.639 $\mu\text{S/m}$ as a function of applied frequency.

Keywords: Ceramics; crystallinity; dielectric properties; nanoparticles, sol-gel method.

1. Introduction

Telecommunication is the most fantastic escalating field of applied sciences that has acquired the interest of public life in the current era. Trending wireless local area networks are rigged in houses, commercial malls, and offices. An antenna is a device that transmits or receives electromagnetic waves from one point to another. These are the primary elements of any wireless structure. The receiving antenna as a part of the system depends on shifting the electromagnetic waves into their original form. Most antennas are resonant radiators, which operate bi-directionally over a relatively narrow frequency band.

It is an actuator that converts electrical energy into electromagnetic energy at the same frequency and plays a vital role in wireless communication.

Currently, multifunctional nanomaterials have got demand in the miniaturization of electronic, optoelectronic, photonic and electrical devices. In general, flame retardant (FR-4) and epoxy glass are preferred as the antenna substrates, while copper, silver, and other metals are used as the patch materials. However, three significant disadvantages associated with the microstrip patch antennas such as a low gain, less efficiency, and narrow frequency bandwidth are needed to compromise. This exhibits the requirement of dielectric materials with high dielectric permittivity and a low dielectric loss to reduce the size of the antenna (Pandirengan, T. *et al.*, 2016). Practically the microstrip patch antennas (MSAs) are demanded in wireless communication. Deschamps explored the microstrip patch antenna in 1950 while its various applications emerged after the pioneer work of Bob Munson in 1972 (Mittal. *et al.*, 2015). The key features of a microstrip patch antenna include its easy integration, less-weight, low-cost, small-size (Vinnik, D.A. *et al.*, 2021). The MPA needed to be modeled to deal with the dissimilar commonness. The MPA is generally employed as directional antennas in telecommunication and comprises alternating current elements above the floor plane. The dielectric material separates the alternating current component and the ground plane. Basically, MSA is a small band radiator, which is unique in wireless technology (Chinnaguruswamy & Perumalsamy, 2021). Among various antennas, the MSAs are well-suited in industrial and commercial applications due to their straight forward design and inexpensive manufacturing cost (Singh, S. & Kumar. J, 2020). Along with the dielectric materials demand, a variant of magnetic-dielectric materials is being explored for fabricating the MPAs (Lopes Matias, J. A. *et al.*, 2021). Further, the researchers reported various types of shapes of the patch for improving the gain and resonant bandwidth (Mukta, Ch. *et al.*, 2021).

The dielectric ceramic materials can be synthesized by using various bottom-up techniques. However, the sol-gel approach is the simplest to prepare the dielectric ceramic composite particles. This technique produced pure nanoparticles with lower sintering temperatures, so it is a low-cost process that consumes less energy (Bokov, D. *et al.*, 2021; Aleksandrova, M. *et al.*, 2020). The spinel zinc aluminate (ZnAl_2O_4) nanoparticles have distinct characteristics such as wide energy bandgap and high phosphorescent quantum yield (Hussain, Tanveer. *et al.*, 2017). Various researchers claimed the preparation and characterization of spinel metal oxide by adding or doping transition metal ions and explored the dielectric characteristics (Rahman, Ashiqur. *et al.*, 2015; Jia-Min Wu. *et al.*, 2011). Zinc aluminate (ZnAl_2O_4) is well recognized in microwave applications. The choice of this material is due to distinct characteristics like good crystallinity, high thermal capability, and excellent chemical registrant. Zinc aluminate is a spinel structure known as gahnite with its formula AB_2O_4 , where A indicates the bivalent cations (Zn, Mg, Cd, and Mn, etc.) with the tetrahedral site. The element B fills the octahedral positions of a close-packed face-centered cubic structure in $\text{Fd}3\text{m}$ space group symmetry. This B position gets occupied by the desired metal elements. It is composed of close-packed 32 oxygen atoms with cations in tetrahedral and octahedral intermissions in a cubic structure. The ZnAl_2O_4 is also employed as a catalyst due to its

high thermal stability, large mechanical resistance, and low surface acidity (Haung, Sh. *et al.*, 2020).

Several reports have been published on the synthesis of ZnAl_2O_4 nanoparticles using cost-effective chemical routes. The crystallite size of ZnAl_2O_4 nanoparticles was found reduced with the increase of the doping concentrations of Cr and Mn. The X-ray diffraction investigation revealed a crystallite size of 23nm (DING, M. *et al.*, 2020). Similarly, the synthesis of Cr-doped ZnAl_2O_4 nanoparticles using the sol-gel method was reported. They explored the influence of doping concentration of the Cr on the variation of its crystallite size (Shang-Pan, Huang. *et al.*, 2020). Similarly, another group reported the dielectric characteristics of ZnAl_2O_4 doped with Mg. They noticed the increased grain size, which was attributed to the ionic radius of the dopant. The dielectric permittivity of the Mg- ZnAl_2O_4 was estimated to be 50, further found increased with the increased doping concentration of Mg (Hussain, Tanveer. *et al.*, 2017). The so-gel-derived ZnAl_2O_4 nanoparticles having their crystallite size of 19.92nm were studied. The dielectric properties analysis using the LCR meter showed dielectric permittivity of 8.7. The microstrip patch antenna made-up of these nanoparticles showed return loss of -25.4dB at the resonant frequency of 12.78GHz (Rahman, Ashiqur. *et al.*, 2015). The hydrothermal method was employed to prepare the Mn-doped ZnAl_2O_4 nanoparticles, and various properties were studied. The average crystallite size of Mn-doped ZnAl_2O_4 nanoparticles was 13nm which further decreased with the increased doping concentration of Mn (Haung, Sh. *et al.*, 2020). The impact of Zn doping in MgAl_2O_4 was studied and claimed the increased dielectric permittivity from 7.9 to 8.56 with the increased concentration of Zn (Chang Wei Zheng. *et al.*, 2007). The sol-gel prepared ZnAl_2O_4 nanoparticles were studied for various investigations, and finally, a prototype microstrip patch antenna for C band communications was demonstrated. They claimed its resonant frequency at 4.64GHz with a return loss of -17.13dB (Srilali, Siragam. *et al.*, 2022).

In this way, by adopting the simple sol-gel method, one can synthesize the nanoparticle of ZnAl_2O_4 after doping with various dopants to tune the dielectric properties for the well-suited application in fabricating the microstrip patch antenna. This paper presents the synthesis of calcium doped ZnAl_2O_4 ceramic nanoparticles and studied their structural, morphological, and dielectric properties. Section 2 presents the materials and methods followed in synthesizing ceramic nanoparticles. The characterized results are discussed in section 3. Lastly, the paper is summarized in Section 4.

2. Experimental

2.1 Materials

Aluminum nitrate nonahydrate ($\text{Al}(\text{NO}_3)_3 \cdot 9\text{H}_2\text{O}$, Sigma-Aldrich), Zinc acetate dehydrate ($\text{Zn}(\text{O}_2\text{CCH}_3)_2 \cdot 2\text{H}_2\text{O}$, Lobychem), Ethylene glycol ($\text{C}_2\text{H}_6\text{O}_2$, SdFine), calcium nitrate tetra hydrate ($\text{Ca}(\text{NO}_3)_2 \cdot \text{H}_2\text{O}$, Sigma-Aldrich), nitric acid (HNO_3 , Lobychem) and ethanol ($\text{C}_2\text{H}_5\text{OH}$, Sigma-Aldrich) were used. As the source of Zn, Al, and Ca, the chemicals $\text{Zn}(\text{O}_2\text{CCH}_3)_2 \cdot 2\text{H}_2\text{O}$, $\text{Al}(\text{NO}_3)_3 \cdot 9\text{H}_2\text{O}$, and $\text{Ca}(\text{NO}_3)_2 \cdot \text{H}_2\text{O}$ were used.

2.2 Synthesis & Characterization

First, aluminum nitrate nonahydrate was mixed in 60 ml ethanol with a constant stirring of 5 min. Then 9.906 gm zinc acetate dehydrate and 0.498 ml ethylene glycol were added to the above-prepared solution, which acted as the chelating agent. Later 1.419 gm calcium nitrate tetrahydrate was added. The obtained solution was kept for 1hr stirring at a temperature of 75°C , and further 0.36 ml nitric acid was added to maintain the homogeneity of the solution. After so, the solution was thermally treated at 75°C for 1 hr. After getting the gel, it was dried at 180°C for 2 hr and calcined in a muffle furnace at 800°C . The calcined sample was ground for obtaining powder of $\text{CaZnAl}_2\text{O}_4$. Figure.1 depicts the sol-gel process of the $\text{CaZnAl}_2\text{O}_4$ ceramic nanoparticles as shown here in the first row. At first, the raw materials were mixed in the beaker at room temperature under a constant stirrer. The solution was kept at temperature 75°C on a magnetic stirrer for 1 hr during the process. The second row (shown in the above picture) illustrates the drying, calcination, and grinding process. For instance, the prepared gel was dried in the oven while maintaining the temperature of 80°C for 2 hr. Later, the sample was calcined in a muffle furnace at temperature 800°C for 30 min and finally ground to obtain the nanoparticles.

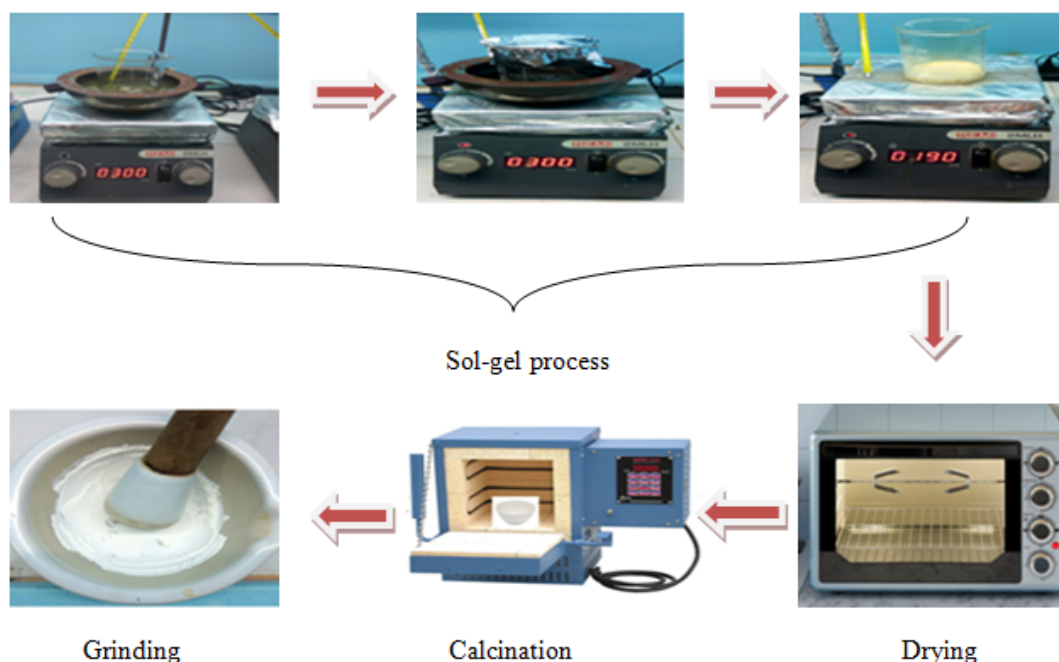


Fig. 1. Sol-gel synthesis process of $\text{CaZnAl}_2\text{O}_4$ nanoparticles.

2.3 X-ray diffraction (XRD)

This technique provides the details of the physical properties of the structure and chemical confirmation of the material under the test. It also gives information on the crystalline types and phases. In this study, we have used an X-ray diffractometer, Bruker D8, Venture.

2.4 Fourier Transform Infrared Spectroscopy (FTIR)

The FTIR is a powerful tool that examines the presence of various chemical bonds in the material. Using this technique, we study the presence of polymers and organic/inorganic substances. Our sample was investigated using FTIR, Perkin Elmer-Spectrum Two, US.

2.5 Transmission Electron Microscopy (TEM)

This technique is used to know the nanoparticles' surface morphology and size distribution. TEM investigation can be done for a tiny sample. We have employed TEM, Talos F200S G2, US in this present work.

2.6 Dielectric Properties

The LCR meter is a technique used to examine the dielectric properties of the specimen. Using this, we study the sample's dielectric permittivity, dielectric loss, conductivity, etc.

3. Results and Discussion

The XRD pattern of $\text{CaZnAl}_2\text{O}_4$ nanoparticles recorded at 2θ range from 10° to 80° is illustrated in Figure 2. We can observe the polycrystalline nature of the synthesized nanoparticles through the XRD pattern.

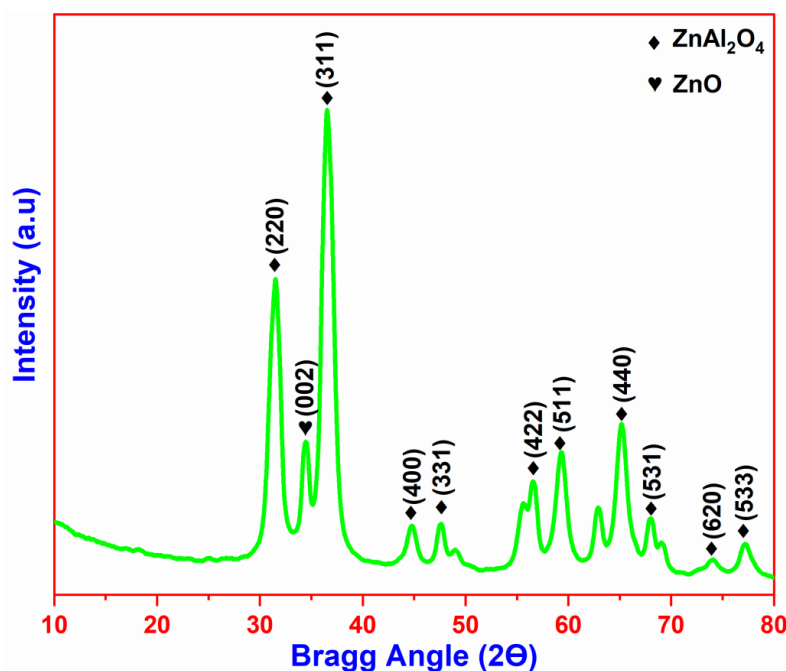


Fig. 2. XRD Pattern of $\text{CaZnAl}_2\text{O}_4$ ceramic nanoparticles.

The diffraction peaks observed at Bragg angle $2\theta = 31.80^\circ, 36.41^\circ, 44.76^\circ, 49.11^\circ, 56.55^\circ, 59.37^\circ, 65.15^\circ, 67.98^\circ, 74.01^\circ$ and 77.22° were ascribed to the planes (220), (311), (400), (331), (422), (511), (440), (531), (620) and (533) respectively. The strong peaks located at $2\theta = 31.80^\circ$ and 36.41° correspond to the face-centered cubic structure of ZnAl_2O_4 (R.S. Dubey. *et al.*, 2022; Reem S, Khaleel. *et al.*, 2022). We have also noticed a diffraction peak at $2\theta = 34.22^\circ$ corresponding to the ZnO of the plane (002). The obtained diffraction data was well-matched with the JCPDS File Nos. 00-050-0426 and 36-1451 (Gurugubelli, T. R. *et al.*, 2021; Reem S, Khaleel. *et al.*, 2020). The mean crystallite size of the $\text{CaZnAl}_2\text{O}_4$ nanoparticles was 13 as computed using Scherrer's equation (Rahman, Ashiqur. *et al.*, 2015). The strong peaks located at $2\theta = 31.80^\circ$ and 36.41° correspond to the face-centered cubic structure of ZnAl_2O_4 (R.S. Dubey. *et al.*, 2022; Reem S, Khaleel. *et al.*, 2022). We have also noticed a diffraction peak at $2\theta = 34.22^\circ$ corresponding to the ZnO of the plane (002). The obtained diffraction data was well-matched with the JCPDS File Nos. 00-050-0426 and 36-1451 (Gurugubelli, T. R., *et al.*, 2021; Reem S. Khaleel, *et al.*, 2020). The mean crystallite size of the $\text{CaZnAl}_2\text{O}_4$ nanoparticles was 13 as computed using Scherrer's equation (Rahman, Ashiqur. *et al.*, 2015).

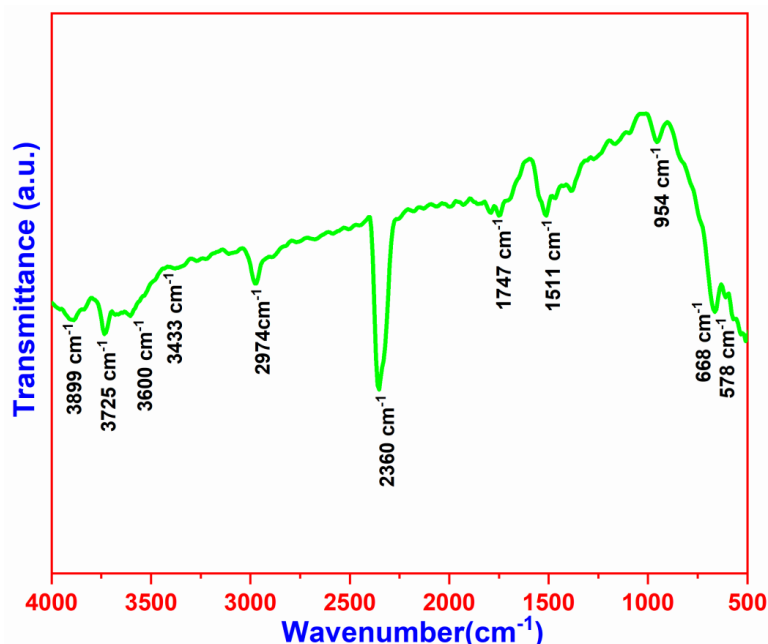


Fig. 3. FTIR spectra of $\text{CaZnAl}_2\text{O}_4$ ceramic nanoparticles.

Figure 3 depicts the Fourier-Transform infrared spectroscopy (FTIR) spectra of $\text{CaZnAl}_2\text{O}_4$ nanoparticles scanned in the region of 4000 to 500 cm^{-1} . The FTIR spectra demonstrates the vibration peaks at wave number values of 578 cm^{-1} , 668 cm^{-1} , 954 cm^{-1} , 1511 cm^{-1} , 1747 cm^{-1} , 2360 cm^{-1} , 2974 cm^{-1} , 3433 cm^{-1} , 3600 cm^{-1} , 3725 cm^{-1} and 3899 cm^{-1} . It can be noticed that the peaks originating at 578 cm^{-1} and 668 cm^{-1} are the characteristic peaks of ZnAl_2O_4 . The peak at 578 cm^{-1} corresponds to Zn-O bond and while the other one aligned 668 cm^{-1} was attributed to the

Al-O bond. The broad absorption band in the wave number range $3433\text{--}3899\text{ cm}^{-1}$. It is found regarded to the stretching vibration of hydroxyl groups, due to the water contents. The band located 2360 cm^{-1} indicates the existence of oxygen bonds. This peak is identified in all spinel compounds related to the grains' spinel structure (Wang, Shi-Fa. *et al.*, 2015). Another peak at 1516 cm^{-1} can be regarded as the stretching vibration of aluminum and oxygen bond. The other vibration peaks in from 500 cm^{-1} to 900 cm^{-1} are ascribed to the inorganic network, related to the metal-oxygen, aluminum-oxygen, and metal-oxygen-aluminum stretching frequencies.

Figure 4(a) depicts the TEM micrograph, which exhibits the agglomerated particles of $\text{CaZnAl}_2\text{O}_4$. Figure 4(b) shows another TEM image recorded at the scale of 20 nm, evidenced spherical morphology of $\text{CaZnAl}_2\text{O}_4$ grains with their average diameter of 16 nm. Selected area diffraction pattern (SAED) was recorded to know the crystallinity of the prepared nanoparticles, as shown in figure 4(c). The concentric rings that appeared in the SAED pattern indicate the prepared nanoparticles' crystallinity. This SAED pattern coincided with the XRD results. We have analyzed the compositional elements present in the sample using the EDS measurements. Figure 4(d) shows the presence of Zn, Ca, Al and O at energy 1.00 eV, 3.80 eV, 1.50 eV, and 0.50 eV, respectively.

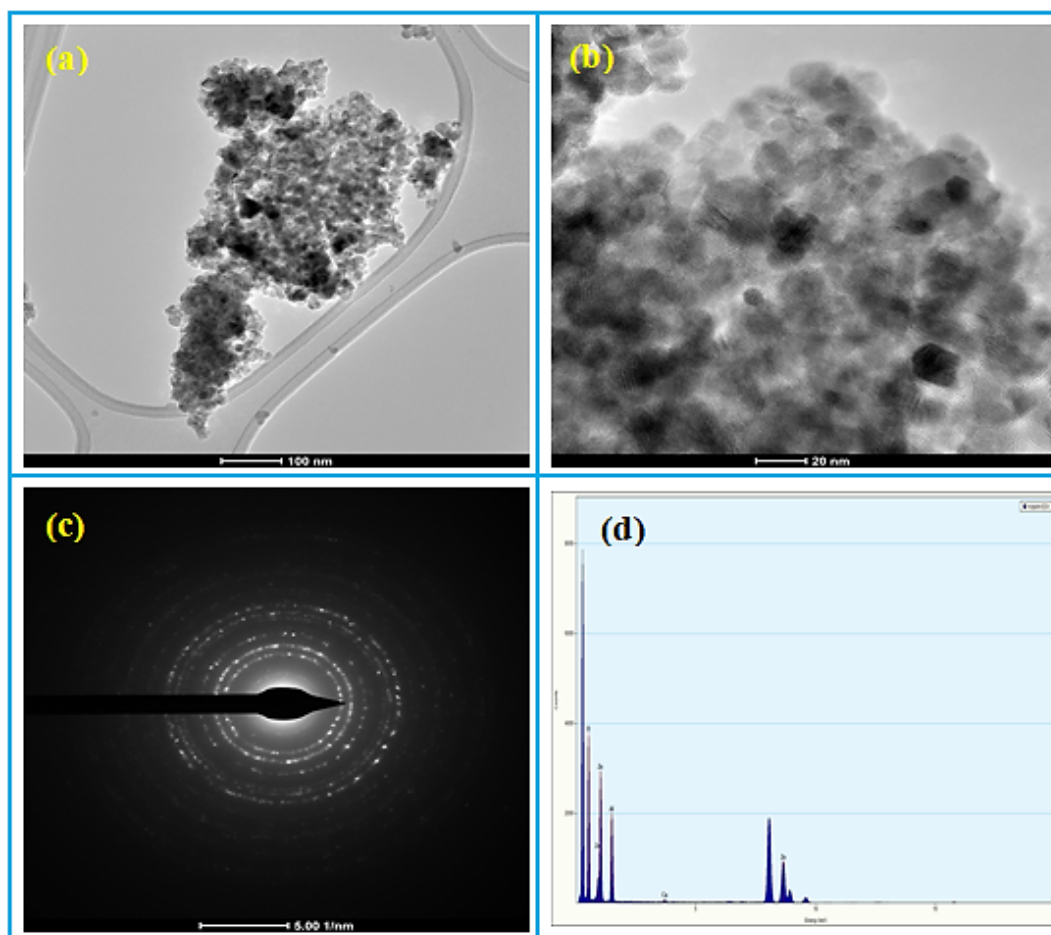


Fig. 4. TEM micrographics at the scale of 100 nm (fig.a), at the scale of 20 nm (fig.b), SAED pattern (fig.c) & EDS spectrum (fig.d) of $\text{CaZnAl}_2\text{O}_4$ ceramic nanoparticles.

Figure.5 depicts the dielectric permittivity of the $\text{CaZnAl}_2\text{O}_4$ ceramic nanoparticles was tested using an LCR meter in the frequency range from 300 KHz to 1MHz. One can notice the change in dielectric permittivity with the increased frequency can be noticed. This evidences the decreased dielectric permittivity with the increased frequency. The dielectric permittivity shows a relatively high value at lower frequencies, with a gradual decrease with the increased frequency. We computed the dielectric permittivity using the simple formula, $\epsilon_r = (Cd/\epsilon_r A)$. Here, ϵ_r is the dielectric permittivity of the sample, C, d are the capacitance, thickness, and cross-sectional area of the pellet. The dielectric permittivity of $\text{CaZnAl}_2\text{O}_4$ was found to be decreased from 22.92 to 21.66, with the applied frequency from 300 KHz to 1MHz. The sample under the test might have a low electrical resistance compared to the grain boundaries due to its crystalline nature. Grains and grain boundaries behave like two sheets with distinct electrical properties. Maxwell-Wagner interfacial polarization can occur in the grains around the grain boundaries due to the carrier's aggregation around these larger resistant boundaries upon the applied electric field (Hussain, Tanveer. *et al.*, 2017). When the applied frequency is raised, the charge carriers seek to reverse their way and again try to line up one another in the way of the applied field. As these charges try to rest, the polarity of the applied field again changes, and so on. As a result, these charges cannot find the time they need to rest, increasing frequency decreasing the polarization. So that at a higher frequency, the dielectric constant decreases.

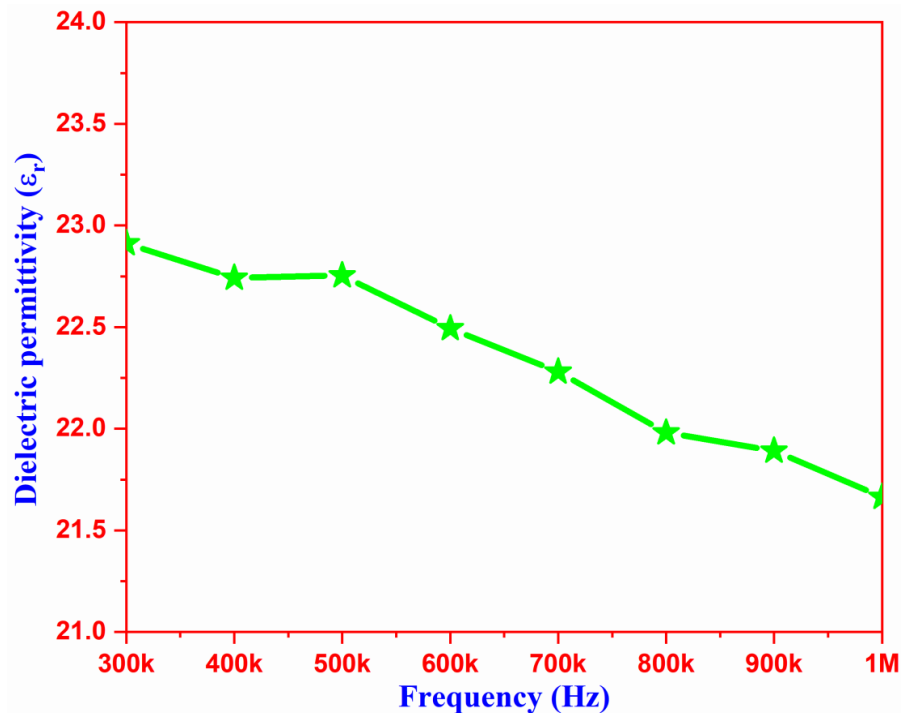


Fig. 5. Dielectric permittivity of $\text{CaZnAl}_2\text{O}_4$ ceramic nanoparticles.

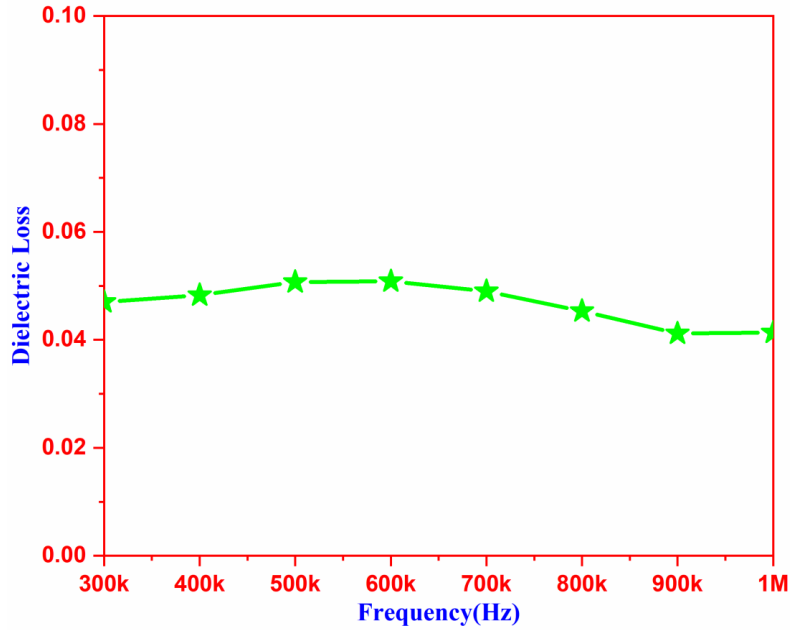


Fig. 6. Dielectric loss of $\text{CaZnAl}_2\text{O}_4$ ceramic nanoparticles.

Dielectric loss refers to the loss of energy in the form of heat due to the movement of charged particles. Figure.6 shows the dielectric loss of $\text{CaZnAl}_2\text{O}_4$ nanoparticles in accordance with frequency from 300 KHz to 1 MHz. It can be observed that dielectric loss was increased with decreased frequency, and the dielectric loss was reduced from 0.047 to 0.039 in the applied frequency range from 300 KHz to 1MHz. High energy is necessary for optimal polarization resonance, resulting in increased energy distraction or high energy loss at lower frequencies. While at higher frequencies, resonance occurs freely with a bit of polarization in the grain boundaries, thus, low energy loss can be observed with the increased frequency (Hussain, Tanveer. *et al.*, 2017).

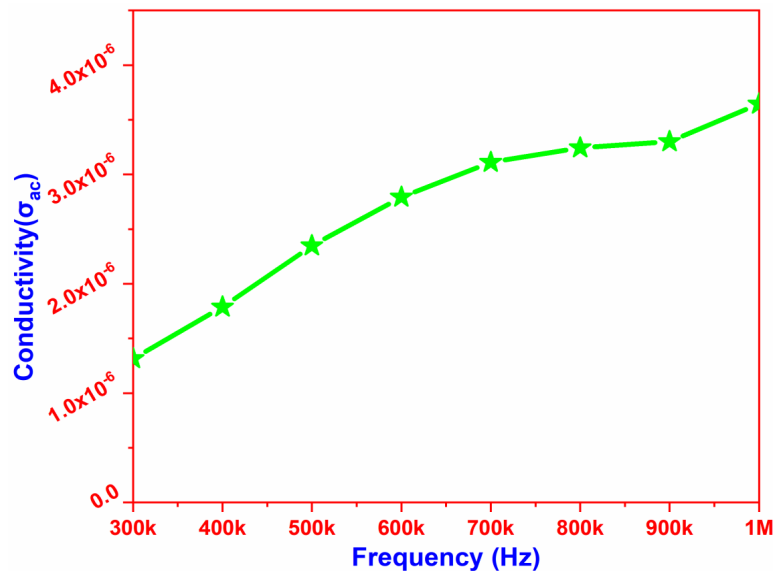


Fig. 7. Conductivity of $\text{CaZnAl}_2\text{O}_4$ ceramic nanoparticles as a function of frequency.

The conductivity of a material indicates its capability to perform electrical current. Figure.7 shows the frequency-dependent ac conductivity of CaZnAl₂O₄ ceramic nanoparticles plotted in the frequency range from 300 KHz to 1MHz at room temperature. We have estimated the ac conductivity using a simple relation $\sigma_{ac} = \omega \epsilon_0 \epsilon_r \tan \delta$, where ϵ_0 is the dielectric constant of free space ϵ_r is the dielectric permittivity of the sample, and $\tan \delta$ is dielectric loss of the material. The material's conductivity depends upon the angular frequency of the applied signal. Figure.7, we observed the increased conductivity with the increased applied frequency. The increasing trend of ac conductivity exhibits space charges scattering cations across the adjacent sites (Hussain, Tanveer. *et al.*, 2017). Here, the ac conductivity was increased from 1.324 $\mu\text{S/m}$ to 3.639 $\mu\text{S/m}$ with increased frequency.

4. Conclusions

The prepared CaZnAl₂O₄ ceramic nanoparticles were synthesized and studied using various techniques. The XRD investigation endorsed the polycrystalline characteristic of the nanoparticles. The FTIR investigation exhibited the presence of various functional groups anticipated in the synthesized nanoceramic compound. The TEM study demonstrated the preparation of spherical grains of CaZnAl₂O₄ with their mean diameter of about 16nm. The SAED pattern confirmed the polycrystalline structure with the formation of concentric rings. The dielectric permittivity of CaZnAl₂O₄ was in the range from 22.92 to 21.66, whereas the dielectric loss was from 0.047 to 0.039. Similarly, conductivity was varied from 1.324 $\mu\text{S/m}$ to 3.639 $\mu\text{S/m}$ with applied frequency. Remarkably, the obtained dielectric permittivity of CaZnAl₂O₄ nanoparticles is increased to 22.92. This enhanced characteristic of the ceramic nanoparticles would be suitable in microwave applications such as fabricating the microstrip patch antenna or resonator.

References

- Aleksandrova. M., Jivov. B., Lakov. L., (2020).**Summary of sol-gel synthesis of materials with electronic applications international scientific journal "materials science. non-equilibrium phase transformations". web issn 2534-8477.
- Bokov.D., Jalil.T.A.,Chupradit.S., Suksatan.W., Ansari.M.J., Shewael.I.H., Valiev.G.H., Kianfar.E.(2021)**Nanomaterial by Sol-Gel Method: Synthesis and Application. Advances in Materials Science and Engineering, Volume 2021, Article ID 5102014, 2
- Chang Wei Zheng; Shu Ya Wu; Xiang Ming Chen; Kai Xin Song (2007).** Modification of MgAl₂O₄ Microwave Dielectric Ceramics by Zn Substitution.,90(5),1483–1486.

Chinnagurusamy, B., & Perumalsamy, M. (2021). Multiband microstrip patch antenna using copper nano radiating element for X band and C band applications. *International Journal of Numerical Modelling: Electronic Networks, Devices and Fields*.

DING.M; WEI.Z; LI.K; Wu.X; SHI.J; HAUNG.Sh (2020). Influence of Cr and Mn co-doping on the microstructure and optical properties of spinel structured $\text{Zn}_{0.95-x}\text{Cr}_{0.05}\text{Mn}_x\text{Al}_2\text{O}_4$ nanoparticles, *Journal of the Ceramic Society of Japan* 128 [11] 927-935.

Gurugubelli, T. R., Babu, B., & Yoo, K. (2021). Structural, Optical, and Magnetic Properties of Cobalt-Doped ZnAl_2O_4 Nanosheets Prepared by Hydrothermal Synthesis. *Energies*, 14(10), 2869.

Huang. Sh; Wei, Zhiqiang; Wu, Xiaojuan; Shi, Jiwen.(2020) Optical properties and theoretical study of Mn doped ZnAl_2O_4 nanoparticles with spinel structure. *Journal of Alloys and Compounds*, 154004

Hussain, Tanveer; Junaid, Muhammad; Atiq, Shahid; Abbas, Syed Kumail; Ramay, Shahid M.; Alrayes, Basel F.; Naseem, Shahzad. (2017) Tunable dielectric behaviour and energy band gap range of ZnAl_2O_4 ceramics mediated by Mg substitution. *Journal of Alloys and Compounds*, 724, 940–950.

Jia-Min Wu; Wen-Zhong Lu; Wen Lei; Xiao-Chuan Wang (2011). Preparation of ZnAl_2O_4 -based microwave dielectric ceramics and GPS antenna by aqueous gelcasting. , 46(9), 1485–1489.

Lopes Matias, J. A., Silva, I. B. T., Sousa, M. E. T., Oliveira, J. B. L., Morales, M. A., & da Silva, D. R. (2021). $(\text{Bi}_{13}\text{Co}_{11})\text{Co}_2\text{O}_{40}-\text{Co}_3\text{O}_4$ nanocomposites: Synthesis, characterization and application as substrate for microstrip patch antenna. *Ceramics International*.ceramint.2021.04.164

Mittal, N.(2015) Design analysis and fabrication of microstrip patch antennas for various applications using electromagnetic band gap and defected ground structures. Ph.D. thesis, Thapar University, Punjab, India.

Mukta, Ch., Rahman,M., and Islam.A.Z.M.T, (2021).Design of a Compact Circular Microstrip Patch antenna for WLAN applications, *International Journal on AdHoc Networking Systems (IJANS)* Vol. 11, No. 3.

Pandirengan, Thiruramanathan; Arumugam, Marikani; Durairaj, Madhavan; ThangaiyanadarSuyambulingam, Gokul Raja (2016). Development of performance-improved global positioning system (GPS) patch antenna based on sol-gel-synthesized dual-phase $(\text{Bi}_4\text{Ti}_3\text{O}_{12})_x-(\text{CaCu}_3\text{Ti}_4\text{O}_{12})_{1-x}$ composites. *Crystal Research and Technology*, 51(6), 366–379.

Rahman, Ashiqur; Islam, Mohammad Tariqul; Zulfakar, MohdSyafiq; Abdullah, Huda (2015). Synthesis and characterization of gahnite-based microwave dielectric ceramics (MDC) for microstrip antennas prepared by a sol–gel method. Journal of Sol-Gel Science and Technology, 74(2), 557–565.

Reem S. Khaleel, Mustafa Sh. Hashim, Samer Gh. Majeed. (2022) Synthesis of ZnO thin film by chemical spray pyrolysis using its nano powder. Kuwait J.Sci., Vol.49, No.(1).

Reem S. Khaleel, Mustafa Sh. Hashim. (2020) Fabrication of ZnO sensor to measure pressure, humidity and sense vapors at room temperature using the rapid breakdown anodization method, Kuwait J. Sci.47 (1) pp. 42-49.

R. S. Dubey, S. Srilali, Y. T. Ravikiran, G. Satheesh Babu and K. V. Katta (2022). Synthesis and characterization of Zn_{x-1}Al₂O₄(TiO₂)_x nanocomposite ceramics and their humidity sensing properties, J Mater Sci, Composites & nanocomposites.

Shang-Pan, Huang; Zhi-Qiang, Wei; Xiao-Juan, Wu; Ji-Wen, Shi (2020). Optical properties of Cr doped ZnAl₂O₄ nanoparticles with Spinel structure synthesized by hydrothermal method. Materials Research Express, 7(1), 015025.

Singh.S, Kumar.J.(2020). A Review Paper on Rectangular Microstrip Patch Antenna National Conference on Industry 4.0(NCI-4.0)

Vinnik, D. A., Zhivulin, V. E., Sherstyuk, D. P., Starikov, A. Y., Zezyulina, P. A., Gudkova, S. A., Trukhanov, A. V. (2021). Electromagnetic properties of zinc–nickel ferrites in the frequency range of 0.05–10 GHz. Materials Today Chemistry, 20, 100460.

Srilali Siragam, R.S.Dubey; Lakshman Pappula.(2022).Investigation of V₂O₅-ZnAl₂O₄ Composite Nanoparticles for C-band Microstrip Patch Antenna Applications, Kuwait Journal of Science, [10.48129/kjs.17783](https://doi.org/10.48129/kjs.17783)

Wang, Shi-Fa; Sun, Guang-Zhuang; Fang, Lei-Ming; Lei, Li; Xiang, Xia; Zu, Xiao-Tao (2015). A comparative study of ZnAl₂O₄ nanoparticles synthesized from different aluminum salts for use as fluorescence materials. Scientific Reports, 5, 12849.

Submitted: 19/12/2021

Revised: 15/03/2022

Accepted: 20/03/2022

DOI : 10.48129/kjs.17809

Newtonian hydro-thermal fluid flow phenomena through a sudden expansion channel with or without baffles

Sandip Saha¹, Pankaj Biswas¹, Kanishka Jha², Apurba Narayan Das³, Rajesh Choudhary^{4,*}

¹*Dept. of Mathematics, National Institute of Technology Silchar,
Silchar-788010, Assam, India*

²*Dept. of Mechanical Engineering, Lovely Professional University,
Jalandhar-144001, Punjab, India*

³*Dept. of Mathematics, Alipurduar University, Alipurduar-736121,
West Bengal, India*

⁴*Dept. of Mechanical Engineering, Sardar Vallabhbhai National Institute of Technology
Surat, Surat-395007, Gujrat, India*

**Corresponding author : rchoudhary@med.svnit.ac.in*

Abstract

This work aims to study the different characteristics of Newtonian fluid flow and heat transfer through a 1:3 sudden expansion channel with or without plane baffles using the finite volume method. The flow is assumed viscous, incompressible, steady, and laminar. The different characteristics of hydro-thermal fluid flow phenomena have been studied for $Re \in [0.1 - 200]$ to demonstrate the influence of the presence of baffles. The profiles of velocity, pressure, skin friction coefficient, friction factor, average Nusselt number, and pumping power have been examined for both the cases of the presence and absence of baffles. It has been observed that the hydro-thermal characteristics become more pronounced with the increase in the number of baffles. In the case of three baffles of equal length, at $Re = 200$ it is calculated that if the thickness of the baffles is same and equal to 10% of the length, then the value of Nu_{av} becomes approximately 1.2 times of that in the absence of baffle. For the same value of Re , it has been found that for the presence of one baffle of length equal to the width of the inlet section of the channel and of thickness 10% of the same, the value of Nu_{av} becomes 1.11 times of that in the absence of baffle, while in the case of three baffles of equal length and of equal thickness like the above mentioned case of one baffle, the value of Nu_{av} becomes 1.25 times of that in absence of baffle. It has also been revealed that the enhancement of thermal phenomena increases with the increase in the baffle's height.

Keywords: Baffles; newtonian fluid flow;nusselt number; pumping power; reynolds number.

NOMENCLATURE

C_p	average pressure coefficients	u_0	average velocity
c_p	specific heat capacity	ρ	density (kg/m ³)

$C_f = \frac{2 \tau_w}{\rho u_0^2}$	local skin friction coefficient	$\eta = \frac{\mu}{\rho}$	kinematic viscosity
$d_1, d_2, d_3, d_4,$ d_5, d_6, d_7	baffle distance baffle or baffles thickness	$Nu = \frac{hL}{k_f}$	local Nusselt number
$ER = \frac{L_d}{L_u}$	expansion ratio	$Nu_{av} = \frac{1}{L} \int Nu dx$	average Nusselt number
$f = \frac{2\Delta p L_d}{L \rho u_0^2}$	friction factor	Δp	absolute pressure drop (Pa) = $ (p_2 - p_1) $
h_i	corner vortex length	$P_p = u_0 \Delta p L_u$	pumping Power
h_u	upstream channel length	τ_w	wall shear stress
h	heat transfer coefficient	Re_{crit}	critical Reynolds number
h_1, h_2, h_3	baffle height	$Re = \frac{u_0 L_u \rho}{\mu}$	Reynolds number
k_f	thermal conductivity (W/mK)	$S_i (i = 1, 2, 3, 4) = \frac{h_i}{L_u}$	normalized vortex length
L	downstream channel length	N	power law index
L_d	width of the channel at the outlet	$\frac{x}{h_u}$	normalize location
L_p	lower side wall width	x_1	location of generating plane
L_u	width of the channel at the inlet	u, v	velocity components along x and y directions
N_e	total number of elements	x, y	Cartesian coordinates
p	pressure (Pa)		
p_1, p_2	pressure at the inlet and outlet sections		
T	temperature (K)		

1. Introduction

Nowadays, researchers are highly engaged in studying the thermo-physical behaviour of fluid flow in different equipment's, which has made significant progress in many engineering fields [Arani *et al.*, (2017); Rahmati *et al.*, (2017); Saha *et al.*, (2023)]. Sudden expansion is a well-known problem in which the flow is expanded in an abrupt way [Karimipour *et al.*, (2015); Akbari *et al.*, 2016a, Akbari *et al.*, 2016b; Saha & Das, 2021)]. With the increase

in Re , many authors, experimentally and numerically, demonstrated that two or more flow separation zones exist at the lower and upper corner walls [Cherdron *et al.*, (1974); Mukhambetiyar *et al.*, (2017)]. The works on sudden expansion channels are essential in various industries, including conversion of energy, electronic cooling equipment, mixing vessels, heat exchangers, environmental control, and chemical manufacturing [Safaei *et al.*, (2014); Al-Ashhab (2019); Torres *et al.*, (2020); Quadros *et al.*, (2020); AL-Jawary (2020); Saha, 2021a, Saha ,2021b] as vortices appear after the backward-facing step and results in considerable heat loss. Therefore, it is important to understand the basic phenomenon of flow characteristics and enhancement of heat transfer through a sudden expansion channel.

Durst *et al.*, (1974) experimentally investigated the Newtonian fluid flow phenomena in a suddenly expanded channel. They stated that flow becomes asymmetric (existence of two corner vortices of different lengths) at $Re > 56$. In a sudden expansion channel, Fearn *et al.*, (1990) experimentally and numerically showed the flow symmetry, after a certain value of Re , losses its stability. Using linear stability analysis, Shapira *et al.*, (1990) studied the flow bifurcation in an expansion channel for different values of ER. They also stated that the flow losses its stability when $Re > Re_{crit}$. To investigate the influence of ER on asymmetric states, Battaglia *et al.*, (1997) conducted linear stability analysis and steady flow simulations. To determine the bifurcation point, they used bifurcation theory and stated an inverse relationship between ER and Re_{crit} . Alleborn *et al.*, (1997) also studied the linear stability analysis to clarify the effect of ER and the characteristics of flow bifurcation phenomena. Using the continuation method, the steady-state bifurcation diagrams were presented for higher values of Re . Drikakis (1997) employed various discretization schemes up to fourth order for the simulations of steady-state bifurcation characteristics in a sudden expansion channel. To compute the value of Re_{crit} , they showed that third and fourth-order finite difference schemes are very much effective. Moreover, they observed that the value of Re_{crit} decreases with the increase of ER. Soong *et al.*, (1998) numerically studied the laminar flow in a sudden expansion channel for asymmetric flow conditions and flow instability. In a two-dimensional case, complex flow patterns were identified, which are associated with unsteady and periodic solutions for large values of Re . In a sudden expansion channel, Hammed *et al.*, (1999) investigated the laminar flow by real-time digital particle image velocimetry (PIV). For different values of Re , they presented the velocity contours to observe the flow characteristics and concluded that the length of vortex varies linearly with the increase in Re . In a suddenly expanded channel, Pinho *et al.*, (2003) investigated the pressure drop characteristics of shear-thinning laminar power-law fluids. They revealed that in the expanded section, the profile of velocity becomes parabolic for small values of Re . In a backward-facing step channel, Oder *et al.*, (2003) studied different phenomena of thermal characteristics for different values of Pr. Thiruvengadam *et al.*, (2005) studied the flow bifurcation and heat transfer characteristics in a symmetric sudden expansion channel. They found that the values of C_f and Nu_{av} were influenced significantly due to the increase in the values of Re . In 2009, Ternik studied the transition of generalized Newtonian fluids over a sudden expansion channel. They found that the increase in the values of n causes increase in recirculation length and Re_{crit} . Ternik (2010) solved the problem of the laminar flow for a wide range of Re through a 1:3 suddenly expanded channel in two-dimension. Considering

power-law index in the range 0.60 to 1.40, they obtained the recirculation length and Couette correction for power-law fluids ($n < 1$ and $n > 1$), and reported that the reattachment and detachment points are influenced by non-Newtonian viscous behaviour. In addition, for $n < 1$, they showed that the increase in the values of n causes increase in the vortex length. However, for $n > 1$, they established a linear relationship between reattachment length and the values of Re . With porous wall, Terekhov & Terekhov, 2017 numerically investigated the thermo-hydraulic phenomena of fluid flow over a backward facing channel. With or without porous block, Galuppo *et al.*, (2017) examined the turbulent flow and the thermal phenomena through a backward expansion channel. They suggested that a porous obstacle beyond the back step can be used to prevent the unexpected rise in the Nu , which is not suitable for some practical applications. Experimentally, Dyachenko *et al.*, (2019) investigated the propagation of static pressure, and the transfer of heat in the separation region formed behind the backward-facing step of a channel. They revealed that the positions of vortex generators are critical parameters that can enhance the rate of heat transfer. They have shown that the rate of heat transfer enhances, when the vortex is generated in the upstream of the channel. Chai & Song, 2019 studied the temporal stability in both the stream wise and span wise slip channels. They stated that critical values of Re are influenced by the stream wise slip and decreased by the span wise slip and concluded that flow is greatly stabilized when equal slips are placed in both the directions.

How the flow dynamics and heat transfer characteristics are affected by the presence of different forms of baffle other than rectangular one can be studied after going through this work. This work can also be generalized by taking other forms of channel embedded with baffles. The simulation results of these models can be compared with those of the case of a channel without baffle to study the effect of the presence of baffles on the flow in the channel.

The dynamics of fluid flow via a sudden expansion channel are of practical and basic interests for having numerous applications in medical research, engineering, and manufacturing processes such as electronic cooling equipment, mixing vessels, and heat exchangers. The most frequent geometry used in heat exchangers is banks of tubes, which may be found in various industrial operations including the nuclear industry. Cross flow through the banks is achieved in shell-and-tube heat exchangers by baffle plates, which are responsible for changing the direction of the flow and increases the heat exchange time between the fluid and the heated surfaces.

Till now, most of the researchers have solved problems on sudden expansion channel considering the variations in the values of ER and n . In addition, it is clear that most of the works are limited to the study of fluid flow characteristics. Only a few works have been performed on both the fluid flow and heat transfer characteristics. From the above literature survey, it has been clear that the effect of the presence of baffles on hydro-thermal flow characteristics through a sudden expansion channel has not been considered so far. This work is an extension of the study of Ternik *et al.*, (2006). They studied the evolution of two-dimensional, viscous, power-law fluid flow phenomena without considering heat transfer phenomena, and the effect of the presence of baffles. In this work, we have demonstrated the effect of baffles on different characteristics of thermo-hydraulic Newtonian fluid flow

phenomena. The variations of different heat transfer characteristics of Newtonian fluid flow have been presented in the form of graphs with the variations in baffle thickness and height for different values of Re.

2. Flow geometry

Two-dimensional computational flow geometry [Ternik *et al.*, (2006)] in a symmetric sudden expansion channel in presence or absence of plane baffles have been illustrated schematically in figures 1(a-b), which is divided into three sections viz., inlet, wall and outlet sections. Flow geometry is prescribed in a Cartesian coordinate system x, y for $ER = 3$. Two-dimensional laminar flow in a sudden expansion channel exhibits clearly a flow transition from symmetric to asymmetric as the value of Re increases. Fluid flow boundary conditions have been taken as per the studies of Ternik *et al.*, (2006) and the thermal boundary conditions have been chosen from the work of Nasiruddin *et al.*, (2006).

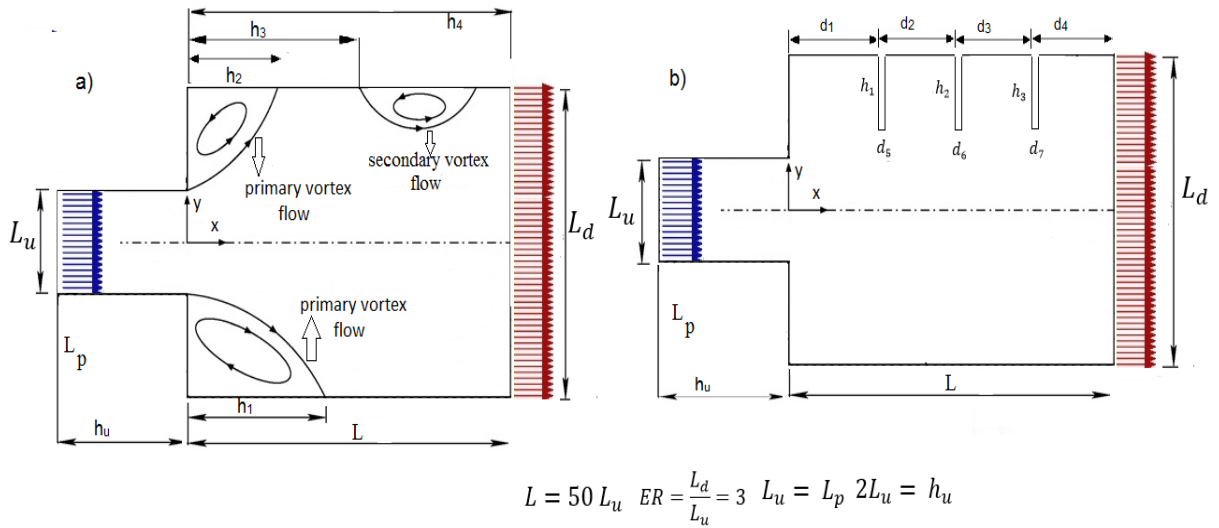


Fig. 1. Schematic diagram in (a) absence of baffles, (b) presence of three baffles where, $d_1 = d_2 = d_3 = d_4$.

3. Formulations

Newtonian fluid flow in a sudden expansion channel is associated with the following equations [Saha *et al.*, 2020; Saha *et al.*, 2022]:

Equation of continuity:

$$\nabla \cdot \mathbf{R} = 0 \quad (1)$$

Equation of x-momentum:

$$(\mathbf{R} \cdot \nabla) \mathbf{u} = \eta \nabla^2 \mathbf{u} - \frac{1}{\rho} p_x \quad (2)$$

Equation of y-momentum:

$$(\mathbf{R} \cdot \nabla) \mathbf{v} = \eta \nabla^2 \mathbf{u} - \frac{1}{\rho} p_y \quad (3)$$

Energy equation:

$$(\mathbf{R} \cdot \nabla) T = \frac{k_f}{\rho c_p} \nabla^2 T \quad (4)$$

With $\mathbf{R} = (u, v)$ and $\nabla = i \frac{\partial}{\partial x} + j \frac{\partial}{\partial y}$.

3.1 Boundary Condition

- i)/ Inlet section: For $x/L_u = -2$ and $-0.5 < y/L_u < 0.5$, at the inlet section, inflow velocity ($u = u_0$) has been imposed, with $u_0 \in [0-0.178]$ m/s and $0 \leq Re \leq 200$. At the channel inlet, the temperature of the working fluid has been set at 27° .
- ii)/ Outlet section: For $x/L_u = 50$, an outflow boundary condition (all flow properties have zero gradients, and the flow is normal to outflow surface) has been applied in the outlet section.
- iii)/ Wall sections: At the channel walls, no-slip ($u_x = 0, v_x = 0$) and no-penetration ($u_y = 0, v_y = 0$) boundary conditions are assumed, to mean that fluid flows steadily through the channel. The no-slip condition for viscous fluids represents that the fluid has no velocity relative to the boundary. Arbitrarily, the walls of the computational domain have been kept at 102°C .

3.2. Computational Procedures, Grid Study, and Validation of Code

Ansys Fluent has been used for simulation and visualization purposes. All the variables defined at the centre of the control volume populating the physical domain have been considered, when solving the governing equations using FVM [Youcef *et. al.*, 2019, Youcef & Saim 2021)]. Each equation is integrated over each control volume to provide a discrete equation that links the variable at the volume's centre to its neighbours. Despite some compelling features of the finite volume method (e.g., the resulting solution satisfies the conservation of quantities such as mass, momentum, and so on), lower order interpolation of the convective terms in the governing equations causes different unwanted numerical effects (e.g., artificial diffusion). To avoid those, the QUICK scheme [Leonard's (1979)] has been utilized for spatial discretization of convective terms in a momentum equation. It is an upwind scheme (two upstream points and one downstream point) that is accurate up to 3rd order for advection terms but up to 2nd order for all other terms (diffusion terms). SIMPLEC algorithm [van Doormaal *et al.*, (1984); Ternik *et al.*, (2006)] resolves the coupling between velocity and pressure. The convergence criteria have been set as 10^{-6} , 10^{-6} , and 10^{-9} for continuity, momentum, and energy equations respectively.

At $Re=60$, the grid test has been performed for both the cases of smooth channel and the baffled channel to study the effect of mesh size [illustrated in figures. 2(a-b)]. To find a numerical solution through discretization of the governing differential equation, the solution is dependent on the number of grid points. Generally, when we increase the number of grid

points, the solution becomes accurate, but main problem is that to what extent we should increase this number of grid point. When our solution does not change with the change in the number of grid points, we select that very number of cells to continue, which means after a certain number of cells, the trend of graph become linear. For smooth channel, we start our calculation with 15,000 number of cells. It has been found that if the number of cells is greater than 15,000, the value of C_p increases continuously, but the graph of C_p becomes linear (marked by circle in the graph), when the number of cells exceeds 60,820. In addition, for 60,820 number of cells and 240,000 number of cells, the solutions are same, it means 60,820 number of cells are optimum for the solution and the solution is not going to change further with the

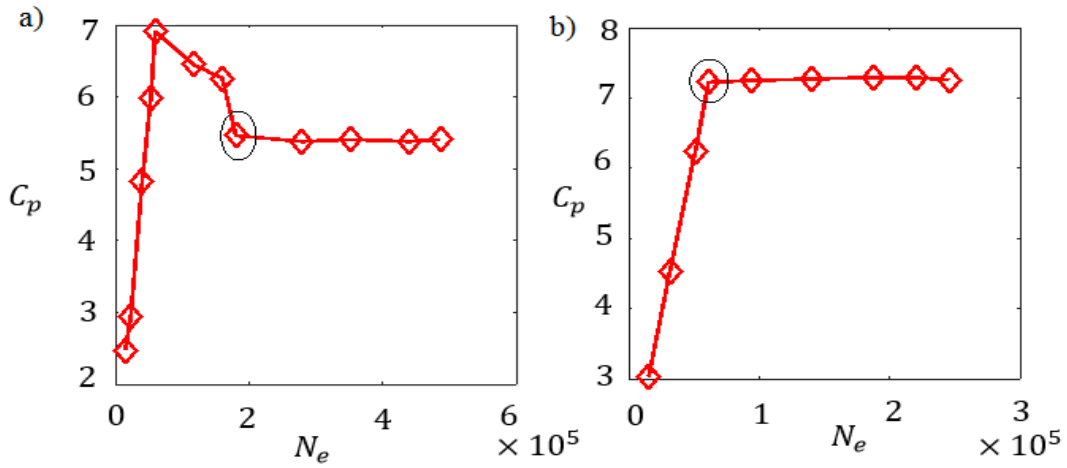


Fig. 2. At $Re = 60$, variations of C_p vs. N_e for (a) no baffle, (b) three baffles cases.

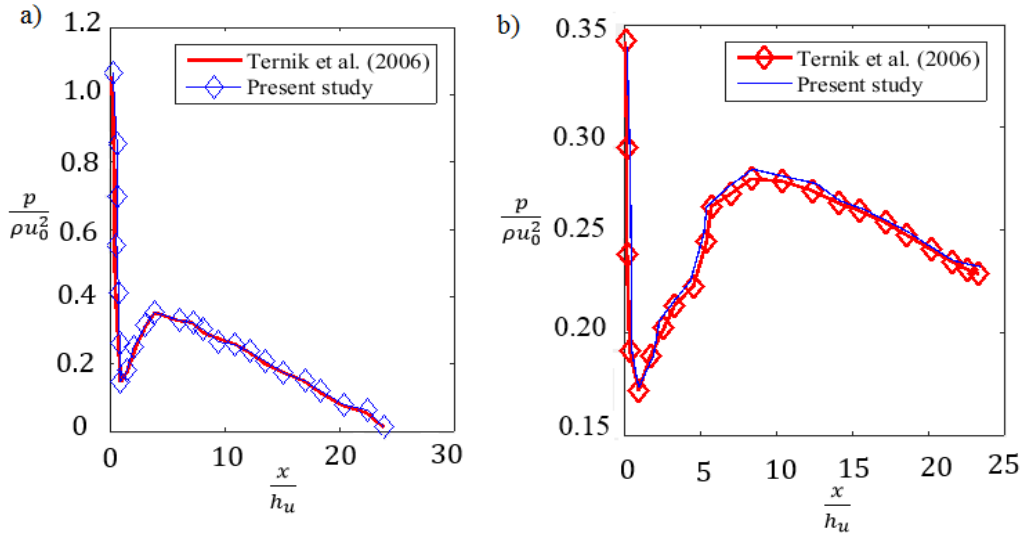


Fig. 3. Plots of $\frac{p}{\rho u_0^2}$ vs. $\frac{x}{h_u}$ at (a) $Re = 50$, (b) $Re = 100$ along the centerline.

increase in the number of grid points. So 60,820 number of cells are optimum grid points [figure. 2(a)] for our solution. Again, for a channel with three baffles, we start our calculation with 15,000 number of cells. It has been found that when the number of cells are greater than 15,000, the value of C_p increases continuously, but if the number cells exceeds 172, 680, the graph of C_p become linear (marked by circle in the graph). Also, further increase in the value

of the number of cells up to 496, 888, the same linear trend has been observed. So 172, 680 number of cells are optimum grid points [figure. 2(b)] for our solution. The code validation has been done with the studies of Ternik *et al.*, (2006) by comparing the results of normalized pressure profile at $Re = 60$ [figure. 3(a)] and $Re = 100$ [figure. 3(b)], which shows a good agreement [figures. 3(a-b)] of those with the present models and provides us enough confidence to carry forward the present work. The table 1 show the % error between the present study and the work of Ternik *et al.*, (2006). The whole computation has been segregated into two different parts with the aid of fine mesh as shown in figure. 4.

Table 1. % error of Ternik *et al.* (2006) and Present study at $Re = 100$

	Ternik <i>et al.</i> (2006)	Present study	
$\frac{x}{h_u}$	$\frac{p}{\rho u_0^2}$	$\frac{p}{\rho u_0^2}$	% error = $\frac{ \text{Ternik } et al. (2006) - \text{Present study} }{\text{Present study}} \times 100$
0.097276	0.342043	0.342101	0.01693
0.194553	0.238183	0.237989	0.08132
1.750973	0.188741	0.188751	0.00498
4.571984	0.222694	0.22251	0.08270
8.365759	0.27481	0.275453	0.23353
17.2179	0.253498	0.253593	0.03733
22.56809	0.23081	0.230853	0.01871
Total % error = 0.39			

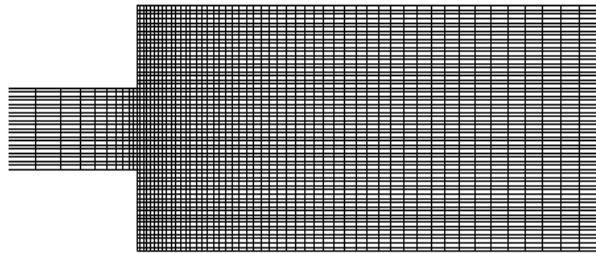


Fig. 4. Mesh geometry in absence of baffles.

4. Results and Discussions

This section describes the influence of the absence and presence of baffles on different characteristics of hydro-thermal flow phenomena with the variations in baffles height, thickness and Re .

4.1./Effect of Presence or Absence of Baffles

Velocity streamlines have been shown in figures. 5(a-d) for different values of Re in the case of smooth channel. When the flow passes through the channel expansion, with the increase in inlet velocity, some vortices arise in the low-pressure regions [figures. 5(a-d)]. In addition,

the vortices are strengthened with the increase in the inlet velocity, and those move towards the outlet of the channel. It is seen that indistinguishable equal corner vortices exist at $Re = 0.99$. It is also found that as Re is increased to 30, the vortices in both the corners are increased in size. Many authors [Samingue *et al.*, (2010); Quadros *et al.*, (2019)] stated that if Re exceeds Re_{crit} , the flow loses its symmetry (i.e., flow bifurcation starts) and reaches its asymmetric state. But it is to be mentioned that for non-zero values of Re , the flow never be symmetric, and this is observed more clearly if Re exceeds Re_{crit} as the flow lost its symmetry highly then [as can be seen in figures. 5(c-d) and figure. 6]. For creeping flow [figure. 5(a)], fluid flow starts to deviate from the axial position, $x = -2h_u$, before the expansion plane. In figure. 6, it is found that for $Re \in [0.1 - 59.8]$, the length of the corner vortices at the lower and upper walls are almost equal. At $Re = 0.99$, two vortices are found at each of the corner walls, see figure. 5(a). In figure. 6, it is found that for $Re \in [0.1 - 59.8]$ corner vortices are developed linearly. However, for $Re > 59.8$, the size of one corner vortex starts to increase, while that of other corner vortex starts to decrease showing that the symmetry of flow changes into a stable asymmetric flow [figures. 5(c-d)]. With the increase in Re , more than two separate zones are found at the channel walls, as shown in figures. 5(c-d). The figure. 7 represents the influence of no baffle [figure. 7(a)], presence of one baffle [figure. 7(b)], two baffles [figure. 7(c)] and three baffles [figure. 7(d)] on the vortex flow patterns. The flow separation causes a recirculation zone in the downstream of the baffles, as the baffles prevent the boundary layer development. As a consequence, the number of vortices as well as the length of the vortices increase. It found in the figures. 7(a-d) that the velocity streamlines become slightly pronounced for the presence of baffles. In addition, it has also been observed that vortices arise in the base of the baffles.

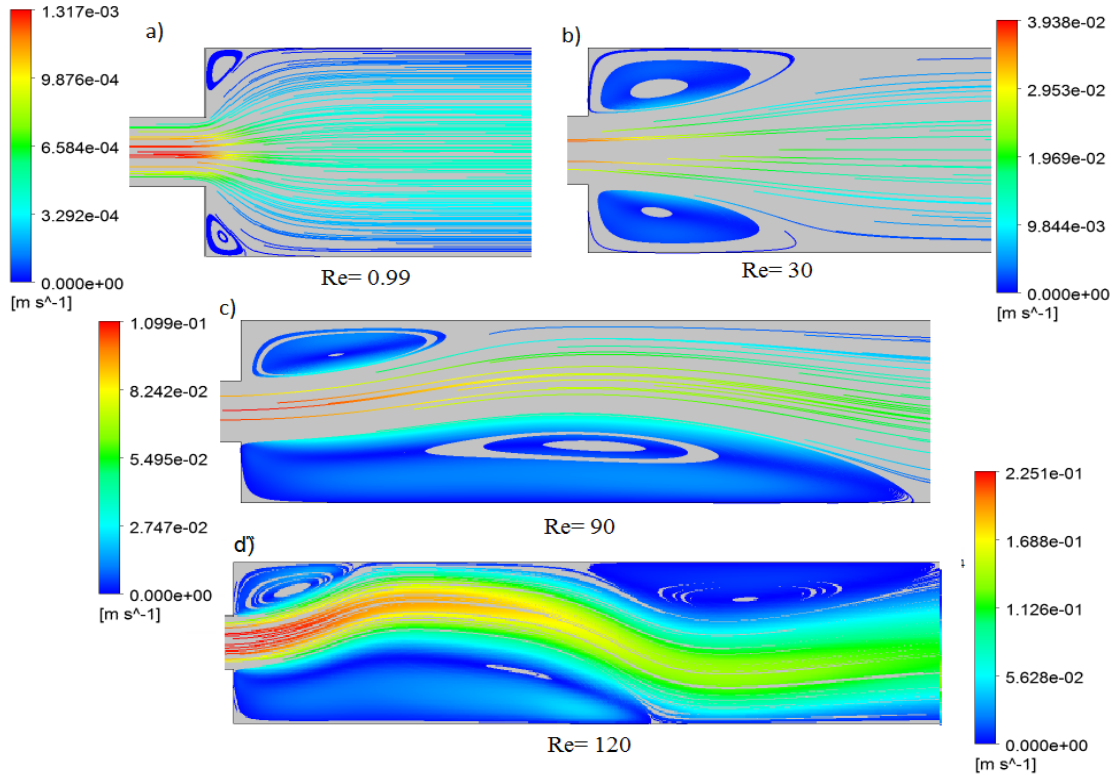


Fig. 5. Velocity streamlines for various Re in absence of baffles.

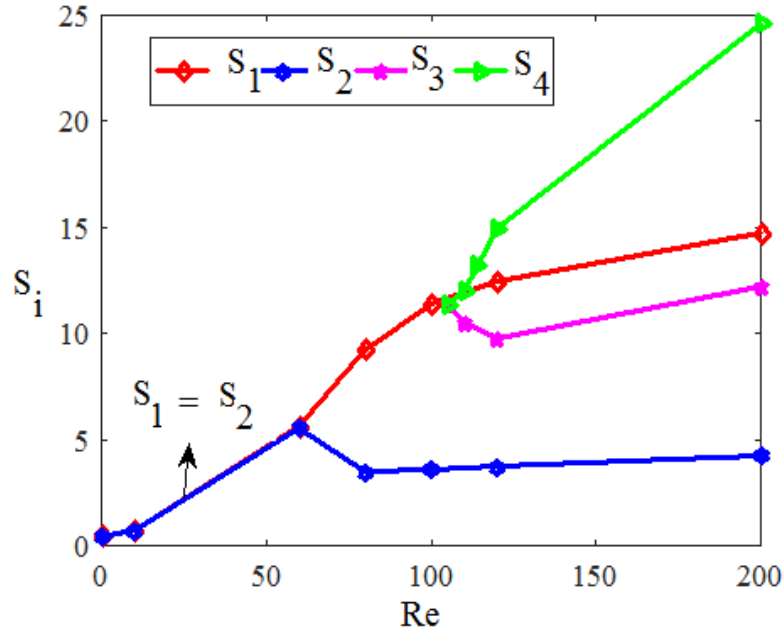


Fig. 6. Variations of normalized vortex length for various Re in absence of baffles.

Moreover, it is found that the number of vortices increases with the increase in the number of baffles in the upper wall of the channel, as expected [figure. 7]. The profile of the temperature contours have been shown in figures. 8(a-d) at $Re = 90$ in the cases of no baffle [figure. 8(a)], presence of one baffle [figure. 8(b)], two baffles [figure. 8(c)] and three baffles [figure. 8(d)]. As expected, the rate of heat transfer increases due to the increase in the length of the vortices. As represented in figures. 8(a-d), there is barely a little difference in temperature among those cases, except near the baffles.

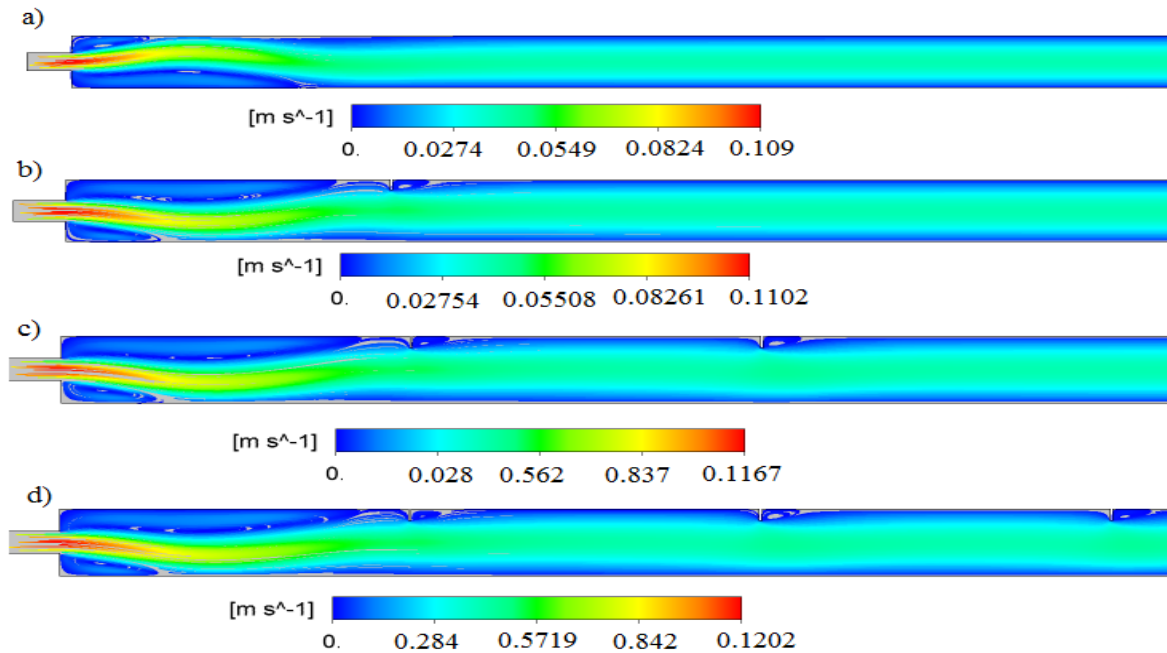


Fig. 7. Velocity streamlines for $Re = 90$ in case of absence of baffles (a), presence of one baffle (b), two baffles (c) and three baffles, where $h_1 = h_2 = h_3 = \frac{L_u}{2}$, and $d_5 = d_6 = d_7$.

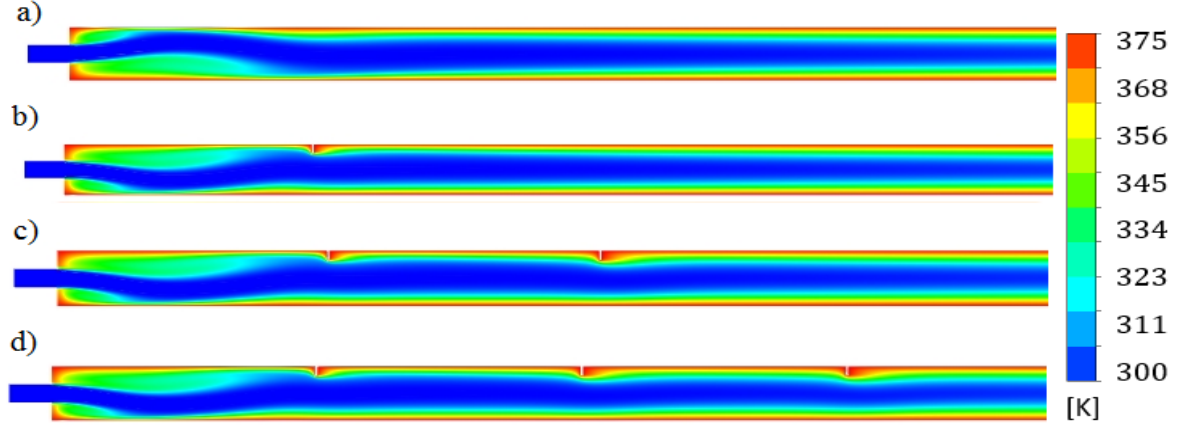


Fig. 8. Temperature profiles for $Re = 90$ in case of (a) absence of baffles, presence of (b) one baffle, (c) two baffles and (d) three baffles, where $h_1 = h_2 = h_3 = \frac{L_u}{2}$, and $d_5 = d_6 = d_7$.

In the absence of baffles, the figure. 9(a) presents the velocity distribution along the centreline for different values of Re . We also note that fluid flow experiences a significant decrease due to the sudden expansion after the expansion zone. Velocity overshoot is observed at the downstream of the expansion portion for higher values of Re . It is found that velocity overshoot remains complicated and diminishes slowly with the increase in Re . At different locations of the downstream section, the centreline velocity distribution is characterized by a monotonic approach of fully developed flow conditions. The figure. 9(b) shows the pressure distribution, which follows the flow velocity profile along the centreline. With the increase in Re , the pressure attains its maximum value at the entrance of the downstream section, and afterward, it gradually decreases as the flow proceeds towards the outlet

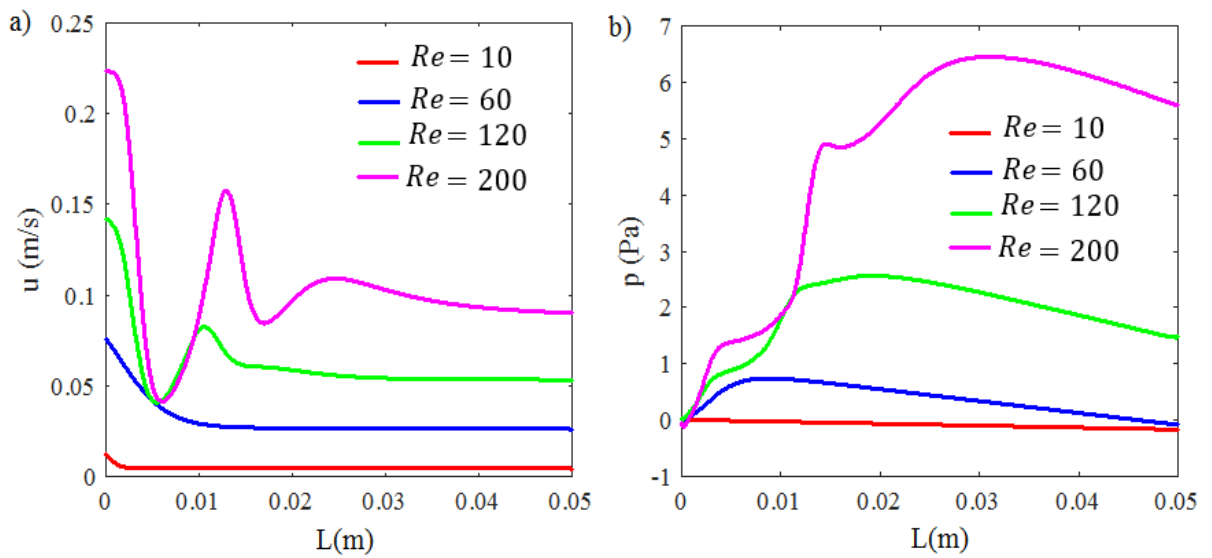


Fig. 9. Plots of (a) velocity and (b) static pressure profiles at various Re in absence of baffles.

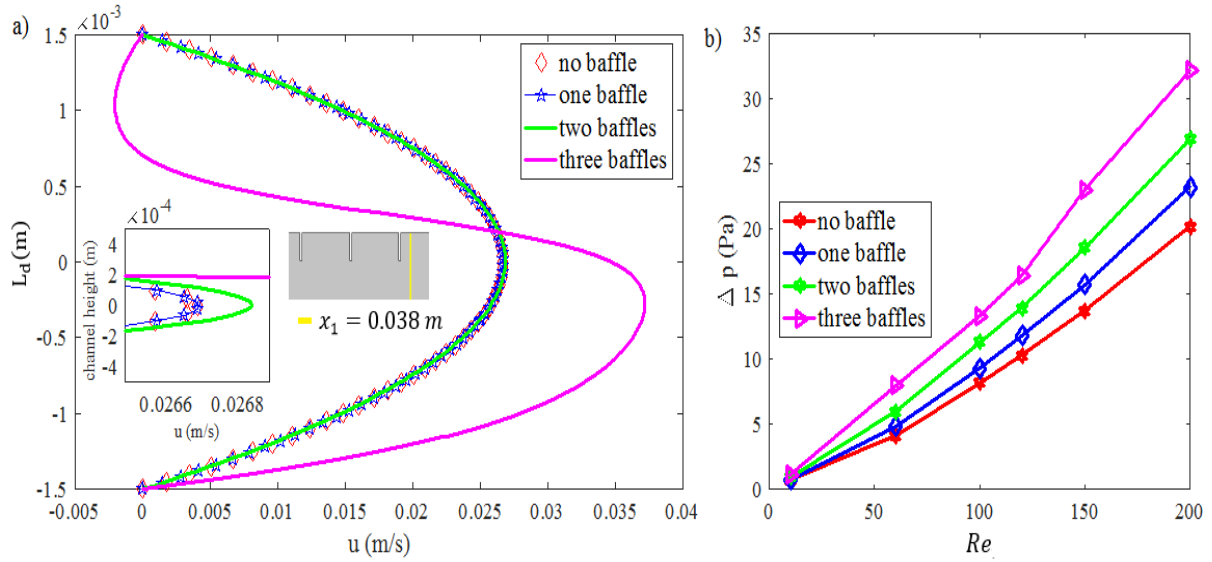


Fig. 10. Plots of (a) velocity profiles at $Re = 60$, $x_1 = 0.038$ m and variations of (b) Δp at various Re .

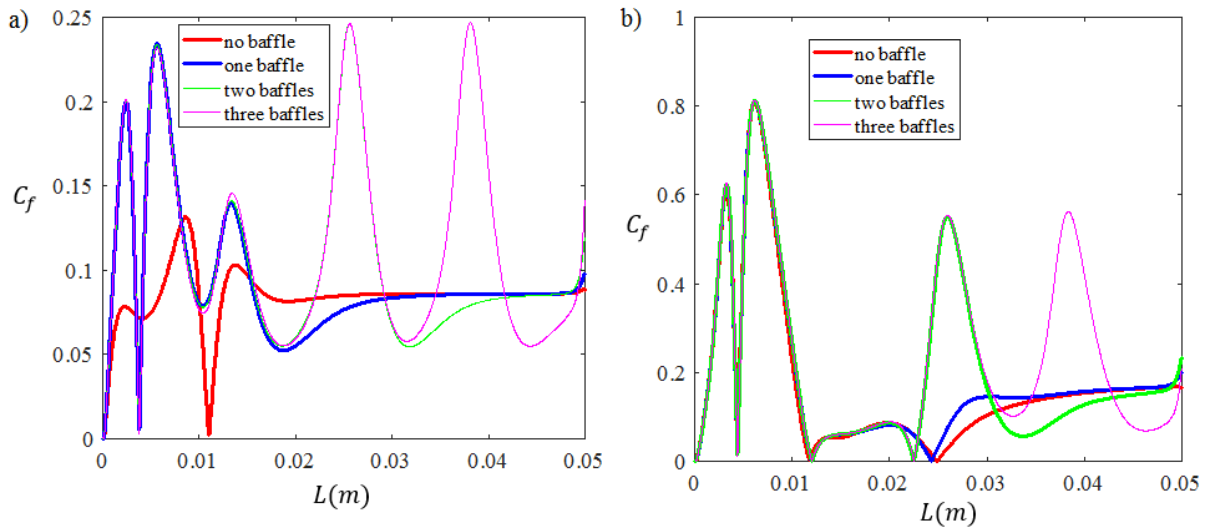


Fig. 11. Profiles of C_f at (a) $Re = 100$ and (b) 200 for various cases.

section of the channel. Secondary vortex flow [figure. 5(d)] has a remarkable effect on the centreline velocity for the Newtonian fluid flow and the first peak in the velocity, which appeared for $Re > 120$, causes the existence of primary vortex flow [figure. 9(a)]. Moreover, it is found that the second peak of the velocity is much smaller than the first one because the fluid flow gradually approaches the fully developed flow conditions. At higher values of Re , the variation of pressure distribution remains complex and causes the existence of different lengths of vortices at the lower and upper corner walls [figure. 9(b)]. At $Re = 60$ and $x_1 = 0.038$ m, the figure. 10(a) presents the variation of velocity plots. It is observed that the velocity becomes more pronounced as the number of baffles in the channel increases. At $x_1 = 0.038$ m and for the presence of three baffles, velocity profiles become more pronounced and of different trends because near the third baffle, the velocity increases after

hitting the baffle. The location of the generating plane (x_1) = 0.038 m is far away from the locations of first and second baffles. However, the location of the generating plane, x_1 = 0.038 m is much closed to the location of third baffle. For the third baffle and at x_1 = 0.038 m, different trends of velocity profile (wavy shape) is observed. This is happened as after hitting the tip of the third baffle, the flow changes its behaviour for which it looks like band wave shape and after hitting the baffle, the flow moves faster with high velocity towards the outlet of the channel.

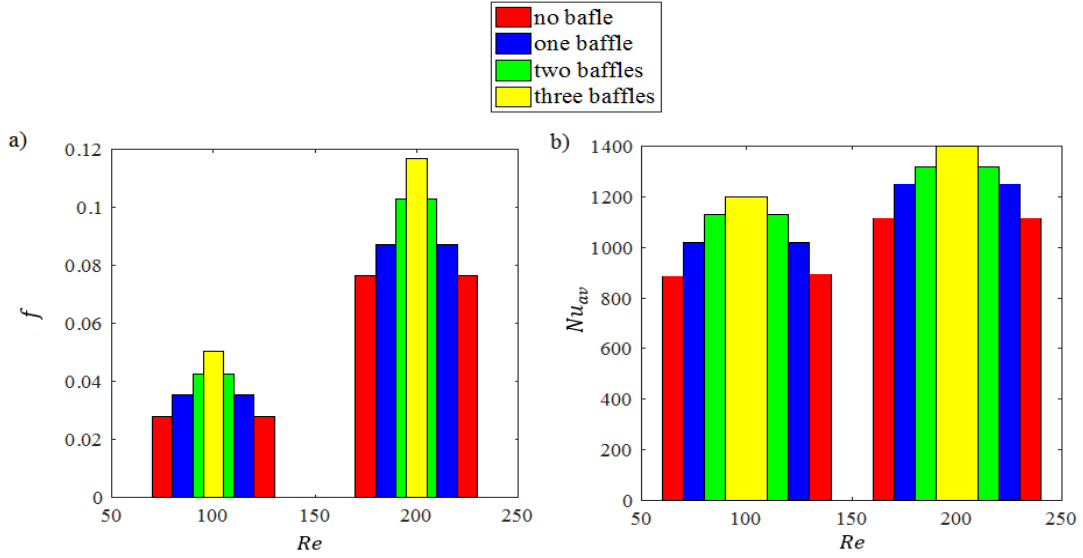


Fig. 12. Variations of (a) f , (b) Nu_{av} at various Re .

The plots of Δp have been presented for the cases of no baffle, one baffle, two baffles, and three baffles [figure. 10(b)]. It has been found that the value of Δp increases with the increase in the number of baffles and Re . It has also been revealed that the baffles interrupt the development of the boundary layer, which causes the existence of vortices near the baffles. Furthermore, at $Re = 200$ and in the case of presence of three baffles, it has also been found that value of Δp become 1.59 times of that of the case of smooth channel. For different values of Re , the figure. 11 depicts the plot of C_f in both the cases of no baffle and the presence of baffles. It has been found that the curve of C_f shows a nonlinear character at higher values of Re . It has also been found that the values of C_f become higher as compared to the case of no baffle [figures. 11(a-b)]. For different values of Re , the variation in f in the presence or absence of baffles has been presented in the figure. 12(a). In presence of baffles, it has been studied that an increase of the length of vortices causes the decreases of the values of f .

Due to the increase in Δp , it has also been demonstrated that the trend of f becomes more significant in the presence of three baffles as compared to no baffle and one baffle cases [figure. 12(a)]. It is also investigated that the value of f remains higher at the higher values of Re because fluid with high velocity remains in contact with the surface walls completely. Furthermore, the C_f curve diminishes with the increase of Re as the fluid does not remain in contact completely with the channel walls. For different cases of the presence of the baffles, the variation in Re with the variations in Nu_{av} are shown in the figure. 12(b).

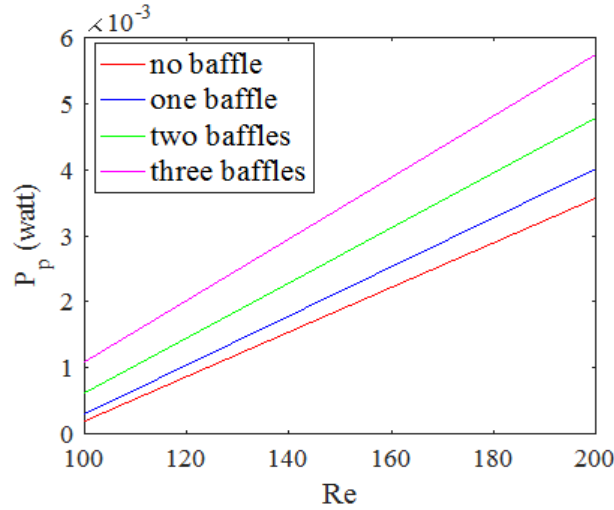


Fig. 13. Plot of P_p for various Re .

It has been found that the value of the Nu_{av} increases when the number of baffles increases. It is also evident that an increase of Re causes the increase in the values of Nu_{av} . At $Re = 200$, it has been found that in the case of one baffle ($h_1 = L_u, d_5 = 0.1 L_u$), Nu_{av} becomes 1.11 times of that of the no baffle case, while in the case of three baffles ($h_1 = h_2 = h_3 = L_u, d_5 = d_6 = d_7 = 0.1 L_u$), Nu_{av} becomes 1.25 times of that of the no baffle case. The figure. 13 presents the pumping power for different values of Re in the presence or absence of baffles. Strong pumps are required to obtain the suitable fluid velocity, and it is revealed that in the case of three baffles, 1.66 times pumping power is needed than the case of no baffle.

4.2./Effect of Baffles Thickness and Height

For various Re , the figures. 14 (a-b) show the effect of baffles thickness on heat transfer characteristics such as f and Nu_{av} . It is observed that an increase in thickness from $0.05 h_1$ to $0.1 h_1$, induces a decrease in the recirculation length, which causes an increase in the value of f . Therefore, an increase in mixing causes the increase of Nu_{av} . It has been found that the value of f increases with the increase in the number of baffles, as shown in the figure. 14(a). Moreover, an increase in the pressure drop causes decrease in the fluid momentum; consequently, fluid encounters the upper wall. For baffles thickness, $d_5 = d_6 = d_7 = 0.05 h_1$ and $d_5 = d_6 = d_7 = 0.1 h_1$, variation of Nu_{av} with Re along with the lower wall has been shown in the figure. 14(b). Heat transfer augmentation is found with the increase in baffles thickness; therefore, baffle thickness plays a crucial role in the thermal flow parameters. At $Re = 200$, it is calculated that when $d_5 = d_6 = d_7 = 0.1 h_1$ then the value of Nu_{av} becomes approximately 1.04 times of that for the case, $d_5 = d_6 = d_7 = 0.05 h_1$. Along the lower wall, variations in Nu_{av} and f have been shown in the figures. 15(a-b) for different values of Re . It is revealed that an increase in the baffle height induces increase in the vortex length, which causes increase in the values of f and Nu_{av} . Furthermore, for baffle height, $h_1 = h_2 = h_3 = 1.3 L_u$, it has been found that the value of Nu_{av} becomes approximately 1.28 times and 1.066 times of that of the smooth channel and for $h_1 = h_2 =$

$h_3 = L_u$. Therefore, from the figures. (14-15), it has been concluded that enhancement of heat transfer becomes more pronounced with the variation in baffles height than with the variation in baffles thickness as due to increase in the baffle thickness, fluid remains at its tip and chance to contact its base reduces. However, if the height of baffle increases, fluid flows directly towards the nearby base of the baffle.

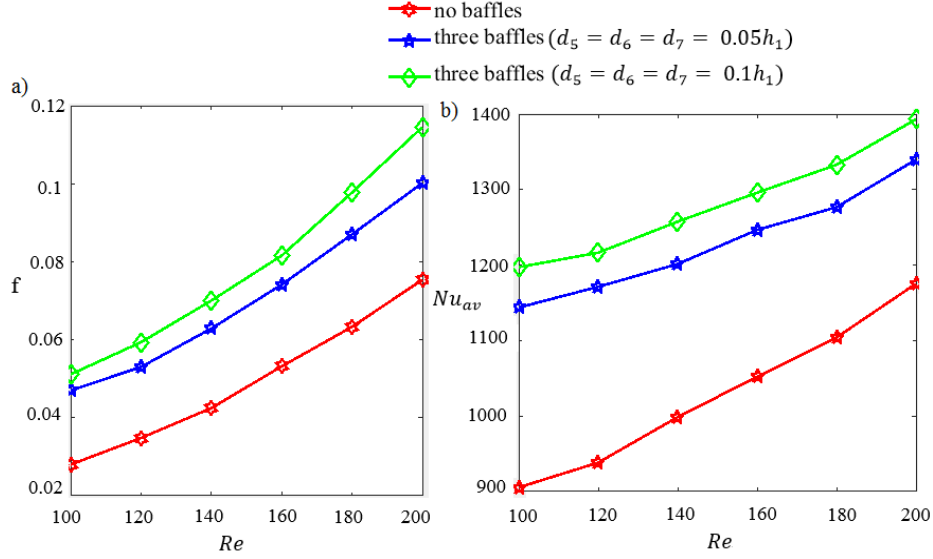


Fig. 14. Variations of (a) f , (b) Nu_{av} at various Re , where, $h_1 = h_2 = h_3 = L_u$.

5. Conclusions

Problem of flow bifurcation transition and heat transfer characteristics through a 1:3 sudden expansion channel in the presence and absence of plane baffles has been solved numerically. Effect of the variation in the values of Re on recirculation characteristics and velocity profiles of viscous, steady, incompressible, and laminar flow have been studied. Simulated results associated with the

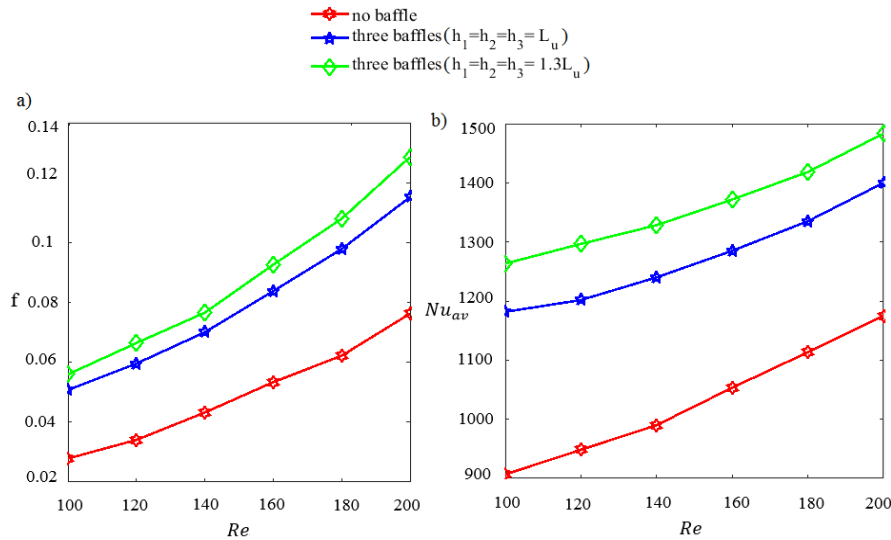


Fig. 15. Variations of (a) f , (b) Nu_{av} at various Re , where, $d_5 = d_6 = d_7 = 0.1 L_u$.

variations in the parameters have been discussed in detail and presented graphically showing that how the presence of baffles affected several results of the case of the smooth channel. Finally, we conclude that:

a./ For a smooth channel, we start our calculation with 15,000 number of cells arbitrarily. It has been found that with the increase in the number of cells, the value of C_p increases continuously, and the graph of C_p becomes linear (marked by circle in the graph), when the number of cells is greater or equal to 60,820. This means that 60,820 number of cells are optimum for the solution, and for a channel with three baffles, we again start our calculation with 15,000 number of cells. It has been found that if the number of cells increases further, the value of C_p increases continuously, but if the number of cells exceeds 172,680, the graph of C_p becomes linear (marked by circle in the graph). So 172,680 number of cells are optimum grid points for our solution.

b./ Though many authors stated that if Re exceeds Re_{crit} , the flow loses its symmetry (i.e., flow bifurcation starts) and reaches its asymmetric state. But the fact is that for non-zero values of Re , the flow never becomes symmetric, and this is observed more clearly if Re exceeds Re_{crit} as the flow loses its symmetry highly then.

c./ It has been demonstrated that hydrothermal flow characteristics become more pronounced with the increase in the number of baffles. It has been found that the value of the Nu_{av} increases when the value of Re and the number of baffles increases. At $Re = 200$ and in the case of three baffles, it is calculated that when the thickness of the baffle is equal to $0.1 h_1$ then the value of Nu_{av} becomes approximately 1.2 times of that of the case of no baffle.

d./ At $Re = 200$ and for $h_1 = h_2 = h_3 = 1.3 L_u$, it is investigated that the value of Nu_{av} becomes approximately 1.28 times of that of the case of no baffle. It is revealed that in the case of three baffles, 1.66 times pumping power is needed as compared to the no baffle case. It has also been concluded that the enhancement of thermal phenomena is clear when baffle height is considered instead of baffle thickness.

ACKNOWLEDGEMENTS

Authors are grateful for the valuable comments made on the earlier version of this work by the reviewers, which lead to an overall improvement of the work.

References

Akbari, O. A., Karimipour, B., Toghraie, D., Semiromi, A., Safaei, R.M., Alipour, H., Goodarzi, M. & Dahari, M. (2016a) Investigation of Rib's height effect on heat transfer and flow parameters of laminar water- Al_2O_3 nanofluid in a two dimensional rib-micro-channel, Appl. Math. Comput, 290: 135-153.

Akbari, O. A., Toghraie, D. & Karimipour, A. (2016b) Numerical simulation of heat transfer and turbulent flow of water nanofluids copper oxide in rectangular microchannel with semi attached rib, *Adv. Mech. Eng.*, 8(4): 1-25.

AL-Jawary, M. (2020) Three iterative methods for solving Jeffery-Hamel flow problem. *Kuwait Journal of Science*, 47(1): 1-13.

Al-Ashhab, S. (2019) Asymptotic Behaviour and Existence of Similarity Solutions for a Boundary Layer Flow Problem. *Kuwait Journal of Science*, 46(2): 13-20.

Alleborn, N., Nandakumar, K., Raszillier, H. & Durst, F. (1997) Further contributions on the two-dimensional flow in a sudden expansion. *J. Fluid Mech.* 330: 169-188.

Arani, A. A.A., Akbari, A. O., Safaei, R. M., Marzban, A., Alrashed, G., Ahmadi, R. & Nguyen, K. T. (2017) Heat transfer improvement of water/single-wall carbon nanotubes (SWCNT) nanofluid in a novel design of a truncated double layered micro-channel heat sink. *Int. J. Heat Mass Tran.*, 113: 780-795.

Battaglia, F., Tavener, J. S., Kulkarni, K. A. & Merkle, L. C. (1997) Bifurcation of low Reynolds number flows in symmetric channels, *AIAA Journal*, 35: 99-105.

Cherdron, W., Durst, F. & Whitelaw, H. J. (1974) Asymmetric flows and instabilities in symmetric ducts with sudden expansions. *J. Fluid Mech.*, 84: 13-31.

Chai, C. & Song, B. (2019) Stability of slip channel flow revisited, *Phys. Fluids*, 31: 84-105.

Drikakis, D. (1997) Bifurcation phenomena in incompressible sudden expansion flows. *Phys. Fluids*, 9: 76-87.

Durst, F., Melling, A. & Whitelaw, H. J. (1974) Low Reynolds number flow over a plane symmetric sudden expansion. *J. Fluid Mech.*, 64: 111-128.

Dyachenko, U. Y., Zhdanov, L. Y., Smulskii, I. Y. & Terekhov, I. V. (2019) Experimental investigation of heat transfer in the separation zone behind a backward-facing step in the presence of tabs. *Thermophys Aeromech.*, 26: 509-518.

Fearn, M. R., Mullin, T. & Cliffe, K. A. (1990) Nonlinear flow phenomena in a symmetric sudden expansion. *J. Fluid Mech.*, 211: 595-608.

Galuppo, C. W. & De Lemos, M. J. S. (2017) Turbulent heat transfer past a sudden expansion with a porous insert using a nonlinear model. *Numer Heat Transf Part Appl.*, 71: 290-310.

Gürçan F. (2003) Effect of the Reynolds Number on Streamline Bifurcations in a Double-Lid-Driven Cavity with Free surfaces, *Computers and Fluids*, 32(9): 1283-1298.

Hammad K. J., Otugen, V. M. & Arik, E. B. (1999) A PIV study of the laminar axisymmetric sudden expansion. *Flow Experiments in Fluids*, 26: 266-272.

Karimipour, A., Alipour, H., Akbari, O. A., Toghraie, D., Semiromi, M. & Esfe, H. (2015) Studying the effect of indentation on Karimipour flow parameters and slow heat transfer of water-silver nanofluid with varying volume fraction in a rectangular Two-Dimensional microchannel, *Ind. J. Sci. Tech*, 8(15): 51-70.

Leonard, P.B. (1979) A stable and accurate convective modeling procedure based on quadratic upstream interpolation, *Comput. Methods Appl. Mech. Eng*, 19: 59-98.

Mukhambetiyar, A., Jaeger, M. & Adair, D. (2007) CFD Modelling of Flow Characteristics in Micro Shock Tubes, *Journal of Applied Fluid Mechanics*, 10(4): 1061-1070.

Nasiruddin, M.H. & Siddiqui, K. (2006) Heat Transfer Augmentation in a Heat Exchanger Tube Using a Baffle, *Int. J. Heat Fluid Flow*, 28(2): 318-328.

Oder, J., Tiselj, I., Jger, W., Schaub, T., Hering, W. & Otic, I. (2020) Thermal fluctuations in low-Prandtl number fluid flows over a backward facing step. *NuclEng Des*, 359: 1104-1116.

Pinho, T. F., Oliveira, J. P. & Miranda, P. J. (2003) Pressure losses in the laminar flow of shear-thinning power-law fluids across a sudden axi-symmetric expansion. *Int. J. Heat Fluid Flow*, 24: 747-761.

Quadros, D. J., Khan, A.S. & Antony, J.A. (2019) Study of Effect of flow parameters on base pressure in a suddenly expanded duct at supersonic Mach number regimes using CFD and design of experiments, *Journal of Applied Fluid Mechanics*, 11: 483-496.

Quadros, D. J. & Khan, A. S. (2020) Prediction of Base Pressure in a Suddenly Expanded Flow Process at Supersonic Mach Number Regimes using ANN and CFD. *Journal of Applied Fluid Mechanics*, 13: 499-511.

Rahmati, R. A., Akbari, O. A., Marzban, A., Toghraie, D., Karimi, R. & Pourfattah, F. (2017) Simultaneous investigations the effects of non-Newtonian nanofluid flow in different volume fractions of solid nanoparticles with slip and no-slip boundary conditions. *Thermal Sci. Eng. Progress*, 5: 263-277.

Safaei, R. M., Togun, H., Vafai, K., Kazi, N. S. & Badarudin, A. (2014) Investigation of heat transfer enhancement in a forward-facing Contracting channel using FMWCNT nanofluids. *Numer. Heat Tran*, 66: 1321-1340.

Saha, S., Biswas, P. & Nath, S. (2020) Bifurcation phenomena for incompressible laminar flow in expansion channel to study Coanda effect, *Journal of Interdisciplinary Mathematics*, 23: 493-502.

Saha, S. (2021a) Numerical simulation of turbulent flow through a sudden expansion channel: comparison between three models. *Lecture notes in Mechanical Engineering*, 49-56.

Saha, S. (2021b) A Survey on Flow Phenomena and Heat Transfer Through Expansion Geometry. *Lecture Notes in Mechanical Engineering*, 257-264.

Saha, S. & Das, N. A. (2021) Flow Bifurcation Phenomena of Shear-Thinning and Newtonian Fluids in a Rectangular Channel in Presence of Intermediate Steps: using Carreau-Yasuda Model. *Journal of Applied Fluid Mechanics*, 14 (4), 1283-1293.

Saha, S., Raut, S. & Das, N. A. (2021) Thermal enhancement and entropy generation of laminar water-Al₂O₃ nano-fluid flow through a sudden expansion channel with bell-shaped surface. *International Journal of Fluid Mechanics Research*, 48 (3): 65-78.

Saha, S. & Das, N. A. (2022) Hydro-thermal analysis of water-Al₂O₃ nanofluid flow through a sudden expansion channel with intermediate step. *Kuwait Journal of Science*, 49(4): 1-12.

Saha, S., Biswas, P., Das, N. A., Kumar, R. A. & Singh, K. M. (2023) Analysis of Blood Flow Bifurcation Phenomena in Mitral Valve: A Numerical Approach to Predict Cardiac Arrest *Journal of Applied Fluid Mechanics*, 16 (3), 491-504.

Sanmiguel, R. E., Pino, C. & Gutierrez, M. C. (2010) Global mode analysis of a pipe flow through a 1:2 axisymmetric sudden expansions. *Phys. Fluids*, 22: 1-4.

Shapira, M., Degani, D. & Weihs, D. (1990) Stability and existence of multiple solutions for viscous flow in suddenly enlarged channels. *Computers Fluids*, 18: 239-258.

Soong, C.Y., Tzeng, Y. P. & Hsieh, D. C. (1998) Numerical investigation of flow structure and bifurcation phenomena of confined plane twin-jet flows. *Phys. Fluids*, 10: 2910-2921.

Terekhov, V. V. & Terekhov, I. V. (2017) Effect of surface permeability on the structure of a separated turbulent flow and heat transfer behind a backward-facing step. *J Appl Mech Tech Phys*, 58: 254-263.

Ternik, P. (2010) New contributions on laminar flow of inelastic non-Newtonian fluid in the two-dimensional symmetric expansion: Creeping and slowly moving flow conditions. *Journal of Non-Newtonian Fluid Mechanics*, 165: 1400-1411.

Ternik, P. (2009) Planar sudden symmetric expansion flows and bifurcation phenomena of purely viscous shear-thinning fluids. *Journal of Non-Newtonian Fluid Mechanics*, 157(1-2):15-25.

Ternik, P., Marn, J. & Zunic, Z. (2006) Non-Newtonian Fluid Flow through a Planar Symmetric Expansion: Shear-thickening Fluids. *Journal of Non-Newtonian Fluid Mechanics*, 13: 136-148.

Thiruvengadam, M., Nie, H. J. & Armaly, F. B. (2005) Bifurcated three-dimensional forced convection in plane symmetric sudden expansion. *International Journal of Heat and Mass Transfer*, 48: 3128-3139.

Torres, M. J., Garca, J. & Doce, Y. (2020) Numerical Study of Particle Dispersion in the Turbulent Recirculation Zone of a Sudden Expansion Pipe using Stokes Numbers and Mean Drift Parameter. *Journal of Applied Fluid Mechanics*, 13: 15-23.

Van Doormaal, J.P. & Raithby, G.D. (1985) Enhancements of the SIMPLE method for predicting incompressible fluid flows, *Numerical Heat Transfer*, 7: 147-163.

Youcef, A., Saim, R., Oztop, H. & Ali, M. (2019) Turbulent forced convection in a shell and tube heat exchanger equipped with novel design of wing baffles, *International Journal of Numerical Methods for Heat & Fluid Flow*, 29(6): 2103-2127.

Youcef, A. & Saim, R. (2021) Numerical Analysis of the Baffles Inclination on Fluid Behavior in a Shell and Tube Heat Exchanger, *J. Appl. Comput. Mech*, 7(1): 312-320.

Submitted: 17/01/2022

Revised: 06/04/2022

Accepted: 17/04/2022

DOI : 10.48129/kjs.18147

Investigation of biomimetic hydroxyapatite formation on titania nanoparticles and lobed nanotubes

¹Murthada Kutheir Abbas, ^{2,*} Mustafa Shakir Hashim

^{1,2} *Dept. of Physics Education college, Mustansiriyah University,
Baghdad, Iraq*

**Corresponding author: mustmust@uomustansiriyah.edu.iq.*

Abstract

An anodizing method was used to produce TiO₂ nanotubes (TNTs) on Ti metal bases. These tubes were transformed into lobed nanotubes (LNTs) by heating at 600⁰C as scanning electron microscopy (SEM) images showed. A rapid break down anodizing (RBA) technique was utilized to produce TiO₂ nanoparticles (TNPs). These particles were deposited on LNTs by the electrophoretic deposition (EPD) method. An X-ray diffraction (XRD) test revealed the polycrystalline composition of the formed LNTs and the amorphous structure of TNPs. The bioactivity of LNTs and the deposited TNPs on the LNTs were tested by immersing them in simulated body fluid (SBF) for one month. For the two samples, XRD patterns showed the appearance of small peaks of hydroxyapatite (HAp), which indicates the bioactivity of these samples. SEM images show that the HAp layer on LNTs was in the form of protrusions, while on TNPs it was in the form of crossed filaments.

Keywords: Anodizing technique; bioactivity; hydroxyapatite; lobed nanotubes; titania.

1. Introduction

Many researchers are interested in accelerating the formation of new bone on new medical implants. This is done by two procedures, the first is concerned with the production of new alloys with improved specifications, and the second with the surface modification of these implants (Mustafa, 2014). For both types, blood flow to the bone implant must be considered, because the process of new bone construction necessitates blood reaching this implant. One of the ways to facilitate the passage of blood to medical implant surfaces is to cover them with separated nanoparticles, as we did in this research.

Despite the long history of producing bioactive medical implants, obtaining complete specifications is difficult. Requirements like corrosion resistance, building strong bonds in a short time and biocompatibility should exist in good implants at the same time (Dabing, 2013). Covering medical implants with bioactive nanoparticles meets the requirements for rapid and efficient building of strong bonds between them and bone (Boutinguiza *et al.*, 2011). Nanomaterials have better cellular compatibility than conventional micron scale materials. When compared to conventional materials,

the nanostructure features of the nano materials promote new bone formation (Zhang *et al.*, 2008); this is due to the large ratio between the areas of a nano material and its volume.

One of the well-known properties of TiO₂ nanotubes (TNTs) is their large surface area, and the deposition of nanoparticles of the same material on them will increase this surface area. This will increase the potential bonds of organic and inorganic materials that will form after the implantation process of the covered Ti with TiO₂ nano particles (TNPs) decorated TNTs inside the bone (Lory, 2011).

The heat treatment for TNTs usually affects their morphologies; for example Naduvath *et al.* converted TNTs to faceted nanoparticles at low temperatures and heating rates (Johns *et al.*, 2015). As the report by Baiju *et al.* confirmed, TNTs begin to collapse to form nanorods when the temperature reaches 400 °C. (Baiju *et al.*, 2010). In current work, there is different titania morphology after heat treatment, as the following paragraphs show.

There are numerous studies that demonstrate the bioactivity of titanium oxide (Mustafa & Reem, 2020; Sang *et al.*, 2007; Chun *et al.*, 2012), but none that demonstrate this activity for lobed nanotubes (LNTs) and deposit TNPs on the LNTs.

The purpose of this post is to test the bioactivity of nano titanium oxide in two different forms: LNTs and deposited TNPs on the LNTs.

2. Experimental part

The procedure of production of TNTs was mentioned in detail by (Mustafa, 2014). The chemical solution of the anodic process is composed of NH₄F:H₂O and glycerol in a weight ratio of 1:20:7. The cathode (Ti) and anode (Ti) were immersed in the solution for one hour. The voltage difference between them was kept at 30V. The transformation of these TNTs to LNTs was done by heating at 600°C for one hour.

The method of preparing TNPs by rapid break down anodizing (RBA) method is described in detail by (Reem & Mustafa, 2020). The Ti foil (0.1 mm thick) with a rectangular form (1 x 2 cm) was submerged in 0.1 M HClO₄ electrolyte after being cleaned with alcohol. Two Ti pieces were utilized in the anodization procedure, one as a working electrode and the other as a counter. The distance between the two electrodes was 0.5 cm, and the applied voltage was 20 volts between them.

The electrophoretic deposition (EPD) method was utilized to deposit TNPs on the Ti base. Deposition details are explained fully by (Dalal, 2018). Two Ti rectangular pieces (1 cm x 2 cm) serve as the cathode and anode in the EPD technique cell. A 0.5 cm gap existed between the two electrodes. Artificial ethanol was used to fill the space between the electrodes. TNPs were added to ethanol to be deposited on the Ti base. A thin Ti oxide layer covered the Ti base after applying 50V between the electrodes for 30s.

To investigate the formation of HAp, coated plates with TNPs were immersed in a concentrated five times simulated body fluid (SBF) for one month. The composition of SBF is shown in Table 1.

Table 1. The composition of SBF and the concentration of (SBF \times 5) (Helebrant,2002).

ITEM	SBF*5 (g m/l)
NaCl	40.18
NaHCO ₃	3.176
KCl	1.125
K ₂ HPO ₄	1.15
MgCl ₂ .6H ₂ O	1.555
CaCl ₂	1.465
NaSO ₄	0.36

The purity and sources of the used chemicals are listed in Table 2.

Table 2. Sources of chemicals and their purity

ITEM	Purity	Source
NH ₄ F	98%	Riedel-de Haen-Germany
glycerol	98%	Phywe-Germany
NaCl	99.5%	Romil-England
NaHCO ₃	98%	Riedel-de Haen-Germany
KCl	99%	Thomas Baker -India
K ₂ HPO ₄	98%	Chem Supply-Australia
MgCl ₂ .6H ₂ O	98%	Riedel-de Haen-Germany
CaCl ₂	98%	Chem Supply-Australia
NaSO ₄	98%	Riedel-de Haen-Germany

The phases of the materials produced were examined using the X-ray diffraction (XRD) technique. A scanning electron microscope (SEM) was used to examine the shapes and sizes of particles. The energy dispersive X-ray spectroscopy (EDS) technique was used to specify the compositions of the used and processed materials.

3. Results and discussions

Figure.1 shows the XRD patterns of LNTs and TNPs. Produced TNPs had an amorphous structure. This result is in agreement with that obtained by (Reem & Mustafa ,2019). After heat treatment, LNTs had a polycrystalline structure with a dominant peak (110). Also, LNTs had a pure rutile phase and there was no trace of an anatase or brookite phase. This result is in agreement with that obtained by (Yu & Anchun, 2018).

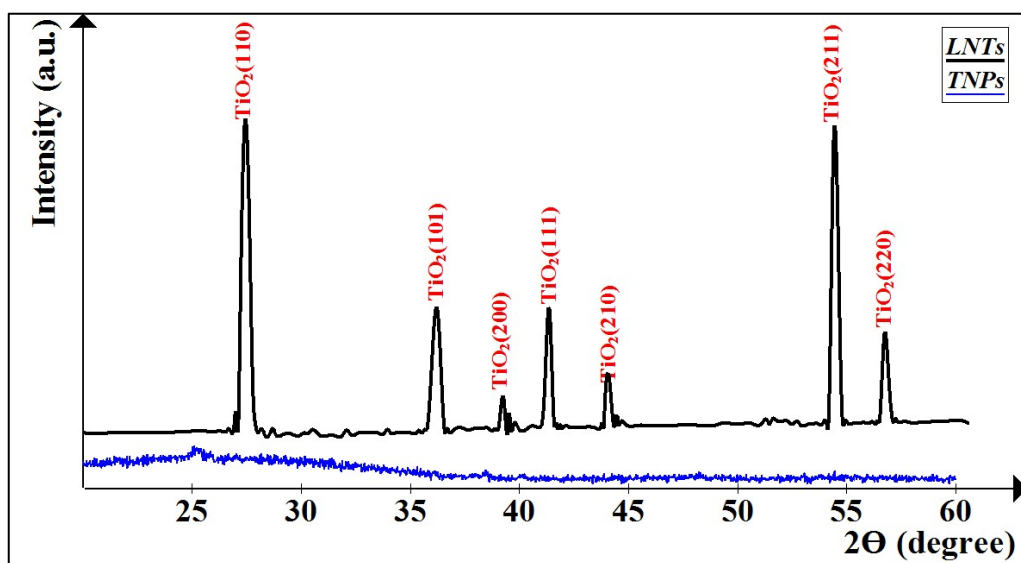


Fig. 1. XRD patterns of TNR and TNPs

After heat treatment, SEM images in Figure. 2 show the disintegration of TNTs into lobed tubes consisting of rings arranged on top of each other, and each ring consisting of a belt of nanoparticles with an average diameter of 32.96 nm (standard deviation 3.32). To our knowledge, this result is not similar to any transformation of TNTs after the heat treatment process.

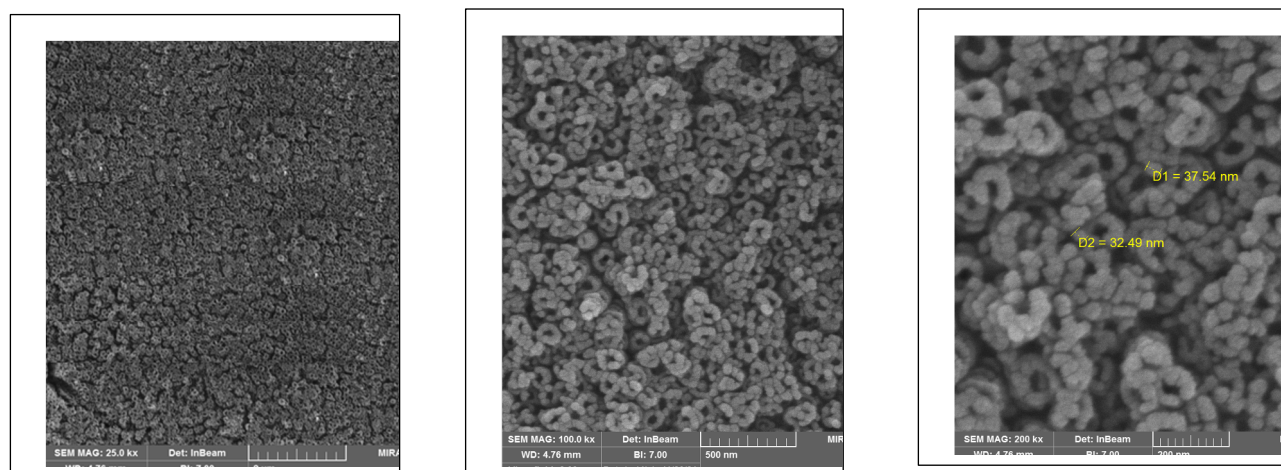


Fig. 2. SEM images of LNTs.

The second anodic process (RBA) produced TNPs as SEM in Figure. 3 illustrates. These nanoparticles were, in general, semi spherical nanoparticles with an average diameter of 13 nm (standard deviation 3.44). The result is similar to that obtained by (Mustafa & Reem, 2020).

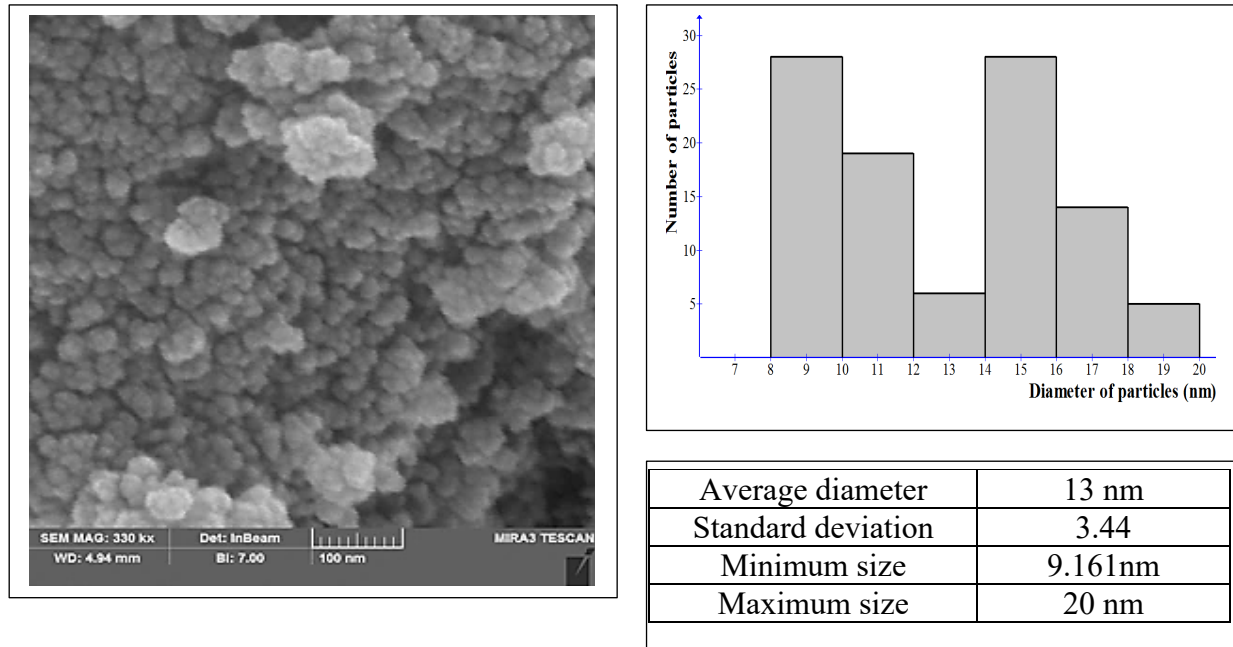


Fig. 3. SEM image of TNPs and some statistical parameters. .

To know the compositions of TNPs and LNTs, the EDS technique was used. The inset tables inside Figure.4 show the elements of the two samples. For the two nanostructures, the atomic percentage of oxygen is approximately twice that of titanium, which indicates the complete transformation of Ti to TiO_2 .

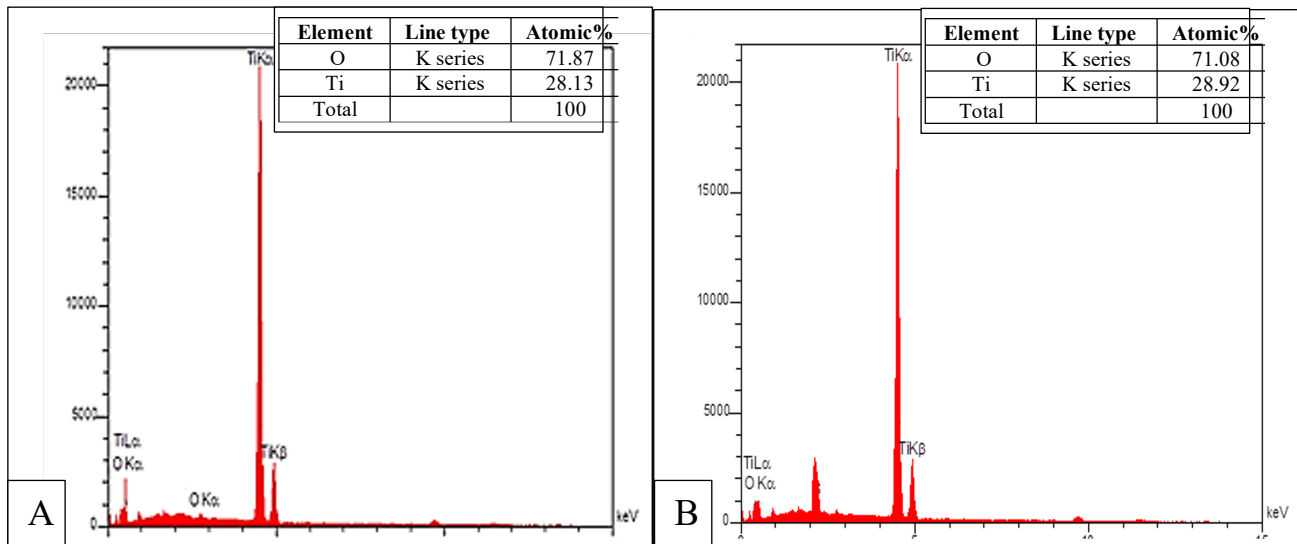


Fig. 4. Results of EDS test for A:TNPs & B:LNTs.

After soaking in SBF, hydroxyapatite (HAp) was formed on two samples (LNTs and the deposited TNPs on the LNTs) as XRD patterns in Figure.5 confirmed. The insets show small peaks for HAp with orientation [211] and [112] in both patterns. Relatively small intensities for these both

HAp peaks might be due to a thin layer of this material. The SBF-based biomimetic approach frequently results in an amorphous, smooth, and homogeneous HAp layer. However, like with (Yaser *et al.*, 2016), this layer was partly crystallized after heat treatment; our results are in agreement with these findings. SEM images and EDS spectra for the two samples confirm the formation of HAp.

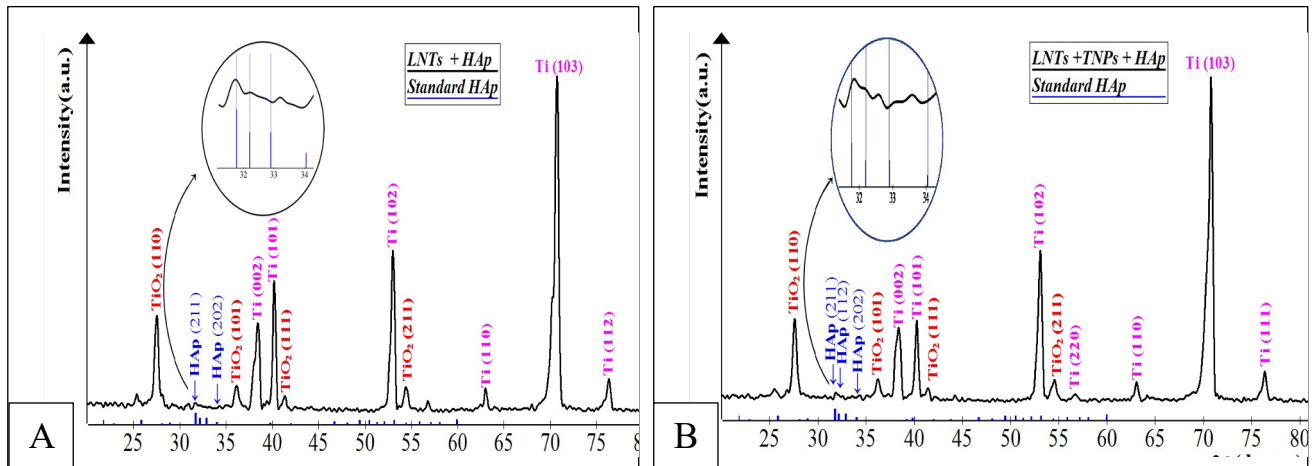


Fig.5. XRD patterns of A: LNTs and B: coated LNTs with TNPs after soaking in SBF.

After taking out the samples from SBF; SEM images in Figure.6 show that the formed HAp has a different morphology on both samples.

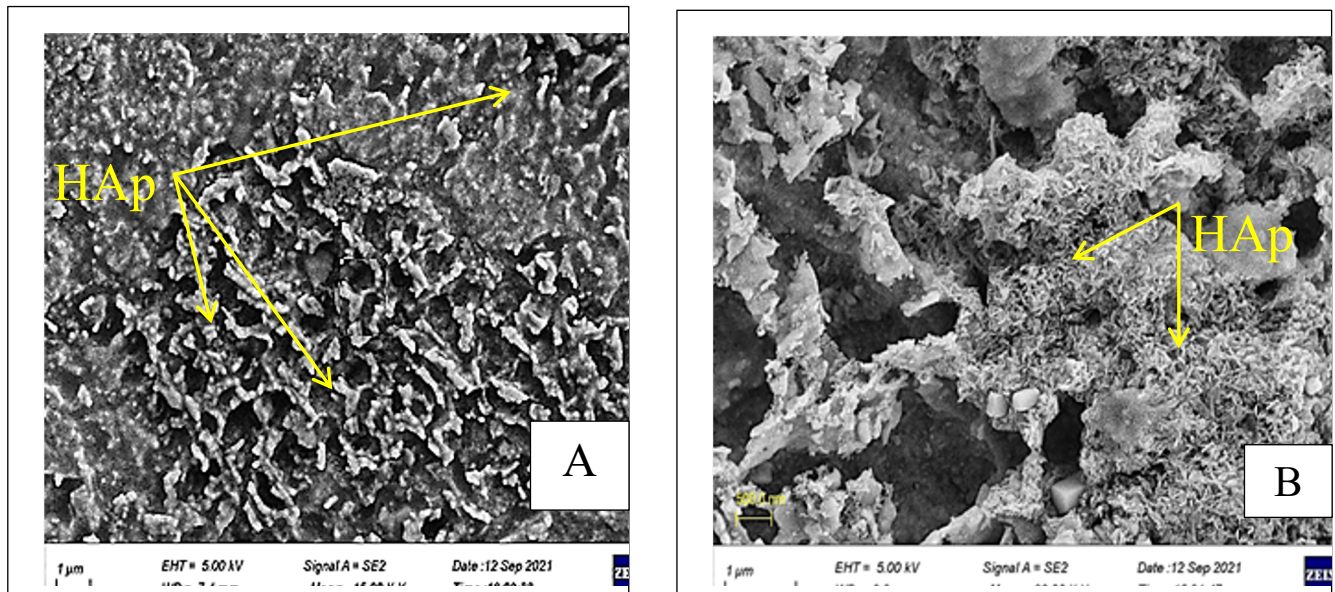


Fig. 6. SEM images of the formed HAp after biomimetic process.

A: On LNTs, B: On coated LNTs with TNPs.

The growth of HAp is affected by the layer under it. Above LNTs the formed HAp has protrusions distributed uniformly. This distribution may be due to the growth of HAp on a semi uniform distribution of the LNTs layer. On the other hand, the deposited HAp on TNPs has a network of interlocking filaments.

EDS spectra of the two samples after soaking inside SBF are displayed in Figure.7. Beside Ti and O peaks there are peaks belong to Ca and P indicating the formation of the HAp layer. The low intensities of HAp inside XRD patterns correspond to the low intensities of calcium and phosphorous in the EDS spectrum.

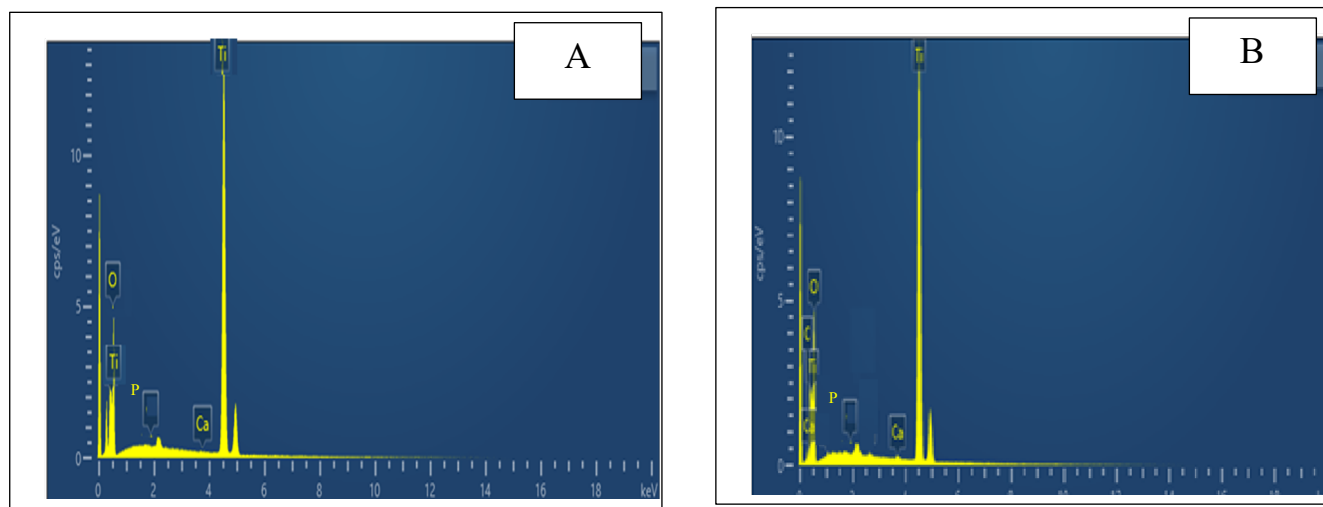


Fig. 7. EDX of A: LNTs + HAp B: coated LNTs with TNPs + HAp.

4. Conclusions

Both TiO_2 nanoparticles (TNPs) and lobed nanotubes (LNTs) are bioactive, and the formed hydroxyapatite (HAp) layers on them have similar XRD patterns and EDS spectra. But these HAp layers have different topographies. According to SEM images, the HAp layer on LNTs was in the form of protrusions, whereas it was in the form of crossing filaments on TNPs.

References

- A.Helebrant, L. Jonasova, L. Sanda (2002).** The influence of simulated body fluid composition on carbonated hydroxyapatite formation, *Ceramics* 46 (1): 9–14.
- Baiju Vijayan, Nada M Dimitrijevic, Tijana Rajh and Kimberly Gray(2010)** Effect of Calcination Temperature on The Photocatalytic Reduction and Oxidation Processes of Hydrothermally Synthesized Titania Nanotubes. *The Journal of Physical Chemistry C* 114(30).

Chun-Yi Chen, Kazunari Ozasa, Ken ichi Katsumata , Mizuo Maeda , Kiyoshi Okada , and Nobuhiro Matsushita (2012). Bioactive Titanium Oxide-Based Nanostructures Prepared by One-Step Hydrothermal Anodization. J. Phys. Chem. C. 116(14) 8054–8062.

Mohamed Boutinguiza, Juan Pou, Fernando Lusquiños and Antonio Riveiro (2011) Production of calcium phosphate nanoparticles by laser ablation in liquid. Physics Procedia. (12)54-59.

Dalal M. Naser (2018) Master thesis, Laser deposition of extracted hydroxyapatite from animal bones Mustansiriyah University. Baghdad Iraq.

Johns Naduvath, Parag Bhargava, and Sudhanshu Mallick(2015) Mechanism of Formation of Faceted Titania Nanoparticles from Anodized Titania Nanotubes. J. Phys. Chem. C. 119(17) 9574–9579.

L. Dabing. (2013) Selection of coating for tribiological applications. M.Sc.Thesis, Jiaotong University (Chine).

Mustafa Sh. Hashim , Ph.D. Thesis(2014) Surface modification of Ti alloys by coating with Iraqi fishbone to enhance osseointegration and improve corrosion resistance (in vitro and in vivo study),Mustansiriyah university.

Mustafa Sh. Hashim and Reem S. Khaleel (2020). The bioactivities of prepared Ti, Zn, TiO₂, ZnO and Al₂O₃ nanoparticles by rapid breakdown anodization technique. Surfaces and Interfaces (20) 100640.

Reem S. Khaleel and Mustafa Sh. Hashim (2020) Fabrication of ZnO sensor to measure pressure, humidity and sense vapors at room temperature using the rapid breakdown anodization method, Kuwait J. Sci.47 (1): 42-49.

Reem S. Khaleel and Mustafa Sh. Hashim(2019). Fabrication of TiO₂ sensor using rapid breakdown anodization method to measure pressure, humidity and sense gases at room temperature. Iraqi Journal of Science. 60(8): 894-1703.

S. Lory. (2011) On the importance of nanometer structures for Implant in corporation in bone tissue, Ph.D.Thesis, University of Gothenburg .

Sang Hun Jeong, YeongJoon Park, Bong Soo Kim and Ho Jun Song (2007). Effects of Oxygen Content on Bioactivity of Titanium Oxide Films Fabricated on Titanium by Electron Beam Evaporation. Journal of Nanoscience and Nanotechnology 7(11):3815-8.

Yaser E. Greish, Ahmed S. Al Shamsi, Kyriaki Polychronopouliu and Ahmad I Ayesh(2016). Structural evaluation, preliminary in vitro stability and electrochemical behavior of apatite coatings on Ti₆Al₄V substrates. Ceramics International 42(16): 18204-18214.

Yu Fu and Anchun Mo(2018) A Review on the electrochemically self organized titania nanotube Arrays: synthesis, modifications, and biomedical applications .Nanoscale Research Letters. **13**:1-21.

Zhang L. , Yupeng Chen, Jose Rodriguez, Hicham Fenniri and Thomas J Webster (2008) Biomimetic helical rosette nanotubes and nanocrystalline hydroxyapatite coatings on titanium for improving orthopedic implants. International journal of nanomedicine. 3(**3**): 323-233.

Submitted : 06/11/2021
Revised : 15/02/2022
Accepted : 20/02/2022
DOI : 10.48129/kjs.18605

Radar cross section (RCS) of perfect electromagnetic conductor (PEMC) cylinder by a Laguerre–Gaussian beam

M. Arfan ¹, A. Ghaffar ^{2,*}, M.Y. Naz ³, M. A. Hanif ⁴

^{1, 2, 3} Dept. of Physics, University of Agriculture, Faisalabad 38000, Pakistan.

⁴ Dept. of Chemistry, University of Agriculture, Faisalabad 38000, Pakistan.

*Corresponding author: aghaffar16@uaf.edu.pk

Abstract

Radar Cross Section (RCS) of perfect electromagnetic conductor (PEMC) cylinder using an incident Laguerre–Gaussian (LG) beam has been investigated. LG beam potential function is used to expand the incident and scattered electromagnetic (EM) field components. The co- and cross-polarized scattered field coefficients are determined by applying the PEMC boundary conditions at the interface i.e., $r = a$. The obtained values for co- and cross-polarized scattered field components would be helpful to find out the scattered field distribution. A comparison of our results for PEMC and PMC for fundamental LG beam with beam mode $p = 0$, $l = 0$, i.e., LG_{00} match with the gaussian beam scattering as witnessed in published work. The effects of OAM mode index (l), beam waist radius (w_0), and PEMC cylinder radius on RCS have been analyzed.

Keywords: Cylinder; Laguerre–Gaussian (LG) beam; PEMC; PMC ;radar cross section (RCS).

1. Introduction

The concern of optical researchers towards Laguerre–Gaussian (LG) beam have increased due to its intrinsic differential field distribution and helical phase front which results transfer of angular momentum along with sensing of small-scale characteristics to the illuminated objects (Friese *et al.*, 1996; Tempere *et al.*, 2001; Mair *et al.*, 2001). Beam with helical/twisted phased profile carrying orbital angular momentum (OAM) is well known for LG beam. The magnitude of OAM associated with each photon is characterized by $l\hbar$ term. The beam indices, p describes the node number of the beam radial profile and l stands for angular degree of freedom about the propagation direction. LG beam form remains stable for free space propagation i.e., scale of intensity profile in a cross-section changes but on the optical axis the zero intensity can be observed. Owing to this, such beams are also renowned for optical vortices (Yao and Padgett, 2011).

Recent works have focused on the LG beam scattering for different orders of OAM through several types of metamaterials such as PEMC sphere (Arfan *et al.*, 2022b) and chiral coated PEMC cylinder (Arfan *et al.*, 2022a) that are being widely used for various purposes. Furthermore, these beams are being used to estimate the RCS of scattered field for various shaped materials as, dielectric slab (Li *et al.*, 2017), complicated biological cells (Yu *et al.*, 2018), chiral particles (Cui *et al.*, 2021), and chiral sphere (Qu *et al.*, 2016).

The suggestion of generality of a perfect electric conductor (PEC) and perfect magnetic conductor (PMC) results in perfect electromagnetic conductor (PEMC) as proposed by (Sihvola, 2007) and this allows us to study the scattering of LG beam as a substitute for the extended waves infinitely using a PEMC cylinder. It has been seen that PEMC, PEC, and PMC differ in that the PEMC contains a supplementary cross-polarized field component. The well-defined boundary conditions at the surface of PEMC are

$$\begin{aligned} \mathbf{n} \times (\mathbf{H} + M\mathbf{E}) &= 0 \\ \mathbf{n} \cdot (\mathbf{D} - M\mathbf{B}) &= 0 \end{aligned} \quad (1)$$

Here, \mathbf{n} is the unit normal and M is the admittance parameter of PEMC cylinder. The limiting values for admittance parameter as $M = 0$ and $M \rightarrow \pm\infty$, the PEMC becomes PMC and PEC respectively.

The study of interaction between EM waves and magnetized plasma slab is discussed to compute the reflection and transmission coefficients. Numerical results explore that reflectance can be tuned by adjusting the effective collision frequency and metallic substrate (Zhao and Xie, 2016). The problem of the scattering of EM radiation for PEMC sphere and PEMC cylinder was theoretically discussed by (Ruppin, 2006b; Ruppin, 2006a). The study related to PEMC scattering for different arrangements has been conducted by many researchers (Ahmed *et al.*, 2011; Ghaffar *et al.*, 2013; Lindell and Sihvola, 2005; Sihvola and Lindell, 2006). In this manuscript, the incident LG beam is expanded using LG potential function. However, the scattering characteristics of LG beam by a PEMC cylinder has not been considered in literature. So, scattering features of LG beam towards PEMC cylinder are treated. The interaction of PEMC cylinder by varying the LG beam order, beam waist, and cylinder radius on the scattered field is computed. The boundary conditions of the PEMC cylinder have been imposed to obtain the scattering field coefficients. In all the calculations, the field dependence for time factor i.e., $e^{-i\omega t}$ is assumed.

2. Description of the problem and governing equations

The geometry of our problem is depicted in Figure. 1. A PEMC cylinder is considered to study the interaction of LG beam. The radius of the cylinder is a with infinite length. The field polarizations are defined as, when the polarized incident field is parallel to the axis of PEMC cylinder, then it is called transverse magnetic (TM) polarization and when the polarized incident field becomes perpendicular to the cylinder axis then it is known as transverse electric (TE) polarization. For PEMC cylinder, the cross polarized TM component appears in the scattered field for an incident LG beam.

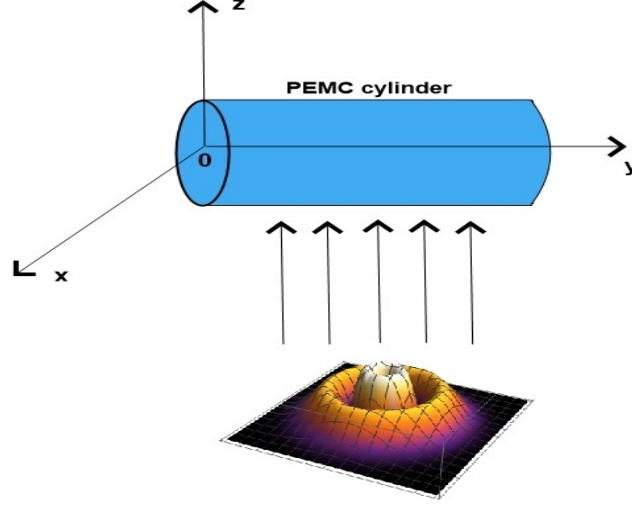


Fig. 1. Geometry of the scattering problem.

Now the LG beam is propagating along the z -axis and its potential with amplitude factor \widetilde{V}_0 in a cylindrical coordinate system is given as (Mendonca *et al.*, 2009; Shahzad and Ali, 2014; Ayub *et al.*, 2011),

$$V(r, t) = \widetilde{V}_0 F_{pl}(r, z) \exp[i(l\varphi + kz - \omega t)] \quad (2)$$

The equation (2) tells that LG potential depends on mode numbers p, l , and azimuthal angle (φ) with helical phase structure through $\exp[i(l\varphi + kz - \omega t)]$ factor. In a cylindrical coordinate system (r, φ, z) , the electric field components can be written as,

$$E_r = -\partial_r V(r, t) = -\frac{1}{F_{pl}} \frac{\partial F_{pl}}{\partial r} V(r, t) \quad (3)$$

$$E_\varphi = -\partial_\varphi V(r, t) = -\frac{il}{r} V(r, t) \quad (4)$$

$$E_z = -\partial_z V(r, t) = -\left(ik + \frac{1}{F_{pl}} \frac{\partial F_{pl}}{\partial z}\right) V(r, t) \quad (5)$$

where the LG mode function is defined as,

$$F_{pl}(r, z) = \frac{1}{2\sqrt{\pi}} \sqrt{\frac{(l+p)!}{p!}} (X)^{|l|} L_p^{|l|}(X) \exp\left(-\frac{X}{2}\right) \quad (6)$$

where $X = \frac{r^2}{w^2(z)}$ and $w(z) = w_0 \sqrt{1 + \left(\frac{z}{z_R}\right)^2}$ be the beam width which turns to beam waist w_0 at $z = 0$. The term $z_R = \left(\frac{1}{2}\right) k w_0^2$ expresses the Rayleigh length. Beam parameters (p & l) denote radial and azimuthal index. $L_p^l(\cdot)$ expresses the associated Laguerre polynomial.

For parallel polarized incident field, plugging equation (2) into equation (5), so

$$E_z^i = -\partial_z V(r, t) = - \left(ik + \frac{1}{F_{pl}} \frac{\partial F_{pl}}{\partial z} \right) \widetilde{V}_0 F_{pl}(r, z) \exp [i(l\varphi + k_0 z - \omega t)] \quad (7)$$

Now using equation (10) of (Kozaki, 1982) under special case i.e., on substituting $\alpha = 0$ and putting in equation (7) so the above mathematical expression for incident field can be modified as,

$$E_z^i = -\widetilde{V}_0 \exp[i(l\varphi - \omega t)] \left(ik F_{pl} + \frac{\partial F_{pl}}{\partial z} \right) F_{pl}(r, z) \sum_{n=-\infty}^{\infty} j^n J_n(k_0 r) e^{in\varphi} \hat{z} \quad (8)$$

The scattered field can be expressed as,

$$\begin{aligned} E_z^s &= -\widetilde{V}_0 \exp[i(l\varphi - \omega t)] \left(ik F_{pl} \right. \\ &\quad \left. + \frac{\partial F_{pl}}{\partial z} \right) F_{pl}(r, z) \sum_{n=-\infty}^{\infty} j^n [a_n H_n^{(2)}(k_0 r) \hat{z} + b_n \left(\frac{in}{k_0 r} H_n^{(2)}(k_0 r) \hat{r} - H_n^{(2)'}(k_0 r) \hat{\varphi} \right)] e^{in\varphi} \end{aligned} \quad (9)$$

Where $J_n(\cdot)$ and $H_n^{(2)}(\cdot)$ are the Bessel functions of the 1st kind and Hankel functions of the 2nd kind, respectively. Prime denotes the derivative of the function with respect to the whole argument. In these expressions, a_n & b_n are the scattering coefficients of co- and cross-polarized field. The magnetic field components H_φ^i and H_φ^s can be known by using Maxwell's equations (Jackson, 1999) on the field equation (8-9).

To find out the unknown coefficients, the tangential and radial EM field components would satisfy the boundary conditions on the surface of the PEMC cylinder i.e., $r = a$ (Ruppin, 2006a) as,

$$H_t^i + ME_t^i + H_t^s + ME_t^s = 0 \quad (10)$$

$$\epsilon_0 E_r^i + \epsilon_0 E_r^s - M\mu_0 H_r^i - M\mu_0 H_r^s = 0 \quad (11)$$

On implementing the above-mentioned boundary conditions, the linear equations are obtained. These are solved simultaneously to determine the co- and cross polarized scattering field coefficients.

3. Results and discussion

The complete theoretical formulation is derived in Section 2 and its implementation into Mathematica program is done in Section 3. In this section, scattering characteristics of the PEMC cylinder illuminated by an LG beam is numerically presented. The source frequency is set at 1 GHz and beam waist radius is $w_0 = 1.0 \lambda$. In Figure. 2, the radial component of the incident electric field at different z positions i.e., $z = z_R, 3z_R$, and $7z_R$ for LG_{01} beam is depicted. The top

Figure. 2a presents the distributions in a quite small area as compared to the remaining Figures. 2(b-c) respectively. It can be seen that for LG beam incidence, a broadening is noted with increasing the propagation distance. The LG electric field distributions lead to a twisted field type structure which gives a strong basis for helical LG beam oscillations.

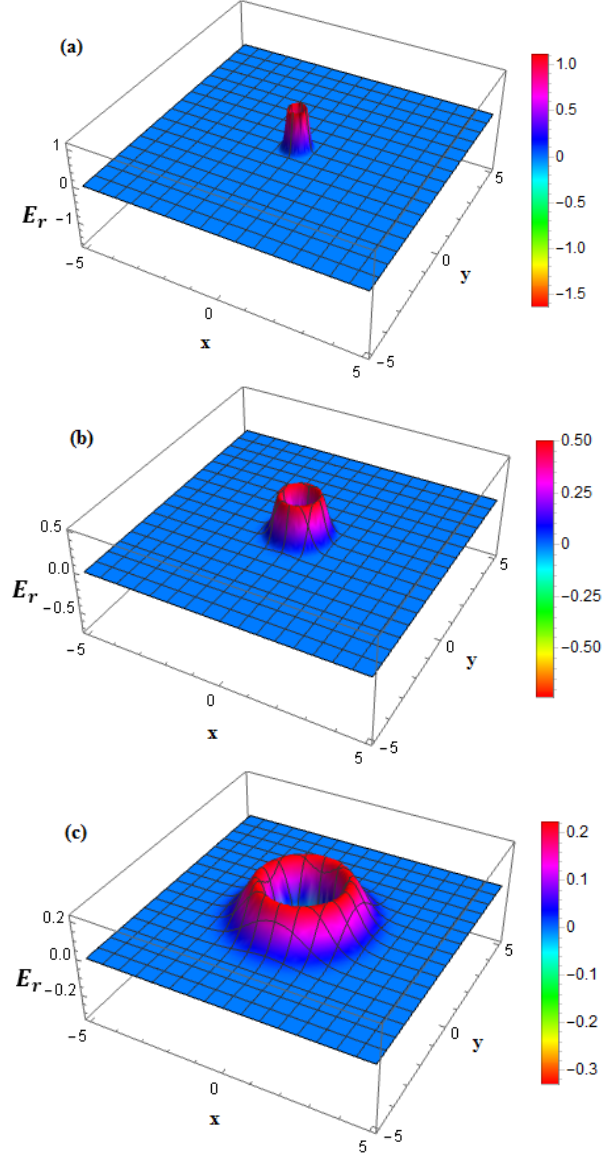


Fig. 2. Radial electric field amplitude associated with LG beam by varying the propagation distance (a) $z = z_R$ (b) $z = 3 z_R$ (c) $z = 7 z_R$.

The scattered field distribution depends on LG beam parameters i.e., topological charge (l) and beam waist radius (w_0). The normalized scattered field distribution is plotted against equation (9) and discussed by varying the different influencing factors. On plotting equation (13) of Ref. (Kozaki, 1982) for ($\alpha = 0^\circ, 90^\circ$) and also keeping the beam parameters i.e., $p = 0$ & $l = 0$ for

different configurations of cylinder (a) PEMC (b) PMC, the scattering behavior of LG_{00} beam and gaussian beam is same. It is observed that scattered field response at $(\alpha = 0^\circ, 90^\circ)$ for equation (13) of a gaussian beam of (Kozaki, 1982) coincides with the PEMC cylinder and PMC cylinder of LG_{00} beam. The results are shown in Figure. 3(a) and 3(b) respectively.

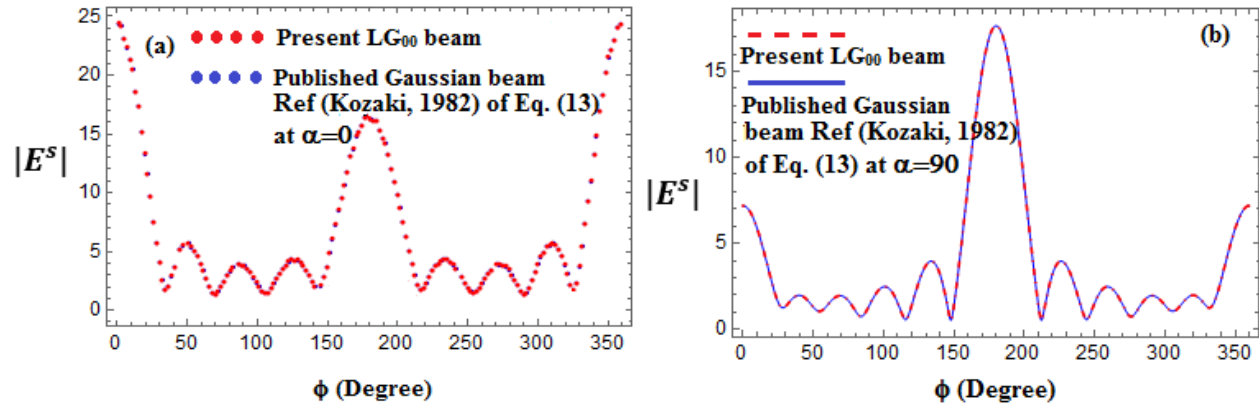


Fig. 3. Comparison of the scattered field of gaussian beam and LG_{00} beam with its mode indices i.e., $p = 0$ and $l = 0$ (a) PEMC cylinder (b) PMC cylinder.

After that we focused to probe the effects of OAM i.e., by varying (l) so, we held the parameter $p = 0$. To layout the effect of the OAM, the scattered field response of LG beam for PEMC cylinder for four feasible cases with different combinations of p and l , that are., (a) $p = 0, l = 1$ (b) $p = 0, l = 2$ (c) $p = 0, l = 3$ and (d) $p = 0, l = 4$ is shown in Fig. 4. For $l = 1, 2$ a smooth field pattern appears in between $\phi = 0^\circ - 150^\circ$ and $\phi = 200^\circ - 350^\circ$, but around the center of optical axis i.e., $150^\circ - 200^\circ$, a peak for the scattered field becomes more prominent. Here a sharp hump can be seen. However, the scattered field has maximum value for $l = 4$.

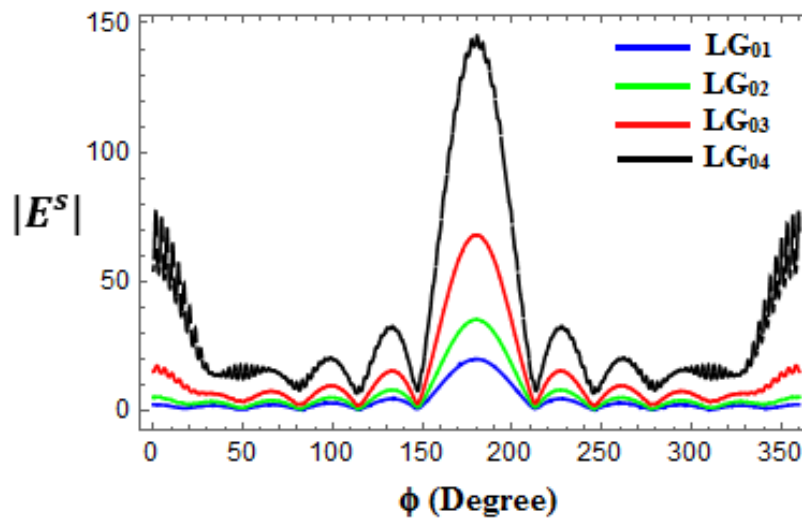


Fig. 4. Scattered field response of LG beam for OAM index $l = 1, 2, 3, 4$ for PEMC cylinder.

The effects of varying the beam waist radius for PEMC cylinder is shown in Figure. 5. The scattered field distribution increases as the waist radius increases. On continuous increasing the waist radius, the size of the hole for the LG beam intensity distribution increases and leads to increase the beam width which in turn increasing the normalized scattered field pattern. The distance among the various peaks becomes shorter due to continuous increasing the waist radius. It seems that field pattern for LG beam increases by increasing the beam waist radius (w_0) as for the gaussian beams.

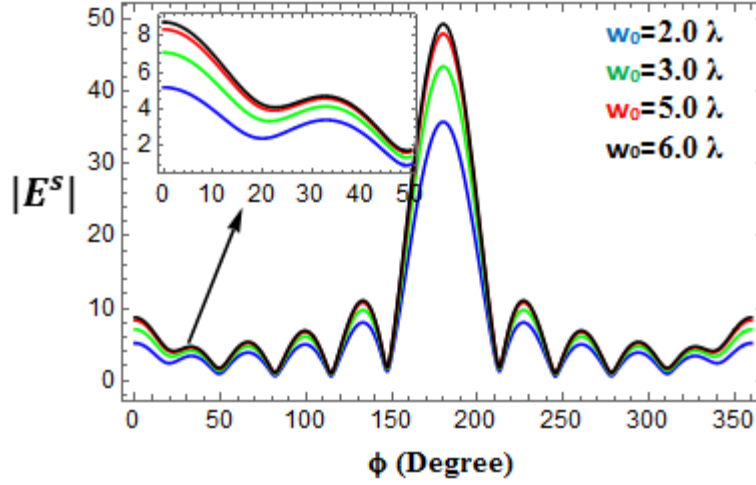


Fig. 5. Scattered field response of *LG* beam for beam waist radius (w_0) for PEMC cylinder.

Figure. 6 shows the scattering behavior of LG beam versus admittance parameter by changing the OAM index. The scattering response increases by increasing the l parameter. The RCS for all the other values of admittance parameter show flat response but at the center of the optical axis, a sharp peak appears which corresponds to the more involvement of internal field modes. The central peak size also increases by increasing the OAM mode number. The difference among various peaks increases from minor to major by increasing the beam l .

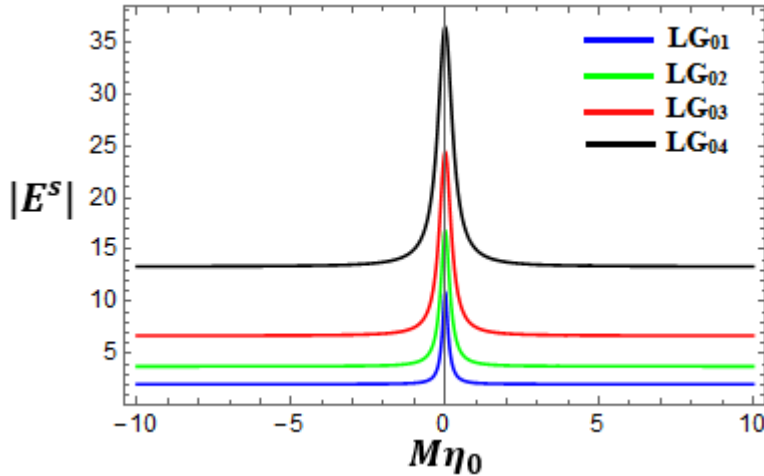


Fig. 6. Scattered field response of *LG* beam versus admittance parameter for PEMC cylinder.

In Figure. 7, the effect of cylinder radius on scattered field has been plotted. The scattered field distribution depends on cylinder radius also. It is clear from the Figure. 7 that when the radius of the cylinder is small the scattered field is small and it increases by increasing the radius. A noticeable pattern is also observed by increasing the cylinder radius. It can be observed that the scattered field for LG incident beam does not always increase with the increase of PEMC cylinder radius. However, there exists an optimum PEMC cylinder size for the maximum scattered field which is also controlled by beam order and beam waist radius.

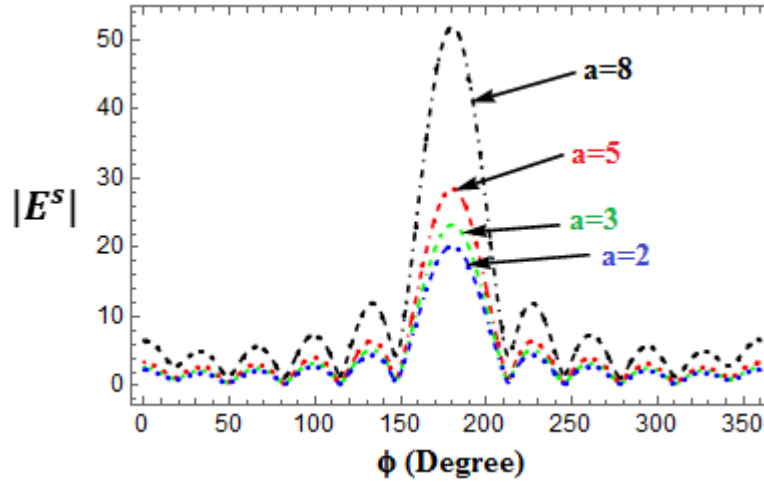


Fig. 7. Scattered field response of *LG* beam for the radius of PEMC cylinder.

4. Conclusions

We have developed an analytical technique to study the scattering field pattern of a PEMC cylinder that is illuminated by an incident LG beam. The field components of LG beam need to be described by mathematical expressions in cylindrical coordinate system. Here, we briefly described an arbitrary incident LG beam by using the method of constructing scalar potential. The present theoretical treatment is considered to be more general for considering any perfect conductor cylinder i.e., (PEC/ PMC/ PEMC). A comparison of the numerical results with the published results under some special case confirm the validity of our analysis. It is concluded that scattered field for PEMC cylinder can be tuned by varying the OAM mode index, beam waist radius, and PEMC cylinder radius.

ACKNOWLEDGMENTS

The authors extend their appreciation to the Higher Education Commission (HEC) of Pakistan for funding this research work through the NRP project number 8576.

References

Ahmed, S., Manan, F., Shahzad, A. & Naqvi, Q. A. (2011). Electromagnetic scattering from a chiral-coated PEMC cylinder. *Progress In Electromagnetics Research*, 19, 239-250.

Arfan, M., Alkanhal, M. A., Ghaffar, A. & Alqahtani, A. H. (2022a). Scattering of Laguerre–Gaussian beam from a chiral-coated perfect electromagnetic conductor (PEMC) cylinder. *Journal of Computational Electronics*, 1-10.

Arfan, M., Ghaffar, A., Alkanhal, M. A., Naz, M., Alqahtani, A. H. & Khan, Y. (2022b). Orbital Angular Momentum Wave Scattering from Perfect Electromagnetic Conductor (PEMC) Sphere. *Optik*, 168562.

Ayub, M., Ali, S. & Mendonca, J. (2011). Phonons with orbital angular momentum. *Physics of Plasmas*, 18, 102117.

Cui, Z., Guo, S., Wang, J., Wu, F. & Han, Y. (2021). Light scattering of Laguerre–Gaussian vortex beams by arbitrarily shaped chiral particles. *JOSA A*, 38, 1214-1223.

Friese, M., Enger, J., Rubinsztein-Dunlop, H. & Heckenberg, N. R. (1996). Optical angular-momentum transfer to trapped absorbing particles. *Physical Review A*, 54, 1593.

Ghaffar, A., Ahmad, S., Fazal, R., Shukrullah, S. & Naqvi, Q. (2013). Scattering of electromagnetic wave by perfect electromagnetic conductor (PEMC) sphere placed in chiral media. *Optik*, 124, 4947-4951.

Jackson, J. D. 1999. Classical electrodynamics. American Association of Physics Teachers.

Kozaki, S. (1982). A new expression for the scattering of a Gaussian beam by a conducting cylinder. *IEEE Transactions on antennas and propagation*, 30, 881-887.

Li, H., Honary, F., Wu, Z. & Bai, L. (2017). Reflection and transmission of Laguerre-Gaussian beams in a dielectric slab. *Journal of Quantitative Spectroscopy and Radiative Transfer*, 195, 35-43.

Lindell, I. V. & Sihvola, A. H. (2005). Transformation method for problems involving perfect electromagnetic conductor (PEMC) structures. *IEEE Transactions on antennas and propagation*, 53, 3005-3011.

Mair, A., Vaziri, A., Weihs, G. & Zeilinger, A. (2001). Entanglement of the orbital angular momentum states of photons. *Nature*, 412, 313-316.

Mendonca, J., Ali, S. & Thidé, B. (2009). Plasmons with orbital angular momentum. *Physics of Plasmas*, 16, 21031-21035.

Qu, T., Wu, Z.-S., Shang, Q.-C. & Li, Z.-J. (2016). Light scattering of a Laguerre–Gaussian vortex beam by a chiral sphere. *JOSA A*, 33, 475-482.

Ruppin, R. (2006a). Scattering of electromagnetic radiation by a perfect electromagnetic conductor cylinder. *Journal of Electromagnetic Waves and Applications*, 20, 1853-1860.

Ruppin, R. (2006b). Scattering of electromagnetic radiation by a perfect electromagnetic conductor sphere. *Journal of Electromagnetic Waves and Applications*, 20, 1569-1576.

Shahzad, K. & Ali, S. (2014). Finite orbital angular momentum states and Laguerre–Gaussian potential in two-temperature electron plasmas. *Astrophysics and Space Science*, 353, 3-8.

Sihvola, A. (2007). Metamaterials in electromagnetics. *Metamaterials*, 1, 2-11.

Sihvola, A. & Lindell, I. V. Possible applications of perfect electromagnetic conductor (PEMC) media. 2006 First European Conference on Antennas and Propagation, 2006. IEEE, 1-4.

Tempere, J., Devreese, J. & Abraham, E. (2001). Vortices in Bose-Einstein condensates confined in a multiply connected Laguerre-Gaussian optical trap. *Physical Review A*, 64, 023603.

Yao, A. M. & Padgett, M. J. (2011). Orbital angular momentum: origins, behavior and applications. *Advances in Optics and Photonics*, 3, 161-204.

Yu, M., Han, Y., Cui, Z. & Sun, H. (2018). Scattering of a Laguerre–Gaussian beam by complicated shaped biological cells. *JOSA A*, 35, 1504-1510.

Zhao, L. & Xie, H. (2016). Interaction between electromagnetic wave and magnetized plasma slab with linearly varying electron density with metallic substrate. *Kuwait Journal of Science*, 43.

Submitted: 20/02/2022

Revised: 11/04/2022

Accepted: 13/04/2022

DOI : 10.48129/kjs.19021/

Assessment of health risk due to Pb, Cd, and Cr concentrations in imported cheese samples in Iraq markets

Ali Abid Abojassim*, Ruaa R. Muneam

Dept. of Physics, Faculty of Science, University of Kufa, Iraq

**Corresponding Author: ali.alhameedawi@uokufa.edu.iq*

Abstract

The aim of this study is to determine three heavy metals (Pb, Cd, and Cr) concentrations in cheese samples in Iraq markets that are produced in Iran and Turkey. The concentrations of Pb, Cd, and Cr were measured using atomic absorption spectroscopy. Human health risk parameters, such as Estimated Daily Intake (EDI), Target Hazard Quotient (THQ), Hazard Index (HI), and Carcinogenic risk (CR) due to heavy metals were calculated in all cheese samples of the present study. The average value concentrations of Pb, Cd, and Cr in cheese samples made manufactured in Iran were 4.33 ± 0.57 mg/kg, 0.135 ± 0.03 mg/kg, and 0.183 ± 0.12 mg/kg, respectively. While those which were made in Turkey, the values were found to be 3.89 ± 0.63 mg/kg, 0.167 ± 0.032 mg/kg, and 0.105 ± 0.07 mg/kg, respectively. The average values of HI in Iranian and Turkish cheese samples were 0.526 ± 0.07 and 0.483 ± 0.26 , respectively. While the average values of $CR \times 10^{-6}$ for Pb, Cd, and Cr in Iranian cheese samples were 0.006 ± 0.0007 , 1.13 ± 0.0007 , and 0.0056 ± 0.7 , respectively. But in Turkish cheese samples were 0.005 ± 0.0008 , 0.37 ± 0.07 , and 0.65 ± 0.4 , respectively. The heavy metal concentrations in the present study were found to be of no statistical significance, compared to the Iranian and Turkish cheese samples, where P-value was ($P > 0.05$). Most values for Pb, Cd and Cr concentrations were found to be higher than the allowed limits according to EU Regulations, while the health risk parameters were within the accepted worldwide average limits. Therefore, it can be concluded that most cheese samples have no health risks by consuming this cheese by consumers in Iraq.

Keywords: Atomic absorptions spectroscopy; carcinogenic risk; cheese; heavy metals; Iraq markets.

1. Introduction

Heavy metals are ubiquitous in nature and have become ecologically more interested as a result of human activities, therefore they have been recognized as a major source of ecological concern across the world (Mance, 2012). Due to their presence in tiny amounts in numerous environmental media (e.g., food, water, and air), heavy metals were regarded as trace elements. The incidence of heavy metals in both terrestrial and aquatic environments is critical. In food, heavy metals pollution is directly link to human health risk and also to other living organisms. Some heavy metals such as lead (Pb), cadmium (Cd), and chromium (Cr) are among the essential micronutrient metals required in minuscule quantities in the human body hardly more than a few mg/day (Arshad, 2020). Urbanization and development in industry and agriculture

led to the exposure of humans to these environmental pollutants which are absorbed by the human body via contaminated inhalation air, polluted drinking water, and contaminated food consumption (through the food chains). So, the heavy metals exposure present in food poses a threat to human health (Elmi, *et al.*, 2019). Various challenges present in heavy metals determination due to matrix complexity and deficient concentration levels in which the elements appeared. Animals receive heavy metals mainly through water and food (Llobet, *et al.*, 2003). Contaminated crops, trace element premises, and supplementary minerals, such as limestone and phosphate are mainly input Cd in animal food (Bilandžić, *et al.*, 2011). Small amounts of Cr in animal food have a positive impact on cow milk production, enabling the animals' immune systems to defend against several illnesses (McNamara & Valdez, 2005). Recently, there has been an increasing trend in the consumption of cheese, including increased nutritional value and it has an important role especially in the different types of age groups; however, the data concerning the occurrence of essential and heavy metals in cheese available in the Iraqi market are scarce. Several studies in different countries have been determined the heavy metals in cheese or milk products samples using different technical such as atomic absorption spectrometer, inductively coupled plasma optical emission spectroscopy (Castro-González, *et al.*, 2018; Singh, *et al.*, 2020; Al Sidawi, *et al.*, 2021; Karadjova, *et al.*, 2000). Concerning heavy metals contaminations levels data in cheese products consumed in Iraq, it is not available. Thereby the determination of some heavy metals (Pb, Cd, and Cr) concentrations in cheese samples (imported from Iran and Turkey) in Iraq markets is the aim of the present study.

2. Materials and methods

2.1/Collection samples

In the present study, thirty kinds of cheese samples as truckles (cow source) from Iraq markets, validity duration Summer 2021 which were made in Iran (symbol IN) and Turkey (symbol T), were chosen. According to the producing country, type (soft or hard), and net weight of each product, the samples were divided into two groups as shown in Table 1.

2.1 Digesting samples

The samples were transferred to the laboratory for measurements after collection. Before measuring heavy metals in cheese samples, they must be digested. The method used for digesting samples under study is called the wet digestive method. Before digestion for heavy metals analysis, each cheese sample was dried at 70°C for 24 h. Each sample was digested with a mixture of HNO₃ and HClO₄ to provide a clear solution for analysis. (1 gram) of each cheese sample was weighed on an analytical balance and placed in a digestion tube, then (10 milliliters) of concentrated nitric acid HNO₃ (65%) was added and the mixture was stood overnight at room temperature, later the mixture was heated on a hot plate till boiling gently to oxidize all the materials that oxidized easily and the color of the mixture changed to brown. After cooling, (1 milliliter) of perchloric acid HClO₄ (70%) was added so the mixture was gently boiled until dense white fumes raised and the color of the digestive mixture turned to clear, approximately (1 milliliter) rest. After cooling, the mixture was filtered and

quantitatively transferred to a volumetric flask, then (25 milliliters) of deionized water was added.

2.2/Atomic absorption spectrometer

An atomic absorption spectrometer model (AA-7000, Shimadzu) with a deuterium background corrector (BGC-D2) was used in this work. Pb, Cd, and Cr in samples were determined by using air/acetylene flame (Air-C₂H₂). The value of slit width was 0.7 nm and the values of lamp current for Pb and Cr elements was 10 mA, while for Cd element was 8 mA. The LOD (BGC-D2) for lead, cadmium, and chromium was 0.03- 0.1, 0.002- 0.008, and 0.005-0.02 ppm; the LOQ (BGC-D2) was 0.1 -0.4, 0.007 -0.03 and 0.02-0.07ppm, respectively. The calibration solution was prepared using the following formula ($C_1V_1=C_2V_2$), where C_1 : the concentration of lead standard solution (1000 ppm), V_1 : the volume needed to be diluted, C_2 : the concentration of the working solution of Pb, and V_2 : the final solution of the working solution of Pb. To prepare (0.2 ppm in 100 mL) as the standard working solution of Pb, we need to apply the above formula twice to prepare two solutions of Pb with concentrations of 100 ppm then 10 ppm from 100 ppm. Therefore, the following approach is used to reduce volume estimation errors. The calibrating working solutions of the remaining elements (Cd and Cr) were prepared in the same manner as described previously. The concentrations needed for the working solution of the Pb were (0.2, 0.5, and 0.7) ppm, and (0.1, 0.2, and 0.5) ppm for Cd and Cr, respectively. Finally, AAS was used to determine the levels of Pb, Cd, and Cr where the wavelengths of Pb, Cd, and Cr were 283.3 nm, 228.8nm, and 357.9 nm, respectively (Rashid, et al. 2016).

2.3/Health risk parameters

Many health risk parameters that were calculated due to heavy metals (Pd, Cd, and Cr) in cheese samples such as Estimated Daily Intake (EDI), Target Hazard Quotients (THQ), Hazard Index (HI), and Carcinogenic risk (CR), as follows:

The equation (1) was used to determine EDI due to heavy metals in cheese samples which depend on the concentration of heavy metals in cheese (C_{metal}), the daily average consumption of cheese (W_{cheese}), and the weight of the human body (BW), as follows (Meshref, *et al.* 2014; Christophoridis, *et al.* 2019):

$$EDI \left(\frac{mg}{kg} \text{ per day} \right) = \frac{C_{metal} \left(\frac{mg}{kg} \right) \times W_{cheese} \left(\frac{kg}{day} \right)}{BW (kg)} \quad (1)$$

In the present study, the value of BW has been used is an adult person that has an average weight of 60 kg, while the value of W_{cheese} was 22 gm/day (Christophoridis, *et al.*, 2019; Renner, 1993) .

The values of THQ in the samples were determined according to United States Environmental Protection Agency (USEPA) that depend on EDI and the oral reference dose (RfD), as the following equation (EPA, 1989a; Khalil, 2018):

$$THQ = \frac{EDI \left(\frac{mg}{kg} \text{ per day} \right)}{RfD \left(\frac{mg}{kg} \text{ per day} \right)} \quad (2)$$

The values of RFD in the unit mg/kg per day for Pd, Cd, and Cr were 3.5×10^{-3} , 1×10^{-3} , and 3×10^{-3} , respectively (EPA, 2008; Zhuang, *et al.* 2009).

The values of HI due to all heavy metals in the present study can be calculated by the sum of THQ as following Equation (EPA, 2011).

$$HI \left(\frac{mg}{kg} \text{ per day} \right) = \sum THQ \quad (3)$$

The value of CR due to heavy metals exposure of populations was determined using the following equation based on the USEPA that depends on many parameters such as Exposure Frequency (EFr), Exposure Duration (ED), EDI, which stands for oral carcinogenic slope factor (CSFo), and Average Time (AT), described in (EPA, 2006; EPA 2010):

$$CR = \frac{EFr \left(\frac{days}{year} \right) \times ED(year) \times EDI \left(\frac{mg}{kg} \text{ per day} \right) \times CSFo \left(\frac{mg}{kg} \text{ per day} \right)}{AT \left(\frac{day}{year} \times 70 \text{ year} \right)} \times 10^{-3} \quad (4)$$

In the present study, the values of EFr, ED, AT were 350 days/ years, 30 years, and 365 days/years \times 70 years, respectively (EC, 2006). While, the value of CSFo in- unit mg/kg per day for Pb, Cd, and Cr was 0.0085, 15, and 41, respectively (EPA, 1989b).

2.4/Statistical analysis

Statistical analysis was performed using the SPSS statistical software package (SPSS for Windows version 20, SPSS Inc., Chicago, Illinois, USA).

3. Results

Heavy metals (Pb, Cd, and Cr) in cheese samples produced in Iran and Turkey that are available in Iraqi markets were determined using AAS techniques. Table 1 shows the concentrations of Pb, Cd, and Cr for 30 cheese samples (15 made in Iran and 15 made in Turkey). The results from Table 1, the Pb, Cd, and Cr concentrations in cheese samples that were produced in Iran were range from 0.93 ± 0.30 mg/kg to 8.36 ± 0.96 mg/kg with a mean value of 4.33 ± 0.57 mg/kg, from ND to 0.434 ± 0.13 mg/kg with a mean value of 0.135 ± 0.03 mg/kg, and from ND to 0.523 ± 0.24 mg/kg with an average value of 0.183 ± 0.12 mg/kg, respectively. While, the concentrations of Pb, Cd, and Cr in cheese samples that were produced in Turkey were ranged from ND to 8.36 ± 0.96 mg/kg with an average value of 3.89 ± 0.63 mg/kg, from ND to 0.375 ± 0.13 mg/kg with an average value of 0.167 ± 0.032 mg/kg, and from ND to 1.05 ± 0.34 mg/kg with a mean value of 0.105 ± 0.07 mg/kg, respectively. The results show the maximum value of Pb concentrations in cheese samples produced from Iran and Turkey were in IN7(Sabah-Arab) and T14 (Alamera), respectively. The minimum value of Pb, Cd, and Cr concentrations of Iranian cheese samples was obtained in sample IN10 (Kala-Amal), while in Turkey cheese samples were obtained in sample T12 (Mersin-Village), respectively. Also, it was found most samples of cheese in the present study have ND (no detection) value, especially of Cr concentrations. Table 2 shows the results of EDI, THQ, and HI due to Pb, Cd, and Cr

concentration in 30 cheese samples products from Iran and Turkey country which were collected from Iraq markets. From Table 2, the average values with standard error (S.E) of EDI for Pb, Cd, and Cr concentration in Iran samples were 1.58 ± 0.21 $\mu\text{g/kg}$ per day, 0.05 ± 0.01 $\mu\text{g/kg}$ per day, and 0.07 ± 0.04 $\mu\text{g/kg}$ per day, respectively, while in Turkey samples in-unit $\mu\text{g/kg}$ per day were 1.43 ± 0.23 , 0.06 ± 0.01 , and 0.04 ± 0.02 , respectively. Furthermore, the average values with standard error (S.E) of TQH for Pb, Cd, and Cr concentrations in cheese of Iranian samples were 0.45 ± 0.06 , 0.05 ± 0.01 , and 0.022 ± 0.01 , respectively, while in cheese of Turkish samples were 0.41 ± 0.06 , 0.06 ± 0.01 , and 0.013 ± 0.008 , respectively. Also, from Table 2, the range of the results of HI in two countries of the present study was 0.097-1.127 with an average of 0.526 ± 0.07 and ND- 0.907 with an average value of 0.483 ± 0.26 . According to equation (4), it is found the values of Carcinogenic risk (CR) for all cheese samples of the present study are listed in Table 3. According to the results in Table 3, the highest value of $\text{CR} \times 10^{-6}$ for Pb concentration for Iranian cheese samples was 0.012 in the IN9 and the lowest value was 0.001 in IN6 sample with an average value of 0.006 ± 0.0007 . Whilst, the values of Cd and Cr concentrations varied from ND to 0.980 with an average of 1.13 ± 0.0007 and from ND to 11.302 with an average of 0.0056 ± 0.7 , respectively. Also, from Table 3, it can be noticed that the range values of Pb, Cd, and Cr concentrations for Turkish cheese samples were from ND to 0.011 with an average value of 0.005 ± 0.0008 , from ND to 0.848 with an average value of 0.37 ± 0.07 , and from ND to 6.458 with an average 0.65 ± 0.4 , respectively.

Table 1. Results of Pb, Cd, and Cr Concentration in different cheese products from Iran and Turkey.

No.	Name of brand cheese	Origin	Sample code	Type of cheese	Net weight (gm)	Concentrations of heavy metals (mg/kg or ppm)		
						Pb	Cd	Cr
1	Sabah (Cream)	Iran	IN1	soft	100	5.57±0.79	0.192±0.09	ND*
2	Kibi		IN2	soft	100	2.79±0.56	0.150±0.08	ND
3	Kiri		IN3	soft	100	4.64±0.72	0.350±0.12	0.523±0.24
4	Sabah (UF)		IN4	soft	300	4.64±0.71	0.050±0.04	ND
5	Labneh		IN5	soft	150	2.79±0.56	0.175±0.07	ND
6	Sabah (Bulgarian paneer)		IN6	soft	400	0.94±0.32	0.083±0.06	ND
7	Sabah (Arab)		IN7	soft	400	8.36±0.96	0.042±0.04	ND
8	Pinka		IN8	soft	120	1.86±0.45	0.150±0.08	0.392±0.21
9	Mimas		IN9	soft	100	8.36±0.90	0.075±0.05	1.83±0.45
10	Kala (Amal)		IN10	soft	100	0.93±0.30	ND	ND
11	Kala (Msdmr)		IN11	soft	100	5.11±0.76	0.067±0.05	ND
12	Kala (Maac)		IN12	soft	100	6.04±0.85	0.058±0.04	ND
13	Baf		IN13	soft	400	5.11±0.77	0.042±0.03	ND
14	Gouda		IN14	soft	150	3.25±0.60	0.158±0.09	ND
15	Sabah (Feta)		IN15	soft	225	4.64±0.69	0.434±0.13	ND
Average±S.E						4.33±0.57	0.135±0.03	0.183±0.12
16	Aynes	Turkey	T1	soft	250	5.57±0.79	0.258±0.10	ND
17	Muratbey (Shallal)		T2	hard	200	0.46±0.23	0.325±0.11	0.261±0.17
18	Muratbey (Braided)		T3	hard	200	6.04±0.82	0.008±0.02	ND
19	Lana		T4	hard	200	3.25±0.60	0.133±0.07	ND

20	Tulum (With black semsem)		T5	soft	250	4.64±0.72	0.325±0.12	ND
21	Tulum (With dill)		T6	soft	250	5.57±0.79	0.375±0.13	ND
22	Mersin (Circassian)		T7	soft	250	6.50±0.85	0.133±0.08	ND
23	Village (With olives and thyme)		T8	soft	250	3.25±0.60	ND	ND
24	Village (dill)		T9	soft	250	5.57±0.79	0.108±0.07	1.05±0.34
25	Village (With thyme)		T10	soft	250	1.39±0.39	0.300±0.10	ND
26	Village (With herbs)		T11	soft	250	ND	0.108±0.06	ND
27	Mersin (Village)		T12	soft	250	ND	ND	ND
28	Muratbey (Van herby)		T13	soft	200	4.64±0.72	0.200±0.09	ND
29	Alamera		T14	hard	200	8.36±0.96	ND	0.261±0.17
30	Manfoush		T15	soft	100	3.25±0.60	0.233±0.11	ND
Average±S.E						3.89±0.63	0.167±0.032	0.105±0.07
The worldwide average						0.02 (Additives, 1993; EC, 2006)	0.05 (E Regulation, 2001)	0.03 (E Regulation , 2001)

*ND is no detection.

Table 2. Results of EDI, THQ, and HI due to Pb, Cd, and Cr Concentration in different cheese products from Iran and Turkey.

No.	Sample code	EDI (µg/kg per day)			THQ			HI
		Pb	Cd	Cr	Pb	Cd	Cr	
1	IN1	2.04	0.070	ND	0.584	0.070	ND	0.654
2	IN2	1.02	0.055	ND	0.292	0.055	ND	0.347
3	IN3	1.70	0.128	0.192	0.486	0.128	0.064	0.679
4	IN4	1.70	0.018	ND	0.486	0.018	ND	0.505
5	IN5	1.02	0.064	ND	0.292	0.064	ND	0.356
6	IN6	0.340	0.031	ND	0.097	0.031	ND	0.128
7	IN7	3.06	0.015	ND	0.876	0.015	ND	0.891
8	IN8	0.68	0.055	0.144	0.195	0.055	0.048	0.298
9	IN9	3.06	0.028	0.67	0.876	0.028	0.224	1.127
10	IN10	0.340	ND	ND	0.097	0.000	ND	0.097
11	IN11	1.87	0.024	ND	0.535	0.024	ND	0.559
12	IN12	2.21	0.021	ND	0.632	0.021	ND	0.654
13	IN13	1.87	0.015	ND	0.535	0.015	ND	0.550
14	IN14	1.19	0.058	ND	0.340	0.058	ND	0.399
15	IN15	1.70	0.159	ND	0.486	0.159	ND	0.645
Average±S.E		1.58±0.21	0.05±0.01	0.07±0.04	0.45±0.06	0.05±0.01	0.022±0.01	0.526±0.07
16	T1	2.043	0.095	ND	0.584	0.095	ND	0.678
17	T2	0.170	0.119	0.096	0.049	0.119	0.032	0.200
18	T3	2.213	0.003	ND	0.632	0.003	ND	0.635
19	T4	1.192	0.049	ND	0.340	0.049	ND	0.389

20	T5	1.702	0.119	ND	0.486	0.119	ND	0.606
21	T6	2.043	0.138	ND	0.584	0.138	ND	0.721
22	T7	2.383	0.049	ND	0.681	0.049	ND	0.730
23	T8	1.192	0.000	ND	0.340	0.000	ND	0.340
24	T9	2.043	0.040	0.383	0.584	0.040	0.128	0.751
25	T10	0.511	0.110	ND	0.146	0.110	ND	0.256
26	T11	ND	0.040	ND	ND	0.040	ND	0.040
27	T12	ND	ND	ND	ND	ND	ND	ND
28	T13	1.702	0.073	ND	0.486	0.073	ND	0.560
29	T14	3.064	ND	0.096	0.876	ND	0.032	0.907
30	T15	1.192	0.086	ND	0.340	0.086	ND	0.426
Average±S.E		1.43±0.23	0.06±0.01	0.04±0.02	0.41±0.06	0.06±0.01	0.013±0.008	0.483±0.26
The worldwide average		3.57 (Tripathi, <i>et al.</i> 1999)	1.0 (Islam, <i>et al.</i> 1.,2014)	---	1(Islam, <i>et al.</i> ,2014)	1(Islam, <i>et al.</i> ,2014)	1 (Islam, <i>et al.</i> ,2014)	1(Islam, <i>et al.</i> ,2014)

Table 3. Results of CR due to Pb, Cd, and Cr Concentration in different cheese products from Iran and Turkey.

No	Sample code	CR×10 ⁻⁶			No.	Sample code	CR×10 ⁻⁶		
		Pb	Cd	Cr			Pb	Cd	Cr
1	IN1	0.007	0.434	ND	16	T1	0.007	0.584	ND
2	IN2	0.004	0.339	ND	17	T2	0.001	0.735	1.614
3	IN3	0.006	0.792	3.229	18	T3	0.008	0.019	ND
4	IN4	0.006	0.113	ND	19	T4	0.004	0.302	ND
5	IN5	0.004	0.396	ND	20	T5	0.006	0.735	ND
6	IN6	0.001	0.189	ND	21	T6	0.007	0.848	ND
7	IN7	0.011	0.094	ND	22	T7	0.008	0.302	ND
8	IN8	0.002	0.339	2.422	23	T8	0.004	ND	ND
9	IN9	0.012	0.170	11.302	24	T9	0.007	0.245	6.458
10	IN10	0.001	ND	ND	25	T10	0.002	0.678	ND
11	IN11	0.007	0.151	ND	26	T11	0.001	0.245	ND
12	IN12	0.008	0.132	ND	27	T12	ND	ND	ND
13	IN13	0.007	0.094	ND	28	T13	0.006	0.452	ND
14	IN14	0.004	0.358	ND	29	T14	0.011	ND	1.614
15	IN15	0.006	0.980	ND	30	T15	0.004	0.528	ND
Average±S.E		0.006±0.0007	1.13±0.0007	0.0056±0.7	Average±S.E		0.005±0.0008	0.37±0.07	0.65±0.4
The worldwide average (EPA, 2010; EPA, 1989c)		10 ⁻⁴ -10 ⁻⁶			The worldwide average (EPA, 2010; EPA, 1989c)		10 ⁻⁴ -10 ⁻⁶		

4. Discussion

Concentration results of Pb of all cheese samples collected from Iraq markets was higher than the worldwide average which equals 0.02 mg/kg according to European (EC, 2006) and Codex standards (Additives, 1993), except samples T11 and T12 (ND). Also found that twenty-two of Cd concentrations results in samples of the present study was higher than the worldwide average (0.05 mg/kg) for cheeses according to EU Regulation (E Regulation, 2001). While the results values of Cr concentrations for most samples were less than that of the worldwide average limit (0.03 mg/kg) for cheeses according to EU Regulation (E Regulation, 2001). From Table 1, it is found that the average concentration of the measured heavy metals is of two order higher in magnitude in Iraq than that of the worldwide. This difference can be attributed to many causes. For instance, these include the cheese preparation process, processing equipment, accidental contamination during storage or packing process. The average value of Pb and Cr concentrations in cheese samples of Iranian is higher than that of cheese samples of Turkish, but T-test confirmed the presence of non-significant concentrations between Iranian and Turkish samples statistically ($P > 0.05$). While, the average value of Cd concentrations in Iranian cheese samples is lower than that of Turkish cheese samples, but T-test confirmed the presence of no significant difference in the concentration mg/kg in samples of the present study between Iranian and Turkish samples statistically ($P > 0.05$). Figure.1 shows the relation of average values for Pb, Cd, and Cr concentrations in the sample of the present. So, from Figure.1 the descending order of Iranian cheese samples and Turkish cheese samples were $Pb > Cr > Cd$ and $Pb > Cd > Cr$, respectively according to the average value. The results in Table 2 show that the EDI values for the studied cheese samples were within the upper intake of world toxic heavy metals of Pb and Cd are 3.57 and 1.0 $\mu\text{g/kg/day}$, respectively (Tripathi, *et al.* 1999). Also, all values of TQH in Table 2 were less than 1 which means the cheese of the present study is safe. The minimum and maximum values in the Iranian samples were obtained in samples IN10 and IN9, while in Turkish samples were obtained in samples T14 and T12, respectively. The internal exposure by heavy metals is controlled by the hazard Index (HI), which is equal to or higher than 1, it indicates the potential health risk (Islam, *et al.* 2014), therefore the results of HI values in all cheese samples products from Iran were less than 1, except sample IN9. Statistically, the data of HI for each of the Iranian and Turkish samples has not been significant at $p > 0.05$. The range of the CR values of the worldwide average limit for heavy metals in food is 10^{-4} - 10^{-6} according to Environmental Protection Agency (EPA, 2010; EPA, 1989c). Therefore, the results of CR due to Pb and Cd concentrations for the studied cheese samples have lower values than the worldwide range value, while the values of CR due to Cr concentrations for some samples IN3, IN8, IN9, T2, T9, and T14 which have higher than the world acceptable range. On the basis of these results of health risk parameters due to heavy metals (Pd, Cd, and Cr) in cheese samples such as Estimated Daily Intake (EDI), Target Hazard Quotients (THQ), Hazard Index (HI), and Carcinogenic risk (CR), it could be said that for most samples there is very little chance of potential health risks through consuming these cheese types. The heavy metals transferred through water and food chains to animals. It is accumulation in dairy animals adversely affects their health and milk production. The heavy metal contaminants enter animal systems due to pollution of air, water, soil, and consumption of contaminated feed; improper manufacturing practices and use of contaminated equipment

also contribute to the contamination of milk with heavy metals. Also, the heavy metals contamination during manufacturing of cheese, potential factors of seasonality, and the chemical affinity of heavy metals with certain ingredients are attributed to the high recorded values and heavy metals variations in some cheese samples. Our measured average value of heavy metal (Pb, Cd, and Cr) concentrations of the investigated cheese samples are compared with the previous studies as presented in Table 4. The average value of concentrations for Pb and Cd in the current study are higher than the values determined in Mexico, India, Georgia, Bulgaria, Iraq, Iran, Turkey and Bangladeshi, while the average value of Cr concentrations were higher than India, Georgia, Bulgaria, Iraq, Turkey and lower than in Iran and Bangladeshi, as illustrated in Table 4. From Table 4, it is found that the current study reports a significantly higher Pb and Cd concentrations than those of the same heavy metals for the same food type made by Iran. These may be due to many reasons such as the difference between the local and imported samples, and storage method of samples in Iraqi markets. From the results of the health risk parameters due to heavy metals in the present study such as Pb, Cd, and Cr in most cheese samples produced from Iran and Turkey were within the worldwide average limit. So, this study indicates that there are no high health risks of cheese samples that consumption by Iraqi people.

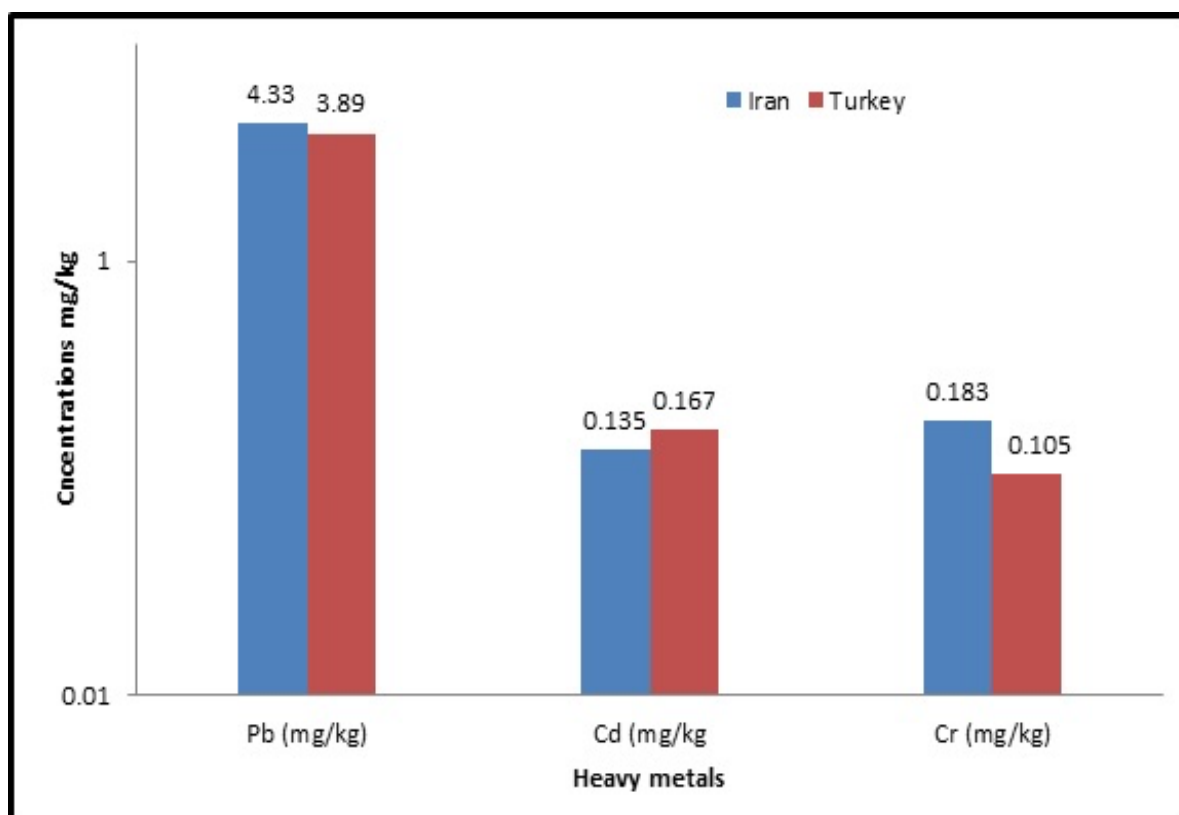


Fig.1. The relation of average values for Pb, Cd, and Cr concentrations in the sample of the present study as a function of the country of productions.

Table 4. Comparison of the average concentrations of Pb, Cd, and Cr in cheese samples of Various countries.

No.	Country	Average of concentrations			Reference
		Pb	Cd	Cr	
1	Mexico	0.11	---	0.02	Castro-González, <i>et al.</i> 2018)
2	India	0.006	0.01	---	(Singh, <i>et al.</i> 2020)
3	Georgia	0.258	0.007	0.079	(Al Sidawi, <i>et al.</i> 2021)
4	Bulgaria	0.0012	0.0039	---	(Karadjova, <i>et al.</i> 2000)
5	Bangladeshi	0.025	0.042	0.886	(Anwarul & Sanjida, 2021)
6	Iraq (Basrah)	0.12	---	---	(Najla & Al-Kaabi, 2020)
7	Iraq (Baghdad)	0.05	---	0.006	(Amir & Al-Azzawi, 2016)
8	Turkey	0.67	---	0.32	(Durali, 2006)
9	Iran	0.015	0.0012	---	(Yasser & Fakhari, 2016)
Present study					
10	Iran	4.33	0.135	0.183	---
	Turkey	3.89	0.167	0.105	

5. Conclusions

From the results of the health risk parameters due to heavy metals in the present study such as Pb, Cd, and Cr in most cheese samples produced from Iranian and Turkish were within the world limit. So, this study indicates that there are no high health risks of cheese samples that consumption by Iraqi people.

ACKNOWLEDGMENTS

Acknowledges all those who have contributed to this research. Special thanks to the staff of the Department of Physics at the University of Kufa.

References

- Additives, F. (1993)** Codex general standard for contaminants and toxins in food and feed (Codex stan 193-1995) 1. Preamble 1.1 scope.
- Al Sidawi, R., Ghambashidze, G., Urushadze, T., & Ploeger, A. (2021)** Heavy Metal Levels in Milk and Cheese Produced in the Kvemo Kartli Region, Georgia. *Foods*, 10(9), 2234.
- Amir A. N., and Al-Azzawi, M. N. A. (2016)** Determination of fungi and some heavy metals in locally cheeses. *Iraqi J Sci*, 57(3C), 2213-2219.

Anwarul Hasan G. M. M. and Sanjida A. Khanam. (2021) Detection of Trace Elements in Selective Dairy Products to assess Human Health Risk of Bangladeshi People. *Orient. J. Chem.*, 37(2), 419-425.

Arshad, Z. (2020) Determination of cadmium in herbal tooth powders purchased from local market in Lahore. *Kuwait Journal of Science*, 47(1).

Bilandžić, N., Đokić, M., Sedak, M., Solomun, B., Varenina, I., Knežević, Z., & Benić, M. (2011) Trace element levels in raw milk from northern and southern regions of Croatia. *Food chem.*, 127(1), 63-66.

Castro-González, N. P., Calderón-Sánchez, F., Castro de Jesús, J., Moreno-Rojas, R., Tamariz-Flores, J. V., Pérez-Sato, M., & Soní-Guillermo, E. (2018) Heavy metals in cow's milk and cheese produced in areas irrigated with waste water in Puebla, Mexico. *Food Additives & Contaminants: Part B*, 11(1), 33-36.

Christophoridis, C., Kosma, A., Evgenakis, E., Bourliva, A., & Fytianos, K. (2019) Determination of heavy metals and health risk assessment of cheese products consumed in Greece. *J. Food Compos. Anal.*, 82, 103238.

Durali. M. (2006) Mineral and trace metal levels in some cheese collected from Turkey. *Food Che*, 96(4), 532-537.

E Regulation, C. E. (2001) Off. J Eur Comm.466.

EC Commission. (2006) Setting of maximum levels for certain contaminants in foodstuffs. Regulation, 1881, 5-24.

Elmi, A., Anderson, A. K., & Albinali, A. S. (2019) Comparative study of conventional and organic vegetable produce quality and public perception in Kuwait. *Kuwait Journal of Science*, 46(4), 120-127.

EPA, U., (1989a) Office of Water Regulations and Standard: Guidance Manual for Assessing Human Health Risks From Chemically Contaminated, Fish and Shellfish. U.S. Environmental Protection Agency, Washington, D.C EPA-503/8-89-002.

EPA, U., (1989b) Guidance manual for assessing human health risks from chemically contaminated, fish and shellfish.

EPA, U., (1989c) Risk-assessment guidance for superfund. Volume 1. Human health evaluation manual. Part A. Interim report (Final) (No. PB-90-155581/XAB; EPA-540/1-89/002). Environmental Protection Agency, Washington, DC (USA). Office of Solid Waste and Emergency Response.

EPA, U., (2006) Risk-Based Concentration Table: Technical Back-Ground Information.

EPA, U., (2008) Baseline Human Health Risk Assessment for the Standard Mine Site Gunnison County. Syracuse Research Corporation, Colorado.

EPA, U., (2010) Risk Based Concentration Table.

EPA, U., (2011) USEPA Regional Screening Level (RSL) Summary Table.

Islam, M. S., Ahmed, M. K., Habibullah-Al-Mamun, M., & Masunaga, S. (2014) Trace metals in soil and vegetables and associated health risk assessment. *Environ Monit Assess.*, 186(12), 8727-8739.

Karadjova, I., Girousi, S., Iliadou, E., & Stratis, I. (2000) Determination of Cd, Co, Cr, Cu, Fe, Ni and Pb in milk, cheese and chocolate. *Microchimica Acta*, 134(3), 185-191.

Khalil, O. S. F. (2018) Risk Assessment of Certain Heavy Metals and Trace Elements in Milk and Milk Products Consumed in Aswan Province. *J Food Dairy Sci*, 9(8), 289-296.

Llobet, J. M., Falco, G., Casas, C., Teixido, A., & Domingo, J. L. (2003) Concentrations of arsenic, cadmium, mercury, and lead in common foods and estimated daily intake by children, adolescents, adults, and seniors of Catalonia, Spain. *J Agr Food Chem.*, 51(3), 838-842.

Mance, G. (2012) Pollution threat of heavy metals in aquatic environments. Springer Science & Business Media.

McNamara, J. P., & Valdez, F. (2005) Adipose tissue metabolism and production responses to calcium propionate and chromium propionate. *J Dairy Sci.*, 88(7), 2498-2507.

Meshref, A. M., Moselhy, W. A., & Hassan, N. E. H. Y. (2014) Heavy metals and trace elements levels in milk and milk products. *J Food Meas Charact.*, 8(4), 381-388.

Najla H. G., and Al-Kaabi, W. J. (2020) Determination of some Heavy Metals Concentration in some Dairy Products from Three Different Regions of Basrah, Iraq. *Basrah J Agr Sci*, 33(2), 1-13.

Rashid, M. H., Fardous, Z., Chowdhury, M. A. Z., Alam, M. K., Bari, M. L., Moniruzzaman, M., & Gan, S. H. (2016) Determination of heavy metals in the soils of tea plantations and in fresh and processed tea leaves: an evaluation of six digestion methods. *Chem Cent J.*, 10(1), 1-13.

Renner, E. (1993) Nutritional aspects of cheese. In *Cheese: chemistry, physics and microbiology* (pp. 557-579). Springer, Boston, MA.

Singh, M., Sharma, R., Ranvir, S., Gandhi, K., & Mann, B. (2020) Assessment of contamination of milk and milk products with heavy metals. *Indian j dairy sci.*, 72(6).

Tripathi, R. M., Raghunath, R., Sastry, V. N., & Krishnamoorthy, T. M. (1999) Daily intake of heavy metals by infants through milk and milk products. *Sci total environ.*, 227(2-3), 229-235.

Yasser S., Ahmadi, F., & Fakhari, F. (2016) Voltammetric determination of Pb, Cd, Zn, Cu and Se in milk and dairy products collected from Iran: An emphasis on permissible limits and risk assessment of exposure to heavy metals. *Food chem*, 192, 1060-1067.

Zhuang, P., McBride, M. B., Xia, H., Li, N., & Li, Z. (2009) Health risk from heavy metals via consumption of food crops in the vicinity of Dabaoshan mine, South China. *Sci total environ.*, 407(5), 1551-1561.

Submitted : 05/03/2022
Revised : 29/03/2022
Accepted : 04/04/2022
DOI : 10.48129/kjs.19245

Thermo-mechanical fe-demo based calculations of high entropy alloys (HEAs) (Fe-Ni-C_x (x=0.3-0.5) ternary alloy system using calphad method

Waseem U Shah^{1,*}, Dil F khan², Haiqing yin³

^{1*, 2} Dept. of Physics, University of Science and Technology Bannu, 28100, KPK, Pakistan

³ School. of material sciences and engineering, Beijing University of Science and Technology
Beijing 100083, P.R China

*Corresponding author: waseemullahshah303@gmail.com

Abstract

The given research shows the thermodynamic analysis and calculation of the basic thermal properties of the high entropy alloy Fe-Ni-C_x (x=0.3-0.5) of concentration. The system is investigated through Thermo-calc package with FEDAT databases and Calphad method. The evaluation of interactions is found maximum at 0.04070 J/m² of interfacial energy in the Fe-Ni-C ternary alloy system. The FCC_A₁ phase is found the phase associated with highest molar volume in the Fe-Ni-C_x (x=0.3-0.5) ternary alloy system. The phase FCC_A₁ is having austenite coordination with increasing density and apparent heat capacity. The temperature variation results the composite phases to be disappears with required level. The system is found highest apparent heat capacity 0.39269 J/mol. The density of phases becomes constant and it indicates the rare temperature withstanding phases. The fluctuations in the density of phases are changing with temperature as a result of phase's nature and stability. The better magnetic properties are found for Basic centered cubic structure with highest interfacial energy. The alloy shows better magnetic coordination and thermodynamic properties enhancement for further analysis.

Keywords: Calphad method, fe-demo databases, high entropy alloys, mechanical study, thermodynamic calculations.

1. Introduction

The recent pattern of alloys generated for the quick structural-materials are Fe-Cr-C with remarkable properties of mechanical-based strength and resistance to deformation forces. The alloys adjusted for the fuel cladding and chemical reactors are Fe-based alloys with Ni-C, Cr-C as an alloying element. The annealing properties of the Fe-Cr-C alloys are strongly dependent on the Cr composition percentage above 15%. Increasing composition of chromium may increase the harmful effect in mechanical properties of the given alloy system. The Fe-based alloys are applicable in the generation wise fusion-reactors and super-critical water reactions process. The alloys having more nickel contents are now a day's much important in research fields as to produce the super alloys, high entropy alloys and those alloys having the mechanical properties enhanced toward the positive need of the industry. The Ni contents results the improvement in the wear resistance, strength, and the low thermal expansion capabilities. (Shi Chen, yong sheng

Li *et al*, 2019; Z.K. Liu, Y. Wang *et al*, 2014). For the special types of steels production, the Ni-rich contents are further increased in the alloys systems. The order and disorder transitions in the FCC phase are reported in the research works carried since 1920 s (J. Liu, L.J. Riddiford *et al*, 2016; I. Ohnuma, S. Shimenouchi *et al*, 2019; B. Hallstedt *et al*, 2010). The additions of more carbon concentration in the nickel based alloys are rejected by researchers because of the production of the dislocation motion in the alloy that results the strength and the ductility range of the Ni alloys. The high temperature investigation of the Fe-Ni-C system is still not performed because of the experimental complications. (L.B. Chen, R. Wei *et al*, 2018; Y. Xu, Q. Jin, X. Xiao *et al*, 2011) The pyro-metallurgical process is carried for the developments of the Ni based alloys to recycle the wastes of the industrial products. (J.M. Jeon, S.Y. Kwon *et al*, 2021) The literature shows the thermodynamic modeling assessments of the Ni alloys and Cr alloys with differential scanning calorimetric process for the report of the enthalpy of the mixing of the alloys (Waseem Ullah Shah *et al*, 2022a).

2. Procedure

The computational based techniques are considering famous part of the materials engineering sciences, which makes us possible for the unknown data prediction and simulations. The Quasi-chemical model is developed for the investigation of the properties of the Fe-Ni-C ternary system. The results are again verified and asymmetric N-rich section was developed by Quasi-chemical-parameters. The study is operated for the 1500⁰ C-1600⁰ C range of carbon composition in the Fe-Ni-C system. The enthalpy of the mixing is found higher ordering in the liquid solution and reproduced successfully. CALPHAD (Calculation of Phase Diagrams) is considered the basic thermodynamic approach based on computational simulations for the calculations of the phase equilibria, for the ternary, binary alloys systems with precise manner (Waseem Ullah Shah *et al*, 2022b; A. Gabriel, P. Gustafson 1987; I. J.H. Weber, encyclopedia *et al*, 2001).

The solidification condition mapping, simulations, and precipitation nucleation based on the diving forces are the remarkable participation of the CALPHAD method. (Gorsse, S. Tancret, F *et al*, 2018). The interest in the evaluation of phase diagrams are marked important on the basis of the thermodynamic databases for the many multi-components systems, like HEA,s, CCA,s (I. Gwalani, B. Gorsse *et al*, 2018; J.-O. Andersson *et al*, 2002). The fully assessed binary and fully assessed ternary systems on the basis of complete thermodynamic assessment are credited by the Calphad method as a set of thermodynamic properties agrees with experimental set ups for the composition and temperature verses (Choudhuri, D. Gwalani *et al*, 2017; Sung- Kwang *et al*, 2015). The Calphad method is based on the following operational correlation cumulant-expansion theorem demonstrated as

$$G = G_{Fe-Cr} x_{Fe-Cr,C} + G_C x_{Fe-Cr} + K_B T (x_{Fe-Cr} \ln x_{Fe-Cr} + x_C \ln x_C) + G_{ex} \quad (1)$$

$$(\Delta H_{Fe-Cr,C})_{order} = (\Delta H_{Fe-Cr,C}) [1 + 8((\Delta H_{Fe-Cr,C})/f_{Fe-Cr,C})] \quad (2)$$

$$\{x_{Fe-Cr}V_{Fe-Cr}^{2/3}[1+u_{Fe-Cr}x_C(\Phi_I-\Phi_C)]+x_CV_C^{2/3}[1+u_Cx_{Fe-Cr}(\Phi_C-\Phi_{Fe-Cr})]\}^2 \quad (3)$$

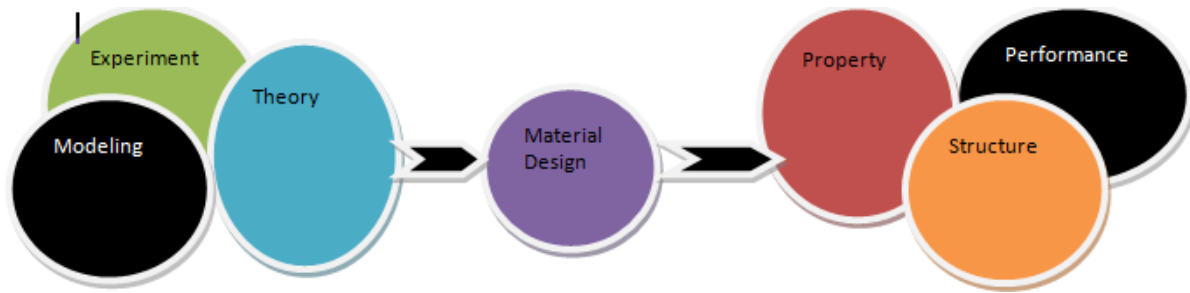
$$f_{Fe-Cr,C}=2pV_{Fe-Cr}^{2/3}V_C^{2/3}[q/p(\Delta n_{ws}^{1/3})^2-(\Delta\Phi)^2-\alpha r/p]/(n_{ws}^{1/3})a^{-1}+(n_{wa}^{1/3})b^{-1} \quad (4)$$

$$G_m^{liquid}=\sum_i x_{Fe-Cr,C}^o G_{Fe-Cr,C}^{liquid}+RT\sum_i x_{Fe-Cr,C}\ln x_{Fe-Cr,C}+\sum_i\sum_{j>1} x_{Fe-Cr,C}x_{Fe-Cr,C}^o L_{Fe-Cr,C}^{liquid} \quad (5)$$

(Senkov, O.N. Miller ,2015; S Sheibani,S Heshmati-manesh *et al*, 2010; Wei Xiong, *et al*, 2012). The X_{Fe-Cr} , X_C terms in the equations shows the concentrations of alloying elements Fe-Cr, C where the Φ shows the electro-negativity of the system. G shows the total Gibbs energy of the system. $\Delta H_{1,2}$ Is the total change in the enthalpy of formation of alloying elements of Fe-Cr, C portion. Ln is for the logarithmic variation of the X composition of elements. N_{ws} represents Normalized wave function short range correlation coefficient. $n_{w1}, n_{w2}, n_{w3}, \dots, n_{ws}$, It is the electron density correlation cumulant-expansion theorem.

3. Flow Chart of modeling

For the process of material designing, the material microstructure is determined as result of phase equilibria and phase distribution. In current research fields the phase transformation is vitally used (Waseem Ullah shah *et al*, 2022c; Sumaryada, T.Sofyan *et al*, 2019).



The Thermo -Calc database software used in order to approach and investigate quantitatively the basic effects of alloying elements particularly the effect of Fe-Ni-C systems by alloying. Thermodynamic calculations and predictions of Meta stable ternary alloys Fe-Ni-C alloys system involves calculation of energies of mixing of the alloying system, excess Gibbs energies, thermodynamic molar activities, coefficient of activities, partial and integral values of enthalpy for the said alloy system at elevated temperatures (1900-2000) K. Obtaining optimal set of thermodynamic parameters for over the whole range compositions of binary systems Fe-Ni, while the carbon mole fraction is maintained at 0.3,0.4,0.5 mass % with temperature investigation for selected alloys. The mode of operation follows the tabulated procedure as given below,

The database selection from main TC window	Sorting Require calculator for calculation	Assessment of results from TC-Prisma
The inserting of alloys from the databases	Adjustment of Ratio of elements	Adjustment of Data with literature
Adjustment of alloying composition on TC databases	Plotting of results on main window	Analysis of the final outcomes

The results are obtained for the complete thermodynamic description of the system for assessment of the properties and applications. The results obtained are novel and prediction basis for the certain thermodynamic and mechanical parameters enhancing properties for the need.

4. Input for methodology.

Composition	Mass %	Flow thermal mode	Flow heat 1/t ²
Annealing range	1901-2001 K	Relaxation fraction value	0.59
Pressure	10 ⁶ Pascal	Vulnerability transition	0.01-0.1
Fe-region comp	99.50 mass %	Type of execution	Grid
Cr-region comp	0.01 mass %	C-range/steps adopted	0.0-1 /10
C-region comp	0.3-0.4 mass %	Proceeding temp	500-3000 /10
Duration of process	30 minutes	Distribution-truncate	3-std
Scheill based temp	2501.15 K	Distribution of total sample	200 Gauss D
Least fraction	1*10 ⁻¹²	Density of dislocation	5.01*10 ¹²
Term-phase amount	0.01	Phase energy addition	0.01 J/mol
Morphology seen	sphere	mobility of phase boundary	10 m ⁴ /Js
Sites of nucleation	Grains/bulks	Phase to deform	FCC_A1
Molar volume	7.0*10 ⁻⁶	Matrix phase	FCC_A1
Sol solid strength	293.20 K	Precipitate phase	FCC_A1
Mean-radius	1.10*10 ⁻⁸	Critical-radius	2.88*10 ⁻⁹

The simulation parameters varied during calculation are tabulated and given for the note. The data represents the input heads for the execution of the results of the alloy system are systematic paths for the execution. The sections of the parameters are adjusted for the better results desired. The pressure of the alloy Fe-Ni-C is kept constant of 10⁶ Pascal to avoid secondary phases in the given ternary system. The bulk properties are adjusted for Ni-site nucleation of the given system. The dislocation density of the alloy shows the symmetric parameters for the response to the phase transition in the given alloy system. The dislocation density is maintained 5.01*10¹² values for smooth alloying. The Gaussian distribution density of the total sample is kept 200 points for the alloy response to demagnetization forces. The critical radius and mean radius of the sample Are maintained 2.88*10⁻⁹, 1.10*10⁻⁸ nm for the sample sintering through computational analysis and execution. The duration of the process are taken 30 minutes with critical radius of 2.88*10⁻⁹mm with morphology seen as a sphere based orientation. The distribution of the sample is 200 Gaussian D with the density of dislocation as 5.01*10¹²mm³ and the phase form to deform is

FCC with austenitic orientation and properties. The mobility of the phase boundaries in the grains are kept as $10 \text{ m}^4/\text{Js}$ with phase energy addition as 0.01 J/mol . The Vulnerability transition formation is executed of the numerical standards as $0.01\text{-}0.1\text{mm}$ with relaxation fraction value of the 0.59 . The required Distribution-truncate for the process are maintained 3-std with annealing range of $1901\text{-}2001\text{K}$. The Fe-region composition is maintained as $99.50 \text{ mass } \%$, the Cr-region composition is tackled as $0.01 \text{ mass } \%$ and C region composition is maintained in the range $0.3\text{-}0.4 \text{ mass } \%$ during the process nucleation.

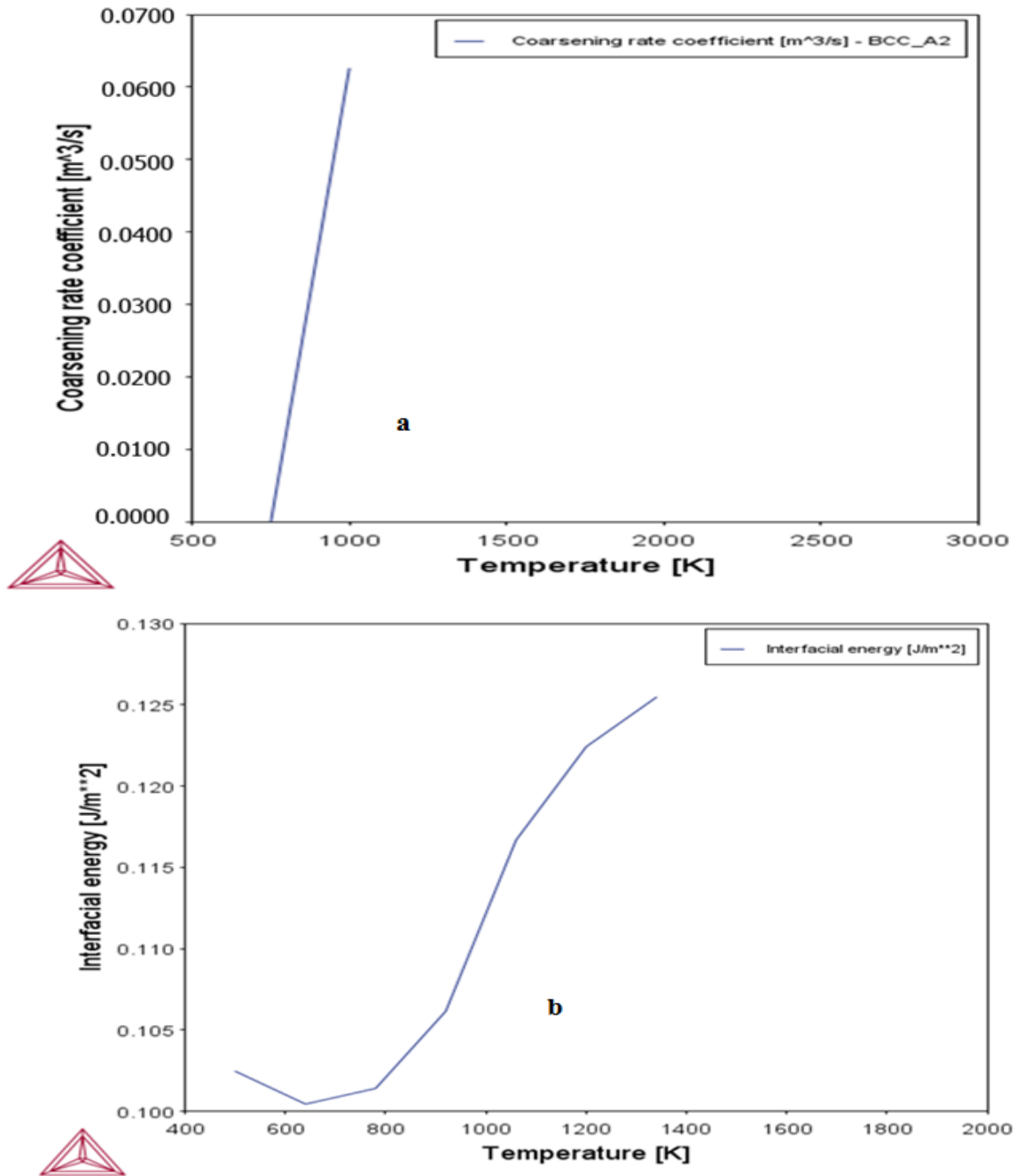


Fig. 1. (a) Coarsening energy rate coefficient (b) Interfacial energy analysis at 1900K .

The coarsening energy analysis and interfacial energy calculations of Fe-Ni-C alloys system is given by Figure 1(a, b). The active phase found for coarsening rate coefficient is BCC_A₂ with different composition of alloying elements. The interfacial energy of the BCC_A₂ is found activated for 500 K, 750 K and 1000 K. the Fe, Ni, C mass percents are found 99.59, 0.01, 0.4 with interfacial energy calculations of (0.04070, 0.02905, 0.01759) J/m². The highest value of coarsening energy is found 0.04070 J/m² indicates the ability of the alloying material to withstand an external magnetic field without demagnetization process and metallurgical fields.

Table. 1 interfacial energy analysis of Fe-Ni-C system.

Coarsening rate coefficient, BCC_A ₂	Temperature [K]	Interfacial energy	Mass % Ni	Mass % C
0.04070	500	0.1025J/m ² ,500K	0.01	0.5
0.02905	750	0.1008, 640K	0.01	0.5
0.01759	1000	0.102, 790K	0.01	0.5
0.01759	--	0.1125,1000K	0.01	0.5
--	1330	0.125	0.01	0.5

The evaluations of interaction of activity components in the alloy are found more 0.04070 times at 500 K. The magnetic properties of the alloy are recorded better at low temperature in Fe-Ni-C system with activated phase of BCC_A₂. Coercive energy calculations of Fe-Ni-C ternary alloy system as per result. The alloy shows increasing coarsening rate at low temperature for Ni contents alloying. At higher temperature, the progress of material to remove grains of carbides and refining the grains are low. interfacial energy increases with increasing temperature as it indicates the imbalanced molecular forces of carbides in the alloying elements. The alloy still shows the stability and performance by lowering its coarsening at higher temperature ranges

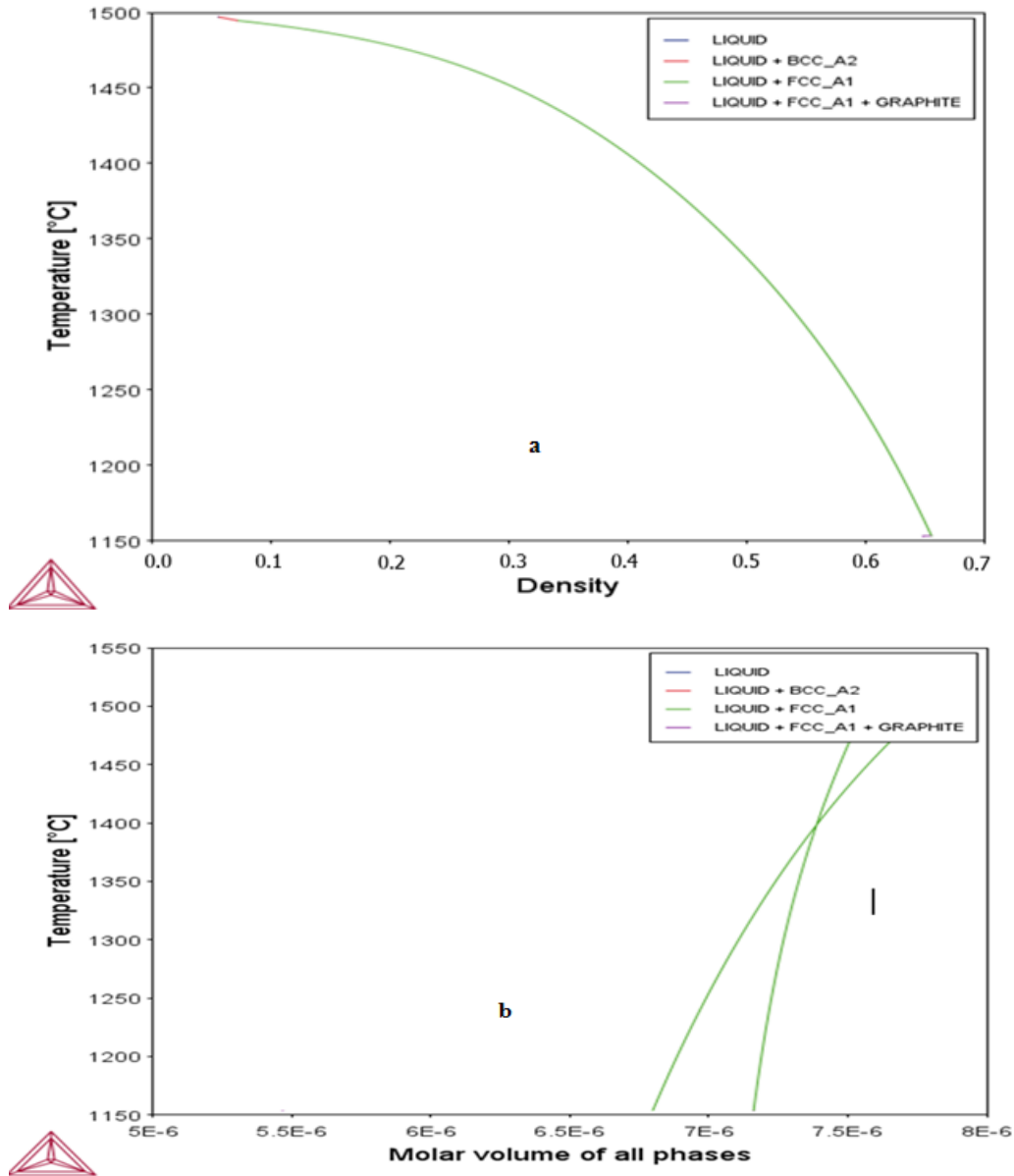


Fig. 2. (a) Fe-Ni-C density analysis (b) Fe-Ni-C Molar Volume analysis profile.

As seen from the simulations that the density of BCC_A2 is seen constant 0.22-0.32 mole fraction by figure 2 (a, b). The alloying order is found magnetically activated for Ni-rich portion. At low temperature range 1497 K. the density of system is found maximum value of 0.056 gm/m^3 , which indicated the majority phases composition in the given alloy system. With the decrease in temperature the composite nature phases overcomes and the most withstanding phases retained with increasing density. At the highest temperature from 1505.72 K, the density of phases becomes peak and it indicates the rare temperature withstanding phases. The fluctuations in the densities of phases are changing with temperature as a result of phase's nature and stability.

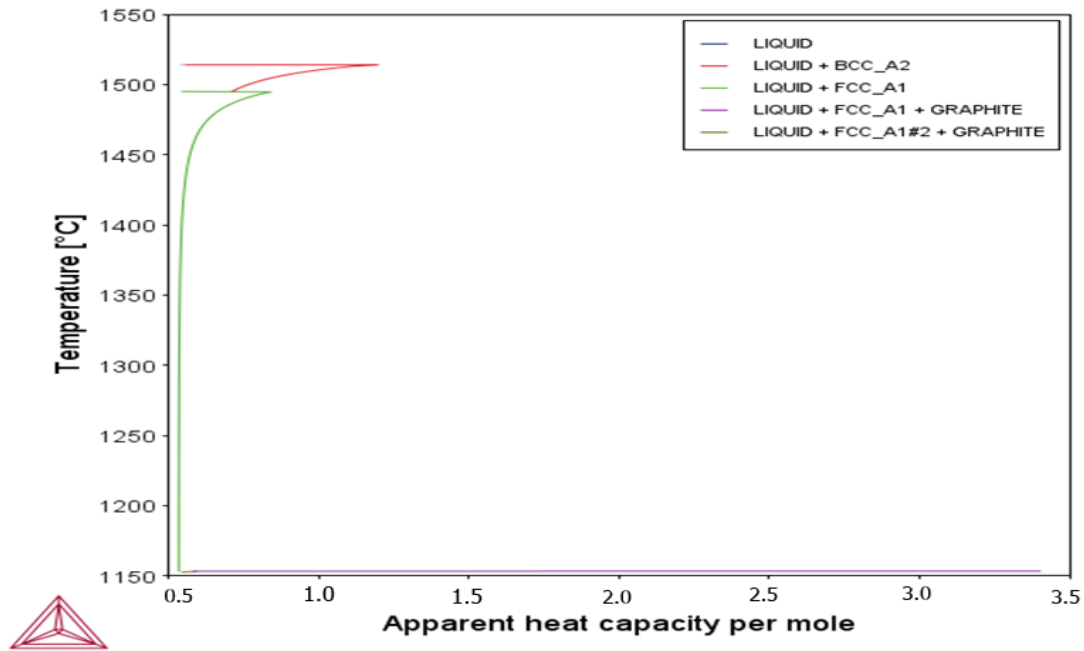


Fig. 3. Apparent heat capacity per mole in Fe-Ni-C system

Table. 2 apparent heat capacity of Fe-Ni-C system.

Apparent Heat Capacity	Temperature [°K]
0.03435	1503.6000
0.06631	1502.6000
0.09628	1501.6000
0.17589	1498.6000
0.19946	1497.6000
0.22174	1496.6000
0.24285	1495.6000
0.26285	1494.6800
0.28044	1494.6800
0.28130	1493.6500
0.31070	1492.6500
0.33807	1492.6500

The given result shows the apparent heat capacity of the carbon elements in the Fe-Ni-C System. The solid phases retained up to 1505.7 K. The highest apparent heat capacity is noted 0.33807 for 1492.6500 K. the increase in temperature results the increase in the apparent heat capacity of phases. The FCC_A1 phase is found the phase associated with highest molar volume in the Fe-Ni-C ternary alloy system with highest apparent heat capacity. The temperature variation results the composite phases to be disappears with required level of annealing. The system is found lowest apparent heat capacity 0.03435 with temperature of 1503.6000 K. The apparent heat capacity of FCC is found more responsive and found in austenite coordination.

5. Conclusion

The thermodynamic properties analysis of the Fe-Ni-C_X (X=0.3-0.5) ternary alloys is investigated through the Thermo-Calc package with FEDAT databases and Calphad method. The Fe-Ni, binary alloy are kept base component, while the Carbon composition is maintained 0.3, 0.4, and 0.5 mass percent for alloying. The interfacial energy fluctuation values are found (0.04070, 0.02905, 0.01759) J/m². The magnetic properties are found activated at low temperature 500 K which shows the maximum withstanding power of the alloy toward demagnetization. The evaluation of interactions is found maximum at 0.04070 J/m² in the Fe-Ni-C ternary alloy system. The system shows more phase's arrangements and compositions at low temperature and at high temperature, the phases arrangements decreases and the vitality range of the alloy decreases. The Fe-Ni-C system shows FCC_A1 phase is stable at temperature variation in the system. At low temperature 1492 K, the density of system is maximum value of 0.33945 gm/m³, which indicated the majority phases composition in the given alloy system. With the increase in temperature the composite nature phases overcomes and the most withstanding phases retained. At the highest temperature from 1505.72 K, the density of phases becomes constant and it indicates the rare temperature withstanding phases. The alloy shows increasing coarsening rate at low temperature for Ni contents alloying. At higher temperature, the progress of material to remove grains of carbides and refining the grains are low. interfacial energy increases with increasing temperature as it indicates the imbalanced molecular forces of carbides in the alloying elements. The fluctuations in the density of phases are changing with temperature as a result of phase's nature and stability. The highest mole fraction is seen at 1484.65 K with 0.35044 of value. The FCC_A1 phase is found the phase associated with highest molar volume in the Fe-Ni-C ternary alloy system. The temperature variation results the composite phases to be disappears with required level. The system is found highest apparent heat capacity 0.39269 with temperature of 1501.02 K. the apparent heat capacity is found maximum in the Ni-rich portion of alloy, indicating the more heat resistive properties of the system. The alloy shows better industrial and research applications.

ACKNOWLEDGMENTS

This study was supported by Beijing University of science and technology Beijing, China for providing simulation and modeling tools of TC window.

References

- A. Gabriel, G.ustafson and Ansara. (1987).** Thermodynamic evaluation of the C-Fe-Ni system, *Calphad*, 11. 203-218.
- B.Hallstedt, Dejan Djurovic, Jorg von Appen, Richard Dronskowski. (2010),** Thermodynamic properties of cementite Fe_3C , *Calphad*, 34(1). 129-133. <http://doi.org/10.106/j.calphad.2010.01.004>
- Gorsse, S.Tancret, F. Tancret, (2018).**Current and emerging practices of CALPHAD toward the development of high entropy alloys and complex concentrated alloys. *J. Mater. Res.* 33, 2899–2923.
- I. J.H. Weber. (2001).** Encyclopedia of Materials: Science and Technology, *Elsevier*, 3.9913.
- I. Gwalani, B. Gorsse, S. Gray, K. Han, T. Everett, (2018).** Modifying transformation in high entropy alloys or complex concentrated alloys via thermo-mechanical processing. *Acta Mater.* 153,169–185.
- I. Ohnuma, S Shimenouchi, T. omori, K.ishada, (2019).** Experimental determination and thermodynamic evaluation of the low temperature phase equilibria in the Fe-Ni system, *calphad*, 67.101677.
- J.-O.Andersson., T.Helander, L.Höglund. P.F.Shi, B.sundman. (2002).** Thermo-Calculations: Computational tools for materials science, *Calphad*. 26, 273–312.
- J. Liu, L.J. Riddiford, C. Floristean, F. Goncalves-Netoa, M.Rezaeeyazdi, L.H. Lewis, and K. Barmak. (2016).** Refractory high entropy alloys, *J. Alloys Compd*, 593.689.
- J.M. Jeon, S.Y. Kwon, D. Lindberg, M.K. Peak. (2021).** Thermodynamic Assessment of Liquid Fe-Ni-C Alloy Using Modified Quasichemical Model, *JOM*, 73,679–687.
- L.B. Chen, R. Wei, K. Tang, J. Zhang, F. Jiang, L. (2018).**Heavy carbon alloyed FCC structured high entropy alloy with excellent combination of strength and ductility *Mater. Sci. Eng. A*, 716. 150-156.
- Senkov, O.N. Miller, J.D. Miracle, D.B. Woodward, C. (2015).** Accelerated exploration of multi-principal element alloys for structural applications. *CALPHAD* 50, 32–48.
- Shi Chen, yong sheng Li. (2019).** Quantitative phase field simulation of composition partition and separation kinetics of Nano-scale phase in Fe-Cr-Al alloy, *journal of Nano-materials*, 11.
- S Sheibani, S Heshmati-manesh. (2010).** Structural investigation on nano-crystalline cu-cr supersaturated solid solution prepared by mechanical alloying, *journal of alloys and compound*, 495,59-62.

Waseem Ullah shah, Dil Faraz khan, Haiqing yin., Athanasius G.(2022a).Thermodynamic calculations of high entropy Fe-Mn binary alloy system using Calphad method based on Thermo-Calc Package and Pbine,fedate databases, *Kuwait J.sc*,49,2(2022)1-11. <https://doi.org/10.48129/kjs.11303>

Waseem Ullah Shah, Dil Faraz khan, Haiqing yin .Saeed Ullah Jan. (2022b). Thermo-mechanical assessment of high entropy (Fe-Ni-Cx ($x=0.3-0.5$), (Fe-Cr-Cx ($x=0.3-0.5$) ternary alloys system using Calphad method, *Kuwait J.sci*, online first, (2022) 1-12. Doi: <https://doi.org/1010.48129/kjs.18613>

Waseem U Shah, Dil F khan, Saeed U Jan Haiqing yin. (2022c). Modeling of thermodynamic properties of (Fe-Ni-C, Fe-Cr-C) alloys using computational approach, *Kuwait J.sci*, online first, (2022) 1-15

Sumaryada, T.Sofyan A. (2019). Simulations of the extra terrestrial and terrestrial performance of GaAs/Ge dual-junction solar cells, *Kuwait J.sc*.46 (2019)4, 58-65.

Sung-Kwang, Wanlin Wang. (2015). Modeling surface tension of multi component liquid steel, Quasichemical modified and constrained Gibbs energy minimization, *metals and materials international* **21**(2015) 765-774. <https://doi.org/10.1007/s12540-015-4619-z>

Wei Xiong. (2012). Thermodynamic and kinetic investigation of the Fe-Cr-Ni system driven by engineering application, Stockholm.

Y. Xu, Q. Jin, X. Xiao, X. Cao, G. Jia, Y. Zhu. (2011). The Effects of Carbon Content on the Microstructure and 650°C Tensile Properties of Incoloy 901 Super alloy
Sci. Eng. A 528, 4600-7.

Z.K. Liu, Y. Wang, and S. Shang. (2014). Thermal expansion anomaly regulated by entropy, *Sci. Rep.* 4, 7043.

Submitted: 07/03/2022

Revised: 28/04/2022

Accepted: 10/05/2022

DOI : 10.48129/kjs.19317

Production of titanium oxide nano wires with bundle structure using single anodic process

^{1,*} Mustafa Shakir Hashim , ²Reem Saadi Khaleel

^{1,2} Dept. of Physics Education college, Mustansiriyah University,
Baghdad, Iraq

*Corresponding author email : mustmust@uomustansiriyah.edu.iq.

Abstract

In a single process, the surface of Ti was transformed into titanium oxide nanowires (TNWs) at room temperature. The rapid breakdown anodizing method (RBA) of producing deposited spherical nanoparticles was modified. Instead, TNWs attached to the Ti metal base were formed. To slow down the reactions of these processes, 25,50, and 75wt % glycerol were added separately to the anodizing solution of RBA. The results of the X-ray diffraction (XRD) tests revealed the amorphous structure of the formed TNWs for all samples. The produced TNWs had the shape of micro bundles with nanowires. Their diameters were less than 50 nm, as shown by scanning electron microscope (SEM) images. The prevalence of titania bundles was more intense when a lower amount of glycerol was used. The tallest length of the nanowires decreased from 32 μ m to 8 μ m with the increase of glycerol; so by using a suitable electrolyte solution, the anodizing process can be effective for controlling the size of TNWs. The decrease in atomic percent oxygen with increasing glycerol was confirmed by energy dispersion X-ray (EDX) spectra.

Keywords: Anodic process; bundle structure; glycerol; nanowires; titania.

1. Introduction

RBA technique was used to produce nano-oxides for different purposes, such as bioactive materials, sensors, and photocatalytic decolorization (Saima *et al.*, 2018; Mustafa & Reem, 2020; Reem & Mustafa, 2020). This method provides a cheap and simple way to produce different nano oxides deposited on different bases with dissimilar shapes and compositions. Utilizing this technique; Mustafa *et al.* produced nanoparticles as precipitated powders of different materials such as ZnO, Cu₂O, MgO, and TiO₂ (Mustafa *et al.*, 2021). In order to use these powders in some applications, like, for example, sensors; a deposition technique must be used to deposit them on appropriate bases. An electrophoretic deposition technique was used to deposit TiO₂ that was produced by RBA on a Ti base to use it as a gas sensor (Reem & Mustafa, 2019). The process of forming precipitated nanopowders and using another technique to deposit them on suitable bases can be shortened by one process, as in the present work.

In general, the methods for producing TNWs can be divided into two categories: hydrothermal and anodizing techniques; but the production of these nano products by the anodizing method is not a one-step process. Usually, TiO₂ nanotubes (TNTs) are converted into TNWs in different ways, Ming *et al.*, fabricated TNWs connected directly with TNTs arrays

following four stages and using two successive anodic processes with different conditions (Ming *et al.*, 2012). Even nanowires made of materials other than titanium oxide often require more than one step; Xiangming *et al.* prepared Cu nanowires using a two-step approach and further studied the thermal oxidation behavior of Cu nanowires in dry oxygen (Xiangming *et al.*, 2021).

Most of the processes that produce nanowires need temperatures greater than room temperature. The hydrothermal process involves relatively high temperatures and pressures (Wenxian *et al.*, 2018). Endre *et al.*, 2007 used the hydrothermal conversion of self-assembled TNTs into nanowires in a revolving autoclave (Endre *et al.*, 2007). When TNTs are manufactured at temperatures exceeding 400°C, nanowires are commonly detected (Shalini *et al.* 2021). Poudel *et al.* transformed TNTs to TNWs by annealing at 650°C (Poudel *et al.*, 2005). The electro spinning technique followed by annealing was also utilized to fabricate well-aligned TNWs with different crystal phases (Zhou *et al.*, 2019).

With this participation, an attempt was made to convert Ti to TNWs at room temperature by using a simple, cheap, and one -step process.

2.Experimental details

After cleaning with absolute alcohol (from Sigma-Aldrich, USA), 0.1 mm thick Ti foils (from Ti foil manufacturer - Baoji Energy Titanium Co, China) with a rectangular shape (1x2 cm²) were immersed in an electrolyte. This electrolyte was made up of 0.1 M HClO₄ (from Sigma-Aldrich, USA) and glycerol (from Phywe, Germany). Three volume percent of 25, 50, and 75% glycerol were added separately to slow down the reactions. The viscosity was measured by hand viscosity meter (Viscolite), PCE Instruments UK Ltd. Table 1 displays some properties of the solutions used in this work. During each electrochemical process, two Ti pieces were used, one as a working electrode (anode) and the other as a control (cathode). The applied voltage was 20 volts, and the distance between the two electrodes was 0.5 cm. The time of the process was 30 minutes at room temperature. The produced surfaces were tested using XRD techniques (Shimadzu X-ray diffractometer-6000)-Japan. The particle sizes and appearances were evaluated using (SEM+EDX), from (ZEISS EVO LS10- Germany. The prepared samples were optically micrographed using an optical microscope (KERN Transmitted light microscope OBL-1)-Germany.

Table1. Density and viscosity of glycerol/water mixtures.

	Glycerol 25%	Glycerol 50%	Glycerol 75%
Density of mixture [kg/m ³]	1053.1	1136.5	1211.1
Dynamic viscosity of mixture [N s/m ²]	1.52*10 ⁻³	5.69*10 ⁻³	4.96*10 ⁻²
Kinematic viscosity of mixture [m ² /s]	1.44*10 ⁻⁶	5*10 ⁻⁶	4.1*10 ⁻⁵

3.Results and discussion

The microbundles with nanowires resulting from the modified RBA process are shown in Figure 1.

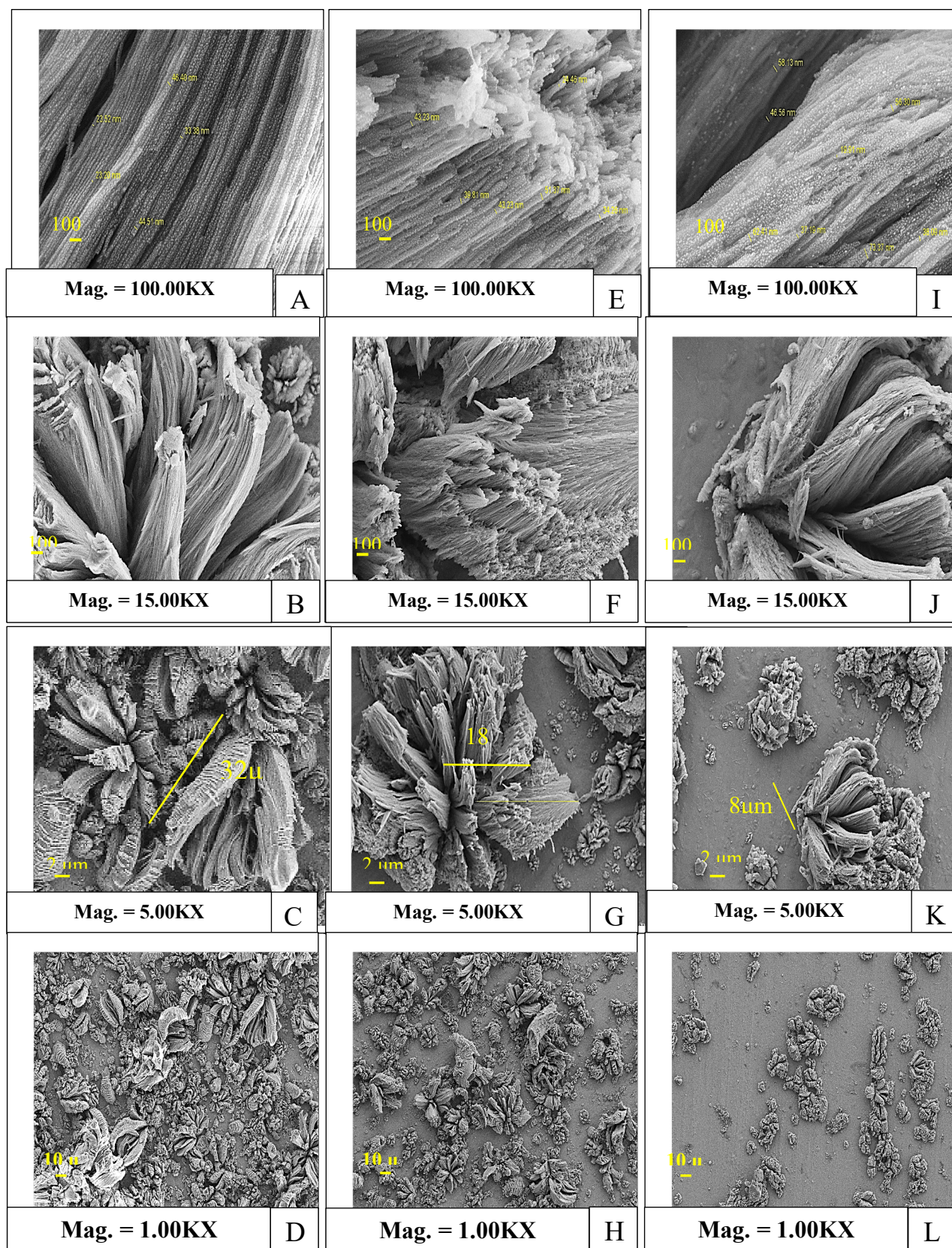


Fig. 1. SEM images of anodized Ti by modified RBA: (A to D) Glycerol 25%; (E to H) Glycerol 50% and (I to L) Glycerol 75%.

SEM images (A, E, and I) in Figure 1 revealed that the TNWs were in the shape of micro bundles. The average nanowire diameter was measured and tabulated in Table 2. This diameter increased with the glycerol volume ratio. Also, Figure 1 shows that; the increase in glycerol did not change the shape of the nanowires but the nanowires' tallest length reduces from 32 μ m to 8 μ m, see images C,G, and K. This result is in agreement with the reports that confirmed that the use of glycerol produced long TNTs due to its high relative viscosity (Zainovia *et al.* 2011).

Table2. Variation of TNWs dimensions with Glycerol volume ratio.

	Glycerol 25%	Glycerol 50%	Glycerol 75%
Nanowires' tallest length	32 μ m	18 μ m	8 μ m
Average Nanowire diameter	36.8nm	39nm	46.8 nm

It can be noticed from the SEM images and optical micrographs (Figure 2) that there are areas free from the effects of anodizing, where the bundle structure is absent from those areas, which indicates that the anodizing process may have attacked only areas containing stresses or weak areas. Increasing glycerol increases the viscosity of the anodizing solution, which affects the movement of ions and thus weakens the process of effective ions attacking the weak sites on the surface of the titanium (Lim *et al.*, 2016).

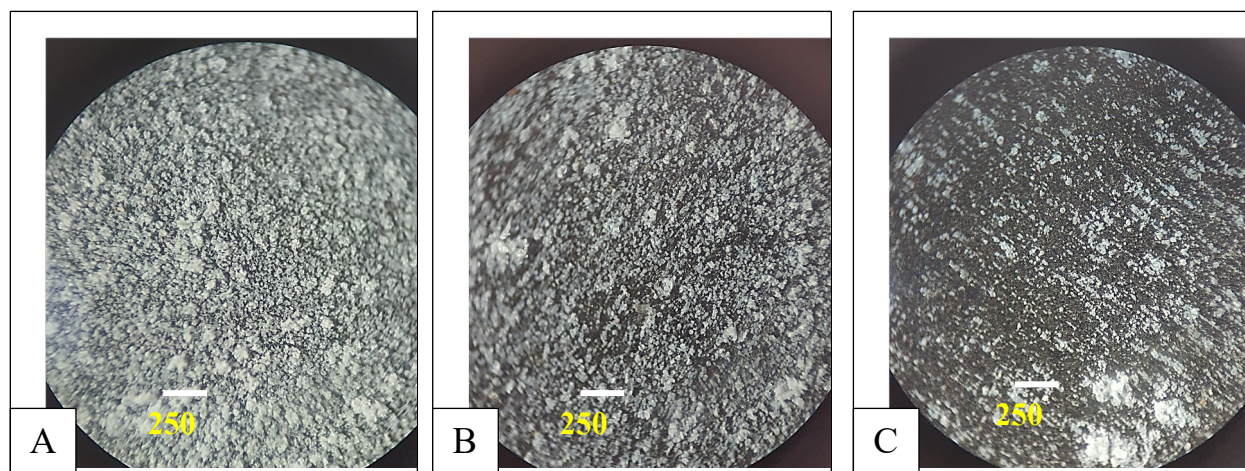


Fig. 2. Optical micrographs for as prepared samples A: Glycerol 25%; B: Glycerol 50%;C: Glycerol 75%.

The atomic compositions that make up the TNWs are shown in EDX spectra in Figure 3; wt% and at% of these elements are tabulated in Table 3.

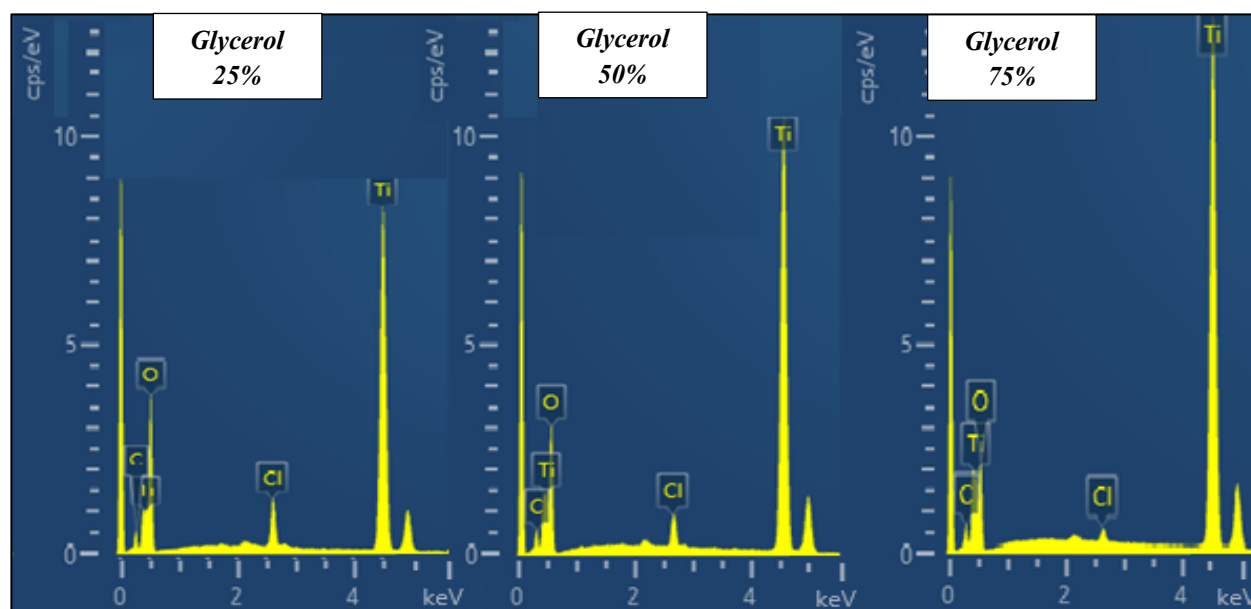


Fig. 3. EDX patterns of the three samples with different glycerol ratio.

Table 3. Weight% and Atomic% for the TNWs elements.

Element	Glycerol 25%		Glycerol 50%		Glycerol 75%	
	Weight%	Atomic%	Weight%	Atomic%	Weight%	Atomic%
Ti	46.3	22.3	54.5	28.3	63.4	36
O	46.2	66.7	39.3	61.2	31.1	52.9
C	4.8	9.2	4.4	9.2	4.6	10.4
Cl	2.63	1.71	1.71	1.2	0.75	0.58
	100.00	100.00	100.00	100.00	100.00	100.00

After anodizing, the presence of oxygen in the Table3 confirmed the oxide production. Observing the Ti/O ratio in this Table shows that it varies with glycerol ratios. The anodized sample with the highest percentage of oxygen had the lowest percentage of glycerol; this clearly indicates the effective role of glycerol in reducing the oxidation process and then forming titanium oxides.

At about 0.2 keV, an extra peak of the C element was identified in the EDX spectra. This element was formed as a result of the glycerol electrolyte that was absorbed by the TNWs during the electrochemical process.

EDX spectra show peaks belonging to chlorine indicating its entry into the structure of TNWs. The source of this element is perchloric acid, which was used in the anodizing solution. Table 3 shows the inverse relationship between the amount of glycerol and the chlorine element, this is a natural result of the materials' percentages used in the anodizing solution for this work.

Figure 4 shows the XRD patterns of the three samples. There are no peaks associated with the titanium oxides, which refers to the amorphous structures of these two phases. All the peaks in these patterns correspond to the pure titanium phase. The intensity of the dominant peak (103) increased when the glycerol percentage was increased from 25% to 75%. The coexistence of titanium oxide amorphous phase with Ti crystalline phase may explain the changes in these patterns.

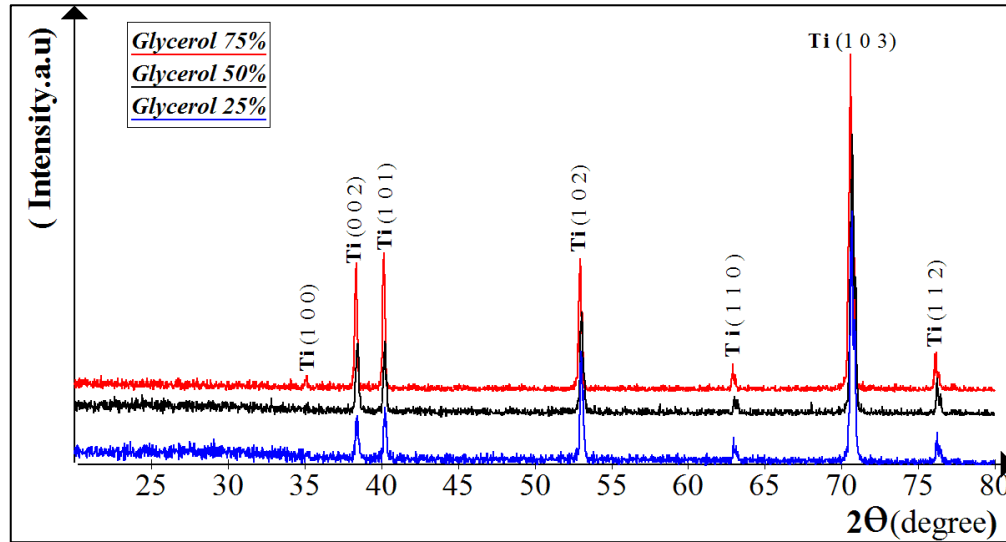


Fig. 4. XRD patterns of as prepared samples by modified RBA technique.

3.1 Mechanism formation of TNWs

The process of the formation of TNWs includes three main steps: oxidation of the Ti surface, etching of the oxidation layer, and building nanowires. After the electrochemical cell's power is turned on, metallic cations (Ti^{4+}) form on the anode's surface:



As shown in eq.2, TiO_2 begins to form on the Ti metal's surface, with O^{2-} species arising from H_2O dissociation (Su *et al.* 2016).



After the formation of the titania starting layer, the electric field inside this layer controls the Ti^{4+} outward migration and the O^{2-} inward movement (Taib *et al.* 2016). Because of this migration, the volume of TiO_2 increased, and the lattice distortion increased. To minimize internal stress, a considerable number of microcracks occur at the oxide/electrolyte contact. The electrolyte instantly fills these gaps.

Chemical etching happens when chloride ions are present, causing cracks to grow bigger and turn into pits. Cl^- ions can also be incorporated into the TiO_2 lattice, see eq. 3.



The oxide layer is formed within the pits as O_2 ions transfer inward from the electrolyte to the metal surface after pitting. The oxidized metal ions Ti^{4+} move outwards, and the Titanium oxide layer that forms is peeled away by the chloride ions, resulting in water soluble $[\text{TiCl}_6]^{2-}$ ions.

When the balance between oxide growth and chemical etching of oxide is maintained, TNWs are generated (Saima *et al.* 2018).

Figure 5 demonstrates the formation of TNWs from nanoparticles with size less than 10 nm, indicating that these particles were created first and then rejoined in the form of nanowires.

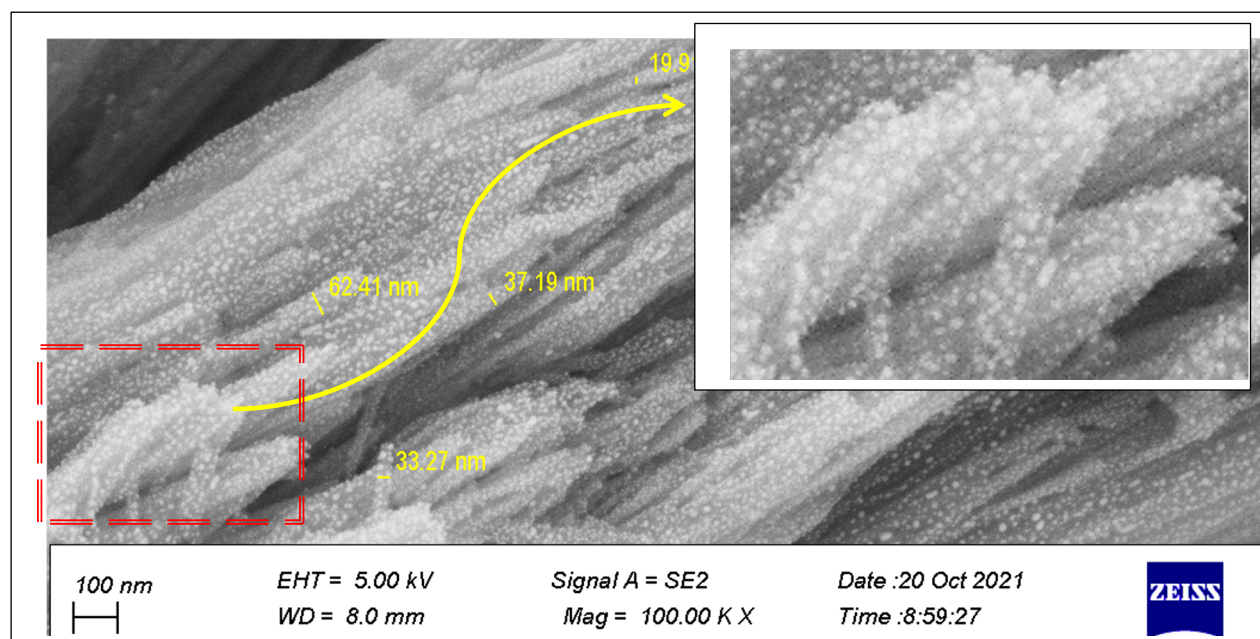


Fig. 5. The formation of TNWs from TNPs.

By comparing the RBA process (without glycerol), which produces TNTs in powder form (Rajini *et al.*, 2011), with the current process of producing TNWs in the presence of glycerol; one found that the separation of TNWs from Ti base into chemical solution stopped and the construction process of TNWs was enhanced. The inseparability of TNWs may be attributed to the reduction of the tensions between them and the Ti base as a result of the presence of glycerol (Fahim *et al.*, 2009). Also, the gases arising from the reactions may separate TNWs from Ti base, but the presence of the high density of glycerol slowed the rate of these gases.

3.2 The role of the electric field during TNWs forming

The electric field between the cathode and the anode affects the RBA process and the construction of TNWs because it affects the ions exchanged during this process. Image D, H, and L in Figure.1 shows that some areas of the Ti base are free of TNWs, which could be attributed to a weaker electric field in those locations and a stronger electric field in others. The presence of strong electric field regions is due to the presence of nano protrusions on these locations, which make them more susceptible to anodizing reactions than others, resulting in the formation of nano bundles only on these locations (Mustafa & Reem, 2018). Therefore, it can be concluded that the number of nano-protrusions decreases in the presence of glycerol because it reduces the stresses that produced them.

Image A, E, and I in Figure.1 show the parallelism of the nanowires to each other, which indicates the effect left by the electric field. As for the curvatures of these wires, they may have resulted from the drying out and evaporation of the water of the chemical anodizing solution.

Finally, one of the properties of the TNWs produced in this research, as shown in Figure.1, is that they adhere to each other and do not exist individually. This connection process may lower the surface energy of TNWs (Sweta *et al.*2020).

4.Conclusions

The anodizing method can be effective for producing TNWs and controlling the dimensions of these nanostructures using a suitable electrolyte solution. The amount of glycerol in the anodizing solution did not affect the overall shape of TNWs, but it could change their lengths and diameters.

ACKNOWLEDGEMENTS

The authors would like to acknowledge the Mustansiriyah University for supporting this research work.

References

B. Poudel , W. Z. Wang , C. Dames , J. Y. Huang , S. Kunwar , D. Z. Wang , D. Banerjee , G. Chen and Z. F. Ren (2005). Formation of crystallized titania nanotubes and their transformation into nanowires. *Nanotechnology*. 16, 1935–1940.

Endre H., Ákos K., Zoltán K. and Imre K. (2007) Hydrothermal Conversion of Self-Assembled Titanate Nanotubes into Nanowires in a Revolving Autoclave. *Chem. Mater.* 19(4), 927–931.

Fahim NF, Sekino T.(2009). A novel method for synthesis of titania nanotube powders using rapid breakdown anodization. *Chem Mater.* 21,1967–1979. doi: 10.1021/cm900410x.

Lim Y. Chin, Zulkarnain Z., Zuraida Kh. and Siti S. Ismail. (2016) Electrochemical synthesis of ordered titania nanotube in mixture of ethylene glycol and glycerol electrolyte. *Malaysian Journal of Analytical Sciences*. 20 (2), 373 – 381.

M. Zhou, Y. Liu, B. Wu, X. Zhang . (2019) Different crystalline phases of aligned TiO₂ nanowires and their ethanol gas sensing properties, *Phys. E Low-Dimensional Syst. Nanostructures*. 114 (113601) [https:// doi:10.1016/j.physe.](https://doi.org/10.1016/j.physe.2019.113601)

Ming-Y. Hsu, Hsin-Ling H., and Jihperng L. (2012) TiO₂ Nanowires on Anodic TiO₂ Nanotube Arrays (TNWs/TNAs): Formation Mechanism and Photocatalytic Performance. *Journal of The Electrochemical Society*. 159 (8) , H722-H727.

Mustafa Sh. Hashim , Reem S. Khaleel, Dalal M. Naser (2021). Synthesis of oxides' nanoparticles to produce aqueous solutions for antimicrobial applications . *Pak. J. Engg. Appl. Sci.* 29, 58–63.

Mustafa Sh. Hashim and Reem S. Khaleel (2020) . The bioactivities of prepared Ti, Zn, Titanium oxide , ZnO and Al₂O₃ nanoparticles by rapid breakdown anodization technique. *Surfaces and Interfaces*. 20(100640) , 1-8.

Mustafa Shakir Hashim, Reem Saadi Khaleel (2018). Fabrication of Gas Ionization Sensor to Recognize Gases and Measure Pressure and Humidity. *Iran J Sci Technol Trans Sci*. 42, 181–189.

Rajini P. Antony, Tom Mathews, Arup Dasgupta, S. Dash, A.K. Tyagi, Baldev Raj. (2011). Rapid breakdown anodization technique for the synthesis of high aspect ratio and high surface area anatase TiO₂ nanotube powders. *Journal of Solid State Chemistry* 184 , 624–632.

Reem S. Khaleel and Mustafa Sh. Hashim (2020) . Fabrication of ZnO sensor to measure pressure, humidity and sense vapors at room temperature using the rapid breakdown anodization method. *Kuwait J. Sci.* 47 (1) ,42-49.

Reem S. Khaleel and Mustafa Shakir Hashim (2019) . Fabrication of Titanium oxide sensor using rapid breakdown anodization method to measure pressure, humidity and sense gases at room temperature. *Iraqi Journal of Science*. 60(8) ,1894-1703.

Saima A., Henrika G., Jouko L. and Simo-Pekka H. (2018) . Titania nanotubes prepared by rapid breakdown anodization for photocatalytic decolorization of organic dyes under UV and natural solar light. *Nanoscale Research Letters*. 13 (179) , 1-14.

Shalini R., Dephan P., Sunaja D. KR. (2021) A review of hierarchical nanostructures of TiO_2 :Advances and applications. Applied surface science advances. 3 (100063), 1-34.

Sweta Shrestha, Bo Wang, Prabir Dutta (2020). nanoparticle processing: Understanding and controlling aggregation, Advances in Colloid and Interface Science. 279, 102162.

Taib, M.A.A., Tan, W. K., Okuno, T., Kawamura, G., Jaafar, M., Razak, K. A. and Lockman, Z. (2016). Formation of TiO_2 nanotube arrays by anodic oxidation in LiOH added ethylene glycol electrolyte and the effect of thermal annealing on the photoelectrochemical properties. AIP Conference Proceedings. 1733, 1-6.

Wenxian L., Xiaofang H., Jie H., Fengcang M., Ying L., Rongkun Z., Abdulmohsen A. Alshehri, Md Shahriar A , Yusuke Y. and Xiaodong W. (2018) .Magnetic coupling in Mn_3O_4 -coated γ - MnOOH nanowires. Surface innovations. 6(4) , 250-257.

Xiangming Z., Peng P., Hao Q., Zuming H., Jiangbin S. (2021) .Preparation of copper nanowires and thermal oxidation behaviour in dry oxygen. Surface Innovations. <https://doi.org/10.1680/jsuin.21.00033>.

Zainovia L. , Syahriza I., Go K. and Atsunori M. (2011). Formation of zirconia and titania nanotubes in Fluorine contained Glycerol electrochemical bath. Defect and Diffusion Forum. 312-315, 76-81.

Submitted: 18/03/2022

Revised: 11/04/2022

Accepted: 24/04/2022

DOI : 10.48129/kjs.19577

Investigating the effects of the different rhodamine 6G laser dye volume ratios on the optical properties of PMMA/PC films

Muhammad S. Jalil^{1,*}, Farah J. Kadhum², Asrar A. Saeed³, Mahasin F. Hadi Al-Kadhemy⁴

¹ Basic Science Branch , Dentistry College, Mustansiriyah University, Baghdad, Iraq ^{2,3,4}Dept. of Physics , College of Science, Mustansiriyah University, Baghdad, Iraq

*Corresponding author: dr.muhammad sami@uomustansiriyah.edu.iq

Abstract

Rhodamine 6G – polymethylmethacrylate/polycarbonate (Rh6G–PMMA/PC) were prepared by a casting method at room temperature with diverse volume ratios of Rh6G dye solution (5, 10, 15, 20 and 25) ml. The as-prepared films were categorised via UV–Vis spectrophotometer, and the optical properties were investigated in the wavelength range of (200-800) nm. The absorption peaks for pure PMMA/PC film were affected by inserting Rh6G dye solution, the wavelength of absorption peak of pure PMMA/PC film is at 300 nm and 340 nm while there are different behaviour at different concentration of RG6 after mixing with PMMA/PC films; there are red shift for concentrations (10 and 25 ml) of RG6 after mixing with PMMA/PC films by appear another peaks at 530 nm and 535 nm respectively. In addition, there is a blue shift for concentrations (15 and 20 ml) of RG6 after mixing with PMMA/PC films, as evidenced by the appearance of new peaks at wavelength 265 nm. Furthermore, new peaks appeared and were absorbed while the energy band gap was influenced, with values ranging from 4.3 eV for pure PMMA/PC film to 4.18 eV for mixtures 10 & 25 ml concentration of Rh6G/ PMMA/PC belonging to the red shift to 4.9 eV and 4.85 eV for mixtures 15 and 20 ml concentration of Rh6G/ PMMA/PC belonging to the blue shift.

Keywords: Dye doped polymer; laser dye; optical properties; PC polymer; PMMA polymer.

1. Introduction

The continuous efforts to find new types of materials as well as the physical properties, such as the optical characteristics of materials with remarkable efficacy in their corresponding field, influence material manufacturing.

Dye-doped polymer solid lasers can be attributed to the incorporation of laser dyes into polymer materials. Using polymers as a host matrix for organic laser dyes has many advantages.

One of the most important laser dyes is Rhodamine 6G, which is used as a gain medium (Th. G. Pavlopoulos,2002). In addition, Rhodamine 6G is widely utilised in photocoagulation therapy and ocular photodynamics due to its large number of wavelengths of high output power laser lithotripsy. Thus, Rhodamine 6G dye is the most commonly used because of its safety and effectiveness (V. I. Gavrilenko *et al*,2006; M. F H. Al-Kadhemy *et al.*,2020a).

Considering optical properties, the polymethylmethacrylate (PMMA) polymer has its specific optical features. This uncrystallised polymer exhibits remarkable transparency (92% light transmission) in the visible range from 380 nm to 780 nm. Thus, this material can be used to create light conductors, such as fibre optic filaments and films. PMMA can also be utilised

in the manufacture of optical products due to its refractive index of 1.49 (V. Raja *et al.*, 2003; C. Hall, 1989).

Polycarbonate (PC) polymers are characterised by their clarity, good electrical properties, high thermal stability and excellent impact strength. Moreover, these polymers are thermoplastic; that is, they are amorphous and transparent. PC polymer have excellent mouldability, low-temperature toughness and flame-retardant properties and are available in a variety of special grades (C. Hall, 1989; H. M. Nasser & O. D. Ali, 2010). Many researchers investigated the optical properties of PMMA, PC and Rh6G alone; they doped these materials with each other or with other organic dyes and obtained notable outcomes and applications (N. J. Hameed & M. R. Fraih, 2011; Asrar A. Saeed *et al.*, 2017; Asrar A. Saeed *et al.*, 2018). Doping the Rh6G dye with the PMMA/PC polymer substantially affected the physical properties, such as absorption, transmission, reflection spectra, refractive index, extinction coefficient and indirect energy gap compared with other parameters, resulting in varying positions of the max wavelength of solution spectra due to the addition of two polymers (PMMA and PC) (R. A. Al-Mousawi *et al.*, 2019). Films that are more stable than the dye solution used as an active medium in the solid laser where the properties of polymer PMMA are nearest to polymer PC are obtained by applying the aforementioned method (H. M. Zidon *et al.*, 2003; Mahasin F. H. AL-Kadhemy *et al.*, 2020b). PMMA/PC films with different Rh6G volume ratios will be investigated in this paper.

2. Experiment

The Rhodamine 6G laser dye processed by Sigma-Aldrich Company is characterised as follows: chemical formula $C_{28}H_{31}N_2O_3Cl$ and molecular weight ($M_w = 479.02$ g/mol) (C. Adnan, 2011). The PMMA with the chemical formula $(C_5O_2H_8)_n$ and molecular weight (200,000 g/mole) is made in Spain. The second polymer is the polycarbonate polymer with molecular formula $[C_{16}H_{14}O_3]_n$ and is processed by the Sabic Company (E. S. Guerra & E. V. Lima, 2013). The two polymers were chosen as host materials for Rh6G due to their excellent optical properties.

The cast procedure was used to prepare the pure PMMA/PC and Rh6G– PMMA/PC films. This casting method considering easy for preparing samples, have stable results and can done in normal environment (Mahasin F. H. AL-Kadhemy *et al.*, 2020c). The PMMA/PC solution was organised by dissolving 0.3 g of PMMA with 0.2 g of PC in 10 ml of chloroform. The PC solution was stirred properly with a magnetic stirrer till the polymer was dissolved and cast onto glass Petri dishes with a 10 cm diameter and then left to dry at room temperature approximately (25 – 30) °C for one day. The Rh6G solution with 1×10^{-5} mole/litre concentration was prepared along with the illustrated method in Ref. (Mahasin F. H. AL-Kadhemy *et al.*, 2020a, W. H. Abbas, 2012). The dissimilar ratios of this dye solution (5, 10, 15, 20 and 25) ml were then added to PMMA/PC solution and mixed well using a magnetic stirrer. Similar to the case using the above-mentioned method, the mixture cast aimed to obtain homogeneous Rh6G–PMMA/PC films. The UV-Vis spectrophotometer type (T70/T80 Series UV/Vis Spectrometer) was used in 200–900 nm of wavelength range to measure the absorption and transmission spectra.

3. Results and Discussion

Figure (1) displays the absorption spectra of pure PMMA/PC and Rh6G–PMMA/PC films for the different volume ratios (5, 10, 15, 20 and 25 ml). The pure PMMA/PC film demonstrated the following two peaks: the maximum wavelength of the 1st peak at 300 nm with 1.504 absorbance and that of the 2nd peak at 340 nm with 1.345 absorbance. This finding matched the results in ref. (Mahasin F. H. Al-Kadhemy, *et al.*, 2020b). The intensity of the peaks decreased with the addition of 5 ml Rh6G dye solution as illustrated in Figure (1) and Table (1).

In addition to the emergence of a peak for the Rh6G dye at 530 nm with 0.683 absorbance, the additional 10 ml dye solution increased the two peaks and resulted in the 530 nm red-shift for the second peak. A split in the peaks of the two polymers was observed at 15 and 20 ml of the dye solution. These peaks became three (265, 300 and 340 nm) with maximum absorbance for the new peak of 265 nm to the concentration of Rh6G (15 and 20 ml). The increased dye solution additive to 25 ml led to the disappearance of 265 nm peak and appeared the peak at 335 nm. Meanwhile, there are a red shift for concentration (10 and 25 ml) of Rh6G after mixing with PMMA/PC and blue shift for concentration (15 and 20 ml) of Rh6G after mixing with PMMA/PC.

The Rh6G dye played a role in splitting the peaks of PMMA/PC films and makes some changes in energy gap by whilst increasing the volume ratio of the dye solution because it raised the number of dye molecules that reduced the role of polymers.

These broad emissions are attributed to deep-level emissions, which can be caused by structural defects in polymer films. The emission attributed to defects in the nanocrystalline of the host or could be due to add the dye depending on the availability of associated structural defects (Akeel M. Kadim, 2022)

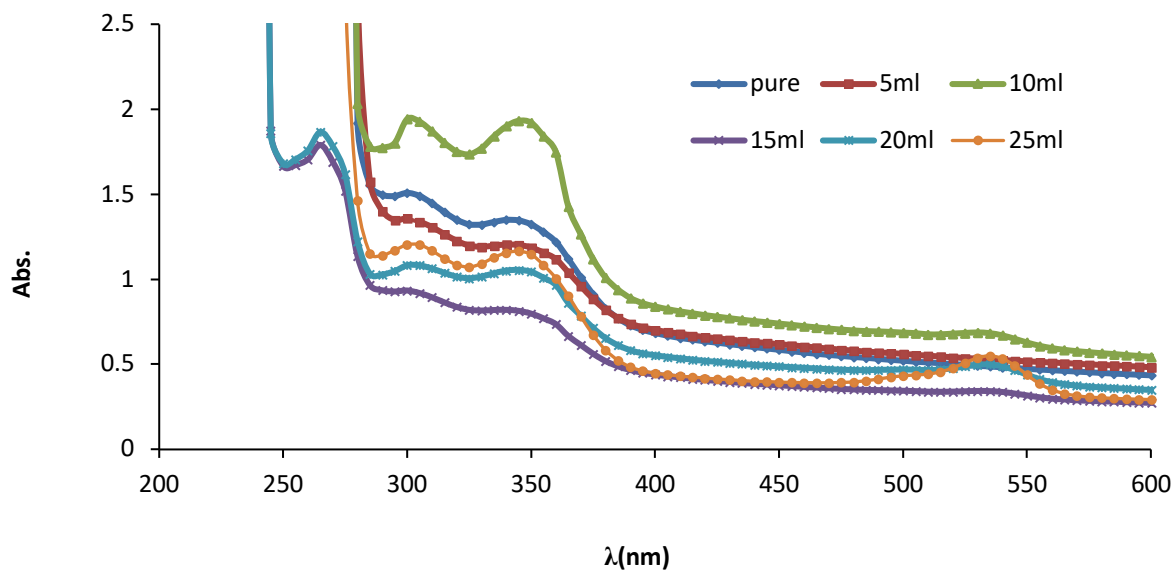
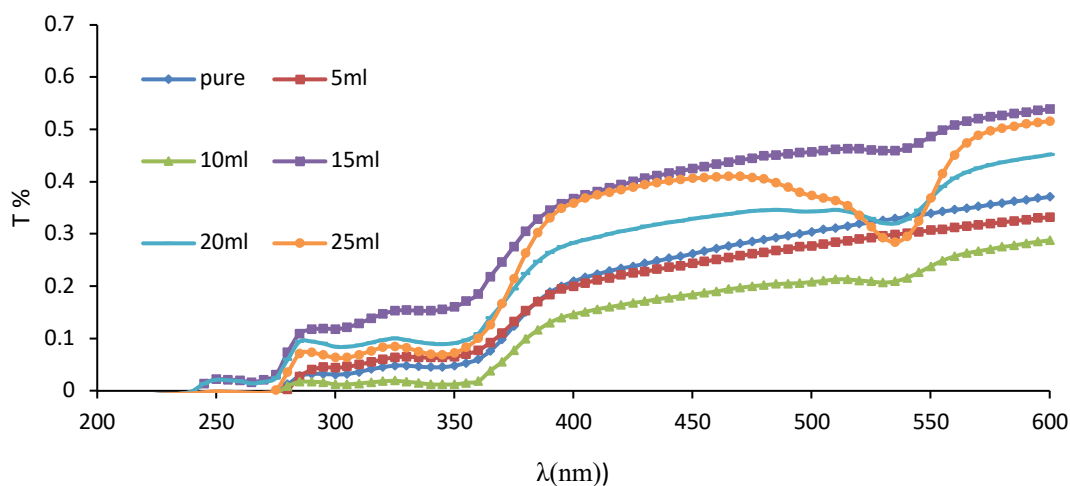


Fig. 1. Absorption spectrum of Rh 6G –PMMA/PC films for dissimilar volume ratios of dye

Table 1. Absorption data about pure PMMA/PC and Rh6G-PMMA/PC films

Samples	$\lambda_{\text{abs.}} \text{ (nm)}$	Abs.	$E_g \text{ (eV)}$
Pure PMMA/PC	300	1.504	4.3
	340	1.345	
5ml Rh6G/ PMMA/PC	300	1.354	4.18
	340	1.2	
10ml Rh6G/ PMMA/PC	300	1.938	4.18
	345	1.928	
	530	0.683	
15ml Rh6G/ PMMA/PC	265	1.786	4.9
	300	0.93	
	340	0.816	
20ml Rh6G/ PMMA/PC	265	1.862	4.85
	300	1.078	
	345	1.051	
25ml Rh6G/ PMMA/PC	300	1.199	4.18
	345	1.161	
	535	0.546	

Figure (2) exhibits the transmission spectra for all samples. The transmittance reveals a reduction in its value with an increase in the absorption spectra and the volume ratio of the dye solution. This finding indicates that the films became blackout or less transparent with the increase in the volume ratio of the dye solution.

**Fig. 2.** Transmission spectra of Rh6G –PMMA/PC films for diverse volume ratios of dye

The reflection spectra can be calculated on the basis of absorption and transmission spectra in accordance with the following law in Equation (1) (L. K. Chopra, & I. Kaur, 1983) as shown in Figure (3).

Figure (3) reveals the high ratio of dye (25) ml; the reflection value increased due to the increased amount of impurities.

$$R+T+A=1 \quad \dots\dots\dots (1)$$

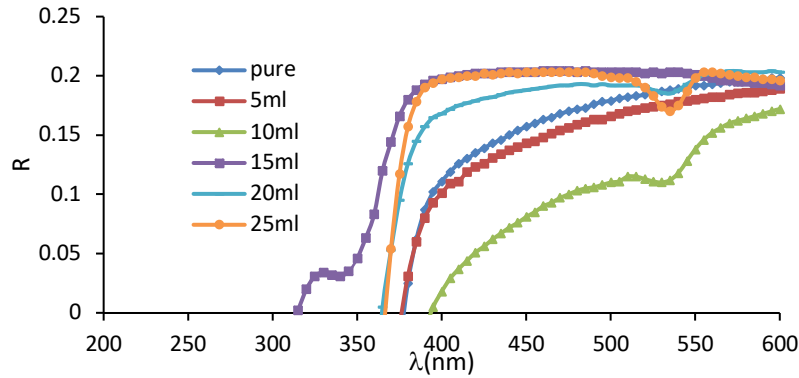


Fig. 3. Reflection spectra of Rh6G –PMMA/PC films for dissimilar volume ratios of dye

The behaviour reflects an increment in the refractive index (n) (Equation (2)) as demonstrated in Figure (4). An extinction coefficient (k) can be computed from Equation. (3); this coefficient represents an amount of energy loss due to the interaction between the spectrum and the charging mediums as shown in Figure (5) (J. L. Pankov, 1971; Asogwa PU, 2011).

$$R = \frac{(1-n)^2 + xK^2}{(1+n)^2 + xK^2} \quad (2)$$

$$K = \frac{\alpha\lambda}{4\pi} \quad (3)$$

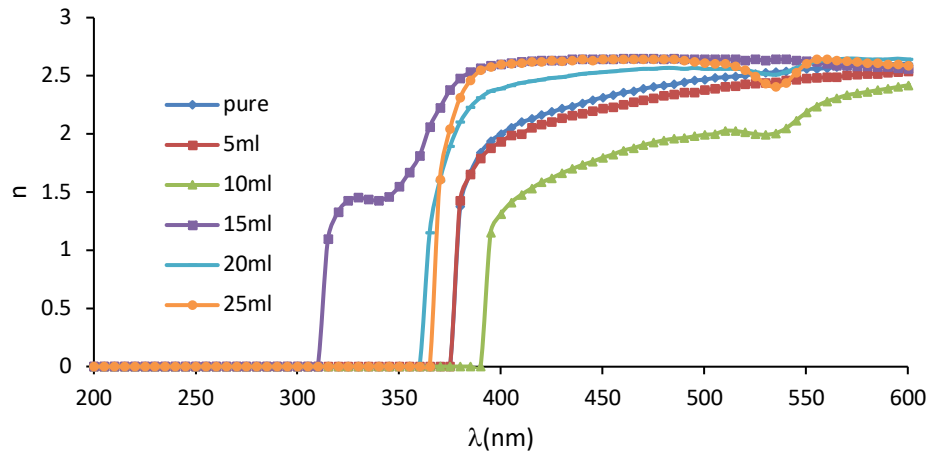


Fig. 4. refractive index (n) as function to wavelength for Rh6G –PMMA/PC films for different volume ratio of dye

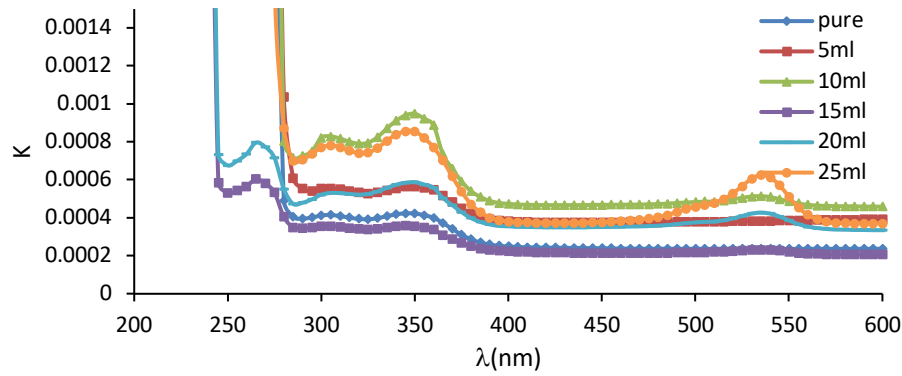


Fig. 5. extinction coefficient (k) based on the wavelength for Rh6G –PMMA/PC films for different volume ratio of dye

Equation (3) illustrates that the coefficient stands for a wavelength function; it depends on the absorption coefficient (α) offered by the coefficient in Equation (4) and defines the capability of materials to reduce the light that provides the wavelength alone, as shown in Figure (6) (Asogwa PU.,2011; Mahasin F. Hadi Al-Kadhemy *et al.*, 2017; Jahja Kokaj, 2011).

$$\alpha = \frac{2.303A}{t} \quad (4)$$

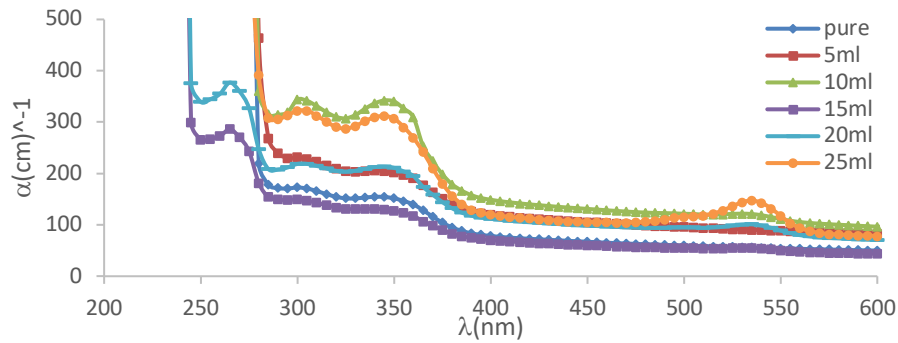


Fig. 6. Absorption coefficient (α) as function to wavelength for Rh6G –PMMA/PC films for different volume ratio of dye

The optical band gap can be estimated from Equation. (5) (L. K. Chopra, and I. Kaur, 1971; Mahasin F. Hadi Al-Kadhemy *et al.*, 2017).

$$(\alpha h\nu)^{1/r} = m(h\nu - E_g) \quad (5)$$

where m stands for constant, E_g represents the optical band gap energy, $h\nu$ stands for the incident photon energy and the exponent r is subject to on the transition kind. $n = 1/2, 2, 3/2$ and 3 based on allowable direct, allowable indirect, prohibited direct and prohibited indirect transitions, respectively.

The suitable transition was verified by approximating the power r that predicts indirect transition for PMMA/PC polymers under study. Nevertheless, the optical band gap was determined by drawing $(\alpha h\nu)^{1/2}$ set against $h\nu$ and extrapolating the straight-line portion of the curve to intercept the energy axis in Equation (5).

The magnitudes for E_g were obtained for the indirect transition of the samples (Figure (7)) and listed in Table (1). The values changed for the indirect transition from 4.18 eV to 4.9 eV as the volume ratio of Rh6G dye solution increased due to the expected partial dissociation of Rh6G dye attributable to polymer reduction (Asrar Abdulmunem Saeed *et al.*, 2020).

The absorption shift to lower wave length (blue shift) means the absorption shifts to higher energy which has a positive accompanied by high degree of order which increases other parameters like band gap. A red shift in the absorption spectra of a material will increase its ability to absorb a wider spectrum of light (more in the visible region) and decrease the band gap. There for according to red shift done with concentration 15 and 20 ml of Rh6G which mixed with PMMA/PC films the energy gap changed from 4.3 eV for pure PMMA/PC films to 4.9 eV and 4.85 eV for mixture with concentration of Rh6G 15 and 20 ml. The opposite appear with blue shift wharas the energy gap decreased from 4.3 eV for pure PMMA/PC films to 4.18 eV for mixture with concentration of Rh6G 10 and 20 ml.

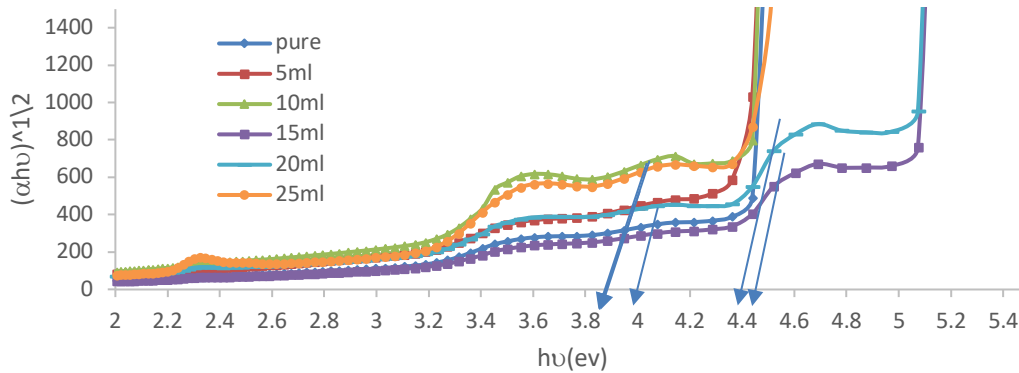


Fig. 7. energy band gap as function for Rh6G –PMMA/PC films for different volume ratio of dye

4. Conclusion

Overall, the paper highlighted the Rh6G-PMMA/PC films, which were primed by the casting technique. The effects of the change in the volume ratio of the Rh6G dye solution on the optical properties of the films had been carefully investigated. The results showed that the PMMA/PC films experienced an increase in intensity after adding the dye, resulting in the appearance of a new peak. Where the intensity change from 1.504 and 1.345 for wavelength 300 and 340 nm respectively belong to pure PMMA/PC film to 1.862, 1.078, 1.051 and 0.495 for wavelength 265, 300, 345 and 535 nm respectively belong to mixture of 20ml Rh6G/ PMMA/PC. Furthermore, the energy band gap had demonstrate big difference after adding Rh6G by decreasing and increasing the energy gap, first of all the decreasing energy gap from 4.3 eV for pure PMMA/PC films to 4.18 eV for concentration of Rh6G (5, 10 and 25 ml) which mixed to PMMA/PC film. The second showed the increasing energy gap to (4.85 and 4.9) eV for concentration (15 and 20) ml respectively for Rh6G after mixing the PMMA/PC films.

ACKNOWLEDGEMENTS

The authors would like to thank Mustansiriyah University (www.uomustansiriyah.edu.iq) Baghdad-Iraq for its support in the present work.

References

- Akeel M. Kadim, (2022)** Fabrication of nano battery from CdS quantum dots and organic polymer, Kuwait J.Sci., Vol.49, No.(1),January.pp(1-9)
- Asogwa PU. , (2011)** Band gap shift and optical characterization of PVA-capped PbO thin films: effect of thermal annealing, Chalcogenide Lett., 8(3), 163–70.
- Asrar Abdulmunem Saeed, Mahasin F. H. Al- Kadhemy, F. J. Kadhum, Z. J. Neamah, (2018)** Study the Effect of Ultraviolet Radiation on the Optical Properties of Pure PC and Anthracene Doping PC Films, Journal of Engineering and Applied Sciences, 13 (24), 10245-10253.
- Asrar Abdulmunem Saeed, Mahasin F. H. Al- Kadhemy and Z. J. Neamah, (2017)** The Effect of Anthracene on Optical Properties of Polycarbonate Films, Journal Of College of Education, 1, 81-94.
- Asrar Abdulmunem Saeed, F. J. Kadhum, Kh. N. Abbas, Mahasin F. H. Al- Kadhemy, (2020)** Effects of Anthracene Doping Ratio and UV Irradiation Time on Photo-Fries Rearrangement of Polycarbonate, Baghdad Science Journal, 17, 2, Special Issue, NICST, 652-662.
- C. Adnan, (2011)** The effects of introduction of Nanoparticles, coated and non-silica coated, on the emission spectra of an aqueous solution of Rh6G, KTH, School of Information and Communication Technology (ICT).
- C. Hall, (1989)** "Polymer Materials", Macmillan Education Ltd., London.
- E. S. Guerra and E. V. Lima, (2013)** Handbook of Polymer Synthesis, Characterization, and Processing, John Wiley & Sons, Inc.
- H. M. Nasser and O. D. Ali. (2010)** "Effect of molecular weight and illumination on optical constants of PMMA thin films" Iranian Polymer Journal 19 (1), 57-63.
- H. M. Zidon, A. Tawansi, and M. Abu – Elnader, (2003)** Miscibility, optical and dielectric properties, of UV – irradiated polyvinylacetate \ poly methyl methacrylate blends, Physica B, 339, 78 – 86.
- J. L. Pankov, (1971)** Optical process in semiconductors, London.
- Jahja Kokaj, (2011)** Characterization of optical and microscopic properties of ZnO films chemically deposited on a glass substrate, Kuwait J.Sci., Eng. 38 (2A) pp. 39-106.
- L. K. Chopra, and I. Kaur, (1983)** Thin film Devices Applications, plenum press, New York.

M. F. H. Al-Kadhemy, Kh. N. Abbas, W. B Abdalmuhdi, (2020)a Physical Properties of Rhodamine 6G Laser Dye Combined in Polyvinyl Alcohol films as Heat Sensor, IOP Conference Series: Materials Science and Engineering, 928(7), 072126.

Mahasin F. H. Al-Kadhemy, R. A. Al-Mousawi, F. J. Kadhum, (2020)b Effects of Adding Coumarin Dye on Physical Properties of Blend (PC-PS) Film, Iraqi Journal of Science, 61(7), 1633-164.

Mahasin F. H. AL-Kadhemy, S. A. Ibrahim, J. A. Salman, (2020)c Studying the Physical Properties Polyvinyl Alcohol Polymer Mixture with Silica Nanoparticles and its Application as Pathogenic Bacteria Inhibitor, The 8th International Conference on Applied Science and Technology (ICAST 2020) AIP Conf. Proc. 2290, 050013-1–050013-8.

Mahasin F. H. AL-Kadhemy, W. H. Abbas, (2012) Absorption spectrum of Crystal Violet in Chloroform solution and doped PMMA thin films, Atti Della Fondazione Giorgio Ronchi, 3, 359-366.

Mahasin F. Hadi Al-Kadhemy, Asrar Abdulmunem Saeed, Rana Ismael Khaleel & Farah Jawad Kadhum Al- Nuaimi, (2017) Effect of gamma ray on optical characteristics of (PMMA/PS) polymer blends, Journal of Theoretical and Applied Physics 11(3), 201-207.

N. J. Hameed & M. R. Fraih, , (2011) "Study of the Optical Constants of the PMMA/PC Blends", Eng. & Tech. Journal, 29(4), 698-708.

R. A. Al-Mousawi, Mahasin F. H. Al-Kadhemy, F. J. Kadhum, (2019) Effect of Adding Coumarin Dye on Optical Properties of Poly Carbonate Films, Al-Mustansiriyah Journal of College of Education 3, 63-80.

Th. G. Pavlopoulos, (2002), Scaling of dye lasers with improved laser dyes, Progress in Quantum Electronics, 26, 193–224.

V. I. Gavrilenko and M. A. Noginov, Ab initio (2006) study of optical properties of rhodamine 6G molecular dimers, J. Chem. Phys. 124, 044301; doi.org/10.1063/1.2158987.

V. Raja, A. K. Sarma and V. V. R. Nara Simha Rao, (2003) (optical properties of pure and doped PMMA – CO – P4VPNO polymer films), Materials Letters, 57, 4678 – 4683.

Submitted: 30/03/2022

Revised: 24/05/2022

Accepted: 26/05/2022

DOI : 10.48129/kjs.19853

Impedance analysis of single walled carbon nanotube/vinylester polymer composites

*Aykut Ilgaz

Dept. of Physics, Balikesir University, Balikesir, Turkey

** Corresponding author: aykut17ilgaz@gmail.com*

Abstract

This study presents impedance characteristics of single walled carbon nanotube/vinylester (SWCNT/VE) glass fiber reinforced polymer (GFRP) composites. The impedance measurements were carried out as a function of the frequency over range of 10^{-2} and 10^7 Hz at various temperatures between 300 K and 420 K. Bode and Nyquist plots of real and imaginary parts of complex impedance (Z^*) were obtained and Cole–Cole approach was used to interpret the impedance characteristics. The results indicated that the bulk resistance of the material decreases significantly as the temperature increases. The frequency-dependent AC conductivities were calculated using the complex impedance data and dimensions of specimen. It has been observed that the alternating current values are compatible with the Jonscher's power law. The behavior of dielectric constant and loss factor at the various temperatures were analyzed as a function of applied frequency. While the sample exhibited high dielectric permittivity in the low frequency region with the Maxwell-Wagner-Sillars (MWS) effect, it was observed that the permittivity decreased as a result of the dipoles' inability to rotate themselves in the field direction at high frequencies. No dielectric relaxation peak was observed in the loss spectra in our limits. From the results, it can be said that the contribution to the dielectric relaxation is due to the interface polarization and DC conductivity. Electric modulus formalism was also used to describe the conductivity and dielectric relaxation processes of SWCNT/VE binary composite. It was found that the obtained peak maximums shifted to higher frequencies as the temperature increased. It is concluded that the frequency regime below the peak maximum defines the range of mobile charge carriers, and in the regime above the maximum, the charge carriers are limited to short distance potential wells.

Keywords: Dielectric properties; electric modulus; impedance; single walled carbon nanotubes; vinylester resin.

1. Introduction

Since their discovery in the early 90s, carbon nanotubes have been used as high-potential reinforcement elements in many applications such as field-effect transistors (Liang *et al.*, 2015), energy storage (Zhu *et al.*, 2014), sensors (Daliri *et al.*, 2018) and composites (Kuilla *et al.*, 2010) over the past 30 years. The number of studies on the use of carbon nanotubes (CNTs) as a

reinforcement additive in traditional glass fiber reinforced polymer (GFRP) composites has increased considerably in the last two decades (Mahapatra *et al.*, 1991; Bouzerara *et al.*, 2011; Puertolas *et al.*, 2017; Das & Dobbidi, 2021). Many researchers reported impedance characteristics, conductivity mechanisms including percolating system, and relaxation phenomena of carbon nanotube reinforced composites (Antonucci *et al.*, 2007; Dang *et al.*, 2011; An *et al.*, 2013; Almuhammadi *et al.*, 2017; Anju & Narayanankutty, 2019; Ganesh *et al.*, 2020).

It is reported dielectric behavior of carbon nanotubes particles-filled polyester polymer composites at different temperatures using the Cole-Cole approach (Samir *et al.*, 2017). It has been proven that AC conductivity increases with increasing nanotube ratio and temperature. Aviles *et al.* studied the conductivity mechanism in the carbon nanotubes reinforced vinylester-based polymer composites. High conductivity is obtained even at low nanotube densities exceeding the percolation threshold (Aviles *et al.*, 2018).

The dielectric and impedance characteristics of multi-walled carbon nanotube (MWCNTs) and graphene oxide-carbon nanotube (GCNTs) reinforced acrylonitrile-butadiene-styrene (ABS) composites were studied comparatively (Jyoti *et al.*, 2018). It has been demonstrated that the materials can be used in electromagnetic interference (EMI) shielding and antistatic materials due to their improved conductivity. The dielectric properties of the MWCNT-modified polyester resin-based composite were investigated and MWCNT-filled polyester-based composites with high dielectric loss were proven to be quality materials for electromagnetic shielding applications (Seng *et al.*, 2018). The capacitive behavior was explained by the charge accumulation on the surfaces of the carbon nanotubes, and the resistive behavior with the tunneling mechanism of the electrons in multi-walled carbon nanotubes-polydimethylsiloxane (PDMS) elastomer composites (Helseth, 2018). It was characterized by the electrical properties and relaxation processes of carbon nanotubes filled epoxy polymer composites using electrical modulus formalism. The dipolar and Maxwell-Wagner-Sillars (MWS) relaxations were investigated depending on filler concentration and temperature using the Havriliak-Negami model (Boukheir *et al.*, 2018).

The present study aims to determine accurately complex impedance, complex dielectric function, and AC conductivity properties for extracting new information about the charge transport mechanism and relaxation process of SWCNT/VE binary composites using impedance spectroscopy in the frequency range 10^{-2} Hz to 10^7 Hz. Bode and Nyquist plots were used to explain real and imaginary impedance components with the Cole-Cole approach. The electrical behavior of the composite was studied depending on temperature and frequency. It is found that the material has exceeded the percolation threshold and a conduction network was formed throughout the material even at low temperatures. The complex dielectric function analysis was also carried out depending on the frequency at low and high temperatures. To bring a different perspective to the relaxation phenomenon, electrical modulus formalism has been applied to the system in addition to dielectric function analysis.

2. Experimental procedure

2.1 Material

The sample used in this study was produced by the hot press method and contains vinylester resin (acid value max. 9 mg KOH/gr, monomer content 42 %, density 1.04 g/cm³), single walled carbon nanotube (purity > 90 wt. %, diameter 10–25 nm, length 20 µm, density 1.87 g/cm³, flash point >150 °C), glass fiber FWR6 (filament diameter 17 µm). In addition to these three important components, the composite product includes peroxide, styrene, zinc sulfide, calcium carbonate, thickening admixture and additives. The percentages by weight of the components that form the material are shown in Figure 1.

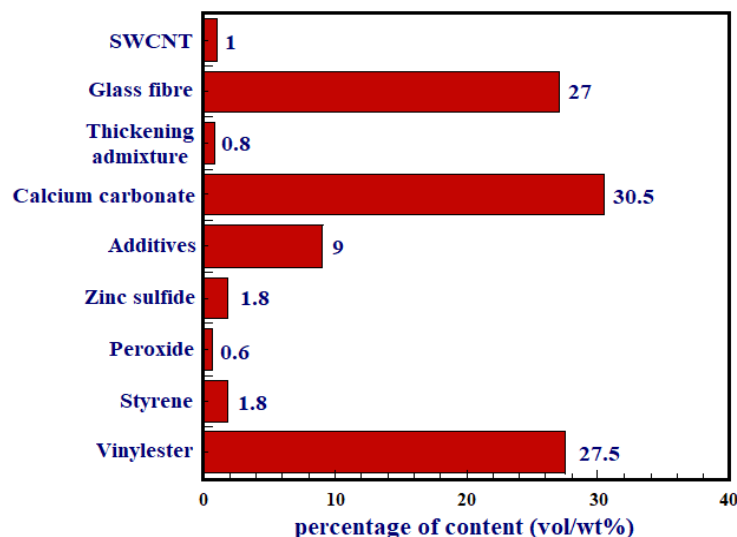


Fig. 1. Components of SWCNT/VE composite

In the production phase, components and vinylester resin were mixed mechanically continuously with the mixer to prevent agglomeration of the components and carbon nanotubes and to increase their integration with each other. When the mixture became viscous pulp, it was transferred onto polyethylene foils. At this point, glass fiber was added to the pulp laid on the carrier band. Another layer of pulp was placed on top of the pulp containing glass fiber chopped. The sandwich structure was passed between the rotating rollers to prevent the gaps between the pulps. The carrier films on the pulps were removed and the material was weighed and placed in the mold brought to the appropriate temperature in the hydraulic press. The pulps softened under high temperature and pressure and flowed into the mold cavity and thus took the desired shape. The molding temperature was 120-160°C and the mold pressure was 80-140 Barr. At the end of the molding period of about 2 minutes, the materials were pressed on the test plates.

2.2 Morphology

SEM analyzes were performed to examine the distribution of components and SWCNTs in the glass fiber reinforced thermosetting vinylester resin-based composite structure and the relevant photographs are presented in Figure 2. Although there was agglomeration in certain regions, the random distribution of SWCNTs into the matrix resulted in a nearly homogeneous structure and it can be said that the single carbon nanotube exhibited well dispersion. As can be understood from the AC conductivity measurements, 1 wt. % of SWCNTs dispersed in the matrix formed a fully 3-dimensional conductivity network throughout the material at room temperature.

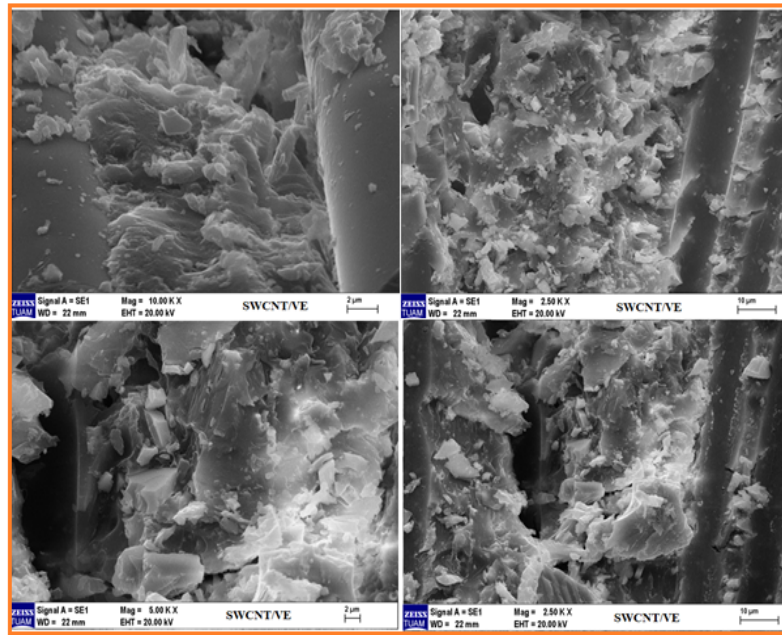


Fig. 2. SEM images of SWCNT/VE composites.

3. Results and discussion

3.1 Complex Impedance

The impedance spectroscopy of SWCNT/VE/GFRP was performed by MFIA Impedance Analyzer in the frequency range 10^{-2} Hz– 10^7 Hz with amplitude of 1 V voltage. Specimens with 15 mm length, 8 mm width and 7 mm thickness were deposited between parallel round plate electrodes. A carbon layer was coated on surface of the specimen to make the electrical contact better. The complex impedance (Z^*) was found as a function of frequency from impedance measurements at different temperatures. The real part (Z') of complex impedance denotes the resistance of the material while imaginary part (Z'') describes loss factor (Jyoti *et al.*, 2018).

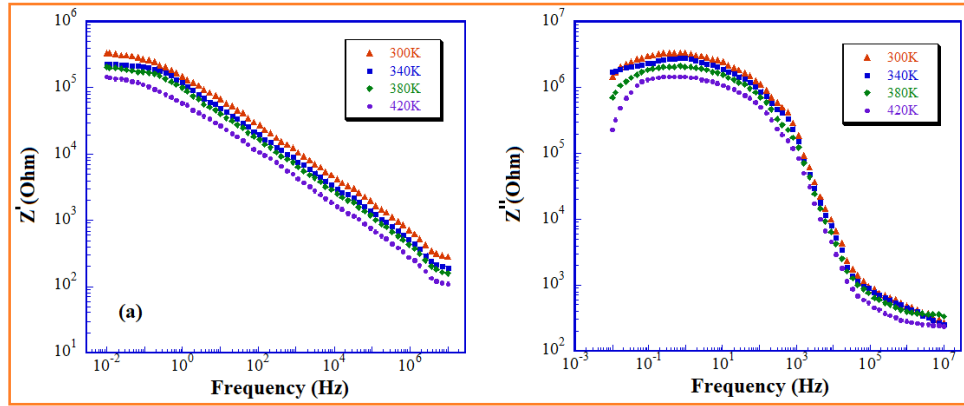


Fig. 3. Bode plots of real and imaginary impedance at different temperatures.

Figure 3 shows Bode plots of Z' and Z'' of SWCNT/VE polymer composite at various temperatures between 300 K and 420 K. As can be seen from the Figure. 3 (a), although the Z' value gives an almost constant appearance at very small frequencies, it decreases monotonically with the increase in frequency at all temperature measurements because of the weakening interface polarization. Figure.3 (b) shows the Z'' characteristics for SWCNT/VE binary composite as a function of temperature and frequency. Maximum was observed at low-frequency regions for all measurements. Maximums in the Z'' graph highlight the presence of dipolar relaxation in that frequency region. It can be also seen that both real and imaginary impedance components are frequency-dependent rather than the temperature.

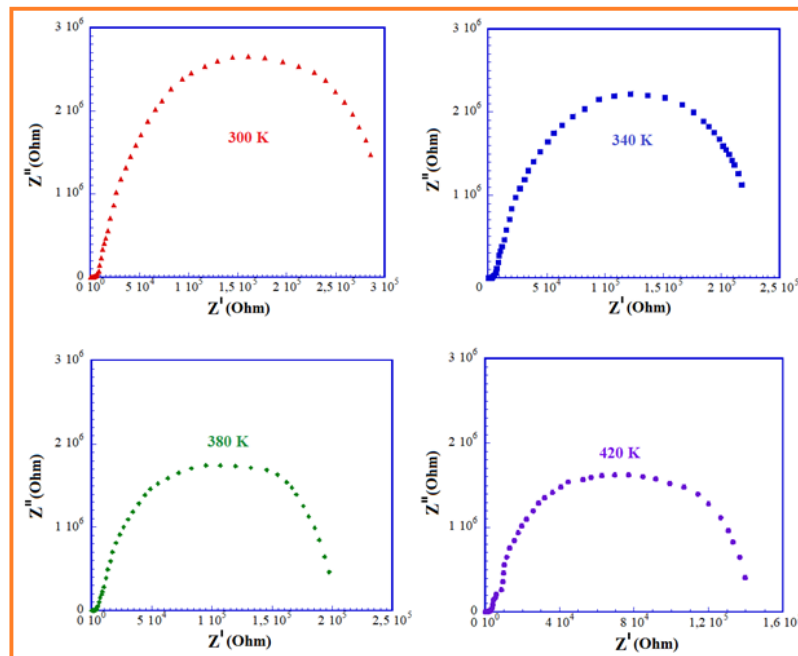


Fig. 4. Nyquist plots of SWCNT/VE composites at various temperatures.

Figure 4 shows Nyquist plots of the complex impedance of the SWCNT filled GFRP composites at various temperatures. A typical shape of Cole-Cole graphs is a semicircle that is almost reached at high-temperature values. When the maximums of the graphs are examined comparatively, the measurement with the smallest diameter magnitude of the possible semicircles is the measurement at 420 K. The electrical conductivity in composite films depends on the radius of arc in complex plane graphs. A large arc radius represents low conductivity and a low arc radius depicts higher conductivity values (Ho *et al.*, 2008). It can be said from plots that the resistance of the composite decreases as temperature increases, conductivity increases, and a less viscous media occurs at 420 K.

3.2 Alternating conductivity (AC)

Disordered conductive materials such as polymer composites show a similar response to the applied electric field as the dielectric response. Conductivity process is characterized by the real part $\sigma'(\omega)$ of the complex electrical conductivity. This component, which is mostly frequency dependent, is known alternating current (AC) conductivity. The AC conductivity consists of two parts and is expressed as (Jonscher, 1977; Almond *et al.*, 1982; Tsonos, 2019):

$$\sigma'(\omega) = \sigma_0 + k \cdot \omega^s \quad (1)$$

where σ_0 is the frequency-independent DC conductivity, k is the constant, ω is the angular frequency and s is the exponent with value ranging of 0-1.

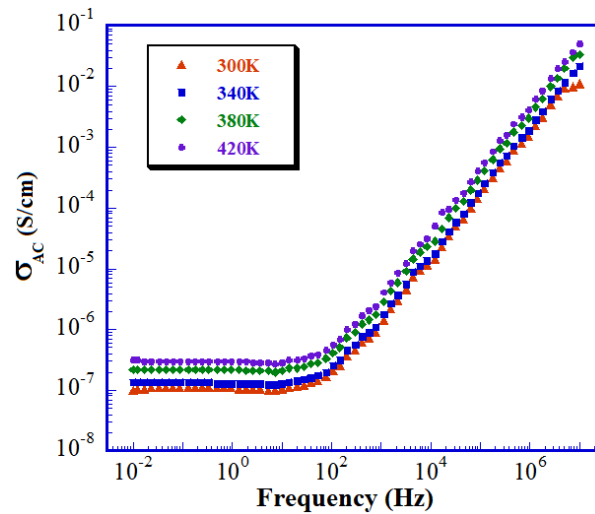


Fig. 5. AC conductivities of SWCNT/VE/GFRP at various temperatures.

It was observed from Figure. 5 that AC conductivities at all temperatures exhibited frequency-independent behaviors in the low-frequency regime. This means that the percolation threshold was exceeded in the SWCNT/VE composite with 1 SWCNT wt. % and the conduction network was ensured directly between the nanotube particles within the polymer matrix at a low-frequency regime. In this region, the conductivity value obtained at high temperatures is

approximately 3 times the value at low temperatures. The AC conductivities showed a linear dependence with frequency after 100 Hz obeying the Jonscher's power law as given in Eq. (1). AC conductivity values are more frequency-dependent than the temperature at high frequencies with similar impedance behavior.

3.3 Dielectric Characteristics

Dielectric analysis determines the real and imaginary components of the complex dielectric function depending on the frequency with the response of a dielectric material to alternating current. The complex dielectric function is expressed as (Boukheir *et al.*, 2018; Savi *et al.*, 2019):

$$\varepsilon^*(\omega) = \varepsilon'(\omega) - j\varepsilon''(\omega) \quad (2)$$

where $\varepsilon'(\omega)$ and $\varepsilon''(\omega)$ correspond to the real and imaginary parts of the complex dielectric function, respectively. The real part of the dielectric function is energy storage component and is known as dielectric constant. Dielectric constant is given by (Jyoti *et al.*, 2018):

$$\varepsilon'(\omega) = Z'' / 2\pi f C_0 Z^2 \quad (3)$$

where f is frequency and C_0 is the geometrical capacitance of sample. Capacitance is defined by the equation (Philipose *et al.*, 2021)

$$C_0 = \varepsilon_0 A / d \quad (4)$$

where ε_0 is the dielectric constant of vacuum, A is area and d is thickness. The imaginary component represents the energy loss due to conduction losses, vibration losses and polarization and is called loss factor (Lvovich, 2012). Contributions to the loss factor originate from interface polarization, DC conductivity and dipole orientations. Loss factor is described as (Jyoti *et al.*, 2018)

$$\varepsilon''(\omega) = Z' / 2\pi f C_0 Z^2 \quad (5)$$

Figure. 6 (a) shows the variation of ε' with applied frequency at different temperatures. It is seen that ε' values depend on frequency at all temperatures. The high values of ε' is shown from the graph at low frequencies due to the charge accumulation at the interface between the insulating region and conductive additives. Since the accumulated charges partly block the external electric field, the dielectric constant increases at these frequency values. The Maxwell-Wagner-Sillars process is an effective mechanism in this frequency regime (Dang *et al.*, 2007; Belhimria *et al.*, 2021). When the frequency of the field is gradually increased, the dipoles can't find enough time to align themselves with the field and the dielectric permittivity is reduced (Mergen *et al.*, 2020).

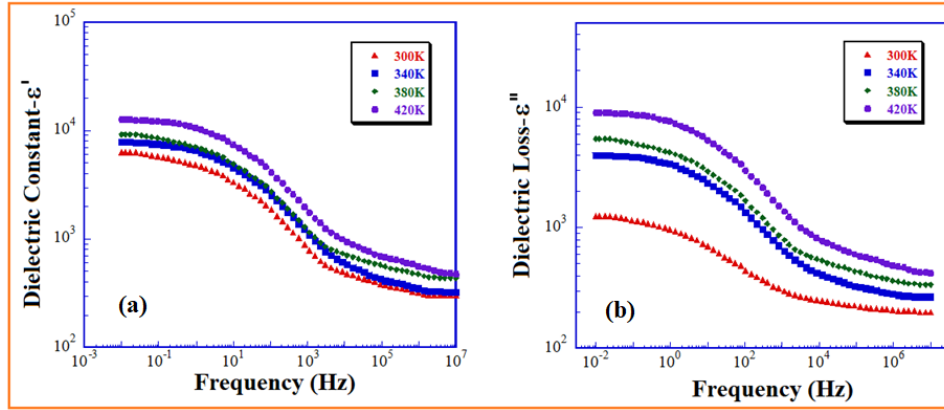


Fig. 6. (a) dielectric constant and (b) dielectric loss depending on frequency.

Figure. 6 (b) shows the plot of the loss factor as a function of frequency at different temperatures. It is seen that the increase in temperature affects the dielectric loss. As the temperature increases, thermally excited dipoles increase the peak value of the losses by following the change of the applied electric fields. Therefore, the loss factor values at 420 K are higher than the other measurements. As shown from the graph, no loss peak was observed in the loss spectra within our frequency and temperature limits. The variation of ϵ'' curves with the applied frequency is similar to the frequency dependence of ϵ' . This correlation of ϵ' and ϵ'' with frequency is associated with capacitance values experimentally. ϵ'' decreases gradually with increasing frequency due to dielectric relaxation. It can be said that the contribution to relaxation is due to interfacial polarization and DC conductivity based on the shape of the plot.

3.4 Electric Modulus

Another useful way to interpret the relaxation phenomenon apart from the permittivity and AC conductivity formalism is the electric module formalism. Electric modulus formalism is a method that has been used and accepted in recent years (Hernandez *et al.*, 2010). A different perspective such as electric modulus will give us more specific results. Since electrode polarization, absorption and interactions of impurities can be neglected in the electric modulus formalism, large variations in components of complex dielectric permittivity can be minimized. The electrical modulus is described as inverse of the complex dielectric permittivity via (Psarras *et al.*, 2011):

$$M^* = \frac{1}{\epsilon^*} = \frac{1}{\epsilon' - j\epsilon''} = M' + jM'' \quad (6)$$

where M' and M'' are the real and imaginary components of the electric modulus, respectively. M' and M'' can be found with the following formulas (Ray *et al.*, 2007):

$$M' = \frac{\epsilon'}{[(\epsilon')^2 + (\epsilon'')^2]}, \quad M'' = \frac{\epsilon''}{[(\epsilon')^2 + (\epsilon'')^2]} \quad (7)$$

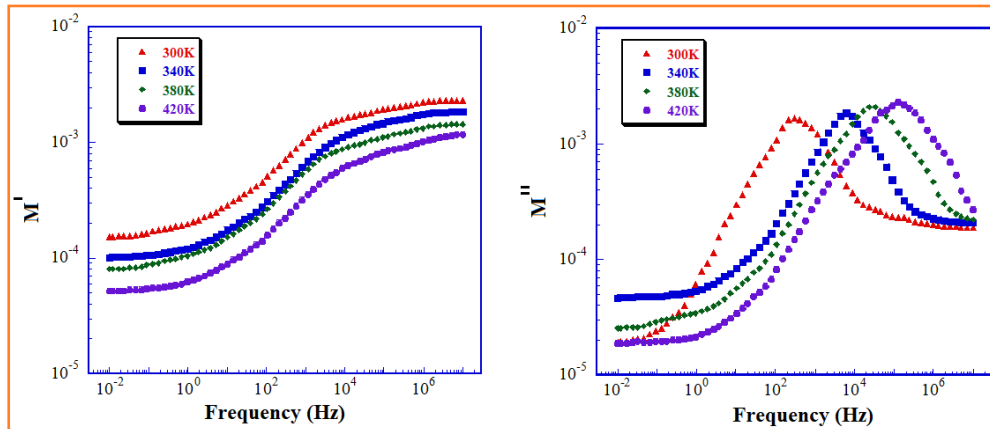


Fig. 7. (a) real part and (b) imaginary part of electric modulus.

Figure. 7 represents the variation of the real and imaginary parts of electric modulus with frequency at different temperatures. As can be seen from Figure.7 (a), the real part of the modulus takes small values in the low-frequency region. This confirms that the contribution of electrode polarization and electrode effects is small in this regime (Howell *et al.*, 1974). In all temperature measurements, the M' reached a constant maximum due to the relaxation process towards high frequencies. Frequency-dependent M'' behavior at various temperatures was shown in Figure. 7 (b). The peak maximums shifted towards higher frequencies as the temperature increased. It can be concluded that the frequency regime below peak maximum defines the range of mobile charge carriers. It can also be said that in the regime above the maximum, the charge carriers are limited to potential wells that are mobile at short distances.

4. Conclusions

Herein, the composite films were prepared by the hot press method to investigate impedance characteristics, AC conductivity, and dielectric behaviors of SWCNT/VE binary composites depending on frequency and temperature. The impedance analyzer was used over a frequency range of 10^{-2} Hz – 10^7 Hz to investigate the effect of temperature on the electrical impedance characteristics. Bode and Nyquist graphs were plotted and the results were interpreted with the Cole-Cole approach. When Nyquist graphs are examined, it is seen that the semi-circle with the smallest diameter belongs to the measurement made at 420 K. Since the diameter and conductivity are inversely proportional, it can be concluded that the increase in temperature enhances the AC conductivity. The conductivities at all temperatures exhibit power-law behavior. The SWCNT loaded matrix has constant conductivity since current flows preferably through the conductive nanotube phase at low frequencies. The conductivity became frequency-dependent after 100 Hz frequency and showed a linear behavior with increasing frequency value. Considering the effect of temperature on the AC electrical conductivity performance of the

material; it can be said that the high-temperature performance is better than that of low temperature. The highest AC conductivity of the order of 5.10^{-2} S/cm was achieved for SWCNT of 1 wt. % to the vinyl ester matrix at 420 K. Analysis of dielectric permittivity functions reported that Maxwell-Wagner-Sillars processes are the dominant mechanism affecting the dielectric constant at low-frequency regions. It has been found that at high frequencies, the polarization mechanisms lose their effectiveness, and the dielectric constant decreases. It also has been revealed that the dielectric properties of the SWCNT/VE/GFRP are affected by temperature variation. It was observed that the dielectric loss in the material increased with increasing temperature. Benefiting from the electric modulus formalism apart from permittivity formalism, dielectric relaxation was analyzed. It is revealed from the frequency dependence of the electrical modulus spectra that the dielectric relaxation detected at low frequencies at room temperature (300K) was related to the MWS process at the SWCNT-polymer interfaces. The relaxation peaks for increasing temperatures (340K-420K) shifted to higher frequencies due to the reorientation of the dipolar groups. The results obtained from the single-walled carbon nanotube-doped vinyl ester-based polymer composite developed for this study are expected to technically improve the design of the sensor and electromagnetic shielding applications.

ACKNOWLEDGEMENTS

The author thanks to Literatür Kimya for manufacturing composites.

References

- Almond, D.P., West, A.R., Grant, R.J. (1982)** Temperature dependence of the ac conductivity of Na β -alumina. *Solid State Communications*, 44(8):1277–1280.
- Almuhammadi, K., Bera, T.K., Lubineau, G. (2017)** Electrical impedance spectroscopy for measuring the impedance response of carbon-fiber-reinforced polymer composite laminates. *Composite Structures*, 168:510-521.
- An, Q., Rider, A. N., Thostenson, E. T. (2013)** Hierarchical composite structures prepared by electrophoretic deposition of carbon nanotubes onto glass fibers. *ACS Applied Materials and Interfaces*, 5(6):2022–2032.
- Anju, V.P and Narayanankutty, S.K. (2019)** High dielectric constant polymer nanocomposite for embedded capacitor applications. *Materials Science & Engineering B*, 249:114418.
- Antonucci, V., Faiella, G., Giordano, M., Nicolais, L., Pepe, G. (2007)** Electrical properties of single walled carbon nanotube reinforced polystyrene composites. *Macromolecular Symposium*, 247(1):172–181.

Avilés, F., May-pat, A., López-manchado, M. A., Verdejo, R., Bachmatiuk, A., (2018) A comparative study on the mechanical, electrical and piezoresistive properties of polymer composites using carbon nanostructures of different topology. *European Polymer Journal*, 99:394–402.

Boukheir, S., Samir, Z., Belhimria, R., Kreit, L., Achour, M.E., Eber, N., Costa, L.C., Oueriagli, A., Outzourhit, A. (2018) Electric modulus spectroscopic studies of the dielectric properties of carbon nanotubes/epoxy polymer composite materials. *Journal of Macromolecular Science, Part B: Physics*, 57(3) 210-221.

Belhimria, R., Samir, Z., Boukheir, S., Teixeira, S.S., Achour, M.E., Casaos, A.A., Dominguez, J.M.G., Costa, L.C., Hasnaoui, M.E. (2021) Thermal and dielectric properties of carbon nanotubes/graphite/polyester ternary composites. *Journal of Composite Materials*, 55 (25) 3741–3750.

Bouzerara, R., Achour, S., Tabet, R. & Zerkout, N. S. (2011) Synthesis and characterization of ZnO/PVA composite nanofibres by electrospinning. *International Journal of Nanoparticles*, 4(1):10–19.

Daliri, O.S., Faller, L.M., Farahani, M., Roshanghias, A., Oberlercher, H., Mitterer, T., Araee, A., and Zangl, H. (2018) MWCNT-Epoxy nanocomposite sensors for structural health monitoring. *Electronics*, 7:143.

Dang, Z.M., Shehzad, K., Zha, J.W., Hussain, T., Jun, N., Bai, J. (2011) On refining the relationship between aspect ratio and percolation threshold of practical carbon nanotubes/polymer nanocomposites. *Japanese Journal of Applied Physics*, 50(8):080214.

Dang, Z.M., Yao, S.H., Xu, H.P. (2007) Effect of tensile strain on morphology and dielectric property in nanotube/polymer nanocomposites. *Applied Physics Letters*, 90(1):012907.

Das, A and Dobbidi, P. (2021) Impedance spectroscopy and ac conductivity in $\text{Ba}_{0.5}\text{Sr}_{0.5}\text{TiO}_3\text{--Ca}_{10}(\text{PO}_4)_6(\text{OH})_2$ ceramic composites: An electrical approach to unveil biocomposites. *ACS Biomaterials Science and Engineering*, 7:2296-2308.

Ganesh, G. K. B. N. V. S., Yadav, A., Hiremath, M. M., Prusty, R. K., Ray, B. C. (2020) Enhancement of mechanical properties of glass fiber reinforced vinyl ester composites by embedding multi-walled carbon nanotubes through solution processing technique. *Materials Today Proceedings*, 27(2):1045-1050.

Helseth, L. (2018) Electrical impedance spectroscopy of multiwall carbon nanotube–PDMS composites under compression. *Material Research Express*, 5:105002.

Hernandez, M., Carretero-Gonzalez, J., Verdejo, R., Ezquerro, T.A., Lopez-Manchado, M.A. (2010) Molecular dynamics of natural rubber/layered silicate nanocomposites as studied by dielectric relaxation spectroscopy and dynamic mechanical spectroscopy. *Macromolecules*, 43:643–651.

Ho, C.H., Liu, C.D., Hsieh, C.H., Hsieh, K.H., and Lee, S.N. (2008) High dielectric constant polyaniline/poly (acrylic acid) composites prepared by in situ polymerization. *Synthetic Metals*, 158:630-637.

Howell, F.S., Bose, R.A., Macedo, P.B., Moynihan, C.T. (1974) Electrical relaxation in a glass-forming molten salt. *Journal of Physical Chemistry*, 78(6):639-648.

Jonscher, A.K. (1977) The ‘universal’ dielectric response. *Nature*, 267:673–679.

Jyoti, J., Kumar, A., Dhakate, S.R., Singh, B.P. (2018) Dielectric and impedance properties of three dimension graphene oxide-carbon nanotube acrylonitrile butadiene styrene hybrid composites, *Polymer Testing*, 68:456–466.

Kuilla, T., Bhadra, S., Yao, D., Kim, N.H., Bose, S., Lee, J.H. (2010) Recent advances in graphene based polymer composites. *Progress in Polymer Science*, 35(11):1350–1375.

Liang, Y., Liang, X., Zhang, Z., Li, W., Huo, X., Peng, L. (2015) High mobility flexible graphene field-effect transistors and ambipolar radio-frequency circuits. *Nanoscale*, 7:10954–10962.

Lvovich, V.F. (2012) Impedance Spectroscopy Applications to Electrochemical and Dielectric Phenomena. Wiley, New Jersey.

Mahapatra, S.P., Sridhar, V. & Tripathy, D. K. (2008) Impedance analysis and electromagnetic interference shielding effectiveness of conductive carbon black reinforced microcellular EPDM rubber vulcanizates. *Polymer Composites*, 29:465–472.

Mergen, O. B., Umut, E., Arda, E., Kara, S. (2020) A comparative study on the AC/DC conductivity, dielectric and optical properties of polystyrene/graphene nanoplatelets (PS/GNP) and multi-walled carbon nanotube (PS/MWCNT) nanocomposites. *Polymer Testing*, 90:106682.

Philipose, U.; Jiang, Y.; Western, B.; Harcrow, M.; Littler, C.; Sood, A.; Zeller, J.W.; Lineberry, B.; Syllaios, A.J. (2021) Impedance Analysis and Noise Measurements on Multi Walled Carbon Nanotube Networks. *Materials*, 14:7509.

Psarras, G.C., Siengchin, S., Karahaliou, P.K., Georga, S.N., Krontiras C.A., Karger-Kocsis, J. (2011) Dielectric relaxation phenomena and dynamics in polyoxymethylene/polyurethane/alumina hybrid nanocomposites. *Polymer International*, 60:1715–1721.

Puertolas, J.A., García-García, J.F., Pascual, F.J., Gonzalez-Domínguez, J.M., Martínez, M.T., Anson-Casaos, A. (2017) Dielectric behavior and electrical conductivity of PVDF filled with functionalized single-walled carbon nanotubes. *Composites Science and Technology*, 152:263–274.

Ray, D. K., Himanshu, A .K., Sinha, T.P. (2007) Structural and low frequency dielectric studies of conducting polymer nanocomposites. *Indian Journal of Pure Applied Physics*, 45:692-699.

Samir, Z., Merabet, Y. E., Graca, M.P.F, Teixeira, S. S., Achour, M.E., Costa, L.C. (2017) Dielectric behaviour of carbon nanotubes particles-filled polyester polymer composites. *Journal of Composite Materials*, 51(13):1831–1837.

Savi, P., Giorcelli, M., and Quaranta, S. (2019) Multi-Walled Carbon Nanotubes Composites for Microwave Absorbing Applications. *Applied Sciences*, 9:851.

Seng, L.Y., Wee, F.H., Rahim, H.A., Malek, F., You, K.Y., Liyana, Z., Jamlos, M.A., Ezanuddin A.A.M. (2018) EMI shielding based on MWCNTs/polyester composites. *Applied Physics A*, 124-140.

Tsonos, C. (2019) Comments on frequency dependent ac conductivity in polymeric materials at low frequency regime. *Current Applied Physics*, 19(4):491–497.

Zhu, J., Yang, D., Yin, Z., Yan, Q., Zhang, H. (2014) Graphene and graphene-based materials for energy storage applications. *Small*, 10(17):3480–3498.

Submitted: 17/01/2022

Revised: 06/04/2022

Accepted: 17/04/2022

DOI : 10.48129/kjs.19891

Mathematical modelling and analysis of temperature effects in MEMS based bi-metallic cantilever for molecular biosensing applications

Miranji Katta^{1,*}, Sandanalakshmi R²

¹*Dept. of Electronics and Communication Engineering, Sir C R Reddy College of Engineering,
Eluru, Andhra Pradesh, India - 605014*

^{1,2}*Dept. of Electronics and Communication Engineering, Puducherry Technological University,
Pondicherry, India - 605014*

**Corresponding author: miranji.katta@gmail.com*

Abstract

As Lab-on-Chip platforms with micro-and nano-dimensions evolve biosensors using miniaturized and high-sensitivity cantilevers are becoming more attractive. Although these sensors function in non-isothermal situations, computational mathematics generally ignores the temperature. Conversely, biosensor cannot be designed with a single-layered cantilever. Yet, in Nano-Electro-Mechanical-Systems, the influence of temperature is more likely to be dominant since the surface-to-volume ratio is higher. In the context of this conclusion, the mathematical modelling comprises temperature and the associated material attributes. This work presents a simple and direct analytical technique for analysing the control of bimetallic cantilevers with NEMS-based sensing and actuation mechanisms. Methodological techniques were used to develop and solve some well-known models of mathematical equations. Parametric analysis data is a major factor in the functioning of all of the other works studied. The findings of FEA comparisons and experiments reveal that the mathematical model's predictions are more than 20% correct.

Keywords: Actuation; bimetallic layers; bioMEMS; biosensors; temperature effects.

1. Introduction

As Lab-on-Chip platforms with micro-and nano-dimensions evolve, biosensors using miniaturized and high-sensitivity cantilevers are becoming more attractive. Although these sensors function in non-isothermal situations, computational mathematics generally ignores the temperature. Conversely, no biosensor can be designed with a single-layered cantilever. Yet, in Nano-Electro-Mechanical-Systems, the micro-electro-mechanical systems (MEMS) have recently enabled the medical sector to develop a new generation of chemical and biological sensors. When it comes to biological sensing, NEMS and the sensors and actuators that go with it are becoming important and it is possible to build sensing systems using micro-and nanoscale parts. The outcome of such systems are more reliable, faster, and accurate (Gupta *et al.*, 2016), (Vasan, Doraiswami and Pecht,

2011). Microsensors and actuators based on silicon were the standards in the early 1990s. MEMS devices have been increasingly popular since they emerged to develop IC manufacturing technologies. It has been claimed that a wide range of MEMS-based sensors may be used in a wide range of scientific fields, including biochemicals, microfluidics, and aeronautical and optical studies. Micro bridges and cantilevers, two components of MEMS and NEMS, have several medical applications. Most intelligent systems are likely to include core structures with numerous layers (Mohd Ghazali *et al.*, 2020). It has only been that novel actuation techniques have evolved in the past few years. An actuation mechanism called the bimetallic effect may be of interest if you wish to regulate displacement in response to temperature changes (Navakul *et al.*, 2017). A NEMS cantilever's deflected free-end characteristic and force relationship are explored here to determine the cantilever's temperature change. To create actuation, the free end of the cantilever must move in a perpendicular direction (Ali *et al.*, 2017). According to Figure 1, a bimetallic cantilever has a typical temperature influence on molecules.

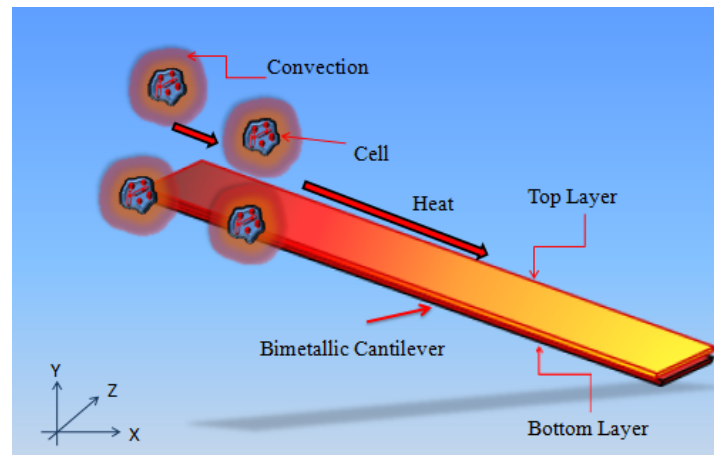


Fig. 1. Temperature effect on bimetallic cantilever with respect to molecular biosensing

1.1 Temperature Effects on Sensing Methods

Many sensing technologies, such as tuneable capacitors have been developed for micro to nano sensing applications (Kouravand, 2011). There are several sources of information on sensing and actuation, with the most widely employed techniques being chemical, optical, thermal, mechanical, piezoresistive, capacitive, piezoelectric, resonant, magnetic, electrostatic, and so on (Cote, Lec & Pishko, 2003), (Fu *et al.*, 2007), (Saylan *et al.*, 2019). This research presents a series of unique integrated capacitive sensing and actuation technologies based on nanostructures. Capacitance fluctuations caused by the deflection of bimetallic cantilevers loaded by linear or nonlinear electrostatic forces and thermal bending forces are used in sensors and actuators (Vineetha *et al.*, 2018), (Hegner & Arntz, 2003). The static behaviour of nano cantilever beams was also investigated (Katta *et al.*, 2020).

Thermal noise is produced when a microcantilever is in thermal equilibrium with its surroundings (vibration caused by thermal agitation). Due to energy dissipation, the mechanical energy stored in a microcantilever is wasted as heat (Khaleel & Hashim, 2020). Random excitation is caused by the multiple microscopic degrees of freedom in a microcantilevers environment. The statistical mechanics "fluctuation-dissipation theorem" captures the relationship between energy dissipation and random thermal excitation (Nordström *et al.*, 2008), (Yu-Jie Huang *et al.*, 2013). Consequently, lower mechanical Q results in a more noticeable noise force. equation. 1 demonstrates the "equi-partition theory" to obtain the mean square vibration amplitude for a certain oscillation mode at temperature T.

$$\frac{1}{2}k_B T = \frac{1}{2}k_B z^2 \quad (1)$$

When the microcantilevers deflection is measured, k_B is the Boltzmann constant, k is its stiffness, and z is its displacement. The spectral density S_F ($4k_B T B / \omega_o Q$) and the force noise (F) in a bandwidth (B) are given by equation. 2 if the noise spectrum is assumed to be white (i.e., frequency-independent) (Kouravand, 2011b).

$$F_{min} = \sqrt{\frac{4k_B T B}{\omega_o Q}} \quad (2)$$

There is a natural cantilever frequency, f_0 , equal to $2f_0$. equation. 3 may represent a minor measurable force on a rectangular cantilever (Neethu & Suja, 2016).

$$F_{min} = \left(\frac{wt^2}{LQ} \right)^{\frac{1}{2}} (k_B T B)^{\frac{1}{2}} (E_p)^{\frac{1}{2}} \quad (3)$$

Its width (w), thickness (t), length (L), E (Yang's modulus), and density (F) are all measured in units of density. In the same way, the mean square root deflection is obtained by equation. 4, (Vineetha *et al.*, 2018).

$$z_{rms} = \left(\frac{kT}{k_B} \right)^{\frac{1}{2}} = \left(\frac{2kT}{wE} \right)^{\frac{1}{2}} \left(\frac{L^3}{t^3} \right)^{\frac{1}{2}} \quad (4)$$

Although equation. 3 and 4 may be utilised to design the sensitivity of microcantilevers, it is clear that very high-quality factors are required for ultrasensitive devices.

1.2 Effect on material properties

The temperature has a significant impact on the characteristics of microcantilever (Neethu & Suja, 2016 and Mathur *et al.*, 2016), (Rosen & Gurman, 2010). For example, elastic modulus decreases

with increasing temperature. For the high-temperature limit, the elastic modulus of silicon has been modelled semi empirically using equation. 5.

$$E(T) = E_0 - BT \exp\left(-\frac{T_0}{T}\right) \quad (5)$$

Where E_0 is Young's modulus at absolute zero degrees Celsius. Temperature-independent constants $B > 0$ and $T_0 > 0$ are aluminium trioxide (Al_2O_3), E_0 is around 4.6×10^{12} dyn/cm², B is 4.41×10^8 dyn/cm², and T_0 is 373°K. Over a wide range of temperatures, the frequency shift of silicon microcantilevers and changes in the Q-factor have been examined (Chen & Feng, 2011 and Kim *et al.*, 2019).

1.3 Effect on Geometry

The geometry of a microcantilever is also affected by temperature, with a rise in temperature being correlated to an increase in dimensions via a metric known as the coefficient of thermal expansion (CTE). A polymer's thermal expansion is in the range of 50–100 parts per million (ppm) per degree Celsius, whereas silicon is 3.2ppm/°C. As can be seen from the explanation presented here, the microcantilevers calibration and operation must be accomplished at the same temperature and within extremely tight tolerances. Differential measurements using coated and uncoated microcantilevers must be carried out without temperature control (Boisen & Thundat, 2009). Perhaps the first time, we used computational modelling to conduct an in-depth and systematic investigation into the influence of Au layer coverage and thickness on the thermo-electro-mechanical characteristics of the sensor. The prediction model is tested by comparing theoretical values to experimental data given in the literature.

2. Literature Survey

In a recent work, researchers discovered that resistive/Joule heating of dc-biased piezoresistors has a considerable impact on the performance of this double piezo - resistive micro/nano cantilevered sensors (Wee *et al.*, 2005). (Lee *et al.*, 2015). Furthermore, it was demonstrated that self-heating induced cantilever deflection, resulting by a variation in the thermal coefficient of expansion (TCE) level in a hybrid cantilever. It is the most significant contribution to thermal drift in sensor output. As a result, the present research will be helpful in answering the following questions: (i) to achieve insight into the effect of multi-layer due to the large TCE, which contributes significantly to TCE stimulated deflection and therefore thermal drift inaccuracy (sensor reliability); and (ii) to optimize not only measurement reliability by diminishing thermal drift but also sensor performance in terms of both electrical and biological sensitivity by optimization the coverage and thickness of each layer.(Wadas *et al.*, 2017; Rao & Wootla, 2007; Miranji & Sandanalakshmi R, 2020a; Katta *et al.*, 2021).

This work uses a finite element method (FEM) based solver owing to the sensors complicated composite construction and multiphysics environment. Even though mathematical models are employed to forecast the cantilever deflection profile, resonant frequency, and TCE induced deflection. Aside from the reasons stated above, the inability of simplified models to predict complex multi-morph deflection, the geometrical influence of the Au patch on the cantilever platform, and the abrogation of the coverage effect of Au on TCE deflection all contribute to the accuracy of computer-based computation model.

2.1 Experimental validation

Computational findings are compared with experimental data from different devices described in the literature to validate the modeling method used in this study. To compare our modeling method, researcher's modeled devices documented in the literature with the same shape and applied thermal, electrical, and mechanical boundary conditions to examine their properties. Table 1 summarizes the comparison of modeling techniques with experimentally reported data.

Table 1. Comparison of modeling techniques with experimentally reported data.

Reference	Simulation Results	Experimental Results	% Change
Relative change in Nominal Resistance($\Delta R/R$)			
Zhou <i>et al.</i> , 2009	1.81×10^{-3}	1.1×10^{-3}	6.45
Loui <i>et al.</i> , 2008	0.65×10^{-4}	0.6×10^{-4}	8.33
Input power-10mW			
Lee <i>et al.</i> , 2007	209°C	200.34°C	4.32
Non-Identical TCE residual deflection			
Zhou <i>et al.</i> , 2009	84.15nm	79.20nm	6.25

According to Lee *et al.*, (2015) modeled and examined the device's temperature profile and maximum cantilever temperature (T_{\max}) to compare thermal modeling approaches. The cantilever's maximum temperature has been taken into account in our calculations. The maximum temperature

of the modeled device is 209°C at a power level of 10mW. However, the device's recorded temperature is 200.34°C, resulting in a 4.32 percent inaccuracy. Furthermore, we simulated a silicon dioxide cantilever sensor described by Zhou (Zhou *et al.*, 2009) to compare the cantilever's thermo-mechanical response ($Z/Z|TCE$). According to the results, the magnitude of $Z/Z|TCE$ for the modeled device is 84.15nm. For the identical device, the reported value of $Z/Z|TCE$ is 79.20 nm, which is 6.25 percent lower than the modeled device. Both point loading ($R/R|p$) and surface stress loading (R/S) are used to verify the electro-mechanical modeling technique. We simulated the device published by Loui *et al.* (Li *et al.*, 2008) to compare electro-mechanical response, i.e., $\Delta R/R$ input due to point loading. The magnitude of $\Delta R/R$ for the modeled device (0.64×10^{-4}) and the experimentally reported value (0.6×10^{-4}) differ by 6.66 percent at an endpoint tip deflection of 1.7mm. A 4.54% deviation in the magnitude of $R/R|s$ produced by modeling the constructed device was found in the results. There is a discrepancy between the simulated device's $R/R|s$ and the stated value of $1.15 \times 10^{-3}m/N$. Because of this, the discrepancy between the model findings and the presented experimental data is considered reasonable.

3. Mathematical Modelling

Figure. 2(a) shows the schematic of the bi-metallic cantilever geometry of the nano actuator with length ℓ , thickness t , width w , and elasticity modulus E . In contrast, bottom layer parameters are indicated with subscript 1, and top layer parameters are indicated with subscript 2. In the designed model, two metallic layers are sandwiched and assumed to be identical in length. Such an arrangement is suitable for providing the maximum force (assuming all other parameters are constant). All other parameters may be dissimilar and denoted with indices 1 and 2, respectively. Let us suppose that where is the coefficient of thermal expansion (see figure 2). Usually, bimetallic nanoactuators use metals deposited onto silicon and conform to this assumption. An embedded heating resistor assumes a homogeneous thermal distribution encircling the cantilever. "X" indicates the length, and "Z" indicates the cross-section at the origin. A beam deflection $w(x)$ alongside the x-axis is presented in figure.2 (c).

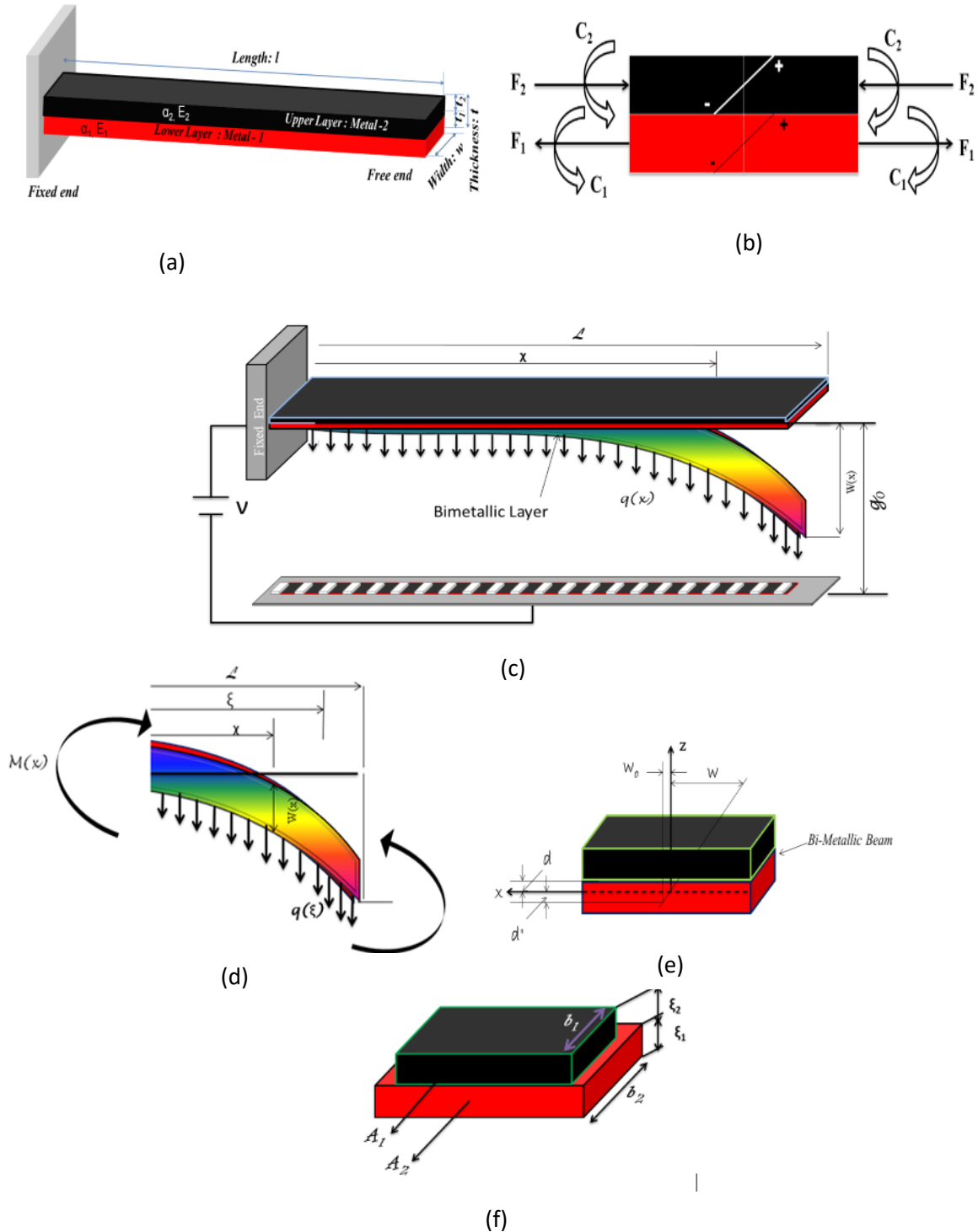


Fig. 2. The cross-sectional area of bimetallic cantilever (a) Forces acting on the cross-section of the segment along the course of the cantilever (b) Moments acting on the cross-section of the segment along its length (c) Schematic of Electrostatic cantilever beam (d) Deflection due to electrostatic force alongside the beam (e) An constituent of bi-layered cantilever beam towards x and z directions (f) Slippage between bi metallic layers.

On the sandwiched beam, segments cross-section is shown in Figure 2(b) as force and moment imposed by increasing temperature. There are tensile and compressive forces F_1 , F_2 , coupled by C_1 and C_2 across the sections of material 1 and 2, which result in different internal stresses. These forces must be in equilibrium over any cross-section of the beam (Miranji Katta & Sandanalakshmi R, 2020) i.e.

$$F_1 = F_2 = F \quad (6)$$

$$\frac{F(t_1 + t_2)}{2} = C_1 + C_2 \quad (7)$$

According to beam Theory

$$C_1 = \frac{E_1 I_1}{r} \quad C_2 = \frac{E_2 I_2}{r} \quad (8)$$

Where E -Young's modulus and I - moment of inertia, r - radius of beam curvature. By using equation (3), (2) can be reduced to

$$\frac{F(t_1 + t_2)}{2} = \frac{E_1 I_1}{r} + \frac{E_2 I_2}{r} \quad (9)$$

Above equation has two unknown parameters F and r , hence one more equation is needed to relate these parameters. At the inner surface, ordinary strain of two sandwiched layers are same, therefore

$$\alpha_1 \Delta T + \frac{F}{E_1 t_1 b_1} + \frac{t_1}{2r} = \alpha_2 \Delta T - \frac{F}{E_2 t_2 b_2} - \frac{t_2}{2r} \quad (10)$$

Here ΔT is the change in temperature and t , w are thickness and width of the cantilever beam, I_1 and I_2 are $\frac{b_1 t_1^3}{12}$, $\frac{b_2 t_2^3}{12}$ respectively.

By solving the above equation for beam curvature $k = \frac{1}{r}$ is

$$k = \frac{1}{r} = \frac{6b_1 b_2 t_1 t_2 E_1 E_2 (t_1 + t_2) (\alpha_2 - \alpha_1) \Delta T}{(b_1 E_1 t_1^2)^2 + (b_2 E_2 t_2^2)^2 + 2b_1 b_2 t_1 t_2 E_1 E_2 (2t_1^2 + 3t_1 t_2 + 2t_2^2)} \quad (11)$$

There are many bimetallic cantilever-based actuators with numerical (nearly non-zero) tip deflections (Chu *et al.*, 1993). In particular NEMS based cantilevers, due to their small dimensions and thickness, the temperature effects are more dominant, and the curvature is existed because of residual stress in the thin-film materials (Mathur *et al.*, 2016). Two basic assumptions are made in

equation (11), which states a linear distribution of strain over the beam thickness and that two sandwiched materials are perfectly bonded at their edges. The equation (11) can represent changes in curvature with temperature in a bimetallic cantilever with non-zero deformation. The curvature derived in equation (12) is different from the below equation of previous publication (Chen & Feng, 2011 and Chun-Hao & Chen, 2009) and is being used in the field of nanomechanics

$$K = \frac{1.5(t_1 + t_2)\Delta\alpha\Delta T}{1.75(t_1 + t_2)^2 - 2t_1t_2 + (E_1b_1t_1^3/E_2b_2t_2) + (E_2b_2t_2^3/E_1b_1t_1)} \quad (12)$$

In addition to tip deflection, the force generated at the bimetallic cantilever's edge (free end) is also studied here. A bimetallic cantilever can deflect as temperatures vary due to the material's temperature coefficient. Therefore, it is necessary to provide an external counter force F_{eq} to the beam to avoid the bi-metallic effect to regulate the cantilever's tip at a fixed point. When a cantilever is loaded at the end, its deflection is given by beam theory as (Chen & Feng, 2011), (Zhou *et al.*, 2009).

$$F_{eq} = 3EI_d/l^3 \quad (13)$$

Here employed the transformed-section technique (Kooser *et al.*, 2003 and Passian & Thundat, 2008) to calculate the composite cantilever EI's flexural stiffness. An axis of neutral rotation doesn't need to be centred on a bimetallic beam's cross-section and cross-sectional dimensions. When the cantilever is subjected to thermal strain, its free end has constant curvature, resulting in a deflection of the magnitude (Yanagida *et al.*, 2017):

$$d = kl^2/2 \quad (14)$$

For $l \ll r$.

Tip force and temperature can be converted to each other with ease if tip deflection is determined as a function of input power or temperature using equation (8). Figure 3(a) shows both the free end bending and the force generated when the electric input power is increased. As shown in Figure 3, a deflection occurs without a tip (b). Analyzing the acquired research results, we compare them to the findings of the finite element method. Figure 4 depicts the cantilever tip deflection as a function of temperature change using a 3-D finite element analysis simulation model.

The cantilever deflection in the second instance is caused by temperature variations and the electrostatic force applied along the beam, as shown in Figure (2a). Figure 2(b) shows that the bending moment is expressed as (Yang *et al.*, 2016):

$$M(x) = \int_x^\ell q(\xi)(\xi - x)d\xi \quad (15)$$

Here $q(\xi)$ is electrostatic force in unit length is obtained from the below equation(Chu *et al.*, 1993)

$$q(\xi) = \frac{\epsilon_o V_b^2 w}{2(g_o - w(\xi))^2} \quad (16)$$

Here ϵ_o , v_b , w , g_o , $w(\xi)$, are air permittivity, bias voltage applied to beam, width of the bi-metallic cantilever beam, preliminary gap and beam deflection respectively. As per the above equation deflection of the beam is nonlinear. From the above two equations, the correlation between deflection of bi-metallic cantilever at a given temperature can be expressed as

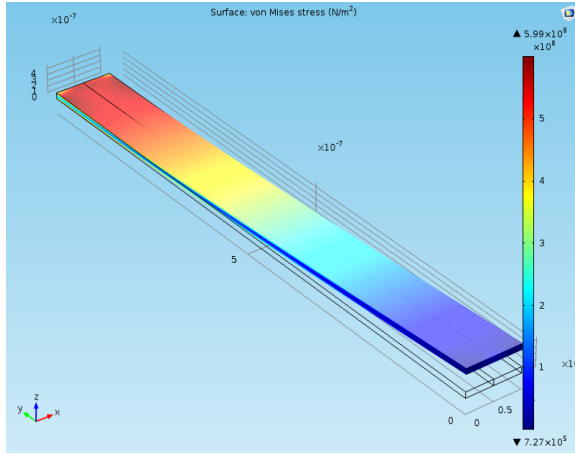
$$\frac{d^2 w}{dx^2} = \frac{12n(\alpha_1 - \alpha_2)\Delta T}{h(n^2 + 14n + 1)} + \frac{6(1+n)\epsilon_o V_b^2}{E_1(n^2 + 14n + 1)h^3} \int_x^l \frac{(\xi - x)}{(g_o - w(\xi))^2} d\xi \quad (17)$$

When the applied voltage or temperature variations are increased, linearizing the above equation concerning w may cause significant errors. This is because “ w ” has a large value relative to the initial gap. As a result, it is recommended that the applied voltage and temperature be progressively raised (Mukhopadhyay *et al.*, 2005 and Kouravand *et al.*, 2011). It is linearized by utilizing the Step-by-Step Linearization Method (SSLM) and generates a linear differential equation that is solved by using the Finite Difference Method (FDM).

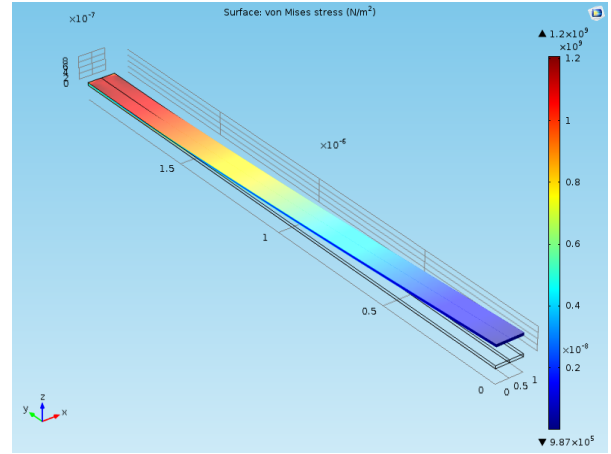
4. Results and Discussions

The dimensional parameters of the cantilevers are $\alpha_1=3.2 \times 10^{-6}$, $\alpha_2=1.85 \times 10^{-5}$, $E_1=150\text{GPa}$, $E_2=60\text{GPa}$, $L_1 = 400\text{nm}$, $L_2 = 350\text{nm}$, $W_1 = 120\text{nm}$, $W_2 = 100\text{nm}$, $t_1=18\text{nm}$, $t_2=25\text{nm}$, they are the same parameters used in [2] for the fabrication and measurement of the devices (see Figure. 3(b)). Using (11), the estimated tip deflection is just 6% off from what the FEA predicted. The computed tip deflection using (12) is clearly incorrect. The nanofabricated bimetallic cantilevers used in this study were tested in two different ways. Researchers assess the bimetallic cantilever temperature anomaly in the atmosphere with respect to electrical power input during the first experiment. The cantilever edge deformation in the air is determined, in the second experiment as a function of electrical input power.

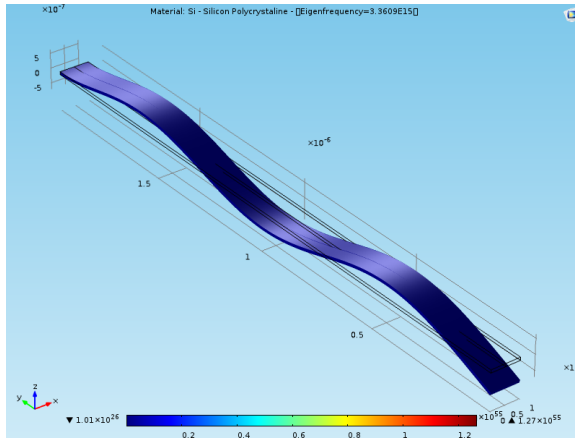
The following simulation results with COMSOL multiphysics in the static and dynamic environment, parametric sweep variable as temperature (T) shows different resonance frequencies (f_o). For the above dimensional parameters, variable temperature 25, 40, 55, 70, 85, 100 in $^{\circ}\text{C}$ shows various resonance frequencies from figure 3(a)-(f). Here double layers of cantilever beam simulated individually for the analysis of TCE effect on deflection and resonance levels.



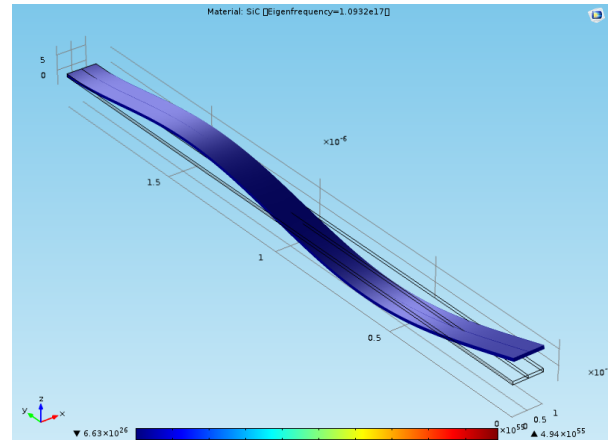
(a)



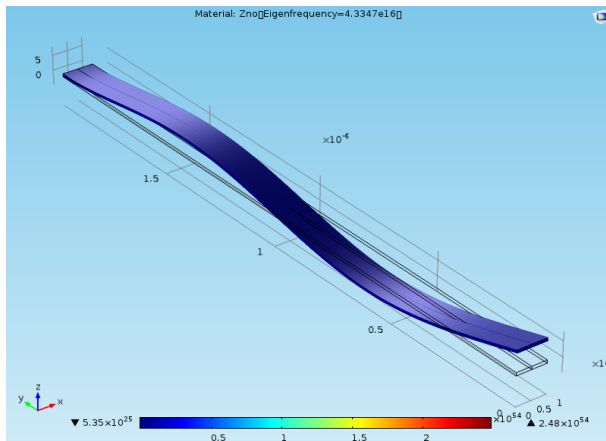
(b)



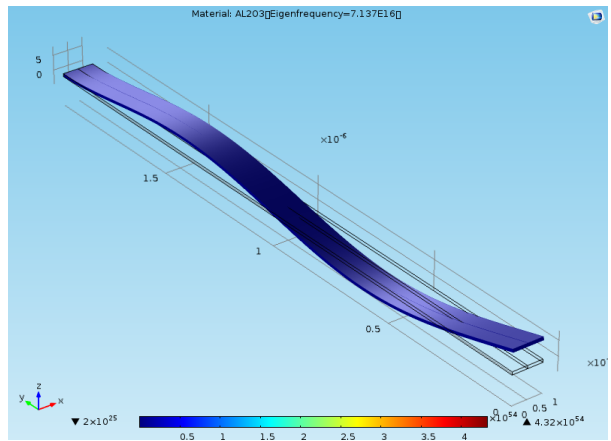
(c)



(d)



(e)



(f)

Fig. 3. COMSOL-Simulation results of cantilever beam under static and dynamic analysis with identical temperature range (a) Deflections capability of top layer (b) Deflections capability of bottom layer (c) & (d). Resonance frequency change in top layer (e) & (f) Resonance frequency change in bottom layer

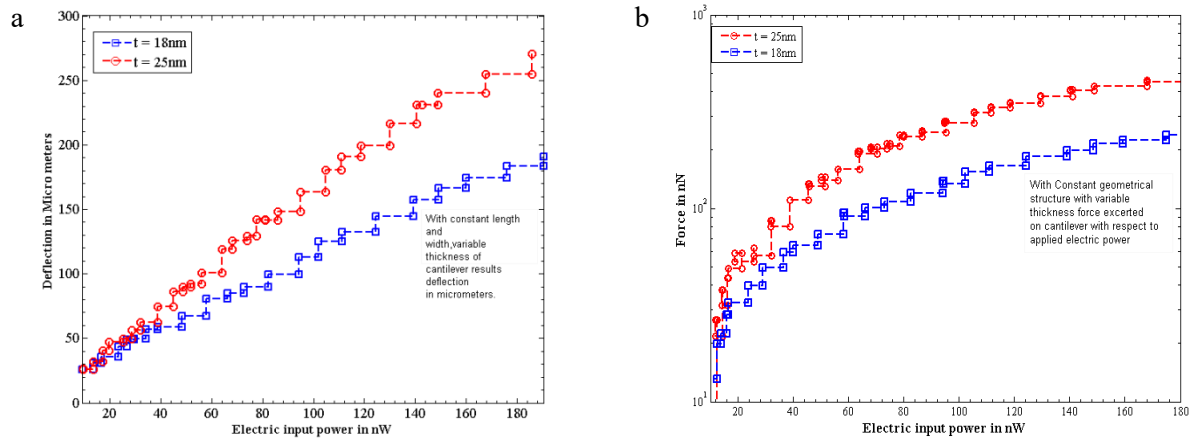


Fig. 4. Response of cantilever beam in air medium (a) Tip deflection with electric power input (b) Force developed due to electric input power.

The cantilever's temperature-dependent tip deflection may be computed by adding the findings from these different experiments. For the bimetallic cantilevers according to Chu *et al.*, (2009), the edge deformation is not zero in the presence of residual stresses. The ambient temperature required to compensate for the pre-set tip deflection may be used to accommodate for the starting curvature. The estimated tip deflection based on equations (12) and (17) are shown in Table 2 precisely, the developed model here provides more accurate results.

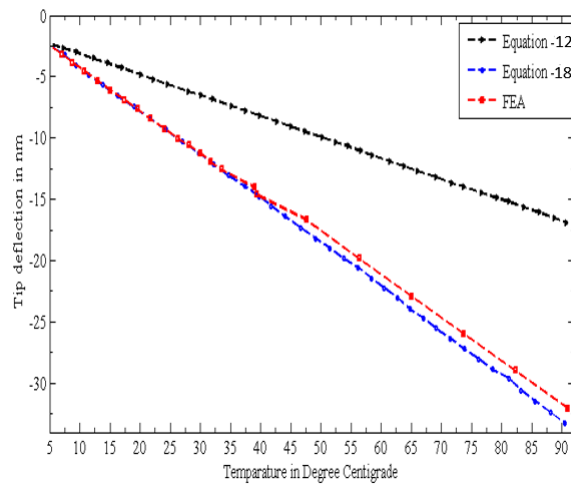


Fig. 5. Estimated edge deformation using (12) and (18) and finite-element analysis

Table 2. Comparison of edge deformation calculated from (7) and (8) with Experimental results

Measured Temperature in (°C)	Measured Tip Deflection in nm	Deflection Calculated using (6)	Deflection Calculated using (7)
25	680	654.78	382.15
40	470	448.92	225.48
55	368	354.68	124.32
70	175	158.14	79.56
85	128	112.25	59.46
90	68	64.78	31.25

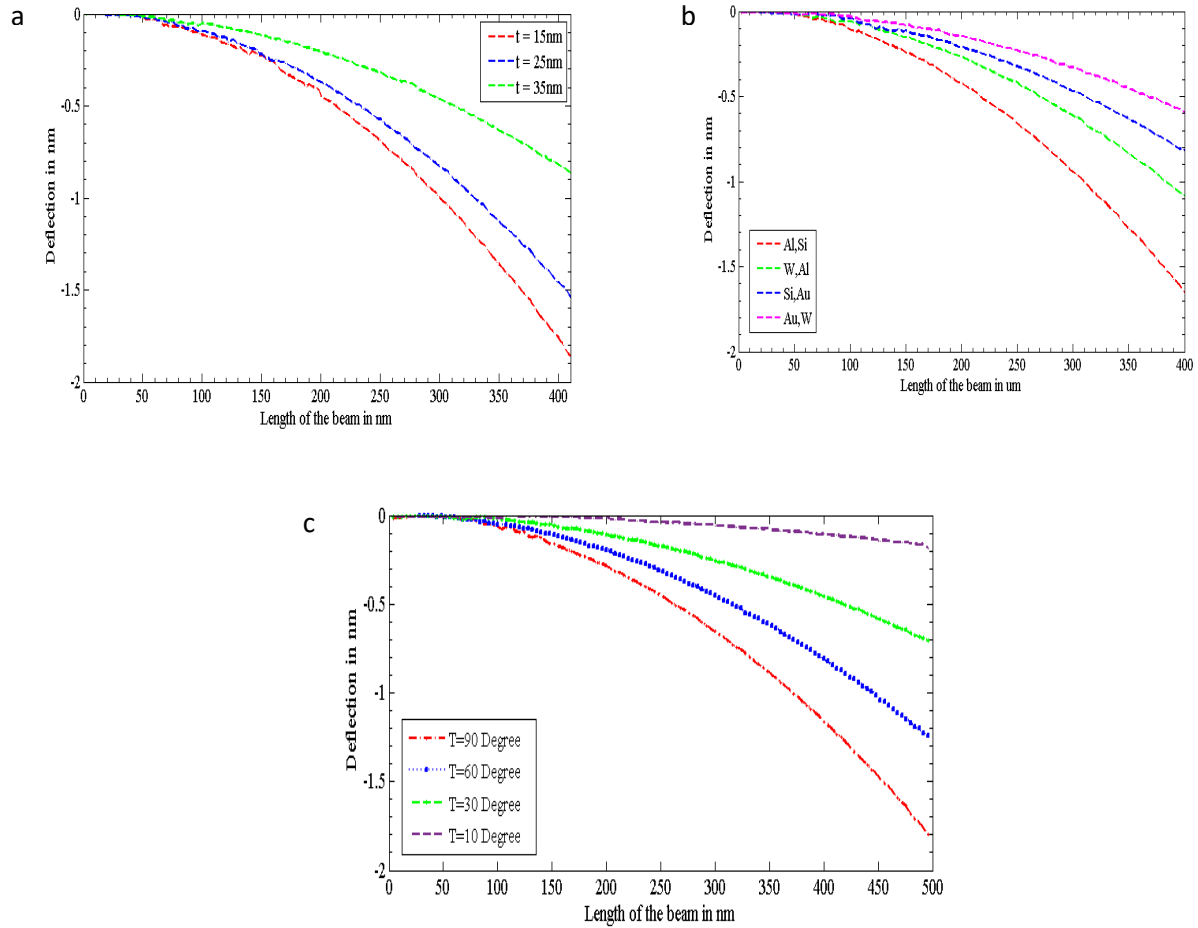


Fig.6. The influence of composite material arrangement on bimetallic beam deflection (a) Reverse relationship between beam deflection and a bimetallic layer thickness (b) Effect of material arrangements on beam deflection in a second model. (c) Deflection of the bimetallic cantilever with respect to temperature for the second model.

Analyzing a bimetallic cantilever nano actuator edge deflection and force using a simple methodical form is presented. Experimental results and comparison with finite element simulation are used to verify the model's validity. Analytical results of the model presented have an accuracy of at least 20% from comparison of tip deflection computed from (12) and (18) with experimental results obtained.

When the temperature does not alter, the bending of a beam is solely dependent on the electric potential applied. Figure 6(c) shows the deflection of the beam structure as the temperature increases. The bias voltage may be changed to adjust the lateral deformation. For a statistical approach, the deformation of a cantilever is calculated using the Finite Difference Method (FDM). Depending on the system's geometrical and material characteristics, simulation output results may vary significantly. The deflections of cantilever beams depend on the type of material and geometrical properties that have been used. For the second model, with a temperature increase of 50°C and a bias voltage of 5 volts, the results are given in Figures 6(a) and (b). Bimetallic cantilever beams were shown in Figure. 3 to show the various impacts of material configurations on displacement. Increasing the variance in thermal expansion coefficients (CTE) between layers increases the suggested model's responsiveness. To further illustrate this, if the thickness of each layer in a bimetallic cantilever beam is increased, the flexural deformation decreases (see Figure. 6 (a)). Therefore, the model's sensitivity to beam deflection has an inverse relationship to the thickness of the bimetallic layer.

5. Conclusion

In this paper, a mathematically modeled nano-electro-mechanical cantilever is investigated. Models are composed of governing equations obtained and solved numerically and analytically. Numerical findings show that using the appropriate materials and geometric characteristics may increase sensitivity. From the simulation findings, the difference between the coefficients of thermal expansion (CTE) of layers increases as the cantilever's length increases. Improvement in cantilever beam deflection when the layer thickness is minimized.

In contrast, this approach has many limitations, which can potentially lead to a muddled system. This limitation arises from the need to select the voltage such that the pull-in phenomenon is avoided when selecting the voltage. Compared with electrostatically actuated thermal actuators, the electro-thermal actuating mechanism has several advantages, such as avoiding static charges on the plates, improving the tuning reliability, and requiring lower driving voltages. Considering these factors as a whole could be necessary for a particular design of MEMS. Moreover, their use at various temperatures is affected by dimensions, materials, the level of sensitivity required, and environmental factors.

ACKNOWLEDGEMENTS

I would like to express my sincere thanks to the Nanosniff technologies center and the NMR Spectroscopy for Pharma and Biotech Research center, both of which are located at the Indian

Institute of Technology, Mumbai, for providing the necessary technical support and valuable guidance during the experimental work.

References

- Ali, J. et al. (2017)** ‘Biosensors: Their Fundamentals, Designs, Types and Most Recent Impactful Applications: A Review’, *Journal of Biosensors & Bioelectronics*, 08(01). doi:10.4172/2155-6210.1000235.
- Boisen, A. and Thundat, T. (2009)** ‘Design & fabrication of cantilever array biosensors’, *Materials Today*, 12(9), pp. 32–38. doi:10.1016/S1369-7021(09)70249-4.
- Chen, S.H. and Feng, B. (2011a)** ‘Size effect in micro-scale cantilever beam bending’, *Acta Mechanica*, 219(3–4), pp. 291–307. doi:10.1007/s00707-011-0461-7.
- Chu, W.H.M., Ehsan M, Robert LM. (1993)** *Analysis of tip deflection and force of a bimetallic cantilever microactuator. JM icromeec Microeng*, 3, pp.4-7.
- Chun-Hao Chen et al. (2009)** ‘A Wireless Bio-MEMS Sensor for C-Reactive Protein Detection Based on Nanomechanics’, *IEEE Transactions on Biomedical Engineering*, 56(2), pp. 462–470. doi:10.1109/TBME.2008.2003262.
- Cote, G.L., Lec, R.M. and Pishko, M.V. (2003)** ‘Emerging biomedical sensing technologies and their applications’, *IEEE Sensors Journal*, 3(3), pp. 251–266. doi:10.1109/JSEN.2003.814656.
- Finot, E., Passian, A. and Thundat, T. (2008)** ‘Measurement of Mechanical Properties of Cantilever Shaped Materials’, *Sensors*, 8(5), pp. 3497–3541. doi:10.3390/s8053497.
- Fu, L. et al. (2007)** ‘Magnetostrictive Microcantilever as an Advanced Transducer for Biosensors’, *Sensors*, 7(11), pp. 2929–2941. doi:10.3390/S7112929.
- Gupta, S. et al. (2016)** ‘Lab-on-Chip Technology: A Review on Design Trends and Future Scope in Biomedical Applications’, *International Journal of Bio-Science and Bio-Technology*, 8(5), pp. 311–322. doi:10.14257/ijbsbt.2016.8.5.28.
- Hegner, M. and Arntz, Y. (2003)** ‘Advanced Biosensing Using Micromechanical Cantilever Arrays’, in Braga, P. C. and Ricci, D., *Atomic Force Microscopy*. New Jersey: Humana Press, pp. 39–50. doi:10.1385/1-59259-647-9:39.
- Katta, M. et al. (2020)** ‘Static and Dynamic Analysis of Carbon Nano Tube Cantilever for Nano Electro Mechanical Systems Based Applications’, *Journal of Computational and Theoretical Nanoscience*, 17(5), pp. 2151–2156. doi:10.1166/jctn.2020.8862.

Katta, M. and Lavanya, K. (2021) ‘simulation approach to design high sensitive nems based sensor for molecular bio- sensing applications’, *Clinical Medicine*, 08(03), p. 9.

Khaleel, R.S. and Hashim, M.S., 2020. Fabrication of ZnO sensor to measure pressure, humidity and sense gases at room temperature by using rapid breakdown anodization method. *Kuwait Journal of Science*, 47(1).

Kim, J.H. et al. (2019) ‘Development of peptide biosensor for the detection of dengue fever biomarker, nonstructural 1’, *PLOS ONE*. Edited by S. D’Auria, 14(9), p. e0222144. doi:10.1371/journal.pone.0222144.

Kooser, A. (2003) ‘Investigation of the antigen antibody reaction between anti-bovine serum albumin (a-BSA) and bovine serum albumin (BSA) using piezoresistive microcantilever based sensors’, *Biosensors and Bioelectronics*, 19(5), pp. 503–508. doi:10.1016/S0956-5663(03)00221-5.

Kouravand, S. (2011a) ‘Design and modeling of some sensing and actuating mechanisms for MEMS applications’, *Applied Mathematical Modelling*, 35(10), pp. 5173–5181. doi:10.1016/j.apm.2011.04.015.

Lee, J. et al. (2015) ‘Enhanced performance of an innovative dengue IgG/IgM rapid diagnostic test using an anti-dengue EDI monoclonal antibody and dengue virus antigen’, *Scientific Reports*, 5(1), p. 18077. doi:10.1038/srep18077.

Li, X. et al. (2009) ‘Integrated MEMS/NEMS Resonant Cantilevers for Ultrasensitive Biological Detection’, *Journal of Sensors*, 2009, pp. 1–10. doi:10.1155/2009/637874.

Mathur, H., Agarwal, V. and Sengar, K. (2017) ‘Finite Element Analysis of MEMS based Piezoresistive Diamond Thin Film Cantilever Pressure Sensor’, 04(02), p. 5.

Miranji Katta and Sandanalakshmi R (2020a) ‘Geometrical Sensitivity Analysis of Bio-Nano Electro Mechanical Systems Using FEM Analysis For Disease Detection’, *Bioscience Biotechnology Research Communications*, 13(2), pp. 49–58.

Mohd Ghazali, F.A. et al. (2020) ‘MEMS actuators for biomedical applications: a review’, *Journal of Micromechanics and Microengineering*, 30(7), p. 073001. doi:10.1088/1361-6439/ab8832.

Mukhopadhyay, R. et al. (2005) ‘Cantilever Sensor for Nanomechanical Detection of Specific Protein Conformations’, *Nano Letters*, 5(12), pp. 2385–2388. doi:10.1021/nl051449z.

- Navakul, K. et al. (2017)** ‘A novel method for dengue virus detection and antibody screening using a graphene-polymer based electrochemical biosensor’, *Nanomedicine: Nanotechnology, Biology and Medicine*, 13(2), pp. 549–557. doi:10.1016/j.nano.2016.08.009.
- Neethu, K. and Suja, K.J. (2016)** ‘Sensitivity Analysis of Rectangular Microcantilever Structure with Piezoresistive Detection Technique Using Coventorware FEA’, *Procedia Computer Science*, 93, pp. 146–152. doi:10.1016/j.procs.2016.07.194.
- Nordström, M. et al. (2008)** ‘SU-8 Cantilevers for Bio/chemical Sensing; Fabrication, Characterisation and Development of Novel Read-out Methods’, *Sensors*, 8(3), pp. 1595–1612. doi:10.3390/s8031595.
- Rao, D.N. and Wootla, B. (2007)** ‘Catalytic antibodies: Concept and promise’, *Resonance*, 12(11), pp. 6–21. doi:10.1007/s12045-007-0110-6.
- Rosen, Y. and Gurman, P. (2010)** ‘MEMS and Microfluidics for Diagnostics Devices’, *Current Pharmaceutical Biotechnology*, 11(4), pp. 366–375. doi:10.2174/138920110791233316.
- Saylan, Y. et al. (2019)** ‘An Alternative Medical Diagnosis Method: Biosensors for Virus Detection’, *Biosensors*, 9(2), p. 65. doi:10.3390/bios9020065.
- Vasan, A.S.S., Doraiswami, R. and Pecht, M. (2011)** ‘Embedded 3D BioMEMS for multiplexed label free detection’, in *2011 IEEE 61st Electronic Components and Technology Conference (ECTC). 2011 IEEE 61st Electronic Components and Technology Conference (ECTC)*, Lake Buena Vista, FL, USA: IEEE, pp. 1412–1419. doi:10.1109/ECTC.2011.5898697.
- Vineetha, K.V. et al. (2018a)** ‘Design of MEMS sensor for the detection of cholera and diarrhea by capacitance modulation’, *Microsystem Technologies*, 24(8), pp. 3371–3379. doi:10.1007/s00542-017-3702-4.
- Wadas, M.J. et al. (2017)** ‘Detection of Traumatic Brain Injury Protein Biomarkers With Resonant Microsystems’, *IEEE Sensors Letters*, 1(6), pp. 1–4. doi:10.1109/LSSENS.2017.2768514.
- Wee, K.W. et al. (2005)** ‘Novel electrical detection of label-free disease marker proteins using piezoresistive self-sensing micro-cantilevers’, *Biosensors and Bioelectronics*, 20(10), pp. 1932–1938. doi:10.1016/j.bios.2004.09.023.
- Yanagida, Y. (2017)** ‘MEMS/NEMS-based Devices for Bio-measurements’, *Electrochemistry*, 85(9), pp. 572–579. doi:10.5796/electrochemistry.85.572.
- Yang, J. et al. (2016)** ‘Piezoresistive Silicon Cantilever Covered by ZnO Nanorods for Humidity Sensing’, *Procedia Engineering*, 168, pp. 1114–1117. doi:10.1016/j.proeng.2016.11.361.

Yu-Jie Huang *et al.* (2013) ‘A CMOS Cantilever-Based Label-Free DNA SoC With Improved Sensitivity for Hepatitis B Virus Detection’, *IEEE Transactions on Biomedical Circuits and Systems*, 7(6), pp. 820–831. doi:10.1109/TBCAS.2013.2247761.

Zhou, Y. *et al.* (2009) ‘Design, fabrication and characterization of a two-step released silicon dioxide piezoresistive microcantilever immunosensor’, *Journal of Micromechanics and Microengineering*, 19(6), p. 065026. doi:10.1088/0960-1317/19/6/065026.

Loui, A., Goericke, F.T., Ratto, T.V., Lee, J., Hart, B.R. and King, W.P., (2008) ‘The effect of piezoresistive microcantilever geometry on cantilever sensitivity during surface stress chemical sensing’. *Sensors and Actuators A: Physical*, 147(2), pp.516-521.

Lee, J.A. and Verleysen, M., (2007). *Nonlinear dimensionality reduction* (Vol. 1). New York: Springer.

Submitted: 12/05/2022

Revised: 21/06/2022

Accepted: 23/06/2022

DOI : 10.48129/kjs.20495

Study physical characteristics of Polyvinyl Alcohol/Carboxymethyl cellulose blend films

Sarah. H. Abead*, Mahasin F. Hadi Al-Kadhemy, Khaldoon N. Abbas

¹*Dept. of Physics, College of Science, Mustansiriyah University,
Baghdad, Iraq*

**Corresponding Author: hashemsara757@gmail.com*

Abstract

The pure polyvinyl alcohol (PVA), pure CarboxyMethyl Cellulose (CMC), and CMC/PVA blend films with different amounts (0.1, 0.2, 0.25, 0.3 and 0.4 g) of both polymers were prepared by simple solution casting method in this study. FTIR and UV-Vis spectroscopies were used to characterize the physical properties of as-prepared samples. FTIR spectroscopy revealed that the original bonds for both PVA and CMC polymers were appearing in blend polymer, but some bonds referring to CMC polymer seemed in high amounts of this polymer. Optical characteristics showed that the absorbance and absorption coefficient of PVA polymer is improved with increased amounts of CMC polymer. The direct relationship between absorbance and absorption coefficient with amounts of CMC polymer will be established. Furthermore, the energy gap of pure CMC (5.24 eV) and pure PVA (4.74 eV) polymers films were estimated. Tuning E_g toward lower value due to change CMC polymer concentration of blend polymer (PVA/CMC) film was achieved. From the findings of optical properties, it concludes that the blend film has the highest absorbance and absorption coefficient and lowest transmittance in the UV region compared to pure PVA and CMC polymers.

Keywords: Blend polymer; CMC polymer; FTIR spectroscopy; PVA polymer; UV-Visible spectroscopy.

1. Introduction

Generally, natural polymeric materials (amber, wool, silk, cellulose, natural rubber etc.) were used in flocculation, textiles, papers, foods, and medicines as well as in several technical operations, such as solar cells, energy storage devices, nano-dielectric structures, and optoelectronic devices [Khoramabadi *et al.* 2020; Pashameah *et al.*, 2022 ; Atta *et al.*, 2021]. Plants' fundamental structural component is cellulose, which is both renewable and biodegradable. It is the world's most abundant natural biopolymer. Natural cellulose fibers are primarily formed by photosynthesis in plants such as grasses, reeds, stalks, and woody vegetation. There are numerous advantages, including renewable, low cost, low density, low energy consumption, high specific strength, nonabrasive, and relatively reactive surface etc., [Al-Bermamy *et al.*, 2013]. Cellulose derivatives like carboxymethyl cellulose (CMC) are biocompatible [Miyamoto *et al.*, 1989], and have been used in medication delivery formulations [Hashim & Hadi, 2017]. Despite their effective applications and inexpensive cost, cellulose derivatives have been neglected [Coviello *et al.*, 2007; Malafaya *et al.*, 2007].

The CMC polymer is one of the significant derivatives of cellulose, which is a cellulose-derived ionic linear polysaccharide. CMC is employed primarily because of its high viscosity, lack of toxicity, and lack of allergenicity. CMC hydro-gel has high water content, superior biodegradability, and a wide range of uses. It can be employed as filler in bio-composite films due to its polymeric structure and high molecular weight [Almasi *et al.*, 2010] CMC can enhance the mechanical and barrier properties of pea starch-based films [Ma *et al.*, 2008]. Furthermore, polyvinyl alcohol (PVA-semicrystalline) is a type of polymer that comes in powders, fibers, and film. This water-soluble polymer is extensively utilized in warp sizing agents, paper coating agents, adhesives, and hydrophilic applications [Atta *et al.*, 2021; Bhat *et al.*, 2005]. PVA has recently been the focus of intense research due to its low cost of production leads to a wide range of industrial applications [Jasim *et al.*, 2020]. PVA polymer with amazing mechanical characteristics compared to CMC-semicrystalline polymer, which has high biocompatibility and biodegradability while suffering from meagre mechanical properties.

Therefore, this study tries to apply the blending technique of PVA/CMC polymers which can improve the physical characteristics of produced materials [Khoramabadi *et al.*, 2020]. Several studies have been done in this area. R. G. Kadhim *et al.* [Kadhim *et al.*, 2017] have studied the structural, electrical, and optical characteristics of a CuO nanoparticle to enhance the physical properties of (PVA/CMC) blend. The absorbance of (PVA/CMC) blend film increases as the number of CuO nanoparticles increases. The energy gap (E_g) and optical constants (extinction coefficient, refractive index, absorption coefficient, imaginary and real dielectric constants) of the (PVA/CMC) blend increases as the weight percentages of CuO increase. A. J. Kadham *et al.* [Kadham *et al.*, 2018], prepared (PVP/CMC/MgO nanoparticles) blend film and investigate the optical properties of the film. The results of the experiments revealed that when the concentration of MgO nanoparticles increases, the absorption and refractive index, and extinction coefficient of the blend film was improved. Furthermore, [Khoramabadi *et al.*, 2020], introduce a review paper that includes the benefit of synthesis of (PVA/CMC) composites and their properties and potential applications (such as electrochemical and energy storage devices, food packaging, and agriculture). [Pashameah *et al.*, 2022], investigated the production and characterization of polymer (PVA/CMC/MnO₂ NPs) nanocomposite; they mentioned to polymer nanocomposite compounds can use in multifunctional applications like (nano-dielectric systems, optoelectronic devices and solar cells).

The current study aims to investigate the effect of applying the blend technique on enhancing the structural and optical properties of (PVA/CMC) composites-based films by taking different amounts of mixing ratios between two polymers, which needs more investigation.

2. Theoretical Part

Absorbance (A) is defined as the ratio of the material's absorbed light intensity (I_A) to the incoming light intensity (I_0) [Soliman *et al.*, 2020]

$$A = \frac{I_A}{I_o} \quad (1)$$

The absorption coefficient α is well-defined as a material's ability to absorb light of a specific wavelength [Hashim & Hadi, 2017]:

$$\alpha = 2.303 \frac{A}{t} \quad (2)$$

Where t is the sample thickness from the following equation can calculate the energy band gap [Jawad & Al-kadhemy, 2021]:

$$\alpha h\nu = B(h\nu - E_g)^x \quad (3)$$

Where E_g : is the optical energy band gap, $h\nu$: is the photon energy, B : is a constant and x : is constant may take values (1/2, 3/2) for allowed and forbidden direct transition, respectively and (2, 3) for allowed and forbidden indirect transition, respectively.

3. Experimental Part

Sodium Carboxymethyl cellulose (CMC) was attained as a powder form (AVONCHEM) with an average molecular weight 67000 g/mole made in the UK. PVA was obtained as a powder form (THOMAS BAKER) with an average molecular weight 14000 g/mole made in India. Synthesis of all films was carried out by solution casting method. To obtain pure PVA, pure CMC, and PVA/CMC blend films, these procedures will be taken. Firstly; the appropriate amounts of PVA and CMC powders were chosen (0.5) g dissolved in (15 ml and 25 ml) of distilled water under stirring and heat (30 °C) for (2 hr. and 24 hrs.), correspondingly. For blend films, initially (0.1, 0.2, 0.25, 0.3 and 0.4 g) of PVA polymer and (0.1, 0.2, 0.25, 0.3 and 0.4 g) of CMC polymer were dissolved separately in 8 ml and 17 ml of distilled water, respectively. The solutions were stirred and heated at (30 °C) for (2 hr. and 24 hrs.), respectively. The blend solutions were obtained by mixing the two solutions to get (PVA 0.1 g/CMC 0.4 g, PVA 0.2 g/CMC 0.3 g, PVA0.25 g/CMC 0.25 g, PVA0.3 g/CMC 0.2 g, PVA0.4 g/CMC 0.1 g). The mixed solutions were continually shaken for (30 min.) at room temperature until they had a uniform viscous appearance. Secondly, all films were attained by leaving the solutions in a petri dish at room temperature (25 °C) for one week to dry and get homogeneous pure PVA, pure CMC and PVA/ CMC blend films.

Using the UV-Visible spectrophotometer type (T80 Series UV/VIS spectrometer) that tests optical properties within the range (200-1100) nm, the absorption and transmission spectra of as-prepared samples are measured. Fourier transformer Infrared spectroscopy (FTIR) was conducted for all films using FTIR spectrometer (type: Bruker-Tensor 27 with ATR unit). Moreover, using a digital micrometre type (Tasha) made in Japan with measurement accuracy (0.001) mm and measurement range (0-150) mm, the thickness of all as-synthesis film was measured.

4. Results and Discussions

FTIR Spectra of pure PVA, pure CMC and PVA/CMC blend films with different amounts of mixing are recorded in the range (4000-400) cm^{-1} to identify the functional groups of as-prepared samples as shown in Figure (1) and Tables (1 and 2). The vibrational spectrum of pure PVA is exposed in Figure (1A), it exhibits the characteristics of the monomer vinyl alcohol and it indicates the modes of vibration. The broad bond absorbed out at 3280.12cm^{-1} assigned to O-H stretching from intermolecular hydrogen bonds. The vibrational bond noticed at 2914.05cm^{-1} and 2938.75cm^{-1} refers to the C-H stretching form alkyl groups. The noticeable peak 1732.61cm^{-1} is due to C=O carbonyl stretching. Furthermore, three peaks in the region (1328.80 , 1373.5 and 1420.45) cm^{-1} are assigned to C-H and CH_2 Bending. All FTIR spectrum peaks in the region (1300 - 1461) cm^{-1} are allocated to C-H and CH_2 bending; it will be appeared discriminate three peaks (1328.80 , 1373.5 and 1420.45) cm^{-1} . At interval (1050 - 1300) cm^{-1} , the peaks (1024.02 , 1046.54 , 1087.13 and 1241.93) cm^{-1} are noticed and referred to C-O stretching, while IR peak at 1241.39cm^{-1} is expected to C-H wagging mode. Finally, IR two peaks 835.00cm^{-1} and 918.58cm^{-1} result from C-C stretching and CH_2 rocks, respectively. All these bonds will be compared with results of previous studies [Abbas *et al.*, 2014; Kharazmi *et al.*, 2015; Yao *et al.*, 2022].

Furthermore, Figure (1B) demonstrates the FTIR spectrum of pure CMC polymer film, and information on locations of IR peaks appeared with types of bonds given in Table (1). The seven peaks positions at (3291.55 , 2920.14 , 1585.21 , 1417.49 , 1265.30 , 1020.30 and 897.28) cm^{-1} correspond to O-H stretching, C-H stretching vibration of the CH, CH_2 and CH_3 , Asymmetrical COO- (stretching carboxyl group), scissoring $-\text{CH}_2$, stretching at ether linkage C-O, bending C-O-C, and 1, 4- β Glycoside of cellulose, respectively. The current results are strongly matched with the result of previous investigates [Jawad *et al.*, 2021; El-Sakhawy *et al.*, 2018, Sohaimy & Isa, 2020].

Further FTIR Spectra are planned for PVA/CMC blend films for different amounts of both polymers as illustrated in Figures (1 C to G) and Table (2), for all amounts mixed between two polymers. The IR two peaks referred to O-H stretching (3200 - 3550) and C-H stretching (2920) cm^{-1} for both CMC and PVA polymers are observed. The bonds (1585.2cm^{-1} , Asymmetrical COO-stretching of carbonyl group, CMC polymer) appeared for all blend films. Moreover, noticeable bonds of C=O carbonyl stretch from vinyl alcohol, acetate 3groups (PVA polymer), 1733.61cm^{-1} looked with (PVA0.25 g /CMC 0.25 g, PVA0.3 g /CMC0.2 g and PVA0.4 g/ CMC 0.1 g) blend films, i.e. with increasing PVA polymer this bond will appear. In all blend polymer films, the two IR absorption bands refer to C-H scissoring (1417cm^{-1}) and C-H bending (1300 - 1461cm^{-1}) (PVA polymer). The new band at 1456.66cm^{-1} (PVA 0.4 g /CMC 0.1 g) film is corresponding to C-H bending. The bond C-O stretch (1050 - 1300) cm^{-1} has appeared in all blend films. While the bond C-C rocking noted for PVA 0.1g/ CMC 0.4g only and IR peak 835.00cm^{-1} corresponds to CMC polymer that acts 1, 4- β Glycoside of cellulose seemed only in (PVA 0.2g /CMC 0.3 g) and (PVA0.25 g / CMC0.25 g) and disappeared in the rest of films. The present FTIR findings strongly agreed with the outcomes of previous studies [Jawad *et al.*, 2021; Thuy *et al.*, 2021].

Table 1. FTIR characteristics of pure PVA and pure CMC films

Pure PVA film		Pure CMC films	
Assignments	Wavenumber (cm ⁻¹)	Assignments	Wavenumber (cm ⁻¹)
O-H stretching (3200-3550)cm ⁻¹	3280.12	O-H stretching	3291.55
C-H Asymmetric stretch form alkyl groups (2800-3000)cm ⁻¹	2938.75 2914.06	C-H stretching vibration of the CH,CH ₂ and CH ₃	2920.14
C=O carbonyl stretch (1550-1780)cm ⁻¹	1732.61	C=O stretching of carbonyl group	1585.21
CH,CH ₂ bending (1300-1461)cm ⁻¹	1420.54 1373.56 1328.80	CH ₂ ,scissoring	1417.49
CH-wagging	1241.93	C-O stretching of ether linkage	1265.30
C-O stretch	1087.13 1046.54 1024.02		
CH ₂ rocky	945.02		
C-C Stretching (625-970)cm ⁻¹	918.58 835.00	1,4-β Glycoside of Cellulose	897.28

Table 2. FTIR characteristics for PVA/CMC blend films

Assignments	Wavenumber(cm ⁻¹)				
	PVA0.1g/CMC0.4g	PV0.2g/CMC0.3g	PVA0.25g/CMC0.25g	PVA0.3/CMC0.2g	PVA0.4g/CMC0.1g
O-H Stretching	3290.96	3275.61	3275.57	3275.99	3275.32
C-H stretching	2920.65	2920.48	2920.96	2920.71	2920.37
C=O stretching carbonyl group	1585.2	1585.2	1585.2	1585.2	1733.61 carbonyl stretching
CH,CH bending	1417.00 1321.02	1418.58 1374.28 1319.02	1417.85 1374.55 1321.02	1417.70 1320.96	1456.66 1319.36
CH-wagging	1263.14	1243.62	1247.30	1260.12	1259.16
C-O stretch	1052.12	1021.68		1053.35	1021.50
CH₂rocky	913.90				
C-C stretching		834.16	827.08		

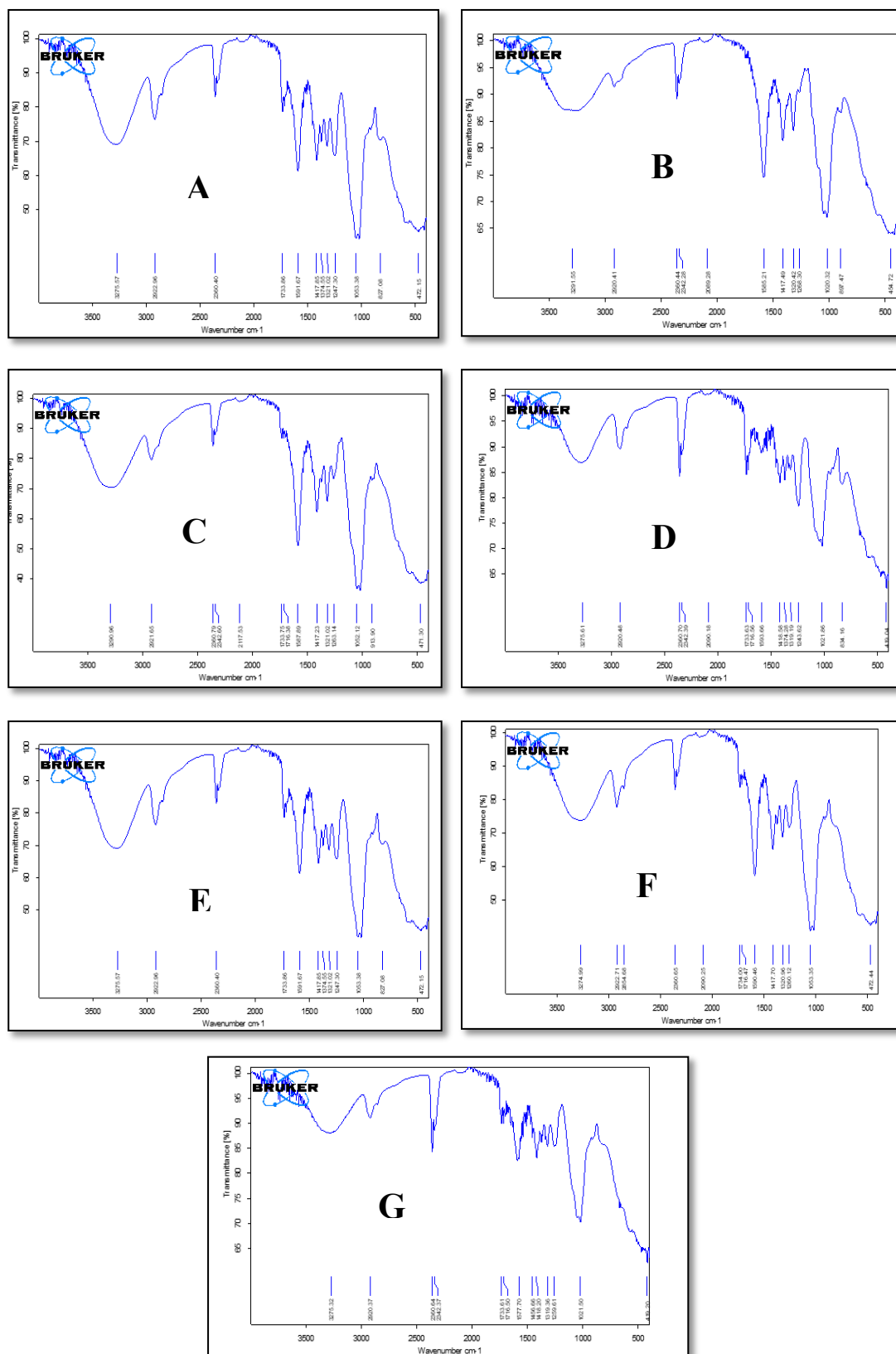


Fig. 1. FTIR spectra for (A) pure PVA, (B) pure CMC, (C) PVA0.1 g/CMC0.4 g, (D) PVA0.2 g/CMC0.3 g, (E) PVA0.25 g/CMC0.25 g, (F) PVA0.3 g/CMC0.2 g, (G) PVA0.4 g/CMC0.1 g

UV-visible absorption spectra are studied for pure PVA and pure CMC films as illustrated in Figure (2). It is clear that the maximum absorption wavelength for pure PVA film is located at 280 nm with maximum absorbance. (0.12). This absorption peak may be attributed to $\pi \rightarrow \pi^*$ electronic transition, this matched with the results of Refs. [Taleb *et al.*, 2009; Behera, 2015; Ram & Mandal, 2004; Kaiqiang & Quyet *et al.*, 2020]. Whereas the behavior of the absorption spectrum of pure CMC film has a wide spectrum, and absorbance is greater than pure PVA film. It reveals that the pure PVA and pure CMC films have mostly early zero absorbance and higher transmittance in the visible region because they are colorless polymers. The transmittance (Figure 3) in the UV region shows a higher decrease than in the invisible region. These results are agreement with aforementioned Ref. [Jawad *et al.*, 2021]. The absorption coefficient (α) was calculated from Equation (2) and plotted against wavelength for pure PVA and pure CMC films in Figure (4). The results indicate that resembles the absorption spectrum in behavior but with greater value, i.e. increasing the absorbance leads to increase the value of α . The advantage of measure absorption coefficient to conclude the transition nature when α greater than 10^4 cm^{-1} , it will be expected direct electronic transition. Whereas, when the value of α less than 10^4 cm^{-1} , indirect transition will be evaluated [Taleb *et al.*, 2009]. It will be concluded from Figure (4), the absorption coefficient less than 10^4 cm^{-1} , so indirect electronic transition will be deduced. Furthermore, the value of energy band gap (E_g) can be determined against photon energy ($h\nu$) as illustrated in Figure (5). the value of (E_g) for pure PVA film is assessed about (4.74) eV, that powerfully agreed with many literature [Taleb *et al.*, 2009; Al-Kadhemy *et al.*, 2020]. The estimated value of (E_g) for pure CMC film is found (5.24) eV, which is matched with both earlier investigates [Jawad *et al.* 2021].

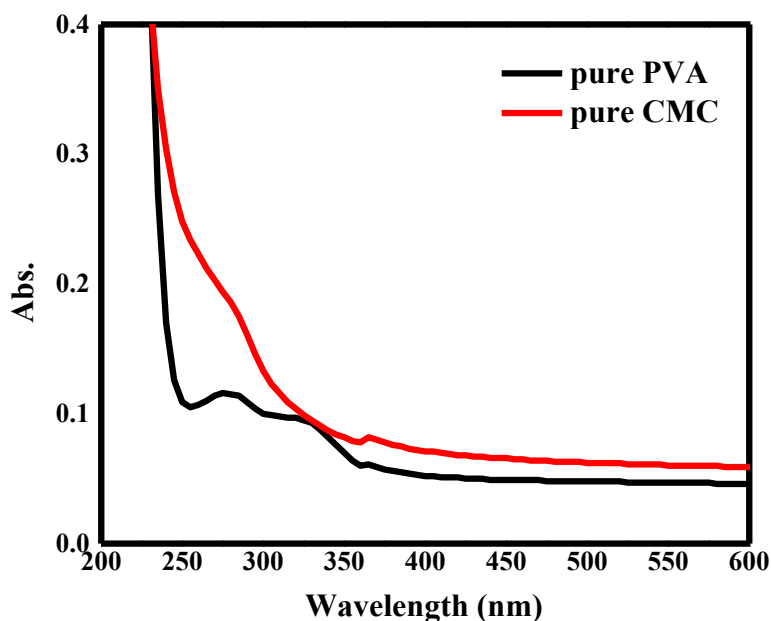


Fig. 2. Absorption spectra of pure PVA and pure CMC films

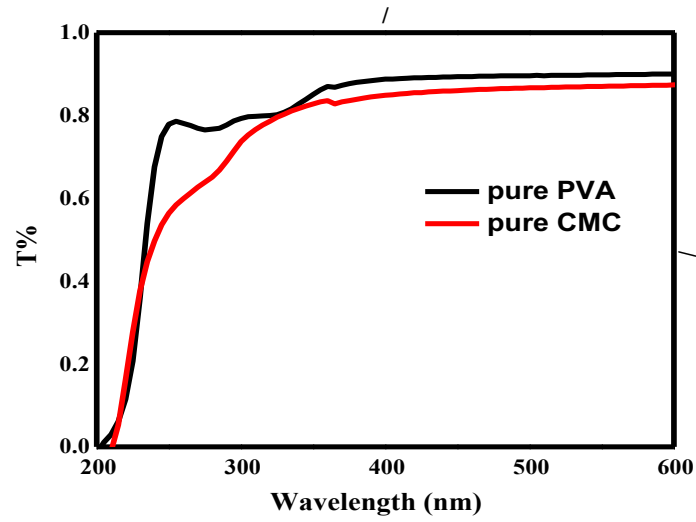


Fig. 3. Transmission spectra for pure PVA and pure CMC films

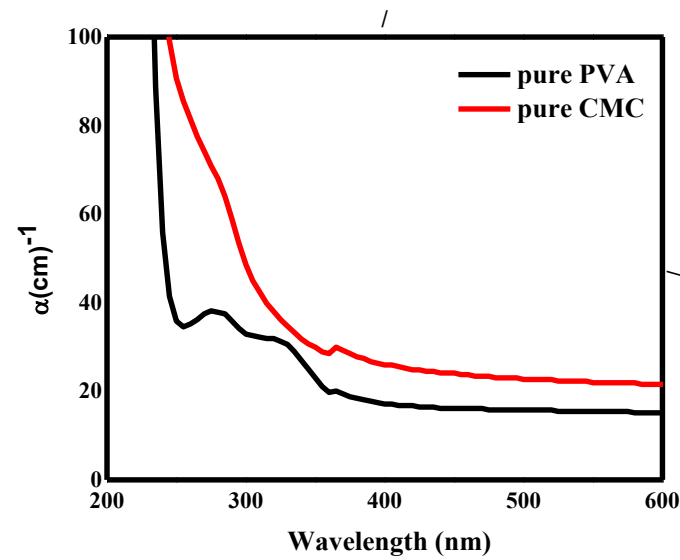


Fig. 4. Absorption coefficient of pure PVA and pure CMC films

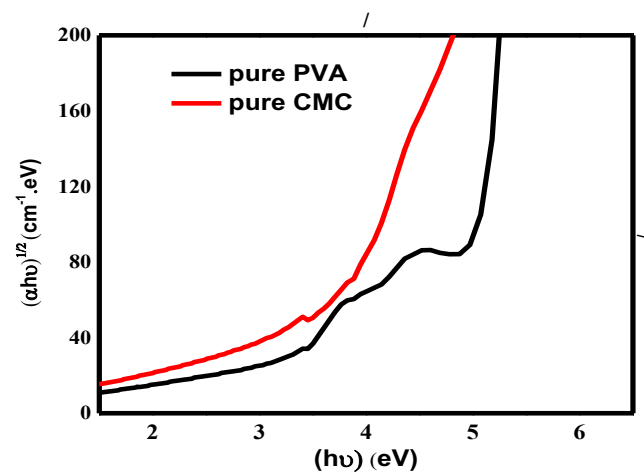


Fig. 5. The allowed indirect transition for pure PVA and pure CMC films

Moreover, the absorption spectrum of PVA/CMC blend polymer is illustrated in Figure (6). the results revealed that direct relationship between the absorbance and the concentration of CMC polymer. The (PVA0.1 g/CMC0.4 g) blend film displays the highest absorbance in both UV and visible regions. These findings may be explained as the absorbance of pure CMC film is higher than pure PVA film, as noted in Figure (2). So, increasing the concentration of CMC molecules in blend film leads to an increase in the absorbance of the (PVA0.1 g/CMC0.4 g) film. The findings of the transmittance spectra of PVA/CMC blend polymer with different mixing amounts demonstrated in Figure (7); which are confirmed the results of UV-Vis spectra of all blend films. When CMC amounts increased, the value of transmittance decreased due to the increasing absorbance of CMC molecules. That can be attributed to the accumulation of CMC inside the polymer matrix [Jawad *et al.*, 2021].

For further inspection of the optical properties of PVA/CMC films, Figure (8) demonstrates the absorption coefficient calculated from Equation (2) and plotted against incident wavelength. It indicates is lowering absorption at low energy, which means that the transitions of electrons are low. The absorption coefficient becomes large at high energy, which shows the high likelihood of transfers of electrons. The findings of Figure (8) revealed that the absorption coefficient for PVA/ CMC blend film is increased by the increase in the additive CMC polymer [Jawad *et al.*, 2021]. The benefit of the absorption coefficient is determining the transition electrons nature when the value of absorption coefficient is high in the higher energy predictable direct transition of electrons. Conservation of momentum and energy can be accomplished before photons and electrons, where the absorption coefficient is low so that indirect transition is expected [Jawad &Al-Kadhemy, 2021]. Conservation of momentum is through phonons alone. Figure (8) shows that the value of absorption coefficient for PVA/CMC blends films is lower than (10^4 cm^{-1}) indicating that it has indirect (E_g). The value of energy gap (E_g) can be calculated for the allowed indirect transition by using Equation (3) as shown in Figure (9) and Table (3). Figure (9) shows a remarkable decrease in the E_g value of (PVA 0.1 g/ CMC 0.4 g) blend film. The inverse relation between (E_g) for indirect transition and the amount of CMC polymer is predictable as confirmed in Table (3). This action may be attributed to the formation of new energy levels in the band gap, resulting in facilitating the crossing of electrons from the valence band to these local levels to [Jawad *et al.*, 2020].

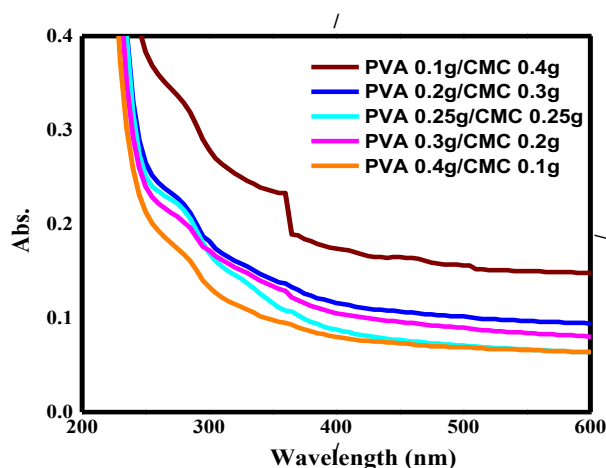


Fig. 6. Absorption spectra of PVA/CMC blend films

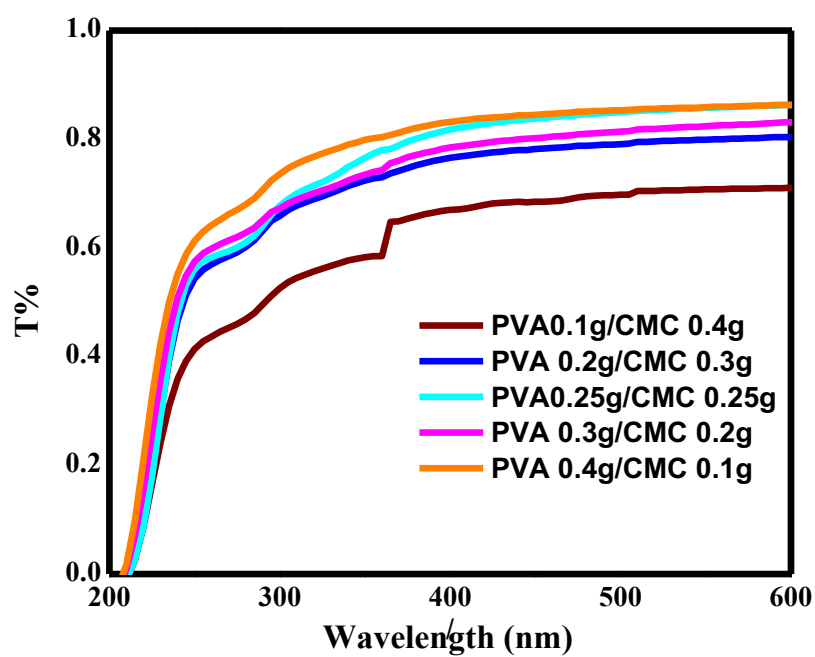


Fig. 7. Transmission spectra of PVA/CMC blend films

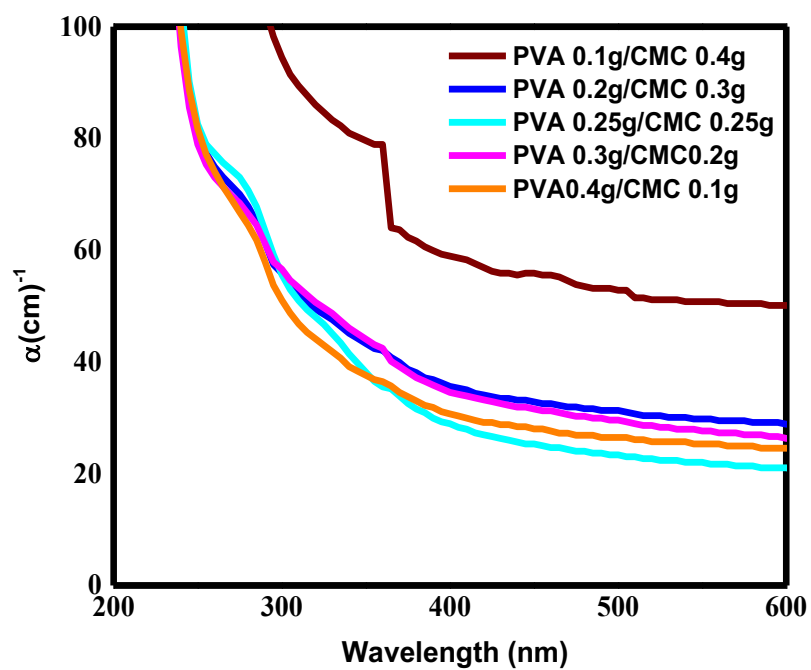


Fig. 8. Absorption coefficient of PVA/CMC blend film

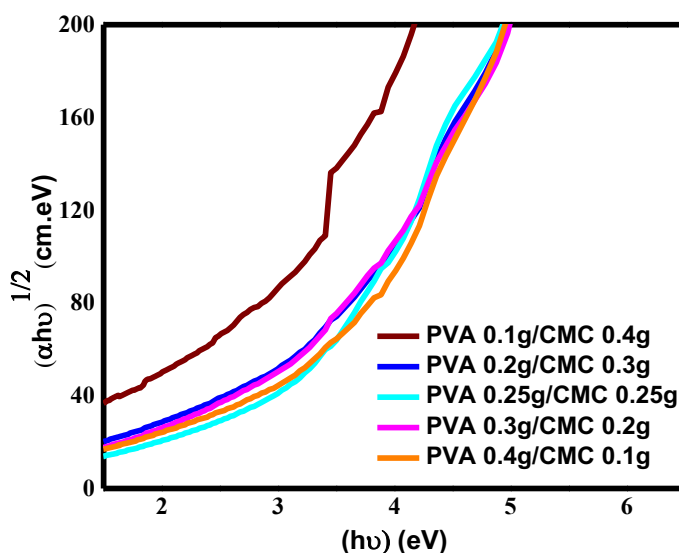


Fig. 9. The allowed indirect transition for CMC/PVA blend film

Table 3. Energy band gap (E_g) for pure CMC, pure PVA and PVA/CMC blend films

Samples	E_g (eV)
Pure CMC film	5.24
Pure PVA film	4.74
PVA 0.1g/CMC0.4g	3.30
PVA0.2g/CMC0.3g	4.76
PVA0.25g/CMC0.25g	4.75
PVA0.3g/CMC0.2g	4.72
PVA0.4g/CMC0.1g	4.71

5. Conclusions

In this study, the solution casting method was used to prepare pure PVA and CMC and PVA/CMC blend films. Different amounts (PVA0.1 g/ CMC 0.4 g, PVA0.2 g/ CMC 0.3 g, were mixed to improve the physical properties of as-synthesis films. FTIR analysis revealed that increased CMC amounts led appearance of some peaks related to it in the polymer blend. The original peak for both PVA and CMC are presented into blend polymer. From optical properties, it will be concluded that the PVA 0.1g/CMC 0.4g blend film has the highest absorbance and absorption coefficient and lowest transmittance in the UV region. The E_g modification of PVA/CMC blend films was achieved in this study. Where the low value of energy band gap of PVA/CMC blend films compared with E_g for pure PVA (4.74 eV) and pure CMC (5.24 eV) was revealed. That suggests a new area of various applications (such as solar cells and optoelectronic devices) of PVA/CMC blend films.

ACKNOWLEDGEMENTS

The authors are thankful to Mustansiriyah University, (www.uomustansiriyah.edu.iq) Baghdad-Iraq College of Science, and the Physics Department for the award of Major Research Project.

References

- Abbas, M., Abdallah, M. and Alwan, T. (2014)** Optical characterization of nickel doped polyvinyl alcohol films, *SOP Transactions on Physical Chemistry*, 1(2), pp. 1–9. doi:10.15764/pche.2014.02001.
- Al-Bermamy, A.-K.J., Kadem, B.Y. and Kadouri, L.T.H. (2013)** Preparation and study the mechanical properties of CMC/PVA composites by sound waves, *Advances in Physics Theories and Applications* 15(Cmc), pp. 11–20. <https://doi.org/10.1007/s10854-021-05701-3>.
- Al-Kadhemy, M.F.H., Ibrahim, S.A. and Salman, J.A.S. (2020)** Studying the physical properties polyvinyl alcohol polymer mixture with silica nanoparticles and its application as pathogenic bacteria inhibitor', *AIP Conference Proceedings*, 2290. doi:10.1063/5.0028817.
- Almasi, H., Ghanbarzadeh, B. and Entezami, A.A. (2010)** Physicochemical properties of starch-CMC-nanoclay biodegradable films, *International Journal of Biological Macromolecules*, 46(1), pp. 1–5. doi:10.1016/j.ijbiomac.2009.10.001.
- Atta, M.R., Alsulami, Q. A. , Asnag, G. M. & Rajeh, A. (2021)** Enhanced optical, morphological, dielectric, and conductivity properties of gold nanoparticles doped PVA / CMC blend as an application in organoelectronic devices. *Journal of Materials Science: Materials in Electronics* 32(2), PP.10443–10457.
- Behera, M. (2015)** An intensive study on the optical, rheological, and electrokinetic properties of polyvinyl alcohol-capped nanogold, *International Nano Letters*, 5(3), pp. 161–169. doi:10.1007/s40089-015-0150-y.
- Bhat, N. V., Nate, M.M., Kurup, M.B., Bambole, V.A., Sabharwal, S. (2005)** Effect of γ -radiation on the structure and morphology of polyvinyl alcohol films, *Nuclear Instruments and Methods in Physics Research, Section B: Beam Interactions with Materials and Atoms*, 237(34), pp. 585–592. doi:10.1016/j.nimb.2005.04.058.
- Coviello, T., Matricardi, P. , Marianecchi C., Alhaique, F. (2007)** Polysaccharide hydrogels for modified release formulations, *Journal of Controlled Release*, 119(1), pp. 5–24. doi:10.1016/j.jconrel.2007.01.004.
- El-Sakhawy, M., KAMEL, S., SALAMA, A. & HEBAT-ALLAH S. T. (2018)** Preparation and infrared study of cellulose-based amphiphilic materials, *Cellulose Chemistry and Technology*, 52(3–4), pp. 193–200.
- Hashim, A. and Hadi, A. (2017)**, Novel lead oxide polymer nanocomposites for nuclear radiation shielding applications, *Ukrainian Journal of Physics*, 62(11), pp. 978–983. doi:10.15407/ujpe62.11.0978.

Jasim, T.A., Saeed A. A., Kadhum, F. J. and Al-Kadhemy, M. F. H. (2020), Effect of Gamma Irradiation on The Optical Properties of PVA/Ag Nano composite, *Global Journal of Scientific Researches*, 8(2), pp. 23–31.

Jawad, Y.M. and Al-kadhemy, M.F.H. (2021), Enhancement Optical Properties of CMC / PAA Polymer Blend by MgO , SiO₂ and Bacteriocin for Antimicrobial Packaging Application, *Journal of Global Scientific Research* 6(9), pp. 1715–1725.

Jawad, Y.M., Al-Kadhemy, M.F.H. and Salman, J.A.S. (2021), Synthesis structural and optical properties of CMC/MgO nanocomposites, *Materials Science Forum*, 1039 MSF(Cmc), pp. 104–114. doi:10.4028/www.scientific.net/MSF.1039.104.

Kaiqiang, Z. & Quyet, V. L. (2020) Bioactive glass coated zirconia for dental implants, *Journal of Composites and Compounds*, 2(2), pp. 10-17. <https://doi.org/10.29252/jcc.2.1.2>.

Kadham, A.J., Hassan D. , Mohammad N., Hashim A. (2018), Fabrication of (polymer blend-magnesium oxide) nanoparticle and studying their optical properties for optoelectronic applications, *Bulletin of Electrical Engineering and Informatics*, 7(1), pp. 28–34. doi:10.11591/eei.v7i1.839.

Kadhim, R.G., Habeeb, M.A. and Jebur, Q.M. (2017) Study the Structure, electrical and optical properties for (PVA-CMC-CuO) Bio nano composites, *Journal of Chemical and Pharmaceutical Sciences*, 10(3), pp. 1120–1127.

Kharazmi, A., Faraji, N., Hussin, R. M. , Elias S. , Yunus, W. M. M. & Behzad, K. (2015) Structural, optical, opto-thermal and thermal properties of ZnS-PVA nanofluids synthesized through a radiolytic approach, *Beilstein Journal of Nanotechnology*, 6(1), pp. 529–536. doi:10.3762/bjnano.6.55.

Khoramabadia, H. N., Arefianb M., Hojjatic M., Tajzadd I., Mokhtarzadee A., Mazharf M., Jamavarig A. (2020) A review of polyvinyl alcohol/carboxymethyl cellulose (PVA/CMC) composites for various applications, *Journal of Composites and Compounds*, 2, PP. 69-76. <https://doi.org/10.29252/jcc.2.2.2>.

Ma, X., Chang, P.R. and Yu, J. (2008) Properties of biodegradable thermoplastic pea starch/carboxymethyl cellulose and pea starch/microcrystalline cellulose composites, *Carbohydrate Polymers*, 72(3), pp. 369–375. doi:10.1016/j.carbpol.2007.09.002.

Malafaya, P.B., Silva, G.A. and Reis, R.L. (2007) Natural-origin polymers as carriers and scaffolds for biomolecules and cell delivery in tissue engineering applications, *Advanced Drug Delivery Reviews*, 59(4–5), pp. 207–233. doi:10.1016/j.addr.2007.03.012.

Miyamoto, T., Takahashi, Sh., Ito H., Inagaki, H., Noishiki, Y. (1989) Tissue biocompatibility of cellulose and its derivatives, *Journal of Biomedical Materials Research*, 23(1), pp. 125–133. doi:10.1002/jbm.820230110.

Pashameah, R.A. El-Sharnouby, M., El-Askary, A., El-Morsy, M. A., Hoda, A. A., Menazea, A. A. (2022) Optical, Structural, Electrical Characterization of (Polyvinyl Alcohol–

Carboxymethyl Cellulose-Manganese Dioxide) Nanocomposite Fabricated via Laser Ablation, *Journal of Inorganic and Organometallic Polymers and Materials* 32, pp. 2863–2872. doi:10.1007/s10904-022-02311-2.

Ram, S. and Mandal, T.K. (2004), Photoluminescence in small isotactic, atactic and syndiotactic PVA polymer molecules in water, *Chemical Physics*, 303(1–2), pp. 121–128. doi:10.1016/j.chemphys.2004.05.006.

Sohaimy, M.I.H.A. and Isa, M.I.N.M. (2020), Natural inspired carboxymethyl cellulose (CMC) doped with ammonium carbonate (ac) as biopolymer electrolyte, *Polymers*, 12(11), pp.1–14. doi:10.3390/polym12112487.

Soliman, T.S., Vshivkov, S.A. and Elkalashy, S.I. (2020), Structural, thermal, and linear optical properties of SiO₂ nanoparticles dispersed in polyvinyl alcohol nanocomposite films, *Polymer Composites*, 41(8), pp. 3340–3350. doi:10.1002/pc.25623.

Taleb, M.F.A., El-Mohdy, H.L.A. and El-Rehim, H.A.A. (2009), Radiation preparation of PVA/CMC copolymers and their application in removal of dyes, *Journal of Hazardous Materials*, 168(1), pp. 68–75. doi:10.1016/j.jhazmat.2009.02.001.

Thuy, N.T.T., Huy, L. H., Vy, T. Th., Tam, N. Th. Th., Thanh, B. Th. L., Lan, N. Th. M. (2021), Green synthesis of silver nanoparticles using plectranthus amboinicus leaf extract for preparation of cmc/pva nanocomposite film, *Journal of Renewable Materials*, 9(8), pp. 1393–1411. doi:10.32604/jrm.2021.015772.

Yao, Y., Sun, Zh., Li X., Tang, Z. , Li Xi., Morrell, J. J., Liu Y., Li, Ch. & Luo, Z. (2022), Effects of raw material source on the properties of cmc composite films, *Polymers*, 14(1), pp. 1–15. doi:10.3390/polym14010032.

Submitted: 17/05/2022

Revised: 10/04/2023

Accepted: 01/08/2023

DOI: 10.48129/kjs.20553

Wormhole solutions and energy conditions in $f(R, T)$ gravity with exponential models

G. Mustafa^{1*}, M. Farasat Shamir², Anum Fazal²

¹*Dept. of Physics, Zhejiang Normal University, Jinhua, People's Republic of China*

²*National University of Computer and Emerging Sciences, Lahore Campus, Pakistan.*

*Corresponding author: gmustafa3828@gmail.com

Abstract

This study explores the new exact solutions of wormhole geometry by imposing the inconsistent Ricci scalar via inhomogeneous spacetime. The current analysis is dealing with the modified $f(R, T)$ theory of gravity. Two different models of gravity that are $f_1(R) = R - \alpha\gamma(1 - e^{-\frac{R}{\gamma}})$ known as exponential gravity model and $f_1(R) = R - \alpha\gamma\tanh(\frac{R}{\gamma})$ known as Tsujikawa model, where α, γ are model parameters with matter coupling are considered for the current study. The new feasible solutions for these models by comparing normal and inhomogeneous spacetimes is calculated. Further, we discuss the different properties of the obtained wormhole solutions by taking suitable values of the model parameters analytically and graphically. Moreover, we consider a specific shape functions i.e., $b(r) = r_0 \log(\frac{r}{r_0} + 1)$ and discuss the energy conditions for both models. The presented wormhole solutions are physically acceptable for the considered exponential and Tsujikawa gravity.

Keywords: Exponential gravity; exotic matter; inhomogeneous spacetime; wormholes; $f(R, T)$ theory of gravity.

1. Introduction

Einstein's general relativity (GR) has been served as the most successful theory of gravitation to explain and understand various mysteries of the astrophysical as well as the cosmological realm. A wormhole is a theoretical connection between remote regions of the universe, reducing travelling time and distance. The wormhole concept has an early history starting with Flamm (1916), who constructed the Schwarzschild solution of field equations as a non-traversable wormhole. Einstein-Rosen bridge proposed (Einstein *et al.*, 1935) the existence of a bridge, which used to join two copies of Schwarzschild spacetime for which the wormhole throat implodes, thus forming a singularity. The topological structure (Ellis, 1973) introduced the traversable wormhole concept by coupling geometry and scalar field, creating a geodesically complete manifold with no horizon. Bronnikov (1973) explored the scalar-electro-vacuum configurations without scalar charge. Clement (1984) gave a class of traversable wormholes in higher dimensions. The wormhole geometry (Morris *et al.*, 1988) proposed the idea of a traversable wormhole by joining two distant cosmic regions (asymptotically flat) by a throat supported by an exotic matter violating the null energy condition (NEC) that keeps the wormhole throat open. The physical viability of wormhole configuration requires confining this matter's usage, which is controversial. There has been extensive work on the construction of wormholes from black hole spacetimes and analysis of their various physical aspects (Richarte *et al.*, 2007., Eiroa *et al.*, 2008., Sharif *et al.*, 2016., Övgün, 2018., Falco *et al.*, 2020).

In curvature, the occurrence of higher-order terms would be feasible for constructing wormholes with thin shells detained by ordinary matter in the framework of the modified theory of gravity (Mazharimousavi *et al.*, 2010, Mazharimousavi *et al.*, 2011). In recent times, solutions of the wormholes have

been studied within the context of modified gravity, for example, Kaluza-Klein gravity (Dzhunushaliev *et al.*, 2011), the theory of Einstein-Gauss-Bonnet (Mehdizadeh *et al.*, 2015, Zangeneh *et al.*, 2015), theory of Einstein-Cartan (Bronnikov *et al.*, 2015, Bronnikov *et al.*, 2016, Mehdizadeh *et al.*, 2017), Brans-Dicke theory (Agnese *et al.*, 1995, Nandi *et al.*, 1997, Lobo *et al.*, 2010, Sushkov *et al.*, 2011), scalar-tensor gravity (Shaikh *et al.*, 2016) and Born-Infeld theory (Eiroa *et al.*, 2012). Recently, modified gravity theories have been considered relating to cosmological matters such as gravastars, wormholes, black holes and strange stars. These theories explain the dark energy problems and can describe the accelerating extension of the universe (Deffayet *et al.*, 2002, Carrol *et al.*, 2004, Nojiri *et al.*, 2003). One such theory with the modified form of Einstein gravity is $f(R, T)$ gravity theory, where R represents Ricci scalar, and T represents the trace of energy-momentum tensor (Harko *et al.*, 2011).

Some captivating cosmological $f(R, T)$ representations are auxiliary scalar field, models of dark matter and models of the anisotropic universe, which has been established using various setups (Houndjo *et al.*, 2012, Jamil *et al.*, 2012). Diverse cosmological uses of the $f(R, T)$ theory of gravity have been given in texts such as thermodynamics, compact stars, phase space perturbations and constancy of collapsing matter (Singh *et al.*, 2014, Shabani *et al.*, 2013, Shabani *et al.*, 2014, Santos *et al.*, 2013, Alvarenga *et al.*, 2013, Baffou *et al.*, 2015). Moraes *et al.*, (2017) obtained general analytic explanations for static wormholes in the $f(R, T)$ theory of gravity. Recently a non-linear $f(R, T)$ function has been defined. The spherical areas where energy conditions are fulfilled for traversable static wormholes have been explored by Godani and Samanta (2019). Shamir *et al.*, (2021) used non-commutative geometry to investigate the wormhole solutions in $f(R, T)$ gravity by considering Gaussian and Lorentzian sources. For the derivation of cosmological forces in various settings, numerous useful procedures for examining the $f(R, T)$ theory of gravity have been done. The split-up scenario which is $f(R, T) = f_1(R) + f_2(T)$ is considered in most cases because of its simplicity and also one can search the impact from T without stipulating $f_1(R)$ and similarly the impact from R without stipulating $f_2(T)$. Such reformation of the $f(R, T)$ theory of gravity is examined (Houndjo, 2012).

In the present paper, we want to find the wormhole solutions using a non-constant Ricci scalar in the framework of the feasible $f(R, T)$ theory of gravity. Inspired by the discussion mentioned above, we study static spherically symmetric wormholes in the $f(R, T)$ theory of gravity background in this article. Following is the organization of this paper: Section II includes the description of the basic formalism and corresponding spherically symmetric, static spacetime in $f(R, T)$ gravity. The discussion of energy conditions is provided in Section III. In Section IV, traversable wormhole solutions with inhomogeneous spacetime have been studied using both exponential gravity and the Tsujikawa model. The entire section V is dedicated to the study of energy conditions using $b(r) = r_0 \log(\frac{r}{r_0} + 1)$. And a summary of the whole study is highlighted in the last section.

2. $f(R, T)$ gravity Wormholes

The action of $f(R, T)$ gravity is as follows

$$S = \frac{1}{16\pi} \int d^4x f(R, T) \sqrt{-g} + \int \mathcal{L}_m d^4x \sqrt{-g}, \quad (1)$$

with R being Ricci scalar and T being trace of energy momentum tensor by T in an random $f(R, T)$ function, \mathcal{L}_m being Lagrangian density and metric determinant is g . Variation of Eq. (1) with metric tensor gives the following field equations (Cognola, 2008)

$$f_R(R, T)R_{\gamma\xi} - \frac{1}{2}f(R, T)g_{\gamma\xi} + (g_{\gamma\xi}\square - \nabla_\gamma\nabla_\xi)f(R, T) = 8\pi(T_{\gamma\xi}) - f_T(R, T)T_{\gamma\xi} - f_T(R, T)\Theta_{\gamma\xi}. \quad (2)$$

By contracting Eq. (2) with $g^{\gamma\xi}$, T and R are found to have a new relation such that

$$f_R(R, T)R + 3\square f_R(R, T) - 2f(R, T) = 8\pi T - f_T(R, T)T - f_T(R, T)\Theta. \quad (3)$$

Covariant derivative has been denoted as ∇ whereas \square denotes d'Alembert operator. Also,

$$f_R(R, T) = \frac{\partial f(R, T)}{\partial R}, \quad f_T(R, T) = \frac{\partial f(R, T)}{\partial T}, \quad \Theta_{\gamma\xi} = g_{\gamma\xi} \frac{\partial T_{\gamma\xi}}{\partial g^{\gamma\xi}}. \quad (4)$$

Here, we will take anisotropic fluid for energy momentum tensor as

$$T_{\gamma\xi} = (\rho + p_t)\mathcal{V}_\gamma\mathcal{V}_\xi - p_t g_{\gamma\xi} + (p_r - p_t)\chi_\gamma\chi_\xi, \quad (5)$$

\mathcal{V}_γ and χ_γ indicates four velocity vectors of the fluid with $\mathcal{V}^\gamma = e^{-\alpha}\delta_0^\gamma$ and $\chi^\gamma = e^{-\beta}\delta_1^\gamma$, hence fulfilling the relations $\mathcal{V}^\gamma\mathcal{V}_\gamma = -\chi^\gamma\chi_\gamma = 1$. By selecting $\mathcal{L}_m = \rho$, we get

$$\Theta_{\gamma\xi} = -2T_{\gamma\xi} - \rho g_{\gamma\xi}. \quad (6)$$

With Eqs. (2), (3) and (6), we attain modified field equations in the given form

$$\begin{aligned} f_R(R, T)G_{\gamma\xi} &= (8\pi + f_T(R, T))T_{\gamma\xi} + \left(\nabla_\gamma \nabla_\xi f_R(R, T) - \frac{1}{4}g_{\gamma\xi}(8\pi + f_T(R, T))T \right. \\ &\quad \left. + \square f_R(R, T) + f_R(R, T)R \right). \end{aligned} \quad (7)$$

In spherically symmetric spacetime, geometry of wormhole is as follows

$$ds^2 = -e^{2\psi(r)}dt^2 + \frac{dr^2}{1 - b(r)/r} + r^2(d\theta^2 + \sin^2\theta d\phi^2), \quad (8)$$

here $b(r)$ and $\psi(r)$ are radial coordinate functions with $b(r)$ being shape function and $\psi(r)$ being redshift function. In the present work, we take constant red shift function i.e. $\psi'(r) = 0$. Now by putting values in Equation (7) with metric given in Equation (8), we get

$$\frac{b'}{r^2} = \frac{(8\pi + f_T(R, T))}{f_R(R, T)}\rho + \frac{X}{f_R(R, T)}, \quad (9)$$

$$\begin{aligned} -\frac{b}{r^3} &= \frac{(8\pi + f_T(R, T))}{f_R(R, T)}p_r + \frac{1}{f_R(R, T)}\left(1 - \frac{b}{r}\right)\left[(f_R''(R, T) - f_R'(R, T)\frac{b'r - F_s}{2r^2(1 - b/r)})\right] \\ &\quad - \frac{X}{f_R(R, T)}, \end{aligned} \quad (10)$$

$$-\frac{b'r - b}{2r^3} = \frac{8\pi + f_T(R, T)}{f_R(R, T)}p_t + \frac{1}{f_R(R, T)}\left(1 - \frac{b}{r}\right)\frac{f_R'(R, T)}{r} - \frac{X}{f_R(R, T)}, \quad (11)$$

where

$$X \equiv X(r) = \frac{1}{4}(f_R(R, T)R + \square f_R(R, T) + (8\pi + f_T(R, T))T). \quad (12)$$

Ricci Scalar for spacetime given in Equation(8) is

$$R = \frac{2b'}{r^2}, \quad (13)$$

and

$$\square f_R(R, T) = \left(1 - \frac{b}{r}\right)\left[f_R''(R, T) - f_R'(R, T)\frac{b'r - b}{2r^2(1 - \frac{b}{r}) + \frac{2f_R'(R, T)}{r}}\right]. \quad (14)$$

The above-mentioned system of equations is not easy to solve for ρ , p_r and p_t as it has higher order derivatives with several unknowns. To make these calculations easy, we choose the split-up scenario which is $f(R, T) = f_1(R) + f_2(T)$. Taking $f_2(T) = \lambda T$ with λ being coupling parameter. Then putting in the form of $f(R, T)$ and making calculations in Eqs. (9-11) a little easier to solve. We obtain

$$\rho = \frac{b'f_R}{r^2(8\pi + \lambda)}, \quad (15)$$

$$p_r = -\frac{bf_R}{r^3(8\pi + \lambda)} + \frac{f_R'}{2r^2(8\pi + \lambda)}(b'r - F_s) - \left(1 - \frac{b}{r}\right)\frac{f_R''}{8\pi + \lambda}, \quad (16)$$

$$p_t = -\frac{f_R'}{r(8\pi + \lambda)}\left(1 - \frac{b}{r}\right) + \frac{f_R}{2r^3(8\pi + \lambda)}(b'r - b). \quad (17)$$

3. Energy Conditions

Null energy condition (NEC), weak energy condition (WEC), strong energy condition (SEC) and dominant energy condition (DEC) are main energy conditions. Aforementioned energy conditions are defined as

$$\begin{aligned} NEC &\Leftrightarrow T_{\gamma\xi} k^\gamma k^\xi \geq 0, & WEC &\Leftrightarrow T_{\gamma\xi} V^\gamma V^\xi \geq 0, \\ SEC &\Leftrightarrow (T_{\gamma\xi} - \frac{T}{2} g_{\gamma\xi}) V^\gamma V^\xi \geq 0, & DEC &\Leftrightarrow T_{\gamma\xi} V^\gamma V^\xi \geq 0, \end{aligned}$$

where k^γ is null vector and V^γ is timelike vector. For DEC , $T_{\gamma\xi} V^\gamma$ is not space like. The following energy conditions with regards to principal pressure are defined as

$$\begin{aligned} NEC &\Leftrightarrow \forall j, \rho + p_j \geq 0, & WEC &\Leftrightarrow \rho \geq 0 \text{ and } \forall j, \rho + p_j \geq 0, \\ SEC &\Leftrightarrow \forall j, \rho + p_j \geq 0, \rho + \sum_j p_j \geq 0, & DEC &\Leftrightarrow \rho \geq 0 \text{ and } \forall j, p_j \in [-\rho, +\rho]. \end{aligned}$$

Here we take these conditions with regards to principal pressures which is as follows

$$\begin{aligned} NEC &: \rho + p_r \geq 0, & \rho + p_t &\geq 0, \\ WEC &: \rho \geq 0, & \rho + p_r &\geq 0, & \rho + p_t &\geq 0, \\ SEC &: \rho + p - r \geq 0, & \rho + p_t &\geq 0, & \rho + p_r + 2p_t &\geq 0, \\ DEC &: \rho \geq 0, & \rho - |p_r| &\geq 0, & \rho - |p_t| &\geq 0. \end{aligned}$$

Theses energy conditions are fulfilled by normal matter because of positive density and positive pressure. Einstein's field theory tells us that wormholes are full of exotic matter which is not similar to normal matter.

4. Traversable Wormhole Solutions with Inhomogeneous Spacetime

Since, inhomogeneous spacetime (Golchina & Mehdizadeh, 2019) merges easily with cosmological background so we study the Ricci scalar of wormhole geometry as

$$R = 6a_1 + \frac{6a_2}{r^n}, \quad (18)$$

with a_1 , a_2 and n being free parameters. Now we have to find wormhole solutions with Ricci scalar given in equation (18). Shape function can be found by comparing equation (13) with equation (18),

$$b(r) = r^3(a_1 + \frac{3a_2}{3-n}r^{-n}) + C, \quad (19)$$

with C being constant of integration. In this work, we take $C = 0$. Following conditions should be satisfied by the shape function $b(r)$ for wormhole solution:

$$\begin{aligned} i) & \quad b(r_0) = r_0, \\ ii) & \quad b'(r_0) < 1, \\ iii) & \quad 1 - \frac{b(r)}{r} > 0. \end{aligned} \quad (20)$$

We can find the value of a_2 by putting condition $i)$ in Equation (19) as

$$a_2 = \frac{n-3}{3} r_0^{n-2} (a_1 r_0^2 - 1). \quad (21)$$

By inserting Equation (21) in Equation (19), shape function is found as

$$b(r) = (r_0^{n-2} - r_0^n a_1) r^{3-n} + a_1 r^3. \quad (22)$$

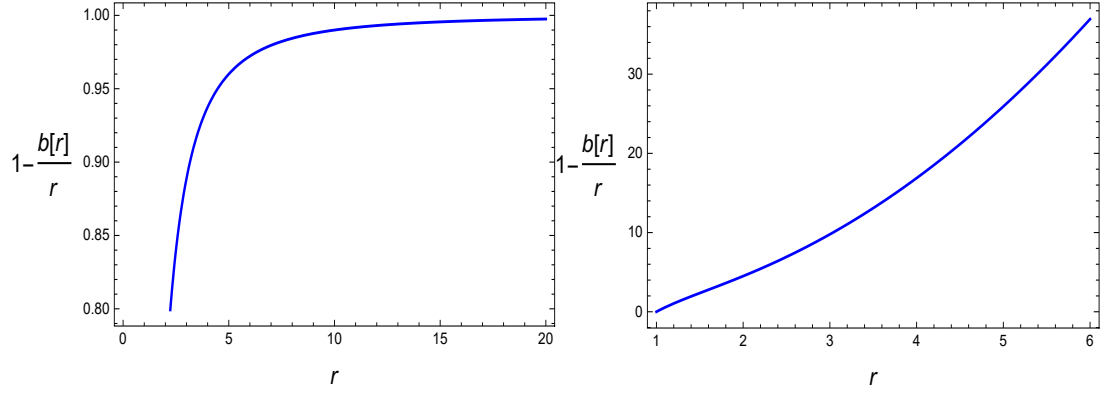


Fig. 1: Shows the asymptotically flat $a_1 = 0$ and asymptotically hyperbolic $a_1 = -1$ wormhole solutions respectively with $n = 4$ and $r_0 = 1$.

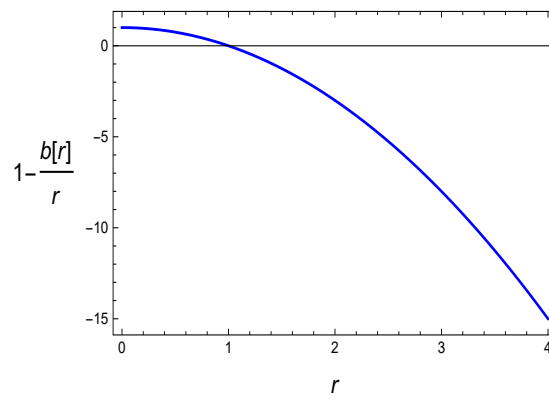


Fig. 2: Shows the asymptotically spherical $a_1 = 1$ wormhole solution with $n = 4$ and $r_0 = 1$.

The shape function for $a_1 = 0, \pm 1$ are shown in Figure 1 and Figure 2. We can also write Equation (22) as

$$\frac{b(r)}{r} = a_1 r^2 + (r_0^{n-2} - a_1 r_0^n) r^{2-n}. \quad (23)$$

Because of the condition *ii*) given in Equation (20) we should put $n > 2$ in Equation (23). Due to the metric (Equation (8)), we deduce that the solutions obtained with $a_1 = 0$, $a_1 = 1$ and $a_1 = -1$ at large value of r matches the flat, spherical and hyperbolic Friedmann-Robertson-Walker (*FRW*) universe respectively. Solutions of wormholes can be obtained for the shape function (22) by using Equations (15-17).

$$\rho = \frac{f_R}{r^2(8\pi + \lambda)} (3a_1 r^2 + r^{2-n}(3-n)(r_0^{n-2} - a_1 r_0^n)), \quad (24)$$

$$p_r = -\frac{f_R''}{8\pi + \lambda} + \frac{f_R'}{2r(8\pi + \lambda)} (3a_1 r^2 + r^{2-n}(3-n)(r_0^{n-2} - a_1 r_0^n)) - \frac{f_r A}{r^2} - \frac{f_R' A}{2r} + f_R'' A, \quad (25)$$

$$p_t = -\frac{f_R'}{r(8\pi + \lambda)} - \frac{f_R}{2r^2(8\pi + \lambda)} (3a_1 r^2 + r^{2-n}(3-n)(r_0^{n-2} - a_1 r_0^n)) + \frac{f_R A}{2r^2} + \frac{f_R'}{r}, \quad (26)$$

where

$$A = \frac{a_1 r^3 + r^{3-n}(r_0^{n-2} - a_1 r_0^n)}{r(8\pi + \lambda)}.$$

Now we consider a captivating $f(R)$ gravity model which is exponential gravity model (Cognola, 2008., Elizalde, 2011.)

$$f_1(R) = R - \alpha\gamma(1 - e^{-\frac{R}{\gamma}}), \quad (27)$$

where α and γ are taken as free positive parameters. We get the following set of equations by using Equation (27) in Equations (24-26)

$$\rho = \frac{C}{r^2(8\pi + \lambda)} \left(1 + \frac{4\alpha C}{r^2} + 2^{n-1} n \gamma \left(\frac{C}{r^2} \right)^{n-1} \right), \quad (28)$$

$$\begin{aligned} p_r = & -\frac{1}{r^3(8\pi + \lambda)} \left(I \right) \left(1 + \frac{4\alpha C}{r^2} + 2^{n-1} n \gamma \left(\frac{C}{r^2} \right)^{n-1} \right) + F \\ & - \frac{1}{2r^2(8\pi + \lambda)} \left(I \right) \left(G \right) - \frac{1}{8\pi + \lambda} \left(H \right) + \frac{1}{r(8\pi + \lambda)} \left(a_1 r^3 + r^{3-n}(r_0^{n-2} \right. \\ & - a_1 r_0^n) \left(-\frac{16\alpha D}{r^3} + \frac{24\alpha C}{r^4} + \frac{4\alpha E}{r^2} + 2^{n-1}(n-2)(n-1)n\gamma \left(\frac{C}{r^2} \right)^{n-3} \left(\frac{D}{r^2} - \frac{2C}{r^3} \right)^2 \right. \\ & \left. \left. + 2^{n-1}(n-1)n\gamma \left(\frac{C}{r^2} \right)^{n-2} \left(\frac{4D}{r^3} + \frac{6C}{r^4} + \frac{E}{r^2} \right) \right) \right), \end{aligned} \quad (29)$$

$$\begin{aligned} p_t = & -\frac{C}{2r^2(8\pi + \lambda)} \left(1 + \frac{4\alpha C}{r^2} + 2^{n-1} n \gamma \left(\frac{C}{r^2} \right)^{n-1} \right) + \frac{1}{2r^3(8\pi + \lambda)} \left(I \right) \left(1 + \frac{4\alpha C}{r^2} \right. \\ & \left. + 2^{n-1} n \gamma \left(\frac{C}{r^2} \right)^{n-1} \right) - \frac{1}{r(8\pi + \lambda)} \left(G \right) + \frac{1}{r^2(8\pi + \lambda)} \\ & \times \left(I \right) \left(\frac{4\alpha D}{r^2} - \frac{8\alpha C}{r^3} + 2^{n-1}(n-1)n\gamma \left(\frac{C}{r^2} \right)^{n-2} \left(\frac{D}{r^2} - \frac{2C}{r^3} \right) \right), \end{aligned} \quad (30)$$

where,

$$\begin{aligned} C &= 3a_1 r^2 + r^{2-n}(3-n)(r_0^{n-2} - a_1 r_0^n), \\ D &= 6a_1 r + r^{1-n}(2-n)(3-n)(r_0^{n-2} - a_1 r_0^n), \\ E &= 6a_1 + r^{-n}(1-n)(2-n)(3-n)(r_0^{n-2} - a_1 r_0^n). \end{aligned}$$

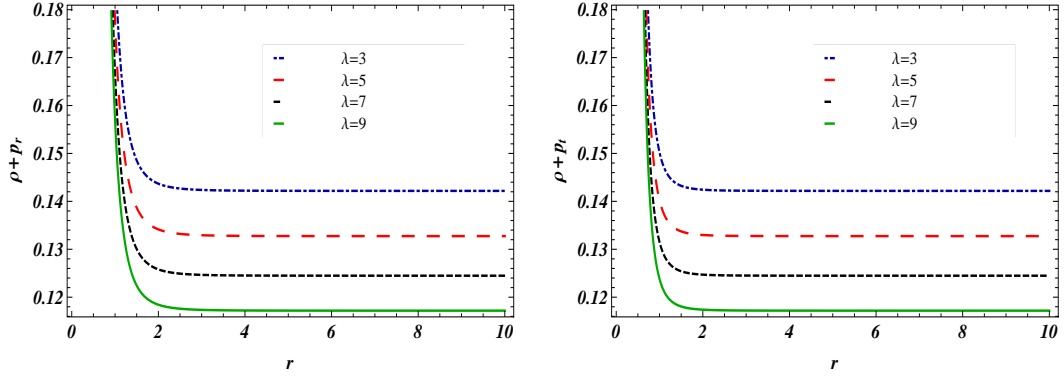


Fig. 3: Shows the development of $\rho + p_r$ and $\rho + p_t$ with $n = 5$, $a_1 = 2$, $r_0 = 0.9$ and $\gamma = 0.5$.

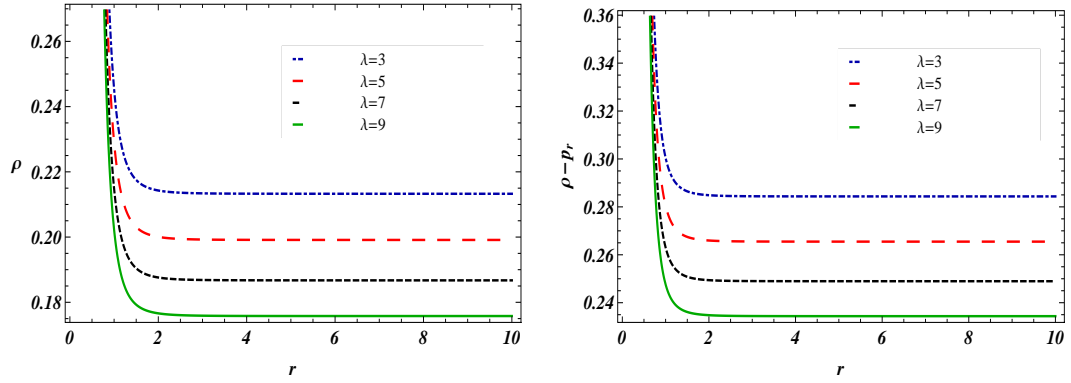


Fig. 4: Shows the development of ρ and $\rho - p_r$ with $n = 5$, $a_1 = 2$, $r_0 = 0.9$ and $\gamma = 0.5$.

$$\begin{aligned}
 F &= \frac{C}{2r(8\pi + \lambda)} \left(\frac{4\alpha D}{r^2} - \frac{8\alpha C}{r^3} + 2^{n-1}(n-1)n\gamma \left(\frac{C}{r^2} \right)^{n-2} \left(\frac{D}{r^2} - \frac{2C}{r^3} \right) \right), \\
 G &= \frac{4\alpha D}{r^2} - \frac{8\alpha C}{r^3} + 2^{n-1}(n-1)n\gamma \left(\frac{C}{r^2} \right)^{n-2} \left(\frac{D}{r^2} - \frac{2C}{r^3} \right), \\
 H &= -\frac{16\alpha D}{r^3} + \frac{24\alpha C}{r^4} + \frac{4\alpha E}{r^2} + 2^{n-1}(n-2)(n-1)n\gamma \\
 &\quad \times \left(\frac{C}{r^2} \right)^{n-3} \left(\frac{D}{r^2} - \frac{2C}{r^3} \right)^2 + 2^{n-1}(n-1)n\gamma \left(\frac{C}{r^2} \right)^{n-2} \left(-\frac{4D}{r^3} + \frac{6C}{r^4} + \frac{E}{r^2} \right), \\
 I &= a_1 r^3 + r^{3-n} (r_0^{n-2} - a_1 r_0^n)
 \end{aligned}$$

Now, considering one more specific and interesting model for $f(R)$ theory of gravity i.e., Tsujikawa

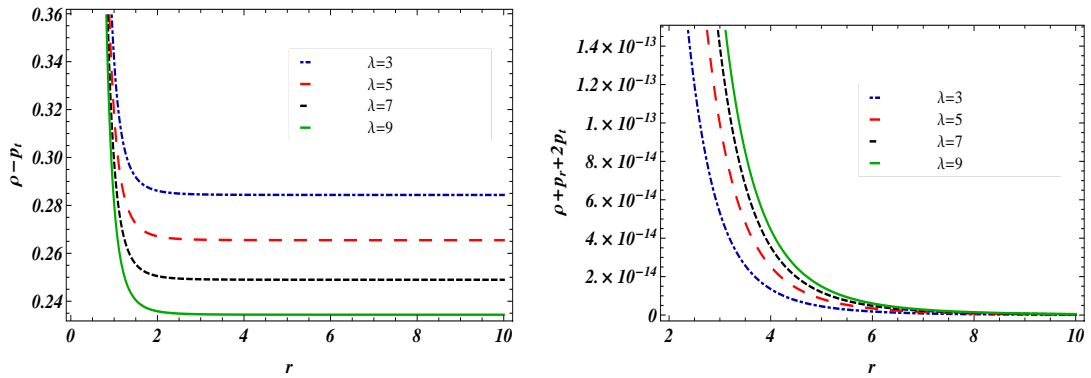


Fig. 5: Shows the development of $\rho - p_t$ and $\rho + p_r + 2p_t$ with $n = 5$, $a_1 = 2$, $r_0 = 0.9$ and $\gamma = 0.5$.

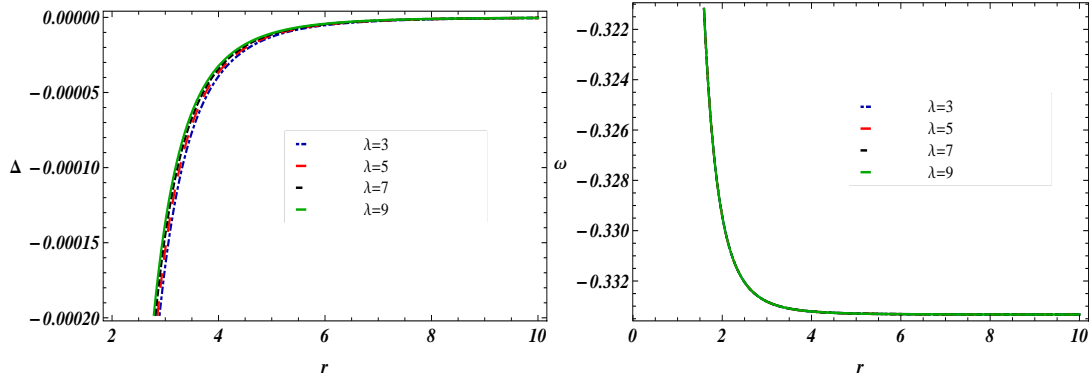


Fig. 6: Shows the development of Δ and ω with $n = 5$, $a_1 = 2$, $r_0 = 0.9$ and $\gamma = 0.5$.

model and is represented as (Tsujikawa 2008., DeFelice 2010.)

$$f_1(R) = R - \alpha\gamma \tanh\left(\frac{R}{\gamma}\right), \quad (31)$$

with α and γ being positive and free parameters of the given model. Now, by inserting the above model (31) in Equations (24-26), we obtain given set of equations:

$$\rho = \frac{C_1}{r^2(8\pi + \lambda)}(1 - \alpha S^2), \quad (32)$$

$$\begin{aligned} p_r = & -\frac{1 - \alpha S^2}{r^3(8\pi + \lambda)}(I) + \frac{\alpha C_1 S^2 T}{r(8\pi + \lambda)}\left(\frac{2D_1}{r^2\gamma} - \frac{4C_1}{r^3\gamma}\right) - \frac{\alpha S^2 T}{r^2(8\pi + \lambda)}(I)\left(\frac{2D_1}{r^2\gamma} - \frac{4C_1}{r^3\gamma}\right) \\ & - \frac{1}{8\pi + \lambda}\left(2\alpha S^4\left(\frac{2D_1}{r^2\gamma} - \frac{4C_1}{r^3\gamma}\right)^2 + 2\alpha S^2 T\left(-\frac{8D_1}{r^3\gamma} + \frac{12C_1}{r^4\gamma} + \frac{2E_1}{r^2\gamma}\right) - 4\alpha S^2 T^2\left(\frac{2D_1}{r^2\gamma} - \frac{4C_1}{r^3\gamma}\right)^2\right) \\ & + \frac{1}{r(8\pi + \lambda)}(I)\left(2\alpha S^4\left(\frac{2D_1}{r^2\gamma} - \frac{4C_1}{r^3\gamma}\right)^2 + 2\alpha S^2 T\left(-\frac{8D_1}{r^3\gamma} + \frac{12C_1}{r^4\gamma} + \frac{2E_1}{r^2\gamma}\right) - 4\alpha S^2 T^2\left(\frac{2D_1}{r^2\gamma} - \frac{4C_1}{r^3\gamma}\right)^2\right), \end{aligned} \quad (33)$$

$$\begin{aligned} p_t = & \frac{-C_1}{2r^2(8\pi + \lambda)}(1 - \alpha S^2) + \frac{1}{2r^3(8\pi + \lambda)}(I)(1 - \alpha S^2) - \frac{2\alpha S^2 T}{r(8\pi + \lambda)}\left(\frac{2D_1}{r^2\gamma} - \frac{4C_1}{r^3\gamma}\right) \\ & + \frac{2\alpha S^2 T}{r^2(8\pi + \lambda)}(I)\left(\frac{2D_1}{r^2\gamma} - \frac{4C_1}{r^3\gamma}\right), \end{aligned} \quad (34)$$

where,

$$\begin{aligned} S &= \operatorname{sech}\left(\frac{2C_1}{r^2\gamma}\right), \\ T &= \tanh\left(\frac{2C_1}{r^2\gamma}\right), \end{aligned}$$

and

$$\begin{aligned} C_1 &= 3a_1 r^2 + r^{2-n}(3-n)(r_0^{n-2} - a_1 r_0^n), \\ D_1 &= 6a_1 r + r^{1-n}(2-n)(3-n)(r_0^{n-2} - a_1 r_0^n), \\ E_1 &= 6a_1 + r^{-n}(1-n)(2-n)(3-n)(r_0^{n-2} - a_1 r_0^n). \end{aligned}$$

Shape function plays a vital part in defining the character of a wormhole structure. Since for each value of radial coordinate r , the energy density is positive. As seen in figure 4 and Figure 8 graphs on the left side, the obtained energy density is non-negative and decreasing. *NEC*, *WEC*, and *DEC* except are

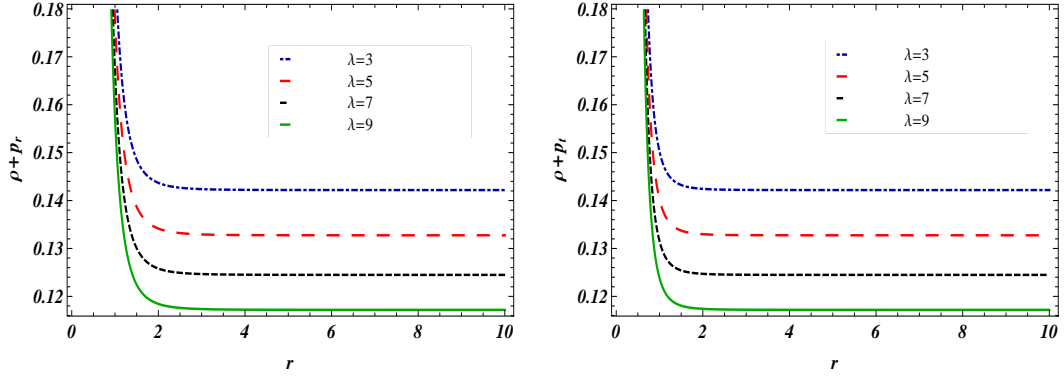


Fig. 7: Shows the development of $\rho + p_r$ and $\rho + p_t$ with $n = 5$, $a_1 = 2$, $r_0 = 0.9$ and $\gamma = 0.5$.

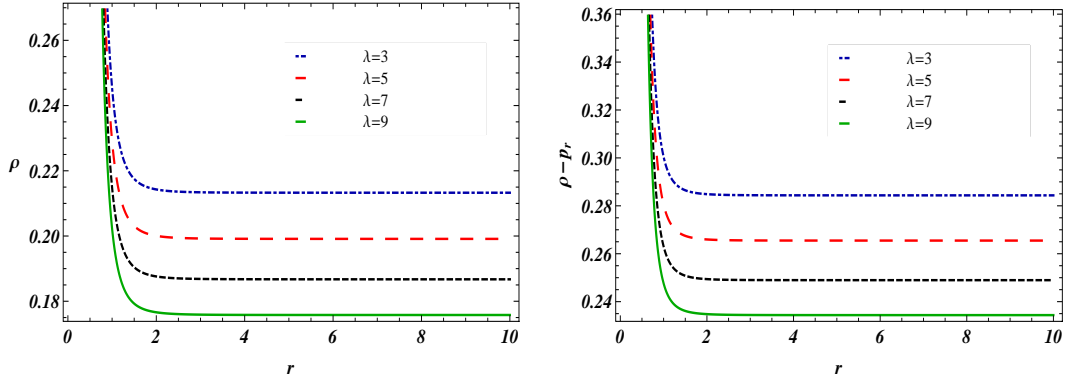


Fig. 8: Shows the development of ρ and $\rho - p_r$ with $n = 5$, $a_1 = 2$, $r_0 = 0.9$ and $\gamma = 0.5$.

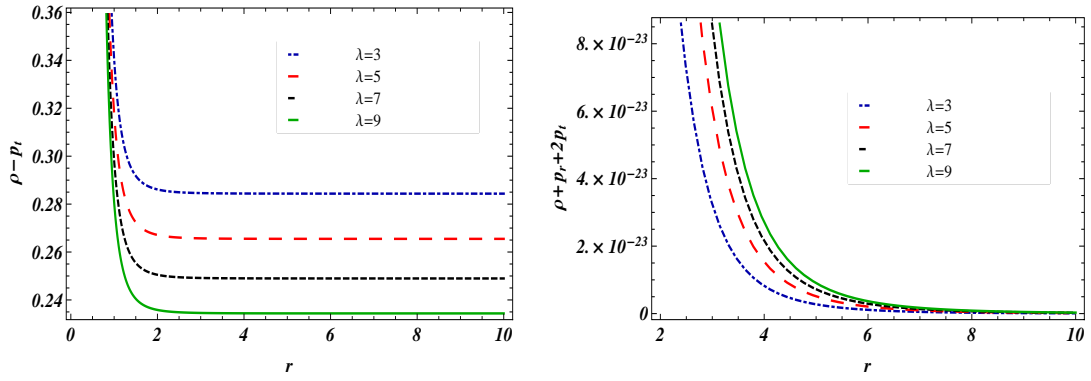


Fig. 9: Shows the development of $\rho - p_t$ and $\rho + p_r + 2p_t$ with $n = 5$, $a_1 = 2$, $r_0 = 0.9$ and $\gamma = 0.5$.

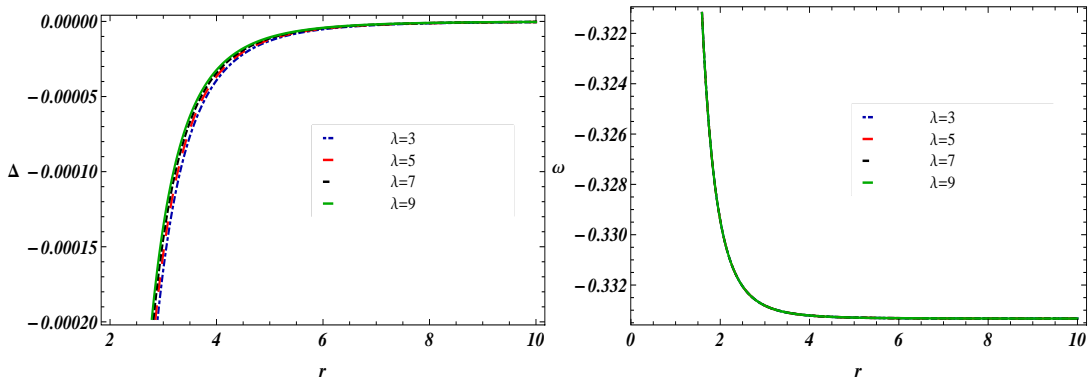


Fig. 10: Shows the development of Δ and ω with $n = 5$, $a_1 = 2$, $r_0 = 0.9$ and $\gamma = 0.5$.

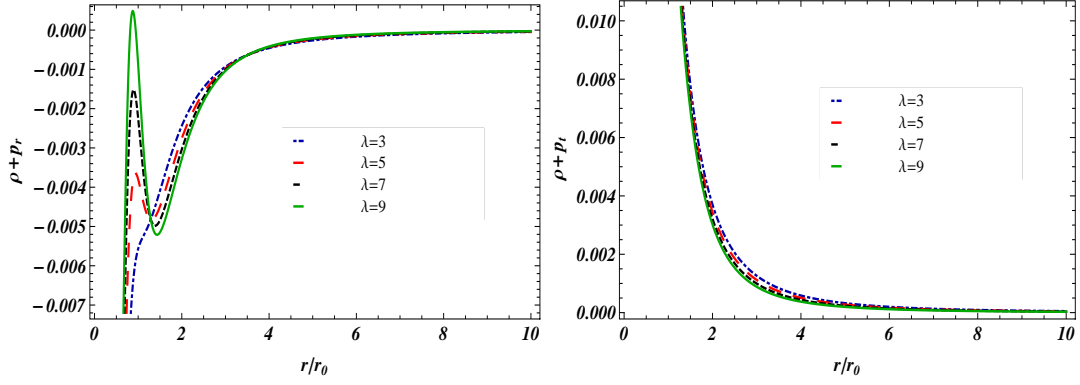


Fig. 11: Shows the development of $\rho + p_r$ and $\rho + p_t$ with $n = 5$, $a_1 = 2$, $r_0 = 0.9$ and $\gamma = 0.5$.

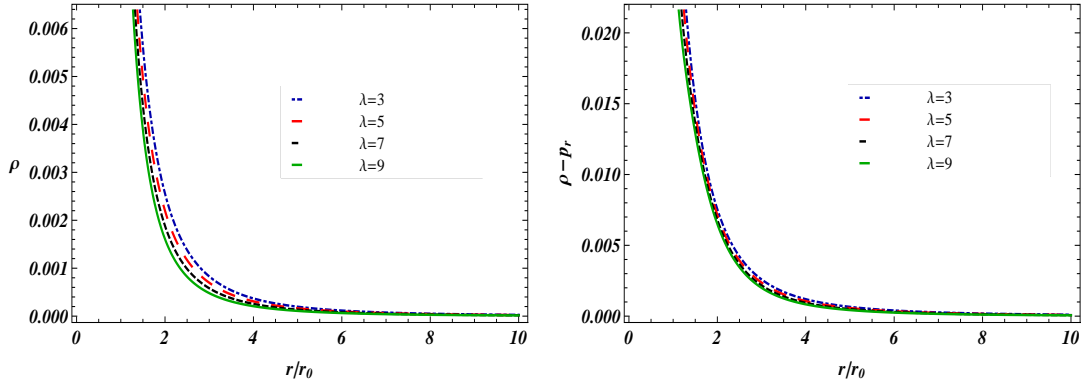


Fig. 12: Shows the development of ρ and $\rho - p_r$ with $n = 5$, $a_1 = 2$, $r_0 = 0.9$ and $\gamma = 0.5$.

satisfied throughout but *SEC* is not see (figures 3-5, and figures 7-9). Anisotropy parameter is denoted as $\Delta = p_t - p_r$. The negative value of Δ represents the attractive geometry of the wormhole, whereas the positive value represents the repulsive nature of geometry. For the given shape function, both the models have a negative anisotropy parameter which shows the attractive nature of geometry inside the wormhole see (figures 6,10). Furthermore in terms of radial pressure, equation of state parameter is defined as $\omega = \frac{p_r}{\rho}$. It tells us the type of fluid filled in the wormhole's structure. For the given shape function, value of ω for both the models is between -1 and 0 that indicates the existence of non-phantom fluid see (figures 6,10). Hence, such solutions to wormholes can occur without the existence of exotic matter.

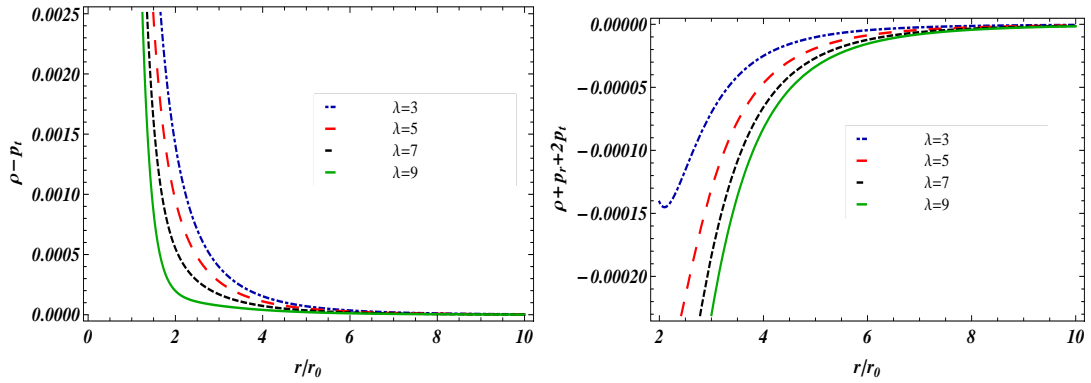


Fig. 13: Shows the development of $\rho - p_t$ and $\rho + p_r + 2p_t$ with $n = 5$, $a_1 = 2$, $r_0 = 0.9$ and $\gamma = 0.5$.

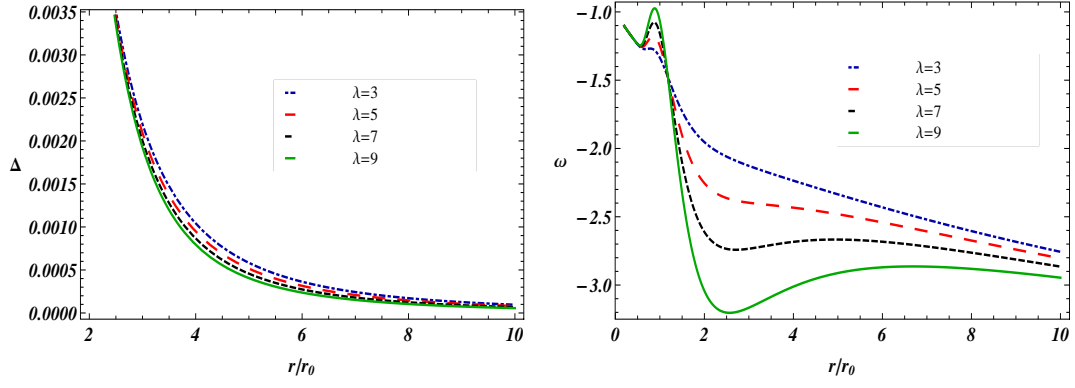


Fig. 14: Shows the development of Δ and ω with $n = 5$, $a_1 = 2$, $r_0 = 0.9$ and $\gamma = 0.5$.

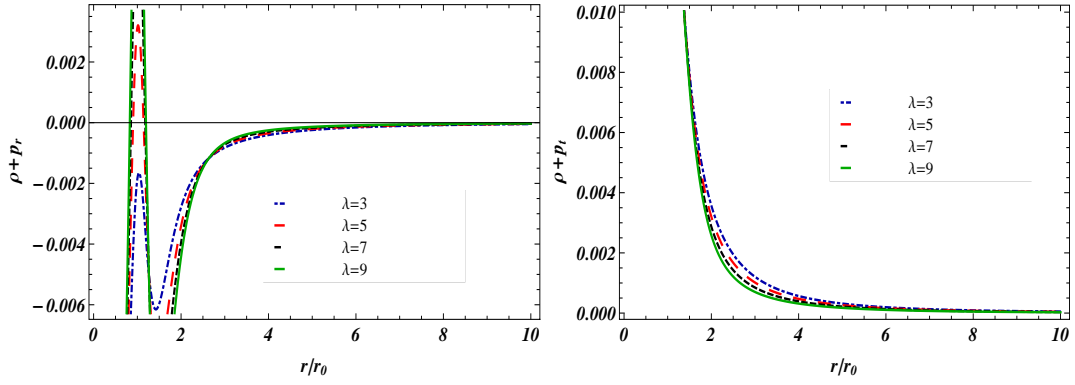


Fig. 15: Shows the development of $\rho + p_r$ and $\rho + p_t$ with $n = 5$, $a_1 = 2$, $r_0 = 0.9$ and $\gamma = 0.5$.

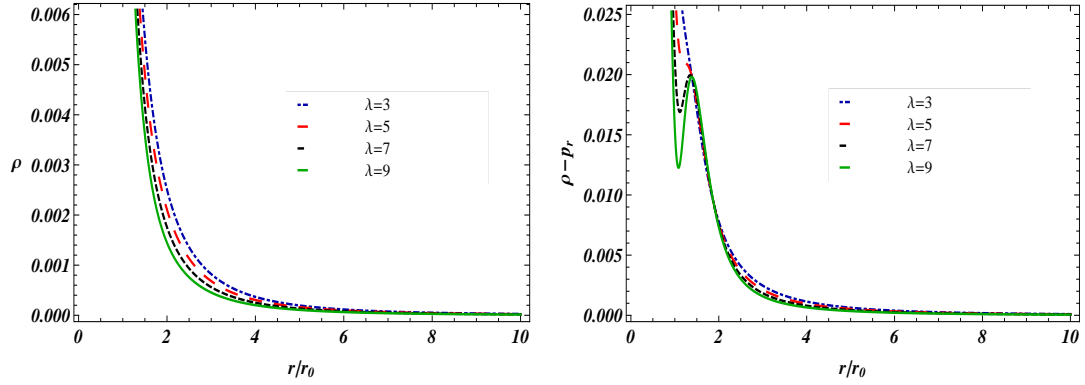


Fig. 16: Shows the development of ρ and $\rho - p_r$ with $n = 5$, $a_1 = 2$, $r_0 = 0.9$ and $\gamma = 0.5$.

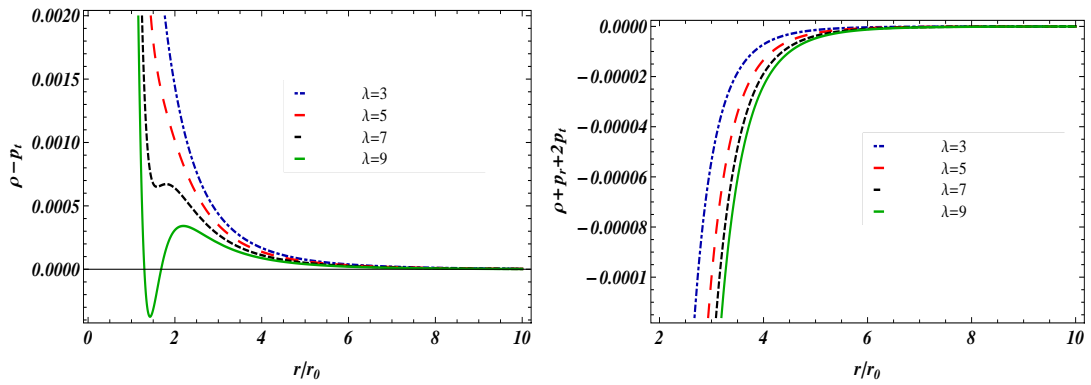


Fig. 17: Shows the development of $\rho - p_t$ and $\rho + p_r + 2p_t$ with $n = 5$, $a_1 = 2$, $r_0 = 0.9$ and $\gamma = 0.5$.

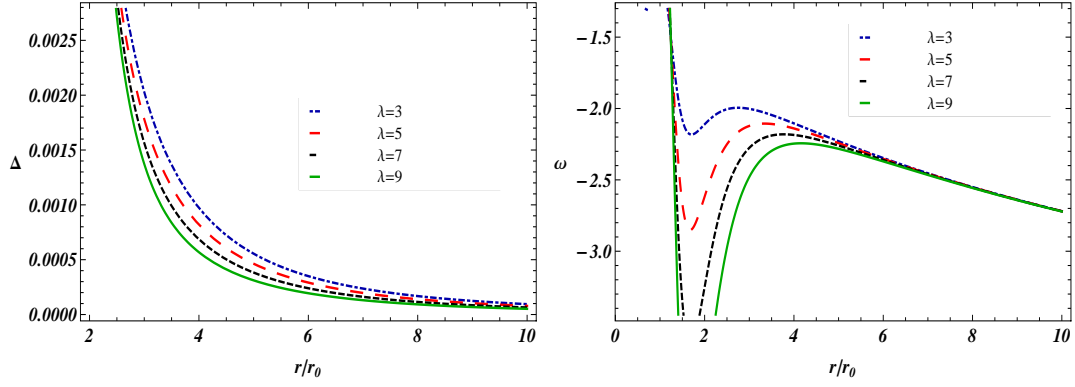


Fig. 18: Shows the development of Δ and ω with $n = 5$, $a_1 = 2$, $r_0 = 0.9$ and $\gamma = 0.5$.

5. NEC and WEC for $b(r) = r_0 \log(\frac{r}{r_0} + 1)$

In this section, energy conditions for a specific shape function (Godani, 2018., Smantha, 2018), which is defined as:

$$b(r) = r_0 \log\left(\frac{r}{r_0} + 1\right) \quad (36)$$

Now, by using Equation (36) in both exponential gravity models, which are given in Equation (27) and in Equation (31) we can check the behavior of energy conditions. As first attempt, we calculated the generic field equations for both models by Equation (27) and Equation (31) in Equations (15-17). The energy density and pressure components for the first model by Equation (27) are calculated as:

$$\rho = \frac{b'(r) \left(1 - \alpha e^{-\frac{2b'(r)}{\gamma r^2}}\right)}{(\lambda + 8\pi)r^2}, \quad (37)$$

$$\begin{aligned} p_r &= \frac{e^{-\frac{2b'(r)}{\gamma r^2}}}{\gamma^2(\lambda + 8\pi)r^7} \left(b(r) \left(\alpha \left(-16b'(r)^2 + r^2 \left(\gamma r^2 \left(2b^{(3)}(r) + \gamma \right) - 9\gamma r b''(r) - 4b''(r)^2 \right) \right. \right. \right. \\ &\quad \left. \left. + 2rb'(r) (8b''(r) + 7\gamma r) - \gamma^2 r^4 e^{\frac{2b'(r)}{\gamma r^2}} \right) + \alpha r \left(-2\gamma r^4 b^{(3)}(r) + 4r^2 b''(r) (b''(r) + 2\gamma r) \right) \right. \\ &\quad \left. \left. = 2(\gamma r^2 - 8) b'(r)^2 + rb'(r) ((\gamma r^2 - 16) b''(r) - 12\gamma r) \right) \right), \end{aligned} \quad (38)$$

$$p_t = \frac{r^2 (b(r) - rb'(r)) + \frac{\alpha e^{-\frac{2b'(r)}{\gamma r^2}} (r((\gamma r^2 + 8)b'(r) - 4rb''(r)) - b(r)(r(\gamma r - 4b''(r)) + 8b'(r)))}{\gamma}}{2(\lambda + 8\pi)r^5}. \quad (39)$$

The energy density and pressure components for the second model by Equation (31) are calculated as:

$$\rho = \frac{b'(r) \left(1 - \alpha \operatorname{sech}^2 \left(\frac{2b'(r)}{\gamma r^2}\right)\right)}{(\lambda + 8\pi)r^2}, \quad (40)$$

$$\begin{aligned} p_r = & \frac{1}{2\gamma^2(\lambda + 8\pi)r^7} \left(-48\alpha(r - b(r)) (rb''(r) - 2b'(r))^2 \operatorname{sech}^4 \left(\frac{2b'(r)}{\gamma r^2}\right) \right. \\ & + 2\alpha (b(r) (r (4b''(r) + \gamma r) - 8b'(r)) (r (\gamma r - 4b''(r)) + 8b'(r)) + 16r \\ & \times (rb''(r) - 2b'(r))^2) \operatorname{sech}^2 \left(\frac{2b'(r)}{\gamma r^2}\right) + 4\alpha\gamma r^2 (-2rb'(r)^2 + r (2r(b(r) - r) \\ & \times b^{(3)}(r) + (8r - 9b(r))b''(r)) + b'(r) (r (rb''(r) - 12) + 14b(r))) \\ & \times \left. \tanh \left(\frac{2b'(r)}{\gamma r^2}\right) \operatorname{sech}^2 \left(\frac{2b'(r)}{\gamma r^2}\right) - 2\gamma^2 r^4 b(r) \right), \end{aligned} \quad (41)$$

$$\begin{aligned} p_t = & \frac{1}{2\gamma(\lambda + 8\pi)r^5} \left(\alpha\gamma r^2 (rb'(r) - b(r)) \operatorname{sech}^2 \left(\frac{2b'(r)}{\gamma r^2}\right) + \gamma r^2 (b(r) - rb'(r)) \right. \\ & \left. - 8\alpha(r - b(r)) (rb''(r) - 2b'(r)) \tanh \left(\frac{2b'(r)}{\gamma r^2}\right) \operatorname{sech}^2 \left(\frac{2b'(r)}{\gamma r^2}\right) \right). \end{aligned} \quad (42)$$

Since we know that the existence of exotic matter in a wormhole is correlated to the violation of *NEC*. In response to the above mentioned energy conditions, we observe that for both models energy density is positive and decreasing (Figure 13) and (Figure 16) for the specific shape function i.e. $b(r) = r_0 \log(\frac{r}{r_0} + 1)$. Development of $\rho + p_r$ and $\rho + p_t$ (*NEC* and *WEC*) can be seen in (Figure 11) and (Figure 15) respectively. For both models, *NEC* is violated because of the negative behavior of $\rho + p_r$, which is evidence of the presence of exotic matter. All the energy conditions are presented graphically for $b(r) = r_0 \log(\frac{r}{r_0} + 1)$ specific model in (Figure 11-18) for both considered model of $f(R, T)$ gravity.

6. Conclusion

Scientists have always been concerned about the construction and occurrence of wormhole solutions in *GR*. The existence of exotic matter is one of the significant settings for producing wormholes because it violates *NEC*. But this is not the compulsory condition for the wormhole presence as long as it is cosmologically acceptable. Wormhole construction is a fascinating topic in terms of modified theories of gravity. In this paper, we have discussed different cases in $f(R, T)$ gravity and shown that the existence of exotic matter is a necessary but not critical condition for wormhole solutions existence. The essential features of the current study are itemized below:

- Firstly, we considered inhomogeneous spacetime in the $f(R, T)$ theory of gravity. Wormhole solutions are found using two captivating $f(R)$ models i.e. exponential gravity model ($f_1(R) = R - \alpha\gamma(1 - e^{-\frac{R}{\gamma}})$) and Tsujikawa model ($f_1(R) = R - \alpha\gamma \tanh(\frac{R}{\gamma})$). The energy conditions are studied and their geometric nature is examined. *NEC*, *WEC* and *DEC* are satisfied everywhere for both models (Figures 3-5, and Figures 7-9). This shows the presence of solutions of wormholes without the existence of exotic matter as *NEC* is satisfied everywhere. The geometric nature of the wormhole is found to be repulsive and is full of non-phantom fluid (Figures 7, 10). Hence, the obtained results show the existence of solutions of wormholes in the presence of non-exotic matter.
- Moving forward, *NEC* and *WEC* for a specific shape function i.e. $b(r) = r_0 \log(\frac{r}{r_0} + 1)$ using both exponential gravity model and Tsujikawa model have been explored. We observe that for the given models, energy conditions are provided in (Figures 11-18), and *NEC* is violated because of the negative behavior of $\rho + p_r$ which is the evidence of the existence of exotic matter.

In a nutshell, the present study gives a detailed discussion on the occurrence of solutions of wormholes in $f(R, T)$ gravity using specific models. In particular, we may conclude from this work that traversable wormholes are conceivable with or without the presence of exotic matter.

Acknowledgements G. Mustafa is very thankful to Prof. Gao Xianlong from the Department of Physics, Zhejiang Normal University, for his kind support and help during this research. Further, G. Mustafa acknowledges Grant No. ZC304022919 to support his Postdoctoral Fellowship at Zhejiang Normal University.

References

- Agnese A. G., and Camera, M. La. (2011).** Wormholes in Brans-Dicke Theory of Gravitation, *Phys. Rev.* **D51**(1995).
- Alvarenga, F. G.(2013).** Dynamics of scalar perturbations in $f(R, T)$ gravity, *Phys. Rev.* **D87**, 103526.
- Bronnikov, K.A.(1973).** Scalar tensor theory and scalar charge, *Acta Phys. Pol.* **B4**, 251.
- Bronnikov, K. A, and Galiakhmetov, A. M. (2015).** Wormholes without Exotic Matter in Einstein-Cartan Theory, *Grav. Cosmol.* **21**, 283.
- Bronnikov, K. A, and Galiakhmetov, A. M. (2016).** Wormholes and Blackholes without Phantom Fields in Einstein-Cartan Theory, *Phys. Rev.* **D94**, 124006.
- Baffou, E. H.(2015).** Cosmological viable $f(R, T)$ dark energy model: dynamics and stability, *Astrophys. Space Sci.* **356**, 173-180.
- Clement, G.(2004).** A class of wormhole solutions to higher-dimensional general relativity, *Gen. Relativ. Gravit.* **16**(1984)131.
- Carrol, S. M., Duvvuri, V., Trodden, M., and Turner, M. S., (2008).** Is Cosmic Speed-up due to New Gravitational Physics? *Phys. Rev.* **D70**, 043528.
- Cognola, G.(2008).** Class of viable modified $f(R)$ gravities describing inflation and the onset of accelerated expansion, *Phys. Rev.* **D77**, 046009.
- Dzhunushaliev, V. and Singleton, D. (1999).** Wormholes and Flux Tubes in 5D Kaluza-Klein Theory, *Phys. Rev.* **D59**, 064018.
- Deffayet, D., Dvali, G., and Gabadadze, G. (2002).** Accelerated Universe from Gravity Leaking to Extra Dimensions, *Phys. Rev.* **D65**, 044023.
- DeFelice, A. and Tsujikawa, S.(2010).** $f(R)$ theories, *Living Rev. Rel.* **13**, 3.
- Einstein, A. and Rosen, N.(1935).** The particle problem in the General theory of relativity, *Phys. Rev.* **48**- 73.
- Ellis, H.G., (1973).** Ether flow through a drainhole: A particle model in general relativity, *J. Math. Phys.* **14**, 104.
- Eiroa, E.F., Richarte. M.G., and Simeone, C.(1973).** Thin-shell wormholes in Brans-Dicke gravity, *Phys. Lett. A* **373**, (2008)1-4.
- Eiroa E. F., and Aguirre G. F.(2012).** Thin-shell Wormholes with a Generalized Chaplygin Gas in Einstein-Born-Infeld Theory, *Eur. Phys. J.* **C72**, 2240.
- Elizalde, E.(2011).** Non-singular exponential gravity: a simple thoery for early and late-time accelerated expansion, *Phys. Rev.* **D83**, 086006.
- Flamm L.(1916).** Comments on Einstein's Theory of Gravity, *Phys. Z* **17**, 448.
- Falco et al., (2020).** General relativistic Poynting-Robertson effect to diagnose wormholes existence: Static and spherically symmetric case, *Phys. Rev. D* **101**, 104037.
- Godani, N., and Samanta, G. C.(2019).** Non Violation of Energy Conditions in Wormhole Modeling, *Mod. Phys. Lett.* **A34**, 1950226.
- Godani, N., and Samanta, G. C.(2018).** Traversable wormholes and energy conditions with two different shape functions in $f(R)$ gravity, *Int. J. Mod. Phys.* **D28**, 19950039.
- Golchina, H., Mehdizadeh, M. R., (2019).** Quasi-cosmological traversable wormholes in $f(R)$ gravity, *Eur. Phys. J. C* **79**:777.
- Harko, T, Lobo, F. S.N., Nojiri, S., and Odintsov, S. D. (2011).** $f(R, T)$ Gravity, *Phys. Rev.* **D84**, 024020.
- Houndjo, M. J. S. (2012).** Reconstruction of $f(R, T)$ gravity describing matter dominated and accel-

erated phases, Int. J. Mod. Phys. **D21**, 1250003.

Houndjo, M. J. S.(2012). Reconstruction of $f(R, T)$ Gravity Describing Matter Dominated and Accelerated Phases, Int. J. Mod. Phys. **D21**, 1250003.

Jamil et al.,(2012). Reconstruction of some cosmological models in $f(R, T)$ cosmology, Eur. Phys. J. **C72**, 1999.

Lobo, F. S. N. and Oliveira, M. A. (2010). General Class of Vacuum Brans-Dicke Wormholes, Phys. Rev. **D81**, 067501.

Morris, M.S., Thorne, K.S., (1988). Wormholes in spacetime and their use for interstellar travel: A tool for teaching general relativity, Am. J. Phys. **56**, 395.

Mazharimousavi, S. H., Halilsoy, M. and Amirabi, Z. (2010). Stability of Thin-shell Wormholes Supported by Normal Matter in Einstein-Maxwell-Gauss-Bonnet Gravity, Phys. Rev. **D81**, 104002.

Mazharimousavi, S. H., Halilsoy, M. and Amirabi, Z. (2011). Higher-Dimensional Thin-Shell Wormholes in Einstein-Yang-Mills-Gauss-Bonnet Gravity, Classical Quant. Grav. **28**, 025004.

Mehdizadeh, M. R., Zangeneh, M. K., Lobo, F. S. N. (2015). Einstein-Gauss-Bonnet Traversable Wormholes Satisfying the Weak Energy Condition, Phys. Rev. **D91**, 084004.

Mehdizadeh, M. R. and Ziaie, A. H. (2017). Einstein-Cartan Wormhole Solutions, Phys. Rev. **D95**, 064049.

Moraes, P. H. R. S, Correa, R. A. C., and Lobato, R. V. (2017). Analytical General Solutions for Static Wormholes in $f(R, T)$ Gravity, JCAP **07**, 029.

Nandi, K. K., Islam, A., and Evans J., (1997). Brans Wormholes, Phys. Rev. **D55**, 2497.

Nojiri, S., and Odintsov, S. D.,(2003). Modified Gravity with Negative and Positive Powers of Curvature: Unification of Inflation and Cosmic Acceleration, Phys. Rev. **D68**, 123512.

Richarte. M.G., and Simeone, C. (2007). Wormholes in Einstein-Born-Infeld Theory, Phys. Rev. **D76**, 087502.

Sharif, M., and Mumtaz,S. (2016). Influence of nonlinear electrodynamics on stability of thin-shell wormholes, Astrophys. Space Sci. **361**, 218.

Övgun, A.(2018). Light deflection by Damour-Solodukhin wormholes and Gauss-Bonnet theorem, Phys. Rev. **D98**, 044033.

Sushkov, S. V., and Kozyrev, S. M.(2011). Composite Vacuum Brans-Dicke Wormholes, Phys. Rev. **D84**, 124026.

Shaikh R. and Kar S. (2016). Wormholes, the Weak Energy Condition, and Scalar-tensor Gravity, Phys. Rev. **D94**, 024011.

Singh, C. P., and Singh V.(2014). Reconstruction of modified $f(R, T)$ gravity with perfect fluid cosmological models, Gen. Relativ. Gravit. **46**, 1696.

Shabani H., and Farhoudi M.(2013). $f(R, T)$ cosmological models in phase space, Phys. Rev. **D88**, 044048.

Shabani H., and Farhoudi M.(2014). Cosmological and solar system consequences of $f(R, T)$ gravity models, Phys. Rev. **D90**, 044031.

Santos, A. F.(2013). Gödel solution in $f(R, T)$ gravity, Mod. Phys. Lett. **A28**, 1350141.

Shamir, M. F, Mustafa, G. and Fazal. A. (2021). Non-commutative Wormhole Solutions in Exponential Gravity with Matter Coupling, New Astron. **83**, 101459.

Smantha, G. C, Godani, N. and Bamba, K. (2018). Traversable wormholes with exponential shape function in modified gravity and in general relativity: A comparative study, arXiv:1811.06834.

Tsujikawa, S.(2008). Observational signatures of $f(R)$ dark energy models that satisfy cosmological and local gravity constraints, Phys. Rev. **D77**, 023507.

Zangeneh, M. K, Lobo, F. S. N. and Dehghani, M. H. (2015). Traversable Wormholes Satisfying the Weak Energy Condition in Third-order Lovelock Gravity Phys. Rev. **D92**, 124049.

Submitted: 25/01/2021

Revised: 22/05/2022

Accepted: 25/07/2022

DOI: 10.48129/kjs.12005

The effect of mixing nanoparticles on the suspension physical stability

Fairooz F. Kareem*, Asrar A. Saeed, Mahasin F. Al-Kadhemy, Farah J. Kadhum

Dept. of Physics, Mustansiriyah University, College of Science, Baghdad, Iraq

Corresponding author: cenderlla78@yahoo.com

Abstract

Energy transfer in a hybrid mixture of Rhodamine 6G (Rh6G) dye laser as a donor and nanoparticles (NPs) as an acceptor were studied. The absorption spectra of 1×10^{-5} M of Rh6G in distilled water showed an increase in peak intensity upon addition of NPs. Notably, the spectra were improved upon addition of Aluminum Oxide (Al_2O_3) NPs. The addition of NPs quenches the fluorescence spectra of Rh6G due to Förster resonance energy transfer (FRET). The efficiency of this energy transfer increases with an increasing concentration of NPs, and a best value of efficiency of energy transfer was found for the Rh6G/Magnesium Oxide (MgO) NP system. A similarly strong relationship was also found for the Rh6G/ Al_2O_3 NP system.

Keywords: Absorption spectrum; Al_2O_3 NPs and MgO NPs; energy transfer efficiency; fluorescence spectrum; Rh6G dye laser.

1. Introduction

The Rhodamine 6G (Rh6G) molecule is an environmentally benign and widely used organic colourant/dye. It has a high fluorescence quantum yield and is water soluble, despite its innate hydrophobic attraction (Lin, Katla & Perez-Mercader, 2021). Rh6G is used in a wide variety of applications because of these characteristics, including in the imaging of cellular or polymeric samples and as an active medium in dye laser applications. It also sees wide use in petroleum dyeing, paper printing, forensic technology, colour photography, cosmetic product additives, laser technology, optical conversion, solar cells, diodes, signal amplification in optics, optical communications, optoelectronics (Al-Kadhemy, Abbas & Abdalmuhdi, 2020). Ionic dyes self-associate to varying degrees in solution, depending on a variety of conditions such as dye concentration, dye structure, temperature, pH, and solvent, among others, resulting in a deviation from Beer's law (Terdale & Tantray, 2017). With respect to functional physical properties, the solvent in which the dye is dissolved plays an important role. Stokes' shifts, fluorescence quantum yields, fluorescence durations, and both radiative and non-radiative rate constants all adhere to a more-or-less linear relationship with the solvent polarity in moderate to high polarity solvents (Barik & Nath, 2003).

There is an ever-increasing application of metal oxide NPs in numerous disciplines such as cosmetic production, electronics, material sciences, catalysis, environmental sciences, energy, and biomedicine (Moorthy *et al.*, 2015). Microelectronics, diagnostics, and biomolecular detection are all potential uses for magnesium oxide (MgO) NPs (Ali *et al.*, 2020). In the field of catalysis, the unique structure of aluminium oxide (Al_2O_3) is employed as the foundation for active phases that are subsequently coated with other materials (Chavali & Nikolova, 2019). The

unit cell of Al_2O_3 belongs to the rhombohedral system of crystal structures, Al_2O_3 exhibits a range of polymorphic forms, including γ -, θ -, κ -, and α -, whereby the α - phase has been determined to be stable, whilst the other phases have been deemed metastable (Abdullah, 2021). When dyes or dye-marked receptors are in close proximity to or associated with NPs, energy transfer or electron transfer can quench their fluorescence (Yun, Javier and Strouse, 2005). The non-radiative process of Förster resonance energy transfer (FRET) involves an electronically-excited donor transmitting its excitation energy to an acceptor, resulting in a drop in fluorescence intensity and the donor's excited state lifetime (Mokashi, Patil & G.B.Kolekar, 2012). For this process to be efficient, the energy gap between the ground state and the excited energy level of the donor and acceptor must be suitably matched. This means that the fluorescence emission spectra of the donor must overlap with the absorption spectrum of the acceptor and vice versa. An optimal distance for the transmission of excitation energy from the donor to the acceptor must also be maintained (Zhang, Wang & Liang, 2015). Saeed et al. demonstrated that changing the mass of Ag NPs present led to enhanced absorption in the absorption spectra of Rh6G dye solution, but this same mass change actually quenched the fluorescence spectra (Saeed, Al-Kadhemy & Al-Arab, 2018). Kareem et al. determined the optimum concentration of Rh6G in (1×10^{-5}) aqueous solution for absorption and the fluorescence spectra with respect to the Beer-Lambert law to be 525 and 554 nm, respectively (Kareem, Saeed & Kadhemy, 2021).

The aim of this study is to characterize the energy transfer of Rh6G dye (as a donor) and NPs (as acceptors) in the liquid phase with distilled water acting as a solvent. Further, we explore the effect of the addition of metal oxide NPs to Rh6G dye.

The aim of this study is to characterize the energy transfer of Rh6G dye (as a donor) and NPs (as acceptors) in the liquid phase with distilled water acting as a solvent. Further, we explore the effect of the addition of metal oxide NPs to Rh6G dye.

2. Theoretical Background

After transmitting its excitation energy to an acceptor molecule, A, an excited donor molecule D^* relaxes and emits a photon. The dipole-dipole coupling interaction between the donor and acceptor causes non-radiative energy transfer, which does not warrant photon emission or re-absorption. This process, described by Thompson and Messina (2019) can be explained as follows:



Energy transfer leads to a reduction in or the quenching of donor fluorescence and thus a decrease of excited state lifetime (Lewkowics & Lakowicz, 2006).

The energy-transferring efficiency E, originally determined by Wahba, El-Enany and Belal (2015), can be expressed as:

$$E = 1 - \frac{F_i}{F_{i0}} \quad (2)$$

Where F_{i0} and F_i are the fluorescence intensity of the donor dye in the absence and presence of and acceptor molecule, respectively.

The Stern–Volmer relationship, as given in eq. (3), is used to discover the kinetics of a photophysical intermolecular deactivation process (quenching). In general, this process can be represented by a simple equation as determined by Yang, Xi and Yang (2005):

$$\frac{F_{i0}}{F_i} = 1 + K[Q] \quad (3)$$

Where K is the Stern-Volmer quenching constant and $[Q]$ is the quencher concentration. Thus, a plot of F_{i0}/F_i versus $[Q]$ should yield a straight line with a slope equal to K .

3. Experimental

Rh6G ($C_{28}H_{31}N_2O_3Cl$), with a molecular weight of $479.02 \text{ g}\cdot\text{mol}^{-1}$ was obtained from Sigma-Aldrich. Rh6G was dissolved in distilled water ($di\text{-H}_2\text{O}$), whose polarity was considered to be 10.2 D (Lide, 2010). Magnesium oxide (MgO) with an average particle diameter of 40 nm and purity of 99.9% was obtained from Intelligent Materials Pvt. Ltd. Aluminium oxide (Al_2O_3), with an average particle diameter of 20-30 nm and a purity of 99.9% was obtained from China. Photographs of the chemicals in powder form used in this study are shown in Figure 1 (A-C).

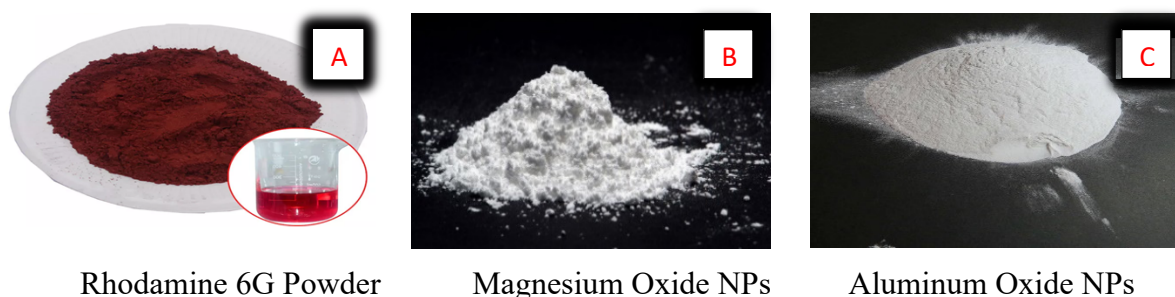


Fig. 1. Chemicals (in powder form) used in the work

Dissolving the required quantity of Rh6G dye, weighted using a Mettler balance sensitive to 0.1 mg, in each solvent yielded a solution with a primary concentration of $1 \times 10^{-2} \text{ M}$. The amount of dye, m , in grams (g) was calculated using equation (4), given by Al-Kadhemy, Hussein and Ali A. Dawood Al-Zuky (2012):

$$m = \frac{M_w V C}{1000} \quad (4)$$

Where M_w denotes dye molecular weight (g/mole), V denotes solvent volume (ml), and C denotes dye concentration (M). The dye was then diluted to obtain concentrations in the range of $1 \times 10^{-2} - 1 \times 10^{-6} \text{ M}$ according to eq. (5) given by Ali and Zainab F. Mahdi (2012):

$$C_1 V_1 = C_2 V_2 \quad (5)$$

Where C_1 represents the high concentration, V_1 represents the volume before dilution, C_2 represents the low concentration, and V_2 represents the total volume after dilution. It was observed that the prepared solutions have a good homogeneity. Figure 2 shows the solutions of Rh6G in the concentration range of $1 \times 10^{-2} - 1 \times 10^{-6} \text{ M}$



Fig. 2. Various concentrations of Rh6G in distilled water

The masses of MgO and Al₂O₃ used in this study were 2.0×10^{-3} and 4.0×10^{-3} g, respectively and were investigated by addition to dye solution. All the samples were prepared by mixing with the use of a hot plate with a magnetic stirrer for approximately one hour until the NPs were dispersed homogeneously throughout the Rh6G solution. All the samples were kept in the dark so as to avoid possible photo-bleaching or fading of the dye. The samples were used immediately after preparation.

A UV-Visible spectrophotometer (T70/T80) was used to record the absorption spectra of all samples, while a Spectrofluorometer was used to record the fluorescence spectra (SHIMADZU RF-5301pc).

4. Results and Discussion

Figures 3 and 4 show the absorption and fluorescence spectra for Rh6G in distilled water. The maximum absorption wavelength (λ_{abs}) was found to be 525 nm, in good agreement with Kruszewski and Cyrankiewicz (2013), with a shoulder peak at 495 nm. The maximum fluorescence wavelength (λ_{flu}) was 555 nm, which is in good agreement with Chen et al. (2008).

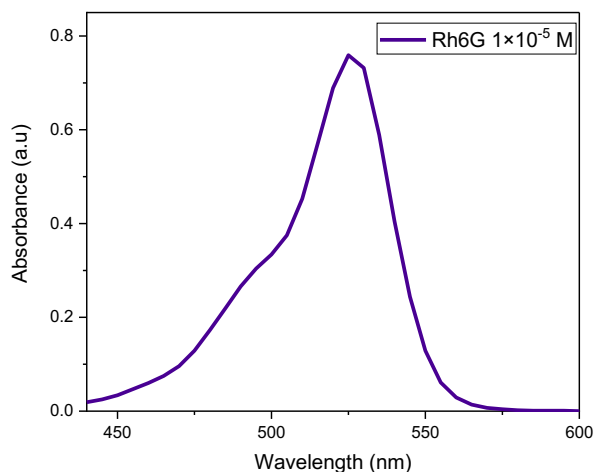


Fig. 3. Absorption spectrum of Rh6G in distilled water

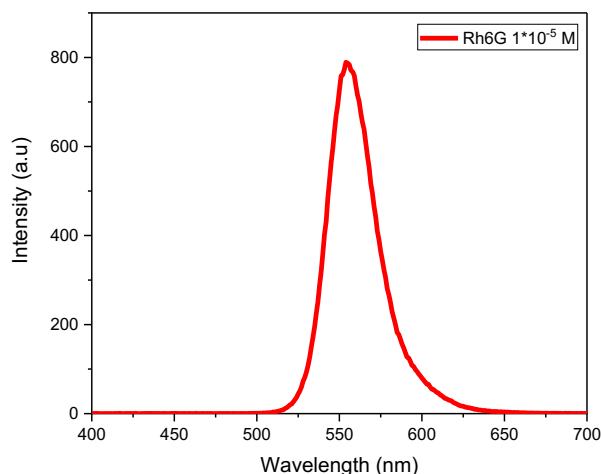


Fig. 4. Fluorescence spectrum of Rh6G in distilled water

Addition of MgO or Al_2O_3 NPs resulted in the Rh6G-NP solution having an enhanced absorption spectrum. At all NP concentrations, the maximum absorption wavelength was found to be consistent at 525 nm. The addition of NPs caused an increase in the absorbance spectrum of Rh6G; when 4.0×10^{-3} g of Al_2O_3 NPs adding, absorbance rose to 1.92, while when 0.004g of MgO NPs were added, absorbance rose to 1.89, as demonstrated in in Table 1 and Figure 4. As a result of the addition of NPs, the photophysical characteristics of Rh6G dye were improved. The absorbance increases to 1.68 when 2.0×10^{-3} g of MgO NPs and 2.0×10^{-3} g of Al_2O_3 NPs in combination. It can be concluded that Al_2O_3 NPs has a large effect, but widens the spectrum's absorption peak. The absorption spectra increased with an increase in NP particle size, which can be explained as with Al being a metal, it may generate electrons and transform to a cation. Al_2O_3 NPs may also absorb water, making them useful as a drying agent. Due to its great stability, it is also considered an oxidizing agent (Stojanovic, Bukvic and Epler, 2018). The full width at half maximum (FWHM) of the absorption spectra increase with an increasing NP concentration in the case of Al_2O_3 , whereas it decreases in the cases of MgO and mixed MgO- Al_2O_3 nanoparticle addition.

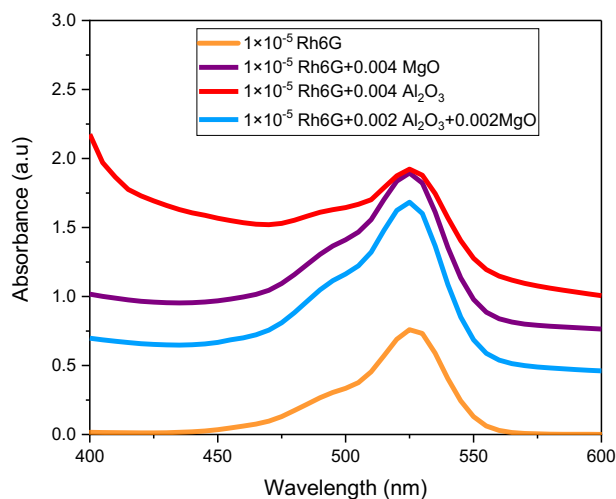


Fig. 5. Absorption spectra of Rh6G laser dye with 2.0×10^{-3} and 4.0×10^{-3} g of MgO and Al_2O_3 NPs.

Figure 6 and Table 1 show the fluorescence spectra of Rh6G with 2.0×10^{-3} and 4.0×10^{-3} g of MgO and Al₂O₃ NPs in all concentrations, where the highest fluorescence wavelength of 555 nm is seen. In Rh6G aqueous solution, the wavelength is 554 nm. A decrease in the intensity upon addition of MgO, Al₂O₃, or mixed MgO-Al₂O₃ NPs to Rh6G aqueous solution is seen. It should be noted that adding NPs led to decrease in the fluorescence intensity with an increase masse of NPs, while the maximum fluorescence peak remains constant. Non-radiative energy transfer between laser dyes and NPs is most likely to be the cause for the emission quenching. (Błaszkiwicz, Kotkowiak & Dudkowiak, 2017). The FWHM for fluorescence spectra increased with the addition of Al₂O₃ NPs, whilst it decreased with the addition of MgO or mixed MgO-Al₂O₃ NPs.

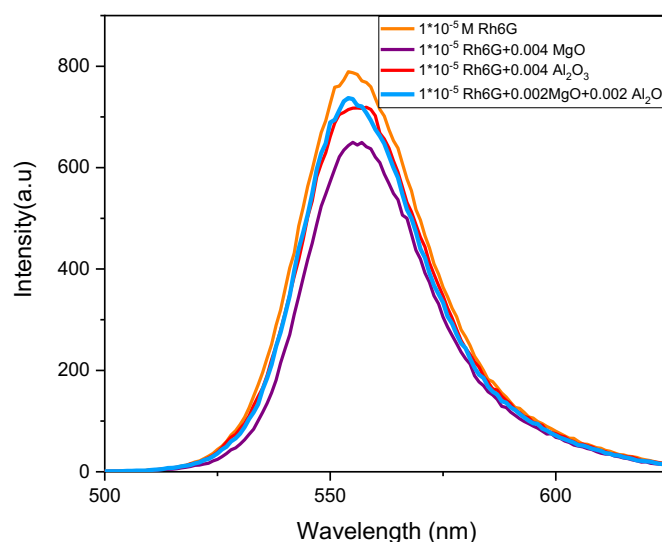


Fig. 6. Fluorescence spectra of Rh6G laser dye with 2.0×10^{-3} and 4.0×10^{-3} g of MgO and Al₂O₃ NPs.

Table 1. Spectral information for Rh6G aqueous solution with addition of NPs

Rh6G 1×10^{-5} M	Amount of MgO NPs (g)	Amount of Al ₂ O ₃ NPs (g)	$\lambda_{\text{abs max}}$ (nm)	I_{abs}	FWHM (nm)	$\lambda_{\text{fluo max}}$ (nm)	I_{Fluo}	FWHM (nm)
	0	0	525	0.75	35	554	789.16	32.96
	0.004	0	525	1.89	58.30	555	649.9	31.83
	0	0.004	525	1.92	83.65	555	717.44	33.12
	0.002	0.002	525	1.68	56.31	555	735.34	31.55

Figure 6 shows the Stern-Volmer plot of 1×10^{-5} M Rh6G aqueous solution with the addition of 2.0×10^{-3} and 4.0×10^{-3} g of MgO NPs. The R^2 metric of goodness-of-fit is almost equal to 1, which means there is a strong relationship between the two parameters (line and point). Furthermore, the Stern-Volmer relationship calculated from equation (3) is found to be 54.87 M^{-1} . All of the samples studied had linear Stern-Volmer dependence, implying a single quenching process (Błaszkiwicz, Kotkowiak & Dudkowiak, 2017).

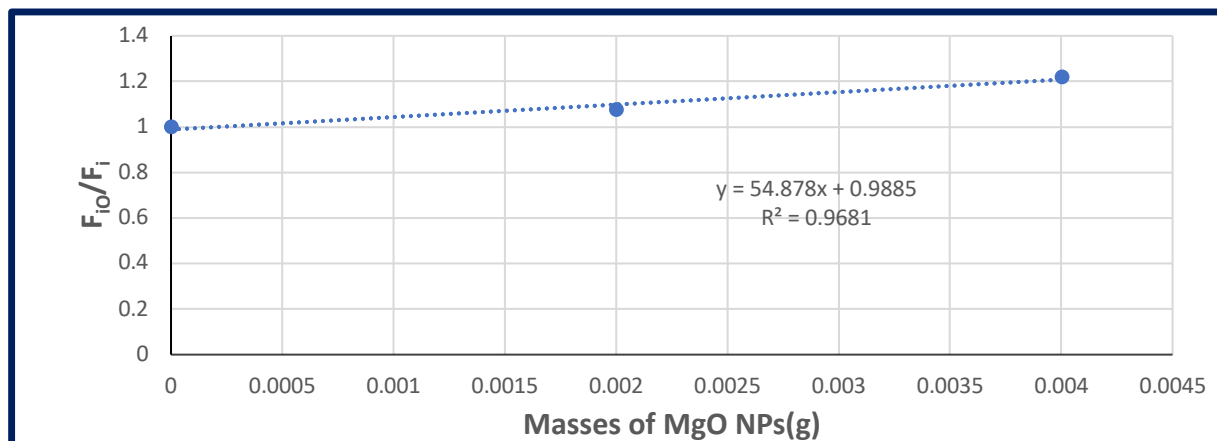


Fig. 7. Stern-Volmer plot of Rh6G with MgO NPs

Additionally, Table 2 show the efficiency of energy transfer of Rh6G with MgO NPs. As the amount of MgO NPs present increases, an increase the energy transfer efficiency is also seen, which can be described by the efficiency of Stern-Volmer equation (2). The curve of Rh6G with MgO NPs can also be regarded as a straight line in low concentration where the ratio here is <10 (Yang, Xi & Yang, 2005).

Table 2. Energy-transfer efficiencies for Rh6G dye with MgO NPs

Rh6G 1×10^{-5} M	Amount of MgO NPs (g)	F_{i0}	F_i	E
	0	789.16	789.16	0
	0.002	789.16	735.34	0.07
	0.004	789.16	649.9	0.18

Figure 8 and Table 3 display the Stern-Volmer relationship and energy transfer of 1×10^{-5} M Rh6G dye solution in distilled water with 2.0×10^{-3} and 4.0×10^{-3} g masses of Al_2O_3 NPs. Again, the R^2 value is very close to 1 indicating a strong linear dependence. The Stern-Volmer quenching constant, K , is 27.778 M^{-1} when it calculated from the eq. (2). Table 3 demonstrates that increasing the amount of Al_2O_3 NPs leads to an increase in the efficiency of energy transfer.

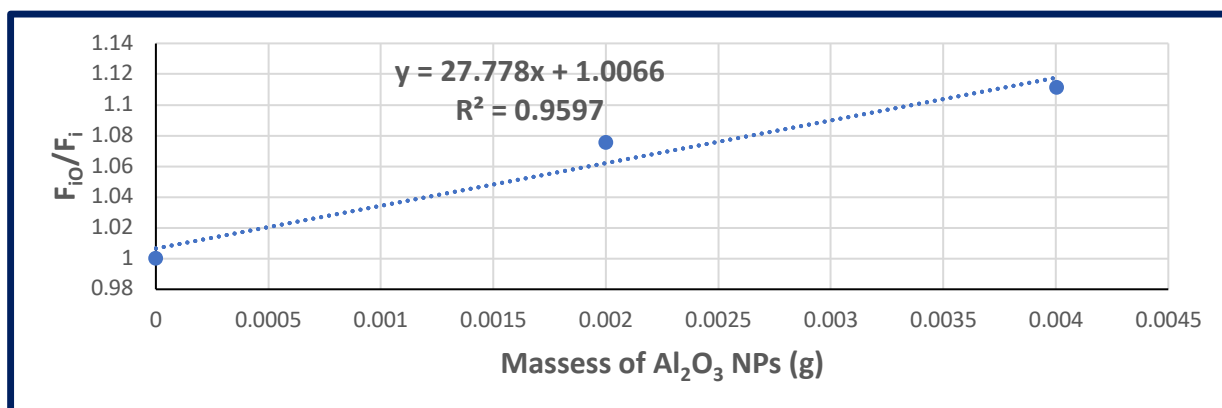


Fig. 8. Stern-Volmer plot of Rh6G with Al_2O_3 NPs

Table 3. Energy-transfer efficiencies for Rh6G dye with Al₂O₃ NPs

Rh6G 1×10 ⁻⁵ M	Amount of Al ₂ O ₃ NPs(g)	F _{io}	F _i	E
	0	789.16	789.16	0
	0.002	789.16	735.34	0.07
	0.004	789.16	717.44	0.1

5. Conclusion

In this work, the effect of adding MgO and Al₂O₃ NPs to Rh6G dye solution was investigated through the use of absorption and fluorescence spectra. The main results can be summarized as follows:

- 1-/ Addition of NPs enhanced the absorption spectrum of Rh6G, particularly in the case of Al₂O₃ NPs.
- 2-/ Addition of NPs quenched the fluorescence spectrum of Rh6G.
- 3-/ There exists a strong relationship between donors and acceptors, particularly in the case of Al₂O₃ NPs where the R² factor is almost 1.
- 4-/ The efficiency of energy transfer in MgO NPs is better than in Al₂O₃ NPs for the studied Rh6G solutions.

ACKNOWLEDGEMENTS

The authors would like to thank Department of Physics, College of Science, Mustansiriyah University (www.uomustansiriyah.edu.iq) Baghdad-Iraq for its support in the present work.

Reference

- A.Barik,S.Nath, H. P. (2003)** ‘Effect of solvent polarity on the photophysical properties of coumarin dye’, Chinese Journal of Physics, 119, pp. 10202–10208.
- Abdullah, M. M. (2021)** ‘Dielectric spectroscopy of aluminum oxide (γ-Al₂O₃)’, Kuwait Journal of Science, 49(2), pp. 1–12.
- Al-Kadhemy, M. F. H., Abbas, K. N. and Abdalmuhdi, W. B. (2020)** ‘Physical Properties of Rhodamine 6G Laser Dye Combined in Polyvinyl Alcohol films as Heat Sensor’, IOP Conference Series: Materials Science and Engineering, 928(7), pp. 1–10.
- Al-Kadhemy, M. F. H., Hussein, R. and Ali A. Dawood Al-Zuky (2012)** ‘Analysis of the Absorption Spectra of Styrene-butadiene in Toluene’, Journal of Physical Science, 23(1), pp. 89–100.
- Ali, A. A. and Zainab F. Mahdi (2012)** ‘Investigation of nonlinear optical properties for laser dyes-doped polymer thin film’, Iraqi Journal of Physics, 10(19), pp. 54–69.
- Ali, R. et al. (2020)** ‘Green synthesis and the study of some physical properties of MgO nanoparticles and their antibacterial activity’, Iraqi Journal of Science, 61(2), pp. 266–276.

- Blaszkievicz, P., Kotkowiak, M. and Dudkowiak, A. (2017)** ‘Fluorescence quenching and energy transfer in a system of hybrid laser dye and functionalized gold nanoparticles’, *Journal of Luminescence*, 183, pp. 303–310.
- Chavali, M. S. and Nikolova, M. P. (2019)** ‘Metal oxide nanoparticles and their applications in nanotechnology’, *SN Applied Sciences*, 1(6), pp. 1–30.
- Chen, Z. *et al.* (2008)** ‘Fluorescence spectral properties of rhodamine 6G at the silica/water interface’, *Journal of Fluorescence*, 18(1), pp. 93–100.
- Kareem, F. F., Saeed, A. A. and Kadhemy, M. F. H. A.- (2021)** ‘Inspect the Influence of Solvents , Magnesia and Alumina Nanoparticles on Rhodamine 6G Laser Dye Spectroscopic Properties’, *Journal of Global Scientific Research*, 6(9), pp. 1695–1709.
- Kruszewski, S. and Cyrankiewicz, M. (2013)** ‘Rhodamine 6G as a mediator of silver nanoparticles aggregation’, *Acta Physica Polonica A*, 123(6), pp. 965–969.
- Lewkowics and Lakowicz, J. R. (2006)** principles of fluorescence spectroscopy. third edit, *Principles of Fluorescence Spectroscopy*. third edit. springer.
- Lide, D. R. (2010)** CRC handbook of chemistry and physics. 90 Ed. Taylor and Francis Group LLC.
- Lin, C., Katla, S. K. and Perez-Mercader, J. (2021)** ‘Enhanced fluorescence emission from rhodamine 6G dye through polymerization-induced self-assembly’, *Journal of Photochemistry and Photobiology A: Chemistry*, 406(September 2020), p. 112992.
- Mokashi, V. V., Patil, S. R. and G.B.Kolekar (2012)** ‘Evaluation of interparticle interaction between colloidal Ag nanoparticles coated with trisodium citrate and safranin by using FRET: Spectroscopic and mechanistic approach’, *J. Photoch. Photobiol. B*, 113, pp. 63–69.
- Moorthy, S. K. *et al.* (2015)** ‘MgO Nanoparticles Neem Leves through Green Method’, *Materials Today: Proceedings*, 2(9), pp. 4360–4368.
- Saeed, A. A., Al-Kadhemy, M. F. H. and Al-Arab, H. S. (2018)** ‘Energy Transfer Efficiency of Silver Nanoparticles with Rhodamine 6G Dye’, *Journal College of Education*, 1, pp. 1–8.
- Stojanovic, B., Bukvic, M. and Epler, I. (2018)** ‘Application of aluminum and aluminum alloys in engineering’, *Applied Engineering Letters*, 3(2), pp. 52–62.
- Terdale, S. and Tantray, A. (2017)** ‘Spectroscopic study of the dimerization of rhodamine 6G in water and different organic solvents’, *Journal of Molecular Liquids*, 225, pp. 662–671.
- Thompson, M. J. and Messina, M. (2019)** ‘A Quantitative Explanation of the Dynamics Underlying the Franck-Condon Principle: A Mostly Classical Viewpoint’, *Materials Today: Proceedings*. First Edit, 5(2), pp. 1–10.
- Wahba, M. E. K., El-Enany, N. and Belal, F. (2015)** ‘Application of the Stern-Volmer equation for studying the spectrofluorimetric quenching reaction of eosin with clindamycin hydrochloride in its pure form and pharmaceutical preparations’, *Analytical Methods*, 7(24), pp. 10445–10451.
- Yang, M., Xi, X. and Yang, P. (2005)** ‘The equal-efficiency-proving of fluorescence quenching and enhancement equation’, *Chinese Science Bulletin*, 50(22), pp. 2571–2574.

Yun, C. S., Javier, A. and Strouse, G. F. (2005) ‘Nanometal Surface Energy Transfer in Optical Rulers, Breaking the FRET Barrier’, American Chemical Society, 127, pp. 3115–3119.

Zhang, J., Wang, P. C. and Liang, X. J. (2015) ‘In vivo tumortargeted dual-modal fluorescence/CT imaging using a nanoprobe co-loaded with an aggregation-induced emission dye and gold nanoparticles’, Biomaterials, 42, pp. 103–111.

Submitted: 20/12/2021

Revised: 23/05/2022

Accepted: 05/06/2022

DOI: 10.48129/kjs.17831

Controlling the nanoparticle size of silica in an acidic environment by using a strong magnetic field and a modified sol-gel techniques

Ashraf M. Alattar^{1,*}, Mohammed J. Alwazzan², Khalida A. Thejeel³

¹ *Dept. of medical physics, College of Science, Al-Karkh university of science.*

Baghdad. Iraq

² *Dept. of Medical Instruments Techniques Engineering, Al hussain University College*

Karbala'a, Iraq

³ *Dept. of Geophysics, College of Remote Sensing and Geophysics,*

Al-Karkh university of science, Baghdad. Iraq

* *Corresponding author: Ashraf_alattar2000@kus.edu.iq*

Abstract

In this study, we were able to create highly dispersed silica nanoparticles with diameters of less than one nm by changing the sol-gel technique. During the poly-condensation process, a strong magnetic field was applied to the silica sol to control particle size. The size of silica nanoparticles has a substantial impact on preparation elements such pH, magnetic field intensity, and exposure time. These parameters can be changed in a systematic manner to reduce or increase particle size. A dynamic light scattering test was also used to investigate the effect of a magnetic field on the particle size and dispersion of silica dust. Despite the fact that silica is naturally diamagnetic, the magnetic field has a considerable impact on their size growth. Magnetic fields altered the typical influence on silicon structure, resulting in crystal formation in the silicon sample under consideration. Many applications require small particle sizes and/or a narrow particle size dispersion. The building blocks of nanotechnology are usually made of low-dimension particles. The experts concluded that additional research into such strange phenomena will be required in the future.

Keywords: Acidic; dynamic light scattering; magnetic field; silica nanoparticle; sol-gel.

1. Introduction

The sol-gel procedure is one of the most well studied and standard methods of synthesizing silica nanoparticles to date. [Battisha, I. K *et. al.*, 2010, Sögaard *et. al.*, 2018]. Since Stöber 1968, [Stöber *et. al.*, 1968] there are plenty of particulate studies on the preparation of silica nanoparticles and nanoparticles size controlling. Significant consideration has been drawn to the effect of a magnetic field on the self-assembly behavior of molecules [Quickel *et. al.*, 2010 – Hirota *et. al.*, 2008], The nucleation and growth process of magnetic materials as well as of magnetic materials [Beecher *et. al.*, 2005, Yildiz *et. al.*, 2006]. However, there seems to be a lack of research in the literature covering a relationship during the sol-gel phase between the applied magnetic field and the resulting scale of diamagnetic nanoparticles.

Predominately, the critical parameter of colloidal systems is their particle size. The information about the size and shape of particulates is critical in predicting the initiate and growth of particulates. The geometry of the nanoparticle has a major effect on changes in properties, as it can influence both the surface-to-volume ratio and the surface energy ratio [Alattar, 2021; Odegard *et. al.*, 2005]. In order to impact high-technology applications, involving particular properties, imposed processing techniques enabling the regulation of the distribution of nanoparticles. The primary importance of effective control of morphology is that it provides open avenues for the prior prediction/optimization of material structures and properties [Zeng *et. al.*, 2008].

1.1 Particle growth mechanism

Based on the sol-gel process [Brinker *et. al.*, 1990], and throughout the sol stage linear structures are shaped, which then converted into nanoglobules, the consistency of which is pH dependent. Its nanoglobules form evenly throughout the sol and then rise in size during the last stages of development, as required by diffusion-limited aggregation [Julien 1989]. The aggregation started via the addition of an accelerator, such as catalyst, to the silica sol and the mechanism of aggregate and destabilization configuration somewhat demonstrated by the Derjaguin–Landau–Verwey–Overbeek (DLVO) theory. Furthermore, the sol stability will be discussed via the slow versus fast aggregation process. [Trompette *et. al.*, 2013– Sandkühler *et. al.*, 2003]. DLCA stands for diffusion-limited cluster aggregation, while RCA stands for reaction-limited cluster aggregation (RLCA).

1.1.1 Magnetic field influence

Strong magnetic fields, on the other hand, are frequently employed for comprehensive material characterization in a broad sense in proportion to the energy density of the applied magnetic field. The energy of interaction (Zeeman energy) between the material and the magnetic field should be small enough [Motokawa 1995]. When a high magnetic field is applied to a crystal during its solidification process, the orientation effect has a significant impact on the crystal's shape. A magnetic field induces a magnetic moment in a diamagnetic substance that is in opposition to the magnetic field that activates it. The classical explanation of diamagnetism regarding Lenz's law is not entirely accurate, where it is a quantum mechanical phenomenon [Stephen 2001]. More novel nanoparticles, however, have recently been studied, with major promises for contemporary physics and instrument applications [Tyagi *et. al.*, 2017].

Up to now, best of knowledge, this study is the first specific study reports the effect of applying a magnetic field on controlling the size of primary silica nanoparticles suspended in the sol phase.

2. Experimental.

2.1/ Materials.

Tetraethylorthosilicate (TEOS > 99.0 % purity), spectroscopic grade and ethyl alcohol (200 proof, > 99.5 % purity), were obtained from Sigma Aldrich. Ammonium hydroxide (28-30 % concentration) supplied by BDH, and Ameresco supplied hydrochloric acid (0.15 M, > 99.0 % purity).

2.2/ Procedure.

In silica sol preparation, condense silica (CS), TEOS and EtOH used as precursor and solvent, respectively. Hydrochloric acid was added to induce the hydrolysis of the precursor at a molar ratio of TEOS: EtOH: HCl (0.01 M) of 1:6.6:0.18, respectively. The pH of the final solution was 2.5, where this recipe denoted as the recipe (I). The irreversible poly-condensation reaction took place, under the presence of a magnetic field, via drop-wise adding of diluted NH_4OH (1.25 mol l^{-1}), as a base catalyst. Firstly, the pH of CS was converted from 2. to 3, with vigorous mixing using a glass rod. The samples kept under magnetic field for 5, 15, 30, 60 and 90 min. Secondly, using two magnetic field sources; 0.5T and 3T, at a fixed exposure time of two minutes, three samples of recipe (I) were studied by DLS. The pH value of these samples varied from 2 to 3, 4, and 5. Another CS recipe was prepared using different TEOS: EtOH: HCl (0.03 M) molar ratio of 1: 3: 1.2, respectively. This recipe denoted as (II) with pH of 2.5. The same poly-condensation procedure, of different pH, was repeated for this recipe as well.

2.3/ Characterization

All samples filtered with 0.22 Super-pure syringe filters, otherwise will be mentioned. Then DLS experiments were done by using Zetasizer Nano-S instrument from Malvern using 632.8 nm laser and measured at the scattering angle of 173 degrees. Ethanol adopted in the DLS test as a dispersion solution.

XRD was performed using a Panalytical X' Pert PRO Alpha-1 XRD via $\text{Cu K}\alpha$ radiation. Due to the liquid nature of the sample, a few drops of each sol were poured on glass substrate then left to dry at room temperature. A light portion is crushing from coated silica as a powder, then used for XRD test.

3. Result

Table 1 shows the results of magnetic field exposure time effect on the silica particle size at pH= 3. The magnetic field showed fast influence on the silica particle size suspended in ethanol. Where, under the existence of a strong magnetic field of 3T, applied for two minutes, the poly-condensation process yielding a reduction in the particle size from 3.36 nm to 1.13 nm according to DLS result, based on particles number method. On the other hand, when the magnetic field exposure time increases for further periods, the silica particle size increased to their initial size range before introducing to the magnetic fields.

Table 1. Influence of magnetic field exposure time on the silica particle size at pH= 3.

Magnetic field (T)	0			3		
Time (min)	0	5	15	30	60	90
Particle size of recipe I (nm)	3.36	1.13	4.28	3.23	3.08	4.00

Under the presence of a high magnetic field, the sol pH value variations showed significant influence on the silica particles size. A dramatic divergence in the particle size was noticed through a slight change in the pH of the silica solution as given in table 2.

Table 2. Influence of magnetic field and pH values on silica particle size at an exposure time of 2 min. The gel time varied from two days to several days, and the sols still stabled for more than one year.

	Magnetic field status					Recipe No.	Magnetic field strength (T)	Dispersant media
	Non		Applied					
	pH 2.	pH 2.5	pH 3	pH 4	pH 5			
particle size (nm)	3.22	3.21	1.16	588*	261*	I	3	Ethanol
Final state	Sol	Sol	Sol	Gel	Gel			
particle size (nm)	3.22	3.21	622*	2.27	0.51	I	0.5	Ethanol
Final state	Sol	Sol	Gel	Gel	Sol			
particle size (nm)	30.1	30.3	5.68	28.1	67.5	II	3	water
Final state	Sol	Sol	Sol	Gel	Gel			

* Samples test without filtering

Figure 1-a and figure 2-b demonstrate the effect of pH value changing on the particle size of recipe (I) silica colloid, which was poly-condensed under two different magnetic field of 0.5 T and 3 T, respectively. The high matching between the three testing methods may confirm the particle size systematic dependence in the polycondensation process. Figure 1-c illustrates the pH value effect on the particle size of recipe II silica colloid. This recipe was poly-condensed under a magnetic field of 3 T.

The idea indicates a rise in suspension stability with increased surface load and decreasing salt levels trends in most loaded particle suspensions. The aggregation rate constants, often within a 2 factor and better, are predicted quite well in the quick regime [Bergström1997, Kobayashi *et. al.*, 2005].

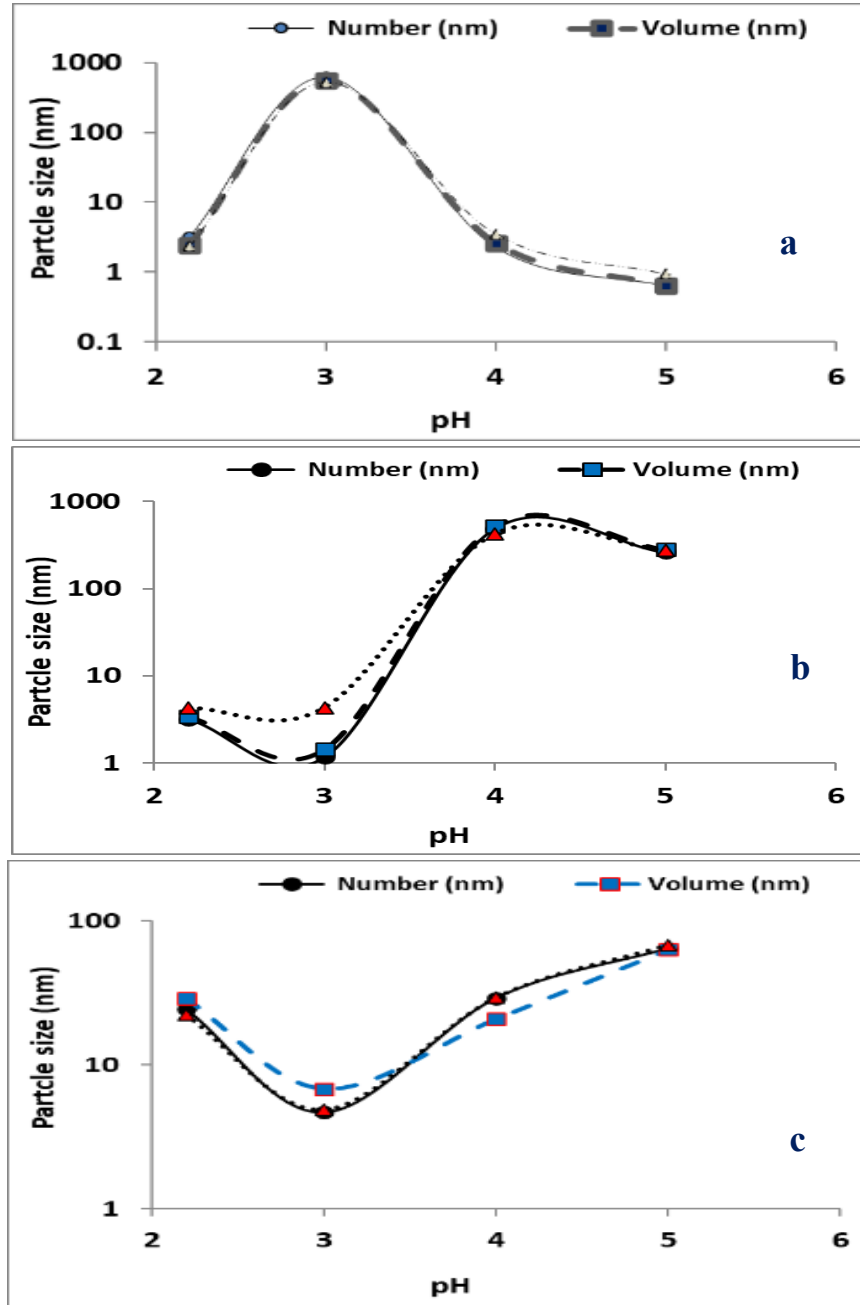


Fig. 1. Particle size results following three testing methods; number, volume, and intensity (a) recipe (I) at 0.5 T (b) recipe (I) at 3 T, (c) recipe (II) at 3 T.

Figure 2 illustrates the distribution of particle size by the number of recettes from the DLS graphical results and show (I) prepared under 3T (a) pH = 2 (b) pH = 3, (c) pH = 5, and under 0.5 T (d) pH = 2.5 (e) pH = 3 (f) pH = 5. Showing different distribution of particle size with different magnetic field the size of the silica particles is smaller than the domain size range (DFMN).

When the temperature rises over the so-called blocking temperature, each particle behaves like a gigantic paramagnetic atom and displays superparamagnetic conduct.

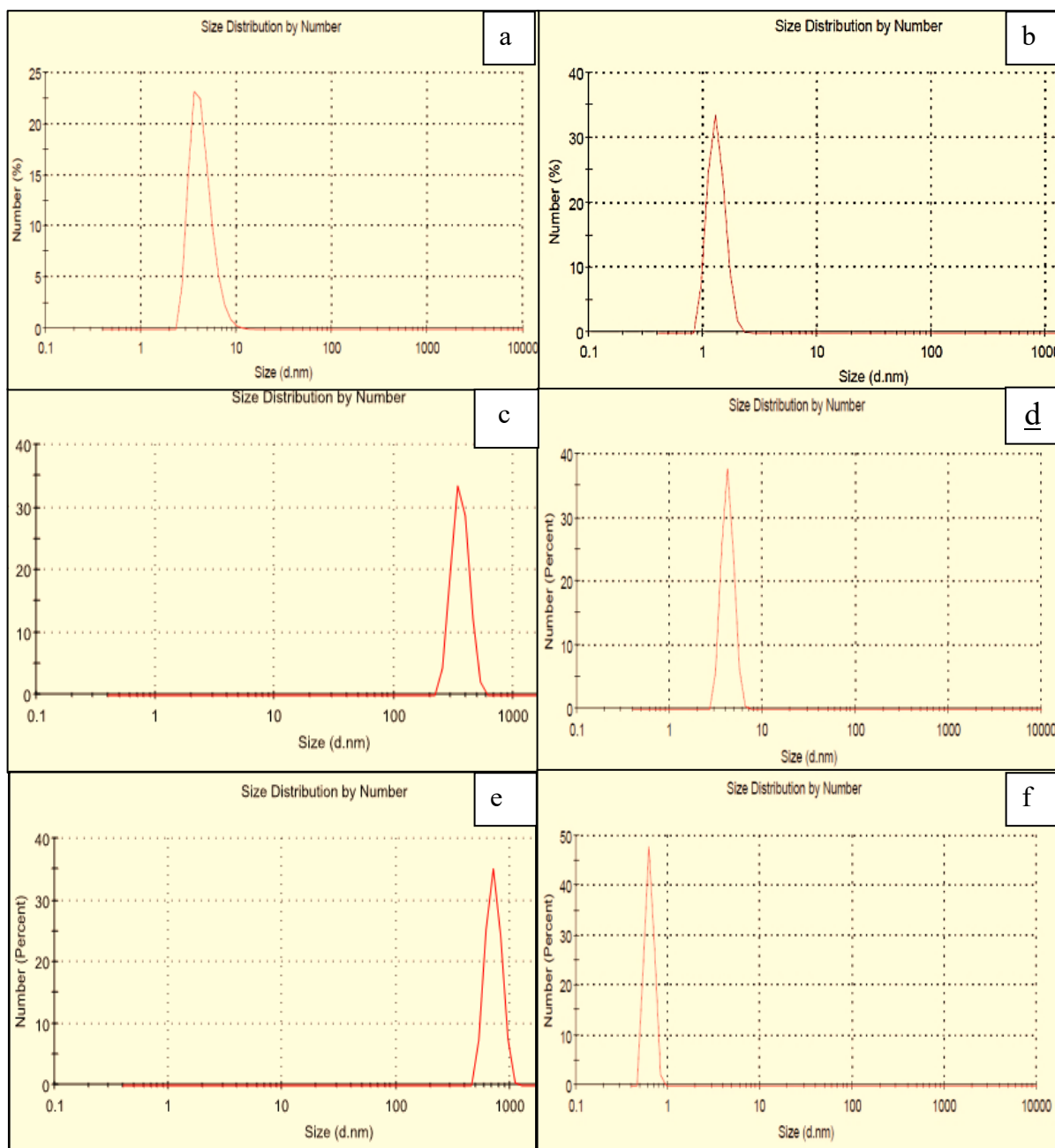


Fig. 2. DLS graphical results show the particles size distrebuion by number for recipe (I) prepared under 3T (a) pH = 2.2 (b) pH = 3,(c) pH = 5, and under 0.5 T (d) pH = 2.2 (e) pH = 3 (f) pH = 5.

4. Discussion

According to the availability of many acidic silica sols for the influence of a magnetic field, it was systematically worked out the route through the odd circumstances that may affect the silica sol. Theoretically, the strong magnetic field drifted the orientation of magnetic dipoles and or raises an energy splitting between the spin states of electrons and protons. As magnetic fields affect charged

particles, therefore, it is possible to force H^+ from one part of the solution to another, causing the local concentration of H^+ to increase instantly. Fundamentally, the pH measured as $-\log [H^+]$, therefore, by changing the concentration of H^+ , the pH will change. However, this effect will be incredibly small, particularly in non-ferrie liquids, and thus hardly noticeable. Furthermore, we can, with full conviction, exclude this scenario, where the sol was continuously mixing during the magnetic field exposure. As a result, like those drifts do not affect varying the acidity of the sol.

Commonly, in DLS test, particle size distributions are calculated regarding particles volume, particles number or scattering intensity. The three methods were adopted; however, they show the same behavior, with a minor variation in the particle size values. Because the DLS technique generates distributions with intrinsic peak growth, there will be a continuous inaccuracy in the depiction of the intensity distribution. The volume and number distributions produced from these power distributions are best employed for statistical applications or for estimating relative proportions [Alattar 2021].

Figure 4 illustrates the magnetic field exposure time effect on the size of silica nanoparticles. Apparently, at the first two minutes of the exposure time, the essential reducing in the particles size has occurred, then the particles size increases. The long exposure time of a strong magnetic field may enhance the locally induce dipole moment in these nanoparticles. Subsequently the polarized nanoparticles were electrically aligned resulting in relatively long (few nanometers) agglomerated chains. These chains may be recorded as bigger size particles in the DLS test.

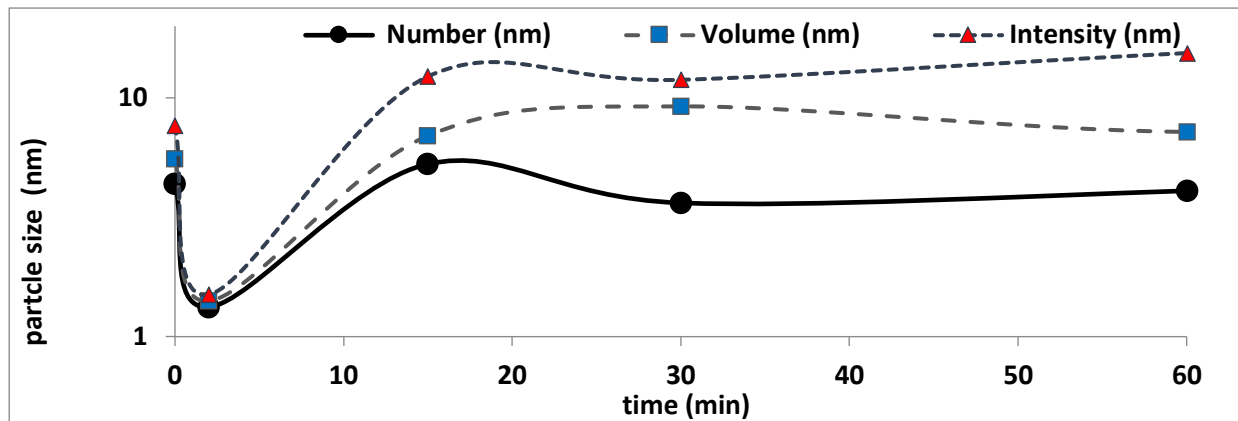


Fig. 4. Particle size results following three testing methods; number, volume, and intensity at different exposing time and pH = 3.

The applied magnetic field found to be of no noticeable effect on the particle size of the sample of $pH = 2.5$ (table 2), which cannot be classified based on the DLVO theory. How to understand the no response of the suspending silica nanoparticles to the high magnetic field. At the moment of zero charge for PZC, it would be logical to presume that the silica surface is unloaded. The behavior of these uncharged particles would also not be affected by the magnetic field. In this context, DLVO's theory defines particle suspension equilibrium by integrating electrostatic and van der Waals forces.

Van der Waals forces are weak outside of silica spheres [Bergström 1997]. This idea has received a lot of attention due to its failure to explain particle activity at lower pH values. Because there is no electrostatic repulsion, the silica particles remain stable at pH levels about 2. (the PZC). As a result of this contradiction, novel non-DLVO interactions, such as those that think the particle's water structure and the so-called "layer of gel," which is thought to exist at low pH, can interact, have been proposed. The stability of smaller nanoparticles at low pH levels may be explained by extra repulsive forces not described in the DLVO theory. Because they are mechanical barriers to particle aggregation and are only a few nanometers from the silica base, poly (silica acid) gel coatings are thought to be the source of these additional forces [Kobayashi *et. al.*, 2005, Johnson *et. al.*, 2008]. Because of its increased surface area, this gel coating has a similar effect on smaller nanoparticles as it does on larger nanoparticles. Because poly (silica acid) deteriorates at higher pH levels, the gel layer is only present at lower pH levels. These findings suggest that the DLVO theory needs to be complemented by studies that have knowledge of particle behavior. In the case of recipe (I), under the presence of high magnetic field 3T. The particles size decreased notably, from 3.22 nm to 1.16 nm when the sol pH value lightly increases from pH = 2.5 to pH = 3 respectively. This decreasing confirms that there is an influence of magnetic field on the particles size growth. Further increasing in sol pH value to pH = 4 will significantly increase the particles size from 1.16 nm to 688 nm, then at pH = 5 the particle size was being redacted to 261 nm.

Under a relatively low magnetic field, 0.5 T, the particles size increased dramatically, from 3.22 nm to 622 nm, when the sol pH value lightly increases from 2.5 to 3 respectively. Further increasing in sol pH value to pH = 4 will dramatically decrease the particles size from 622 nm to 3.27 nm, then at pH value of pH = 5, to 0.51 nm.

To the best of our knowledge, there is no theoretical model cover these odd behaviors. It may be that, if the intensity of the applied magnetic field is strong enough (for example 3T), it may snatch the attached water molecules from the silica surface. Whereas the silicone oxide-derived sol-gel networks produce mainly linear or arbitrarily branched polymers under acid-catalyzed conditions [Moon *et. al.*, 2017]. The strong magnetic field may attack then broke the weak points inside the polymerlike nanoparticles itself as well. At pH = 3, this attacking then the broking process will lead subsequently to tiny silica nanoparticles (from 3.22 nm to 1.16 nm). Taken into consideration the almost uncharged silica nanoparticles under pH = 3 environment. However, further investigations should be carried out so that to confirm this postulation.

At higher pH values, pH = 4 and pH = 5, the surface of the silica particles will be more charged. However, it can be concluded that soliton-type excitation occurs on the silica chain, for example, as polymers are used, and this excitation plays a role as an electrical conductor. Ring currents on loops produce magnetic moments perpendicular to loops in silica networks. The loops tend to align, thus, perpendicular to the magnetic field. Now, this may mean that the excitement is not limited to this type; there may be excitement around magnetic moments. In such case, parallel to the magnetic field, the silica chains are aligned. The crystallites were then oriented with their crystallographic axes in the direction of the magnetic field applied during the preparation of the light. The magnetic field applied during the preparation of the gel is thus supposed to make the structure of the silica particles anisotropic. Taking into account that there is an easy direction of

magnetization in silica particles, therefore, the reduction in magneto-crystalline anisotropy energy may drive the reduction of the silica particle size in the sol under application of a strong magnetic field. Furthermore, the applied magnetic field may build up a barrier around the silica particles preventing the grain growth process. Nano-magnetism, however, typically recognizes so-called single-domain particles; for single-domain size, the typical values range from 5 to 125 nm. All of these particles are domain-free magnetic nanoparticles because a single particle with a size equal to the minimal domain size isn't divided into domains. This means that particles are smaller than the range of domain sizes (DFMN). Each particle functions like a gigantic paramagnetic atom and manifested super-paramagnetic conductivity during the moment when the temperature exceeds the so-called blocking temperature. On the other hand, in case of the presence of relatively low magnetic field, 0.5 T, there was a reverse scenario. At a little shifting from ZPC, pH = 3, the presence of such magnetic field snatches the attached to the molecules of water from the silica surface. This snatching might cause the hydration layer to breakdown, allowing aggregation to occur, leading to a 622 nm wide agglomerated particle. We should take into account that the silicon dioxide is diamagnetic material; basically, these materials have a little response for such relatively low magnetic fields. While at higher pH values, pH = 4 and pH = 5, the surface of the agglomerated silica particles will be charged. This sizable charged particles then polarized owing to the applied magnetic field, inducing inner electrical dipole moment. Therefore, the combination of the electric dipole moment and electrically charged sizable particles, as repulsive forces, maybe excesses the agglomeration adhesion force.

So this perturbation may detonate this sizable particle to tiny nanoparticles, 0.6 nm in size. The monotonically decreasing in the silica particle sizes according to the increases of pH value, Table 2, may confirm the influence of the detonating power suggested above. Take into account monotonically increasing pH values reveals an increase in surface charges then dipole moment resulting in high detonating power.

5. Conclusion

Applied of magnetic field throughout the preparation of the gel is thus supposed to make the structure of the silica particles anisotropic. Taking into account that there is an easy direction of magnetization in silica particles, therefore, the reduction in magneto-crystalline anisotropy energy may drive the reduction of the silica particle size in the sol under application of a strong magnetic field. Furthermore, the applied magnetic field may build up a barrier around the silica particles preventing the grain

growth process. Nano-magnetism, however, typically recognizes so-called single-domain particles; for single-domain size, the typical values range from 10 to 140 nm

However, the accurate monitoring of the scale of nanoparticles using this method has proven to be a challenging task and further investigations should be carried out in order to improve all experimental parameters.

Due to the large number of searches for influences that are important in controlling the size of nanoparticles, where many studies have used light such as laser and others, or heat, pressure, or electricity, but the magnetic field is also important and this is proven through this study, this study is modern in its kind and application.

ACKNOWLEDGEMENTS

We would like to acknowledge the Al-Karkh university of science and Iraqi ministry of higher education and scientific research for their generous supports.

References.

- Alattar, A.M., (2021).** Spectral and structural investigation of silica aerogels properties synthesized through several techniques. *Journal of Non-Crystalline Solids*, 571, p.121048. <https://doi.org/10.1016/j.jnoncrysol.2021.121048>
- Andrews, R. and Weisenberger, M.C., (2004).** Carbon nanotube polymer composites. *Current opinion in solid state and Materials Science*, 8(1), pp.31-37. <https://doi.org/10.1016/j.cossms.2003.10.006>.
- Battisha, I.K., Badr, Y., Shash, N.M., El-Shaarawy, M.G. and Darwish, A.G.A., (2010).** Detection of up-conversion in nano-structure BaTiO₃ co-doped with Er³⁺ and Yb³⁺ ions. *Journal of sol-gel science and technology*, 53, pp.543-550. <https://doi.org/10.1007/s10971-009-2129-5>.
- Beecher, P., Shevchenko, E.V., Weller, H., Quinn, A.J. and Redmond, G., (2005).** Magnetic-Field-Directed Growth of CoPt₃ Nanocrystal Microwires. *Advanced Materials*, 17(8), pp.1080-1083. <https://doi.org/10.1002/adma.200401566>.
- Bergström, L., (1997).** Hamaker constants of inorganic materials. *Advances in colloid and interface science*, 70, pp.125-169. [https://doi.org/10.1016/S0001-8686\(97\)00003-1](https://doi.org/10.1016/S0001-8686(97)00003-1).
- Brinker, C.J. and Scherer, G.W., (1990).** The physics and chemistry of sol-gel processing. *Sol-gel science*, 3, pp.115-119.
- Douglas, J.F. and Garboczi, E.J., (1995).** Intrinsic viscosity and the polarizability of particles having a wide range of shapes. *Advances in chemical physics*, 91, pp.85-153. <https://doi.org/10.1002/9780470141502.ch2>
- Firouzi, A., Atef, F., Oertli, A.G., Stucky, G.D. and Chmelka, B.F., (1997).** Alkaline lyotropic silicate– surfactant liquid crystals. *Journal of the American Chemical Society*, 119(15), pp.3596-3610. <https://doi.org/10.1021/ja963007i>.
- Hirota, N., Ando, T., Shimada, T., Wada, H. and Sakka, Y., (2008).** In situ observation of magnetic orientation process of feeble magnetic materials under high magnetic fields. *Science and Technology of Advanced Materials*. <https://doi.org/10.1088/1468-6996/9/2/024211>

Johnson, A.C.J., Greenwood, P., Hagström, M., Abbas, Z. and Wall, S., (2008). Aggregation of nanosized colloidal silica in the presence of various alkali cations investigated by the electrospray technique. *Langmuir*, 24(22), pp.12798-12806. <https://doi.org/10.1021/la8026122>.

Julien, R. (1989) Usp. Fiz. Nauk. Fractal systems .157, 339–357

Kobayashi, M., Juillerat, F., Galletto, P., Bowen, P. and Borkovec, M., (2005). Aggregation and charging of colloidal silica particles: effect of particle size. *Langmuir*, 21(13), pp.5761-5769. <https://doi.org/10.1021/la046829z>.

LeBaron, P.C., Wang, Z. and Pinnavaia, T.J., (1999). Polymer-layered silicate nanocomposites: an overview. *Applied clay science*, 15(1-2), pp.11-29. [https://doi.org/10.1016/S0169-1317\(99\)00017-4](https://doi.org/10.1016/S0169-1317(99)00017-4).

Moon, S. and Lee, K.J., (2017). Simultaneous control of size and surface functionality of silica particle via growing method. *Advanced Powder Technology*, 28(11), pp.2914-2920. <https://doi.org/10.1016/j.appt.2017.08.019>.

Motokawa, M., (2004). Physics in high magnetic fields. *Reports on Progress in Physics*, 67(11), p.1995. DOI 10.1088/0034-4885/67/11/R02.

Odegard, G.M., Clancy, T.C. and Gates, T.S., (2005). Modeling of the mechanical properties of nanoparticle/polymer composites. *Polymer*, 46(2), pp.553-562. <https://doi.org/10.1016/j.polymer.2004.11.022>.

Quickel, T.E., Le, V.H., Brezesinski, T. and Tolbert, S.H., (2010). On the correlation between nanoscale structure and magnetic properties in ordered mesoporous cobalt ferrite (CoFe₂O₄) thin films. *Nano letters*, 10(8), pp.2982-2988. <https://doi.org/10.1021/nl1014266>.

Sandkühler, P., Sefcik, J., Lattuada, M., Wu, H. and Morbidelli, M., (2003). Modeling structure effects on aggregation kinetics in colloidal dispersions. *AIChE journal*, 49(6), pp.1542-1555. <https://doi.org/10.1002/aic.690490618>.

Sögaard, C., Funehag, J. and Abbas, Z., (2018). Silica sol as grouting material: a physio-chemical analysis. *Nano convergence*, 5, pp.1-15. <https://doi.org/10.1186/s40580-018-0138-1>.

Stephen, B., (2001). Magnetism in condensed matter. *Department of Physics, University of Oxford*. Oxford University Press.

<http://www.physics.fudan.edu.cn/tps/people/jzhao/Book&Paper/Magnetism%20in%20Condensed%20Matter.pdf>

Stöber, W., Fink, A. and Bohn, E., (1968). Controlled growth of monodisperse silica spheres in the micron size range. *Journal of colloid and interface science*, 26(1), pp.62-69. [https://doi.org/10.1016/0021-9797\(68\)90272-5](https://doi.org/10.1016/0021-9797(68)90272-5).

Tamar, Y. and Sasson, Y., (2013). Examination of the regime controlling sol–gel based colloidal silica aggregation. *Journal of non-crystalline solids*, 380, pp.35-41. <https://doi.org/10.1016/j.jnoncrysol.2013.08.018>.

Trompette, J.L. and Meireles, M., (2003). Ion-specific effect on the gelation kinetics of concentrated colloidal silica suspensions. *Journal of colloid and interface science*, 263(2), pp.522-527. [https://doi.org/10.1016/S0021-9797\(03\)00397-7](https://doi.org/10.1016/S0021-9797(03)00397-7).

Twej, W.A., Alattar, A.M., Drexler, M. and Alamgir, F.M., (2017). Tuned optical transmittance in single-step-derived silica aerogels through pH-controlled microstructure. *International Nano Letters*, 7, pp.257-265. <https://doi.org/10.1007/s40089-017-016-0>.

Tyagi, A.K. and Banerjee, S. eds., (2017). Materials under extreme conditions: recent trends and future prospects.

Yildiz, E., Dost, S. and Yildiz, M., (2006). A numerical simulation study for the effect of magnetic fields in liquid phase diffusion growth of SiGe single crystals. *Journal of Crystal Growth*, 291(2), pp.497-511. <https://doi.org/10.1016/j.jcrysgro.2006.03.040>.

Zeng, Q.H., Yu, A.B. and Lu, G.Q., (2008). Multiscale modeling and simulation of polymer nanocomposites. *Progress in polymer science*, 33(2), pp.191-269. <https://doi.org/10.1016/j.progpolymsci.2007.09.002>.

Submitted: 04/06/2022

Revised: 29/08/2022

Accepted: 12/09/2022

DOI : 10.48129/kjs.20819